



UNIVERSITY OF
LIVERPOOL

Characterisation of Irradiated Planar Silicon Strip Sensors for HL-LHC Applications

Thesis submitted in accordance with the requirements of
the University of Liverpool for the degree of Doctor in Philosophy
by

Sven Wonsak

October 2016

Supervisors:
Prof. Gianluigi Casse (Liverpool)
Dr. Michael Moll (CERN)

Sheldon: *I'm a physicist. I have a working knowledge of the entire universe and everything it contains.*

Penny: *Who's Radiohead?*

Sheldon [after twitching for a minute]: *I have a working knowledge of the important things.*

THE BIG BANG THEORY, SEASON 2 EPISODE 18

Abstract

Characterisation of Irradiated Planer Silicon Strip Sensors for HL-LHC Applications by *Sven Wonsak*.

The upgrade of the Large Hadron Collider (LHC) to the High Luminosity LHC (HL-LHC) will increase the requirements on radiation hardness of silicon sensors of the two multi-purpose experiments, ATLAS and CMS, at CERN. For this purpose the CERN RD50 collaboration is investigating radiation hard semiconductor detectors for high luminosity applications. The work for this thesis was done within this framework.

Charge multiplication can be beneficial in this context because the collected charge of irradiated devices decreases with increasing irradiation fluence. Thus the effect of different read-out strip pitch values and strip widths, as well as double implant energy or double diffusion time and intermediate strips, have been investigated for irradiated sensors. Intermediate strips have not shown any benefits, but sensors with a low width-over-pitch (W/P) ratio collect more charge than sensors with higher W/P values. This can be improved by doubling the implant energy. Annealing the sensors irradiated to $5 \times 10^{15} \text{ n}_{\text{eq}}/\text{cm}^2$ has shown that at bias voltages higher than 1000 V the collected charge can increase with increasing annealing time.

Measuring the collected charge of highly irradiated $50 \mu\text{m}$ thick sensors has been challenging because random noise peaks could be misidentified as signal due to the low signal value at fluences larger than $1 \times 10^{16} \text{ n}_{\text{eq}}/\text{cm}^2$. New analysis methods were tested and the use of a different fit function shows promising results.

The measurement of the current of irradiated sensors with thicknesses from $50 \mu\text{m}$ to $298 \mu\text{m}$ has shown that the effective energy value has an upper limit, given by the literature value. For the current related damage rate of highly irradiated sensors the literature value describes an upper limit as well. The knowledge of these limits allows the design of large detector systems.

A novel approach was tested to generate a multiplication layer close to the strip surface by irradiating sensors with low energy protons at the Birmingham irradiation facility. The target thickness of this multiplication layer is approximately 10 to $20 \mu\text{m}$, but in the irradiations shown in this thesis this target has not been reached. However, the results have improved the knowledge of the irradiation facility and the simulation so that it should be possible to reach the expected thickness in a future irradiation.

Contents

Abstract	5
1. Introduction	11
2. Silicon as Particle Detector	15
2.1. Interaction of Particles with Matter	15
2.1.1. Energy Deposition	16
2.2. Semiconductors	18
2.2.1. Doping	19
2.2.2. The pn-Junction	21
2.3. Silicon Strip Detectors	32
2.3.1. Working Principle of Silicon Detectors	32
2.3.2. Detector Production	33
2.3.3. Electric Field and Ramo's Theorem	37
2.3.4. Noise	41
2.4. Radiation Damage	43
2.4.1. Bulk Damage	43
2.4.2. Annealing	47
2.4.3. Surface Damage	48
3. Measurement Setups	55
3.1. IV-CV	55
3.1.1. Probe Station	55
3.1.2. Cold IV (old)	57
3.1.3. Cold IV (new)	59
3.1.4. CERN IV	60
3.2. Charge Collection	61
3.2.1. ALiBaVa System	62
3.2.2. ALiBaVa Data Analysis	66
3.2.3. Calibration	74
4. Charge Multiplication Study	79
4.1. Charge Collection Measurements	79
4.1.1. Unirradiated Sensors	83
4.1.2. Proton Irradiation, $1 \times 10^{15} \text{ n}_{\text{eq}}/\text{cm}^2$	83
4.1.3. Neutron Irradiation, $1 \times 10^{15} \text{ n}_{\text{eq}}/\text{cm}^2$	85

4.1.4. Neutron Irradiation, $5 \times 10^{15} \text{ n}_{\text{eq}}/\text{cm}^2$	88
4.2. Annealing Study	93
4.3. Long-term Bias Test	99
4.4. Summary	106
5. Thin Sensors	109
5.1. Charge Collection Measurement	110
5.2. Data Analysis	115
5.2.1. Analysis Methods	115
5.2.2. Simulated Data	117
5.2.3. Real Data	121
5.3. Annealing	125
5.4. Summary	128
6. Study on Leakage Current	131
6.1. Measurement Setup	131
6.1.1. Methodology	134
6.2. Measurements of Unirradiated Sensors	134
6.3. Measurements after Irradiation	136
6.4. Effective Energy	139
6.5. Current Related Damage Rate	148
6.6. Comparison with Data Measured at CERN	157
6.7. Comparison with Peltier Setup	159
6.8. Comparison with Freiburg Data	162
6.9. Summary	169
7. Generation of a Shallow Irradiation Damage Layer	171
7.1. Geant4 Simulations and Irradiations	172
7.1.1. Simulation Details	173
7.1.2. Simulations for the First Irradiation	175
7.1.3. First Irradiation in December 2015	178
7.1.4. Simulations after First Irradiation	183
7.1.5. Second Irradiation in April 2016	187
7.2. Measurement Results	191
7.2.1. Measurements after Birmingham Irradiation	191
7.2.2. Measurements after Ljubljana Irradiation	194
7.3. Summary	199
8. Summary and Conclusion	201
A. Appendix	207
A.1. ALiBaVa Daughterboard Calibration Factors	207
A.2. Beetle Chip Settings	208
A.3. Charge Multiplication Sensors	209

A.4. List of Sensors for IV study	212
A.5. Micron and Hamamatsu Detector Properties	213
A.6. Effective Energy	214
B. Acronyms and Abbreviations	215
List of Figures	219
List of Tables	223
Bibliography	225
Acknowledgement	233

1. Introduction

The goal of particle physics is to find the equations that describe fully the interactions of all particles. With this we would have a working knowledge of the entire universe and everything it contains. Currently this is not the case. 68.3% of the universe consists of dark energy and 26.8% of dark matter [ESA16], which up to now are not understood. Only 4.9% of the universe is made of ordinary matter. From this ordinary matter we know so far that it is made of quarks, leptons, gauge bosons and the Higgs boson which was only experimentally discovered in 2012. This classification is called Standard Model [CER16b] and there are equations which describe the interaction of these particles with each other.

We identify four fundamental forces in nature: the weak and the strong force, the electromagnetic force and gravitation. While the first three can be described within the Standard Model, there is no current description of gravity within this model. There are open questions beyond the Standard Model: What is the origin of the matter-antimatter difference? Is there a quantum theory of gravity? Is it possible to unify the fundamental forces at very high energies? We have a working knowledge of some aspects of the universe, but it is far away from describing everything it contains. For this reason physicists around the world use various experiments on earth and in space to extend our knowledge about the universe. The largest particle physics experiment in this context is the Large Hadron Collider (LHC) at CERN¹ near Geneva, Switzerland. Here protons are collided with a centre of mass energy of up to 14 TeV and the properties of the generated particles are measured. This is done by the two multi-purpose experiments ATLAS (A Toroidal LHC Apparatus [ATL16]) and CMS (Compact Muon Solenoid [CMS16]) as well as the more specialised experiments LHCb (Large Hadron Collider beauty experiment [LHC16]) and ALICE (A Large Ion Collider Experiment [ALI16b]).

The aim for ATLAS and CMS is to identify all generated particles in the proton-proton collisions. They are built in an onion like way, with different detector layers. Close to the collision point are silicon pixel detectors, followed by silicon strip detectors. With their high position resolution they are used to determine the primary and possible secondary interaction points. As these detectors are embedded in a magnetic field, the tracks of charged particles will be bent due to the Lorentz force, and with the precise determination of the bending it is possible to determine the charge and the mass of the particle, which allows their identification. But because

¹Conseil Européen pour la Recherche Nucléaire [CER16a]

these detectors are very close to the collision point they suffer from radiation damage. Not single protons are used, but clouds of approximately 10^{11} protons in a so called bunch. Therefore not a single proton-proton interaction is observed in a bunch crossing, but several.

For the LHC upgrade to the High Luminosity LHC (HL-LHC) the expected radiation damage received by the silicon detectors will increase. For example for the ATLAS detector the expected fluence for the innermost pixel layer is approximately $2 \times 10^{16} \text{ n}_{\text{eq}}/\text{cm}^2$ and the highest fluence for strip sensors will be approximately $5 \times 10^{14} \text{ n}_{\text{eq}}/\text{cm}^2$ [ATL12]. At the same time the number of interactions for each bunch crossing (pile-up) in the ATLAS experiment will increase from currently 35 [Mar14] to a conservative estimated value of 200 [ATL12], which requires a high granularity of the sensors. Silicon sensors are ideal for this purpose. The CERN RD50 collaboration [Mol16] has the goal to investigate radiation hard semiconductor detectors for very high luminosity applications. This thesis is done within the RD50 framework and aimed to characterise irradiated planar silicon strip sensors for HL-LHC applications.

Chapter 2 will give a brief overview of the physics of semiconductor detectors and the production method for silicon strip sensors. Furthermore the effects of radiation damage are discussed. This is followed by a description of the used measurement setups in chapter 3, including current measurements (IV) at room temperature as well as temperatures below 0°C , which are essential for the detector characterisation. For this thesis a new cold IV system has been developed and built to improve the measurement method. Charge collection measurements with the ALiBaVa system allow the characterisation in a way that is close to real sensor applications.

Several different studies are described in this thesis to improve the knowledge of irradiated silicon sensors and find optimal parameters for HL-LHC applications. The first in chapter 4 describes the attempt to produce sensors with built-in charge multiplication by changing the strip geometry (width, pitch, intermediate strips) and the fabrication method (implantation, diffusion). The sensors were irradiated with protons and neutrons and charge collection measurement results will be presented. Some of the devices have been used for an extensive room temperature annealing study and the results will be shown.

The use of thin sensors can be beneficial when a low material budget is required. In chapter 5 some results for irradiated $50 \mu\text{m}$ thick sensors will be presented. The analysis of the collected charge can be challenging and two new methods will be discussed in this chapter.

For the design of large detector systems it is crucial to know the current of irradiated silicon sensors to plan the powering scheme. In chapter 6 the current of sensors irradiated up to $2 \times 10^{16} \text{ n}_{\text{eq}}/\text{cm}^2$ is investigated. Previous studies have presented the values for the effective energy and the current related damage rate up to $1 \times 10^{15} \text{ n}_{\text{eq}}/\text{cm}^2$ and part of the work in this thesis is the comparison with the

literature values for higher irradiation fluences.

Charge multiplication can be beneficial for irradiated sensors. One method to create a sensor with a built-in multiplication layer is shown in chapter 7: the novel concept is to use a low energy irradiation to create a shallow damage layer close to the strip surface which acts as multiplication layer. Results from the first irradiations will be presented.

2. Silicon as Particle Detector

The aim for high energy particle physics experiments is to understand the fundamental laws of nature by reconstructing collisions of particles and analyse the outcome. For the track reconstruction different detector technologies have been invented and are in use to measure the quantities of known particles and possibly discover new ones. The particles of the Standard Model (quarks, leptons, gauge bosons and the Higgs boson) interact through the weak, strong and electromagnetic forces. Which interaction a particle can exhibit depends on its properties, like charge or colour. Semiconductors can be used for the detection of charged particles. Silicon, a material that can be widely found in nature and is one of the fundamental components in all current computer chips, is well suited for the construction of those detectors.

This chapter will give a very brief description of the working principle of silicon semiconductor strip detectors and of radiation damage. Section 2.1 gives a brief overview of the interaction of particles with matter. This is followed by a description of the basic working principle of a semiconductor in section 2.2. Section 2.3 describes how a semiconductor can be used in physics as a particle detector, with an emphasis on silicon strip detectors. For high energy physics the detectors will suffer from radiation damage due to the working environment. Section 2.4 gives a brief overview of the basic radiation damage effects.

[Har09, Spi09, Sze07] have been used as the main sources for this chapter.

2.1. Interaction of Particles with Matter

All particle detectors use the interactions of the particles with the detector material to determine their properties, such as their electrical charge and mass, which can be used to distinguish between them. In an experimental setup like the LHC at CERN high energy protons are brought into collision to investigate the properties of the generated particles. This gives a better understanding of the laws of physics and also allows the discovery of new particles, like the Higgs boson in 2012 [Aad12].

General purpose experiments like ATLAS or CMS are used to detect as many of the produced particles as possible. Therefore they are built around the interaction point (vertex) in an onion-like way: closest to the vertex are precise silicon detectors for the reconstruction of the particle tracks. These are surrounded by calorimeters

to measure the energy of the particles. A strong magnet within the detector bends the tracks of charged particles. The outermost layer consists of muon detectors, because they are the only detectable known particles that can pass the calorimeters. This very basic overview does not reflect the complexity of the real detectors. More details can be found for example in [Kle05, Gru93].

The different detectors use their own specific methods, depending on the type of detector. Amongst others, optical sensors or detectors that detect charged particles are used. Interactions of the particles are determined by their properties like energy, momentum or charge and can be classified into three categories: charged particles can interact through ionisation and produce electrons, emission of Cherenkov light and emission of transition radiation (photons). Photons, depending on the energy, can interact via the photoelectric-effect creating electrons, Compton scattering or pair creation. Neutrons can not interact through the electromagnetic force, but they can scatter or induce nuclear fission. For their detection neutrons need to interact through the strong force with a nucleus and produce charged particles. Neutrinos are a special case because they only interact through the weak force and the cross section is so small that they are not relevant for this thesis. In general purpose detectors their presence is indicated by missing energy, assuming conservation of energy in the physical process and the ability to measure the energies in all directions¹.

Semiconductor detectors are sensitive to charged particles when they create electron-hole pairs through ionisation.

2.1.1. Energy Deposition

Particles lose energy when they interact with matter. For heavy charged particles (mass larger than electron mass) the mean energy loss dE through ionisation per distance dx travelled in an absorber is given by the Bethe-Bloch equation [Gru93, Kle05]:

$$-\frac{dE}{dx} = \frac{4\pi r_e^2 m_e c^2 N_A Z z^2}{A\beta^2} \left[\ln \left(\frac{2m_e c^2 \beta^2 \gamma^2}{I} \right) - \beta^2 \right] \quad (2.1)$$

with the Avogadro number N_A , the atomic number Z and mass number A of the absorber, the electron mass m_e , the charge z and velocity $v = \beta c$ of the moving particle, the classic electron radius r_e , the ionisation potential of the absorber I and the Lorentz gamma factor $\gamma = \frac{1}{\sqrt{1-\beta^2}}$.

This equation has a minimum at $\beta\gamma \sim 4$, as can be seen in Figure 2.1. ‘In practical

¹Because of construction limitations in the experiments a complete energy measurement is only possible in the plane perpendicular to the initial proton flight path (transverse energy). Service pipes (power, cooling, data), magnet components and the beam pipe itself result in areas with less or no detectors.

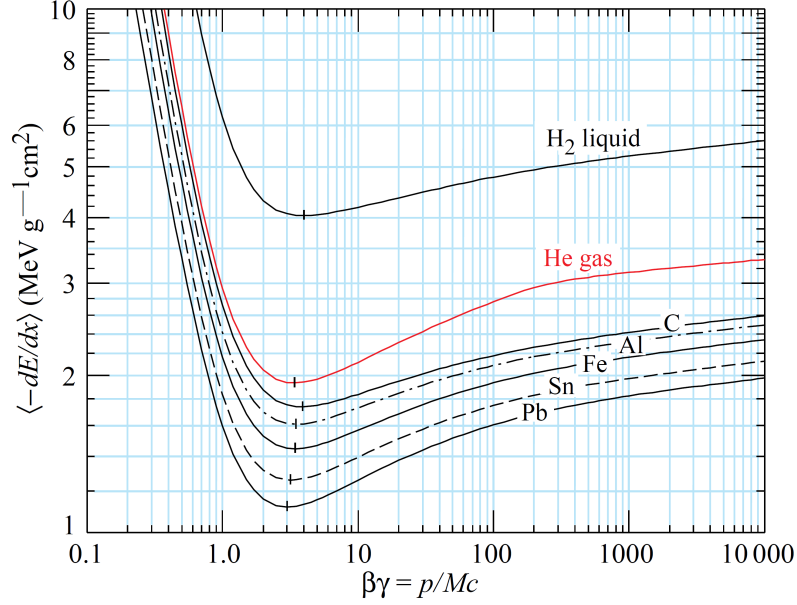


Figure 2.1.: Bethe-Bloch energy loss for different materials from [Par16a]. A minimum at $\beta\gamma \sim 4$ can be seen for all material types.

cases, most relativistic particles (e.g., cosmic-ray muons) have mean energy loss rates close to the minimum; they are “Minimum-Ionizing Particles,” or MIP’s [Par16a].

The energy loss of electrons is slightly different. At low electron energies the main energy loss is through Bremsstrahlung. For the calculation of the ionisation energy loss special care needs to be taken because the mass of the interacting particles are equal. Equation 2.1 changes therefore to [Gru93]:

$$-\frac{dE}{dx} = \frac{4\pi N_A r_e^2 m_e c^2 Z}{A\beta^2} \left[\ln \left(\frac{\gamma m_e c^2 \beta \sqrt{\gamma-1}}{\sqrt{2}I} \right) + \frac{1}{2}(1-\beta^2) - \frac{2\gamma-1}{2\gamma^2} \ln(2) + \frac{1}{16} \left(\frac{\gamma-1}{\gamma} \right)^2 \right] \quad (2.2)$$

The number of produced ions through ionization n_T is proportional to the energy loss ΔE in matter [Kle05]

$$n_T = \frac{\Delta E}{W_i} \quad (2.3)$$

where W_i is the energy loss per produced ion pair (in silicon a electron-hole pair). The required mean energy W_i to produce a electron-ion pair in gases is between 41 eV in helium and 22 eV in xenon. It is much smaller in semiconductors: 3.5 eV in silicon and 2.85 eV in germanium. The number of produced electron-hole pairs in semiconductors is much higher for the same total energy loss and therefore the

fractional statistical fluctuation of the number of produced electron-hole pairs is lower.

2.2. Semiconductors

Particle detectors can utilize various solid, liquid or gaseous media and the choice depends strongly on the requirements of the experiment. In general there are three types of solid materials, classified by their electrical conductivity: insulators, semiconductors and conductors. These categories can be described using the band-model of solid state physics: according to the Schrödinger equation electrons can only have certain energies which are depicted by the so called bands. Following the Pauli principle these are filled in multi-atomic systems with electrons starting at the lowest energy level. The band with the highest energy which still contains electrons at a temperature of 0 K is called valence band while the next higher band is the conduction band. Figure 2.2 shows the valence band and conduction band configuration for the three material categories. In an insulator the energy difference between the two bands (band gap) is so high that even thermal excitation is not enough to lift electrons into the conduction band. For conductors the two bands interfere with each other so that a current flow is always possible. The band gap for semiconductors is small compared to insulators, but with increasing temperature the thermal energy is sufficient to lift individual electrons into the conduction band. This leaves an empty space in the valence band, the so called hole. For germanium the energy gap is approximately 0.66 eV at 300 K while it is 1.12 eV for silicon [Sze07]. While germanium has a lower band gap, silicon as material is widely used in industry for the production of microchips and is relatively easy available in the form of silicon-dioxide, a main component of sand.

Silicon sensors were first used in particle physics in the NA11 and NA32 experiments at the Super Proton Synchrotron SPS at CERN in 1980-86 [Max17]. The basic principles of this technology are still used today for silicon sensors, as well as for the fabrication of integrated circuits.

The occupation probability for electrons in an intrinsic semiconductor (no impurities) is given by the Fermi-Dirac statistics where the Fermi energy E_F is the energy at which the occupation probability of a possible state is one half [Lut99]. This means that in the band-model the Fermi energy is close to the middle between valence band and conduction band. The density of free electrons (n) and holes (p) can be calculated using the Fermi-Dirac statistics (see [Sze07]):

$$n = N_C \exp\left(-\frac{E_C - E_F}{k_B T}\right) \quad (2.4)$$

$$p = N_V \exp\left(-\frac{E_F - E_V}{k_B T}\right) \quad (2.5)$$

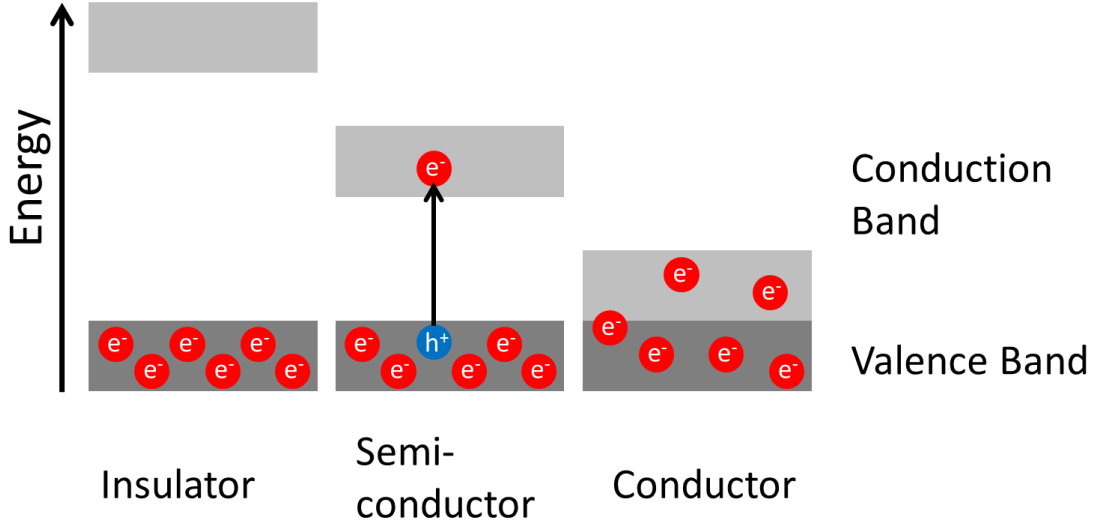


Figure 2.2.: Schematic view of material classification according to the electric properties. The position of electrons (e) and holes (h) depends on the Pauli principle, the material type and their energy.

where N_C and N_V are the effective densities of states in the conduction and valence bands, E_C is the lowest energy level of the conduction band and E_V the highest energy level of the valence band. k_B is the Boltzmann constant and T the temperature in Kelvin. The Fermi level for intrinsic semiconductors E_i can be found from the requirement that the number of electrons and holes are equal ($n = p = n_i$) [Spi09]:

$$E_F = E_i = \frac{E_C + E_V}{2} - \frac{k_B T}{2} \log\left(\frac{N_C}{N_V}\right) \quad (2.6)$$

This allows to rewrite the equations 2.4 and 2.5 to [Lut99]:

$$n = n_i \exp\left(\frac{E_F - E_i}{k_B T}\right) \quad (2.7)$$

$$p = n_i \exp\left(\frac{E_i - E_F}{k_B T}\right) \quad (2.8)$$

The product of electron and hole concentration only depends on the band-gap energy $E_G = E_C - E_V$:

$$n \cdot p = n_i^2 = N_C N_V \exp\left(-\frac{E_G}{k_B T}\right) \quad (2.9)$$

In silicon at 300 K the intrinsic carrier concentration n_i is $1.45 \cdot 10^{10} \text{ cm}^{-3}$ [Spi09].

2.2.1. Doping

Pure silicon as a single crystal has a diamond like lattice structure: each atom is surrounded by 4 close neighbours and shares its four valence electrons with them. Adding other materials into the silicon lattice will change the electrical properties. This method is called doping and results in two different types of silicon: n-type and p-type. The number of doping atoms, or impurities, is small compared to the total number of silicon atoms.

n-type For n-type silicon an excess of electrons in the conduction band is created, which creates free negative charge carriers. This is done by doping the silicon with an element of the 5th group of the periodic system, which has five valence electrons. Four of them are required for the covalent bonding to the neighbouring silicon atoms in the lattice while one is free to increase the conduction. Because the number of conduction electrons is increased this type of impurity is called donor. Typical elements for creating n-type silicon are arsenic or phosphorous.

p-type To create a p-type silicon, which has additional holes in the valence band, an element of the 3rd group is used (positive charge carrier). With only three valence electrons one is missing to complete all covalent bonds to the neighbouring atoms, a hole is created. This might be filled with an electron from a neighbouring atom and in return the hole has ‘moved’. Typical elements, called acceptors, are boron and gallium.

The three different silicon types (intrinsic, n- and p-type) are shown in Figure 2.3, showing the free electron or the hole in the lattice structure.

The doping of the silicon with atoms of other elements creates localized energy levels in the band gap for donors (E_D) and acceptors (E_A). These are typically very close to the corresponding valence band or conduction band energy. For example for phosphorous the energy difference between conduction band and donor level is 0.045 eV and for boron the difference of the acceptor level to the valence band is as well 0.045 eV. With these localized levels the total Fermi energy changes and becomes dependent of the donor concentration N_D and the acceptor concentration N_A respectively.

Figure 2.4 shows the change in the density of states for doped silicon in comparison with intrinsic silicon. The change in the Fermi-level, which is caused by the introduced defect states, can be seen as increase for n-type and decrease for p-type. For both types the carrier concentrations n and p changes as well, but $pn = n_i^2$ stays valid.

If the conductivity is dominated by one type of carrier, like it is for the case n- or p-type silicon, the Fermi level can be determined according to [Spi09]. The

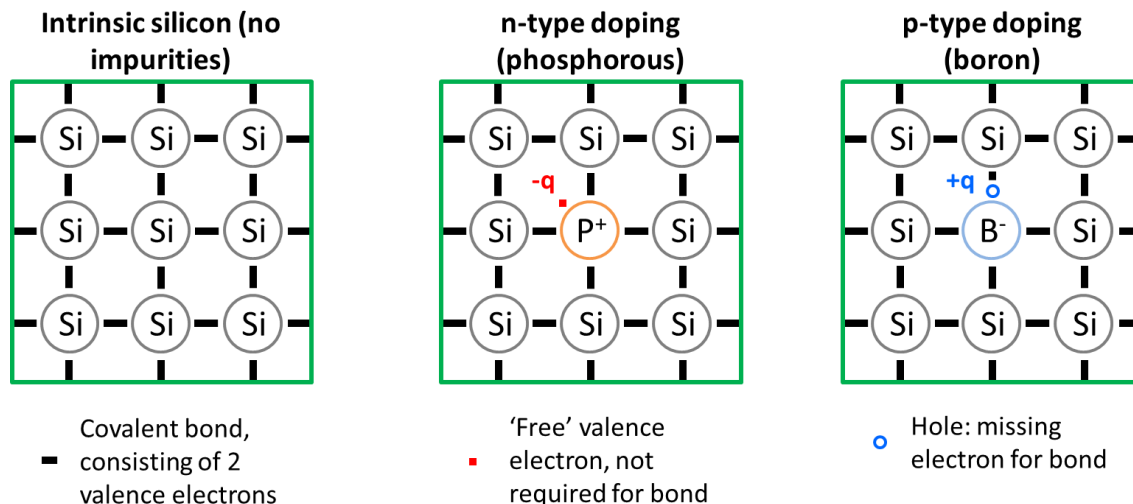


Figure 2.3.: Bond pictures for doped silicon as shown in [Sze07]. The left picture shows a silicon lattice without impurities where each Si atom is covalent bound to its four neighbours. Introducing a donor with five valence electrons for n-type silicon (middle picture) introduces a **n**egative charged electron to the conduction band. A **p**ositive hole in the valence band can be created by using a donor atom with only three valence electrons as dopant for p-type silicon (right picture).

equality $n = p$ only holds for pure crystals. Impurities tips the balance towards either electrons or holes. For doped silicon this changes to $p + N_D = n + N_A$. If for example $p \gg n$ ($N_A \gg N_D$) this can be rewritten as $p = N_A - N_D$. Substituting this in Equation 2.8 computes to:

$$E_F = E_i - k_B T \ln \left(\frac{N_A - N_D}{n_i} \right) \quad (2.10)$$

and analogue for $N_D \gg N_A$:

$$E_F = E_i + k_B T \ln \left(\frac{N_D - N_A}{n_i} \right) \quad (2.11)$$

For example, if $N_D \gg N_A$ then E_F is larger than E_i and therefore the Fermi level lies close to the conduction band.

Although the doping creates local differences in charge the crystal as a whole stays electrically neutral. This becomes important when two differently doped pieces of silicon are attached to each other and create a pn-junction.

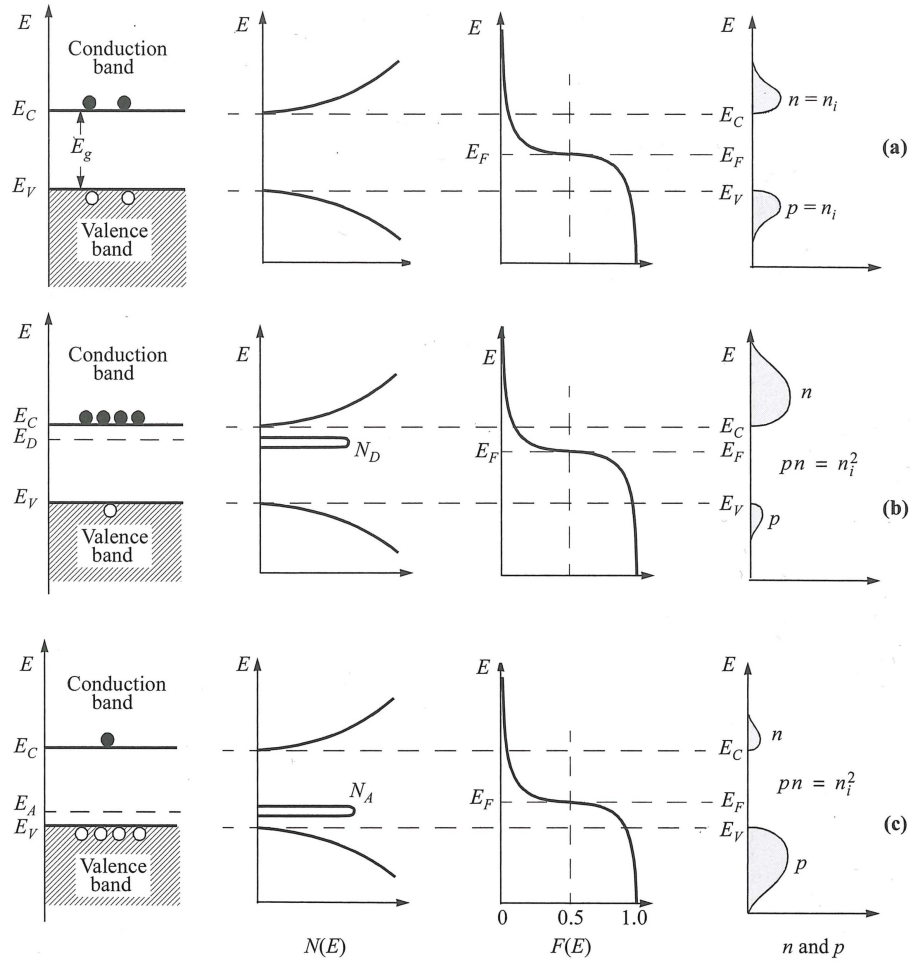


Figure 2.4.: Schematic band diagram, density of states $N(E)$, Fermi-Dirac distribution $F(E)$ and carrier concentration (n and p) for (a) intrinsic, (b) n-type and (c) p-type semiconductors at thermal equilibrium [Sze07].

2.2.2. The pn-Junction

Using the two different silicon types allows the creation of basic electronic components. The simplest configuration is realised by attaching an n-type piece of silicon to a p-type, which creates a diode. A transistor, which is the fundamental component in all modern computer chips, can be realised by bringing two diodes together back to back, which in the end can be realised as a n-p-n or p-n-p structure of doped silicon.

In a very basic model the principle of a diode can be explained in the following way: when attaching the n-type silicon to the p-type silicon the loosely bound electrons of the n-side can fill the holes of the p-side (see Figure 2.5 b) by diffusion, while the charged atom cores remain. In the n-type silicon the nucleus of the donors has a surplus of protons which generates a positive space charge while in the p-type a negative space charge is created by the now filled holes (more electrons than protons for the acceptors). These space charges are not mobile and due to the opposite sign create an electric field which opposes the electron movement direction. With more electrons filling holes the field strength increases until an equilibrium is reached when the electric field is so strong that further electrons from the n-side can not reach holes in the p-side. The region with the electric field, which has no free charge carriers, is called space charge region (SCR) or depleted region and the measurable potential difference between n- and p-side is called built-in voltage (V_{bi}). It depends on the donor and acceptor concentrations [Spi09]:

$$V_{bi} = \frac{k_B T}{e} \log \left(\frac{N_A N_D}{n_i^2} \right) \quad (2.12)$$

with the electrical charge e .

The pn-junction can be described in the band-model as well (see Figure 2.6): When a p- and a n-type semiconductor are brought into contact the electrons move to the lower Fermi level while the holes move towards the higher. In the case of an equilibrium the Fermi energy is constant everywhere. This is achieved by a potential shift of the value of V_{bi} , creating a potential barrier that the free charge carriers can not cross. Using the Poisson equation for the electrostatic potential to calculate the built-in voltage leads to [Har09]:

$$V_{bi} = \frac{1}{2\mu\rho\epsilon_{Si}} w_{dep}^2 \quad (2.13)$$

with the resistivity $\rho = \frac{1}{e\mu N}$, the charge carrier mobility μ , the permittivity $\epsilon_{Si} = 11.9 \cdot \epsilon_0$ and the depletion width w_{dep} .

In practical applications the donor and acceptor concentrations are not equal; usually one type is much higher than the other. Therefore the space charge region is much larger in the material with the lower doping concentration because the total

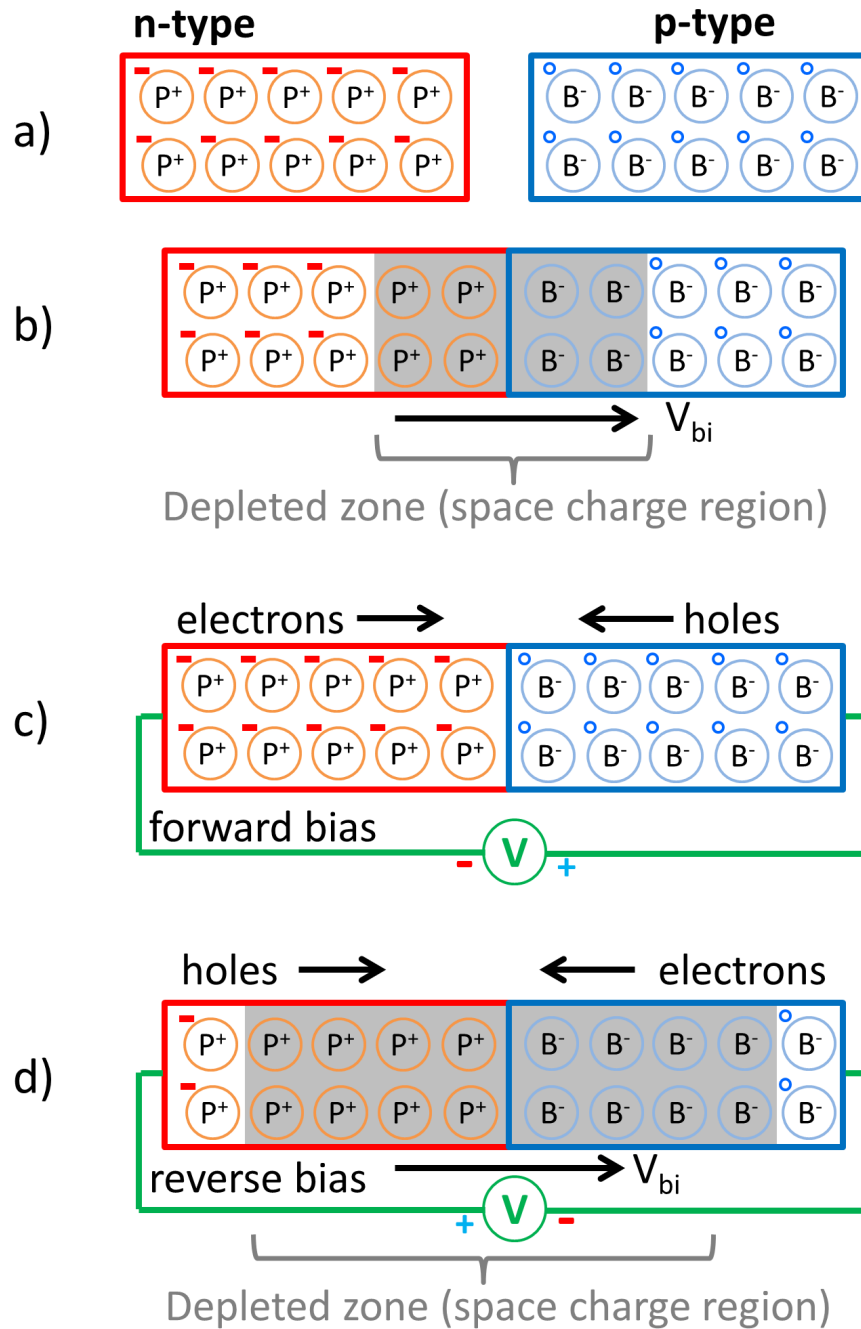


Figure 2.5.: a) n-type and p-type silicon crystals. Only the dopants and their mobile charge carriers are shown.
 b) Bringing n- and p-type material together creates a space charge region without mobile charge.
 c) Forward bias: external bias voltage is applied in opposite direction of the built in voltage (positive at p-type and negative at n-type). This removes the SCR and current can flow between p- and n-side.
 d) Reverse bias: external bias voltage in direction of V_{bi} . The SCR increases and no current can flow.

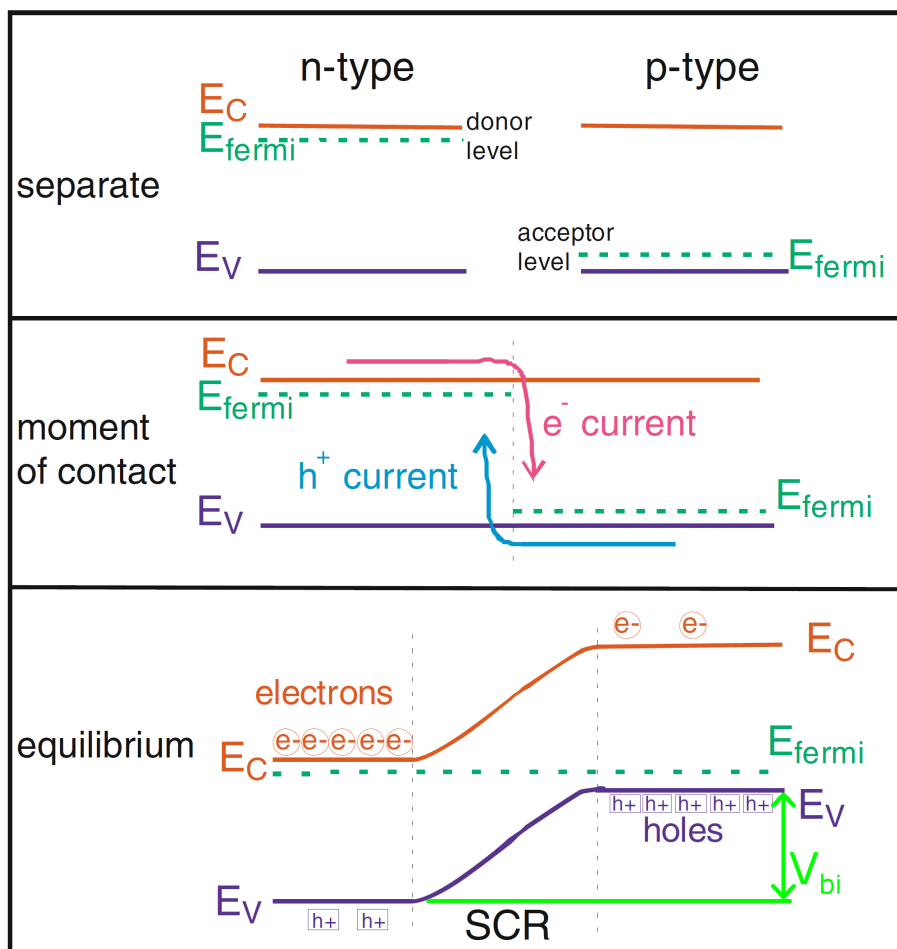


Figure 2.6.: pn-junction in band model (from [Har09]): when contacting p- and n-type the electrons move to the lower Fermi level and the holes to the higher, building up a space charge region (SCR). In the equilibrium the Fermi level is constant everywhere. This is achieved by the shift of the potentials by the built-in value V_{bi} .

charge in both sides must be equal. A commonly used approximation is to neglect the very small SCR in the highly doped material. For the two cases the equations for the resistivity can be written as:

$$N_A \gg N_D: \rho_n = \frac{1}{e\mu_n N_D} \text{ major depletion zone in n-type}$$

$$N_D \gg N_A: \rho_p = \frac{1}{e\mu_p N_A} \text{ major depletion zone in p-type}$$

with $\mu_n \approx 1350 \text{ cm}^2/\text{Vs}$ and $\mu_p \approx 450 \text{ cm}^2/\text{Vs}$ [Har09]. Depending on which case is realised the proper values have to be used in Equation 2.13. A high doped semiconductor type is often highlighted with a superscripted + for example $p^+ \text{-n}$ represents a highly doped p-type and a normal doped n-type junction.

Applying an external bias voltage (V_b) affects this equilibrium. There are two possible cases how the voltage can be applied: in forward bias direction or in reverse bias direction.

Forward bias In this case the positive potential of the voltage source is connected to the p-type while the negative is connected to the n-type silicon (see Figure 2.5 c). Therefore the potential of the voltage source is in the opposite direction to V_{bi} . The excess of free electrons from the source can compensate the positive atom nuclei of the dopants and decrease the space charge zone. On the p-side the lower potential of the voltage source attracts the electrons, that have filled the holes. In forward bias direction a current flow across the pn-junction is possible.

Reverse bias Applying a negative voltage to the p-side and a positive voltage to the n-side is called reverse bias (Figure 2.5 d). The electrons in the n-type semiconductor are attracted by the positive potential of the voltage source and the holes of the p-type are filled with electrons from the source. Therefore the space charge zone increases and no current can flow through the diode. If the applied bias voltage is high enough the full semiconductor gets depleted.

With an applied external bias voltage Equation 2.13 can be rewritten to calculate the depletion depth to [Spi09]:

$$w_{dep} = \sqrt{2\varepsilon_{Si}\mu\rho(V_b + V_{bi})} \quad (2.14)$$

Because the built-in voltage is in general small compared to the bias voltage it can be neglected.

The depleted volume is free of mobile charge carriers and therefore can be approximated by a parallel plate capacitor with the undepleted region as conducting plates. This results in the equation for the capacitance C [Har09]:

$$C = \begin{cases} A\sqrt{\frac{\varepsilon_{Si}}{2\rho\mu(V_b + V_{bi})}} & \text{for } V_b \leq V_{dep} \\ A\frac{\varepsilon_{Si}}{w_{dep}} = const. & \text{for } V_b > V_{dep} \end{cases} \quad (2.15)$$

where A is the area of the pn-junction, V_{dep} the full depletion voltage at which the whole semiconductor is depleted and w_{dep} the full depletion width. This relation between capacitance and bias voltage can be used to determine the full depletion voltage. The capacitance is measured for a range of reverse bias voltages and $1/C^2$ is plotted versus V_b (the built-in voltage is neglected). Figure 2.7 shows an example graph. Up to approximately 200 V the $1/C^2$ increases with increasing bias voltage. When the full device is depleted the capacitance stays constant for all higher bias voltages. Because $1/C^2 \propto V_b$ a straight line fit in both cases can be used and the voltage at which the fit lines intersect is the full depletion voltage.

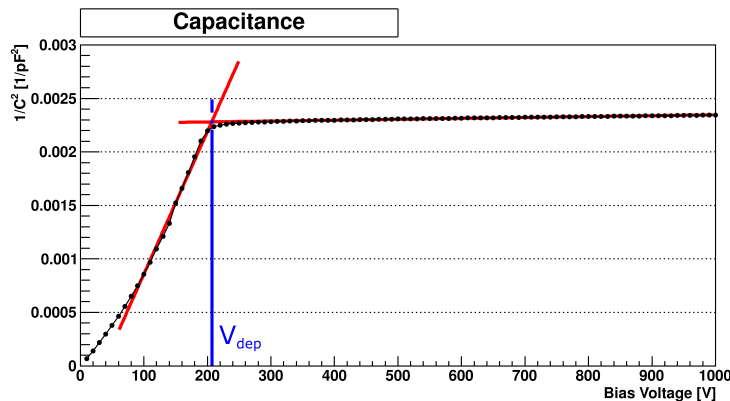


Figure 2.7.: Example for V_{dep} determination from capacitance measurement. Up to approximately 200 V the $1/C^2$ value increases with increasing bias voltage. When the full device is depleted the capacitance stays constant. The intersection voltage for the two fitted straight lines is the full depletion voltage.

Reverse Bias Current The behaviour of the pn-junction has been discussed on a very basic level, in which no current flows when the bias voltage is applied in reverse direction, but this is not representing the reality. Without any external voltage there are two opposite currents in the pn-junction. The diffusion current is generated by the concentration gradient of the differently doped materials, which leads to the flow of electrons from the n-side to the p-side (and vice versa for holes). Additionally the electric field, due to the space charge in the depleted region, drives a drift current (also known as generation current) in opposite direction. In thermal equilibrium both currents are equal, which leads to the condition that the Fermi level must be constant throughout the junction region, resulting in the creation of the potential difference between n- and p-side of the magnitude of the built-in voltage. Applying an external bias voltage leads to a condition that differs from the equilibrium so that the Fermi level is not constant throughout the junction. For example in the forward direction the electric potential across the junction decreases which result in a decrease of the drift current. The diffusion current exceeds the drift current and therefore a net current flow can be observed.

The total current density J is described by the Shockley equation [Sze07]:

$$J = J_0 \left[\exp\left(\frac{qV_b}{k_B T}\right) - 1 \right] \quad (2.16)$$

where J_0 is the saturation current density, depending on drift and diffusion constants as well as the intrinsic carrier concentration n_i . Figure 2.8 shows the current-voltage relation. If a reverse bias voltage is applied the current saturates at the value J_0 while in forward bias an exponential increase can be seen. The temperature dependence

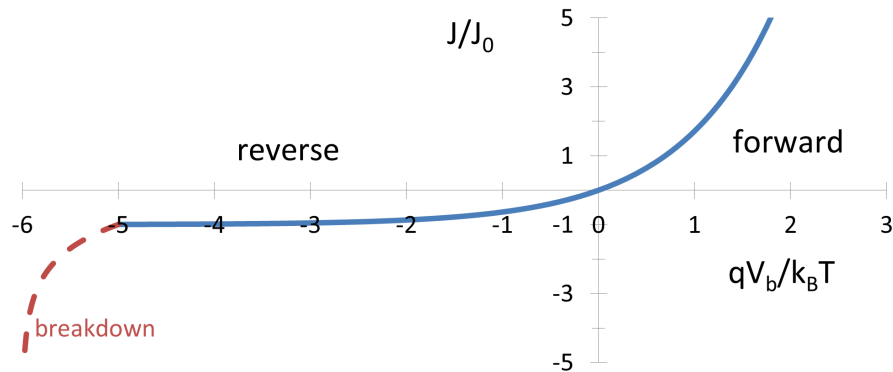


Figure 2.8.: Ideal current-voltage characteristics after [Sze07] for an external voltage in forward and reverse polarity. The dashed red curve shows an example of breakdown at higher reverse bias voltages.

of the saturation current can be approximated to [Sze07]:

$$J_0 \propto T^{3+\gamma/2} \exp\left(-\frac{E_G}{k_B T}\right) \quad (2.17)$$

where γ is a constant. The $T^{3+\gamma/2}$ term is not important compared to the exponential term so that the temperature dependence is determined mainly by the band gap energy E_G . This equation describes the ideal case but deviations have to be taken into account, which will change the value of J_0 . They can be caused by generation and recombination of carriers in the depletion layer, tunnelling of carriers, impurities in the material resulting in defect levels in the band gap or surface effects. These can lead to hole emission, which promote an electron from the valence band to a defect level in the band gap. In electron emission this electron then can proceed to the conduction band, which will increase the current. In the electron capture process a defect level can capture an electron from the conduction band, which in turn can capture a hole and they recombine which leads to a reduction of the current.

For high reverse bias voltages the current decreases fast in a so called breakdown (indicated as red dashed line in Figure 2.8). Three major effects can lead to it: thermal instability, Zener breakdown and avalanche breakdown.

- Thermal instability: Because of the heat dissipation at high reverse bias voltages the junction temperature increases. This leads to an increase of the reverse current which then increases the temperature. This positive feedback effect is also called thermal runaway.
- Zener breakdown: If the reverse bias voltage is well above the band gap, occupied energy levels in the valence band of the p-type line up with empty conduction band levels in the n-type. Movement of the electrons is prevented by the potential barrier, but it can be overcome by the quantum mechanical tunnel

effect. The tunnelling probability has a strong (exponential) dependency on the inverse electric field which means for higher field strengths the potential width decreases and therefore the tunnelling probability increases. At a field strength of approximately 10^6 V/cm [Sze07] significant current begins to flow by the tunnelling process.

- **Avalanche breakdown:** If a charge carrier acquires enough kinetic energy in the electric field it can generate a secondary electron-hole pair by impact ionization. ‘Significant multiplication of electrons starts at an electric field strength between 10 and 15 V/ μm ’ [Köh11]. The generated secondary carriers can themselves trigger the generation of more charge carriers and if the field is high enough this leads to an avalanche multiplication and the breakdown.

Comment: The Shockley equation for the current uses negative bias voltages for the reverse direction and positive for the forward direction. Because of the connection points of a power supply, one of the sides is connected to ground, while the voltage is applied at the other. In the example shown in Figure 2.8 ground (negative) would be connected to the n-side and the positive output to the p-type. The applied voltage is positive for forward bias and negative for reverse bias. But it is also possible to connect the ground connector to the p-side and the ‘positive’ connector to the n-side. In this situation forward biasing would require the application of a negative voltage (the potential at the n-side is lower than at the p-side) or a positive voltage for reverse bias. The signs of the current changes as well (positive current for reverse bias voltage). Within this thesis the reverse bias voltage was chosen to be positive, resulting in a positive current. This choice has no influence on the results and is only based on the preference of the author.

Schottky barrier When metal makes contact with a semiconductor a barrier is formed at the interface. This Schottky barrier is responsible for controlling the current conduction as well as its capacitance behaviour. Its height is defined by the alignment of the Fermi levels in metal and semiconductor. The specific contact resistance depends on the doping concentration in such a way that a higher doping concentration reduces the specific contact resistance [Sze07]. Therefore, for a good ohmic contact of a semiconductor through a metal layer a high doping concentration is preferred.

2.3. Silicon Strip Detectors

2.3.1. Working Principle of Silicon Detectors

The previous section has given an overview of the basic principles of doped semiconductors and what happens at the pn-junction. The question remains how this

can be used to produce a detector which can detect particles in high energy physics experiments. While the ionization energy is low in semiconductors, the number of free charge carriers through thermal excitation is large compared to that created through energy loss. In intrinsic silicon of a standard sensor size ($300\ \mu\text{m}$ thick, $1 \times 1\ \text{cm}^2$) there are approximately 10^9 free charge carriers [Har09], but only about 2×10^4 generated electron-hole pairs. The signal would be lost in this high background; so to be useful as particle detector the number of free carriers has to be reduced. Possible are two mechanisms: cooling to very low temperatures and therefore reducing the available thermal energy or depleting the silicon of free charge carriers. The second mechanism is based on the previous section: by applying a sufficient reverse bias voltage to a pn-junction the whole volume can be depleted of free charge carriers. This allows the detection of charged particles when they pass the depleted silicon region. Typically the main part of the detector (bulk) is lightly doped with one silicon type while the second part of the junction is created by a heavy doped but thin layer of the other doping type on the surface of the bulk. With a large area diode it is only possible to tell whether a particle has been in this area or not. For a better position resolution the highly doped part can be segmented in strips. They allow a good determination of the position perpendicular to the strip direction, while it is not possible to register the traversing particle position along the strip direction. At least two strip detectors, orientated with an angle between the strip directions, are required to get a valid position in space of a traversing particle. Two configurations are widely used: p-type strips in a n-type bulk (also known as p-in-n or n-type) or n-type strips in a p-type bulk (known as n-in-p or p-type). Typical doping concentrations for high energy physics (HEP) detectors are [Har09]:

$$\begin{aligned} \text{Si atoms: } & 5 \times 10^{22}\ \text{cm}^{-3} \\ \text{HEP bulk: } & 10^{12}\ \text{cm}^{-3} \\ \text{HEP strip: } & 10^{14} - 10^{16}\ \text{cm}^{-3} \end{aligned}$$

Figure 2.9 shows a schematic overview of a strip sensor, where the bulk material is n-type silicon. The backside is covered with a highly doped n^{++} layer which itself is covered with an aluminium layer for the backside contact. p^+ strips on the top side are used for the determination of the position of the traversing particle. The strips are covered with a thin SiO_2 film and on top of each strip is a aluminium strip. This configuration allows the AC readout of the strip. To apply the high voltage to deplete the sensor a via in the SiO_2 film is directly connected with the DC aluminium pad. For the application of the high voltage to all strips at the same time the whole strip area is surrounded by the bias ring. Each strip is connected to this ring with a polysilicon bias resistor. A guard ring surrounds the bias ring for shaping the electric field. This is necessary because lattice defects at the cut edge of the sensor can result in high electric field regions which result in a breakdown. Therefore the edges are kept at ground potential without the SCR reaching it. The example detector in the picture has an additional n^{++} ring at the cut edge to further

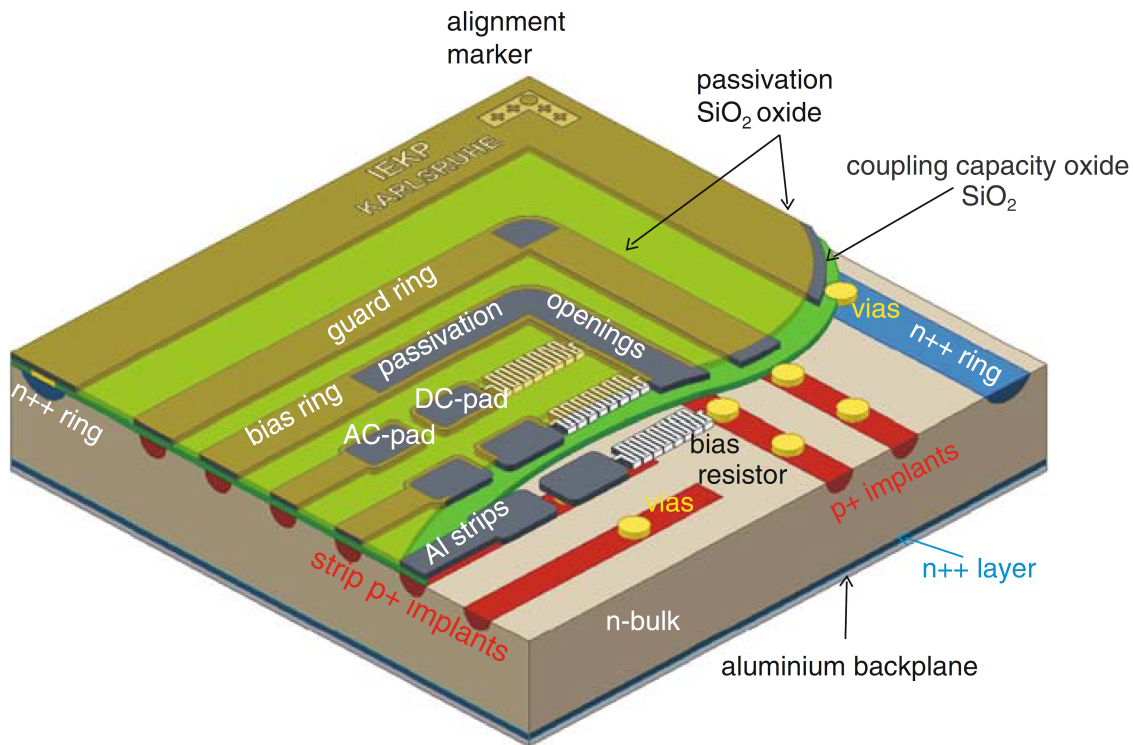


Figure 2.9.: 3D schematic sketch of a strip sensor [Har09].

prevent high fields in this region.

2.3.2. Detector Production

Silicon is very suitable for the production of semiconductor detectors. It is used in the microelectronic industry to build micro-chips and therefore the production processes are at an advanced level. Furthermore, it can easily be found in nature in the form of quartzite (SiO_2), the main component of sand. The production of detectors requires very pure single-crystal pieces of silicon, which are at least the size of the detector.

A possible series of processing steps, as described in [Har09], starts with the preparation of metallurgical grade silicon (95-90 % pure) by a series of melting processes at different temperatures and the addition of carbon as catalyst. In the next step HCl is added at approximately 300°C to form trichlorsilane, which removes many impurities. By distillation a purity of less than 1ppba (parts per billion active) can be achieved. Through chemical vapour deposition (CVD) at $900 - 1100^\circ\text{C}$ pure silicon can be gained. It then grows on approximately 1000°C hot slim rods to electronic grade polycrystalline silicon (99.99999999 % pure). To produce detector grade single-crystal silicon these slim rods are broken into pieces, dopants are

added and everything is melted in a quartz crucible to grow the single-crystal by the following process:

Czochralski ('Cz'), Figure 2.10a: The melt is held few degrees above the melting point and a rotating single-crystal is inserted from the top as a seed. By pulling it up slowly the melt solidifies in perfect crystal orientation at the boundary. The whole mechanism is inside a closed environment. It is possible to add oxygen, which will dissolve in the melt and then homogeneously enrich the final crystal. This is interesting for HL-LHC applications because oxygen can improve the radiation hardness.

Float Zone ('FZ'), Figure 2.10b: This second method to grow a single-crystal requires an intact polycrystalline silicon rod. A single crystal is attached at the bottom and then the rod is locally melted with a RF-coil from the bottom to the top. Impurities tend to stay in the melting zone (different diffusion constant) and are therefore removed from the pure single-crystal. Special doping techniques are required to produce doped silicon.

Both methods are widely used and result in a final single-crystal cylinder, the ingot. They are then cut into thin slices, called wafers. These need to be cleaned by lapping (grinding away large imperfections), etching (chemical polishing) and polishing to prepare them for the production of silicon detectors.

A third method, although not so common, is the epitaxial growth: Here the single-crystal is grown on a substrate of polycrystalline silicon, usually by chemical vapour

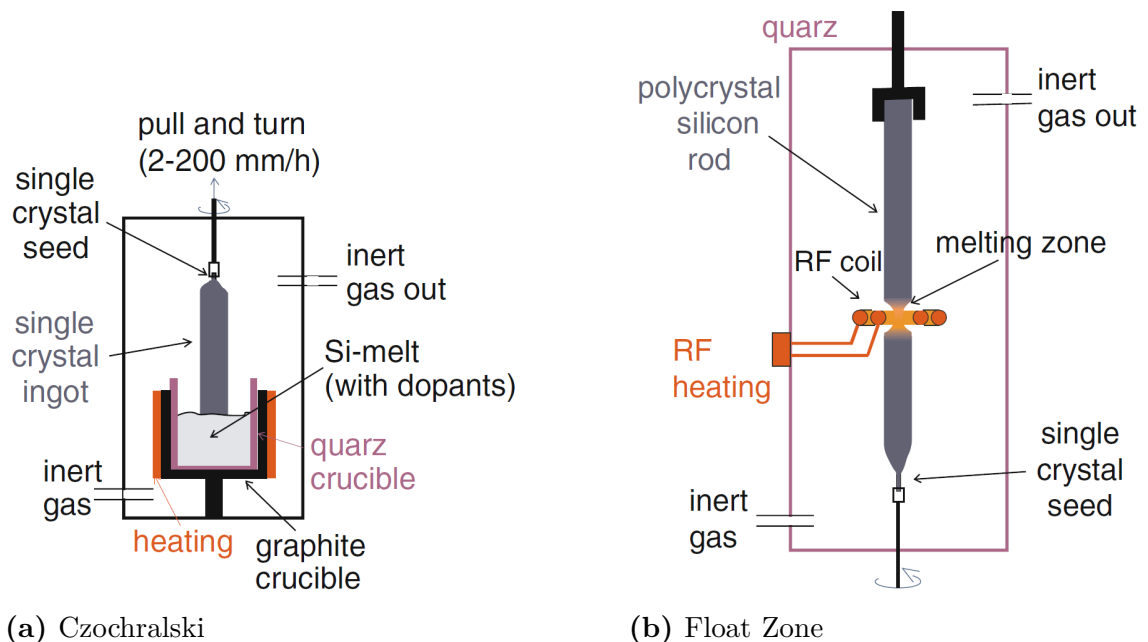


Figure 2.10.: Diagram of the single-crystal growth of silicon by either the Czochralski method (left) or the Float Zone method (right) [Har09].

deposition. At the end the substrate is removed. This method is much slower (and more expensive) than the others and usually only used to create thin wafers.

The wafers then can be used to produce silicon detectors or micro-chips. Figure 2.11 gives a general overview of the required steps, similar to those presented in [Har09]. Here only very basic processes are shown, while in a real production several more steps might be needed.

To allow processing, the wafer first is subject to oxidation, which covers it with a SiO_2 layer. To produce a segmented (strip) sensor the top side is covered with photo-resist, followed by the development with UV light through a photo mask (Figure 2.11 [1]). After the development a negative pattern is left (Figure 2.11 [2]) which then allows the etching of the SiO_2 . By removing the photo-resist (Figure 2.11 [3]) the bare silicon bulk is accessible through the holes in the silicon-dioxide. In the next step (Figure 2.11 [4]) those areas are implanted. The example shows the production of a n-in-p sensor with a p-doped bulk and n-doped strips, therefore the top side is exposed to phosphorous for implantation. At the backside a highly doped layer of the same type as the bulk is implanted to create a good ohmic contact (Figure 2.11 [5]). After a high-temperature annealing step the dopants migrate further into the bulk, which smooths the edges (Figure 2.11 [6]). To use the device as particle physics detector the deposited charge has to be read. This is done by an AC coupled aluminium strip above the doped strip. In a first step the whole sensor is again oxidated to fully cover it with high quality SiO_2 (Figure 2.11 [7]). The top side is then covered with photo-resist while the oxide at the backside is etched away in step [8]. After removing the photo-resist a thin SiO_2 layer is left above the strip implants (Figure 2.11 [9]), which allows the AC coupling. Both sides of the sensor are then covered with aluminium. Additional photo-resist is applied and the top side undergoes a development step to implement the strip pattern in the aluminium surface. It can be seen in Figure 2.11 [12] that the protective cover on the top side is wider than the implant, which helps shaping the electric field between neighbouring strips. Finally all unnecessary aluminium is etched away and the photo-resist is removed which leaves the AC coupled aluminium strips above the n^+ implant (Figure 2.11 [13]). The aluminium on the backside is used to guarantee a good electrical contact. Usually the whole top side is covered with a passivation layer of SiO_2 to protect it. Only small openings allow the contact of the different pads and the bias ring.

The described steps give a very basic overview how the strips are created. To apply the bias voltage to deplete the sensor additional steps at the end of the strips are required. The shown example in Figure 2.12 describes the process for a n-type sensor, but they do not differ for p-type devices. First the sensor is fully oxidized and then covered with a layer of polysilicon. The resistivity is defined by a controlled ion implantation (here boron). In a photo-lithographic process, similar to the production of the strips, most of the polysilicon is removed and only the meandered resistor structure is left. The bias resistor resistivity is now defined by the resistivity of the

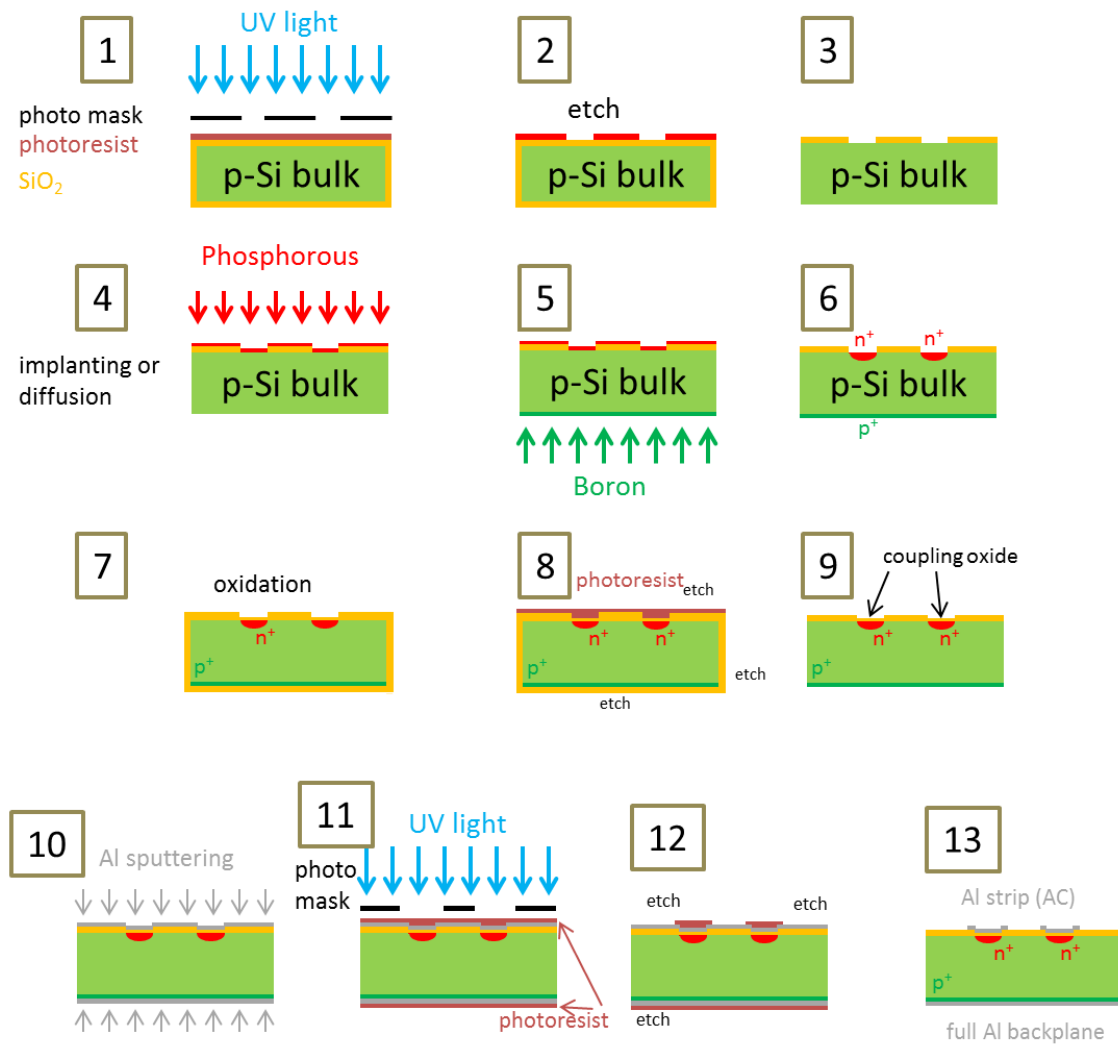


Figure 2.11.: Overview of the sensor production steps according to [Har09]. [1] Bulk is covered with SiO_2 , photo-resist on surface is developed through mask with a pattern. [2] Etching where photo-resist is developed to open gaps in SiO_2 . [3] Removal of SiO_2 in uncovered regions. [4] Implantation in uncovered bulk regions. [5] Backside implantation. [6] High temperature annealing for implant diffusion. [7] New oxide layer (high quality). [8] Photo-resist to cover strips, etching of unnecessary oxide. [9] Thin coupling oxide above strip implants is left. [10] Application of aluminium for strip and backside contacts. [11] Create pattern on aluminium surface for strip structure. [12] Etching of surplus aluminium. [13] Final sensor. (A detailed description of the steps can be found in the text.)

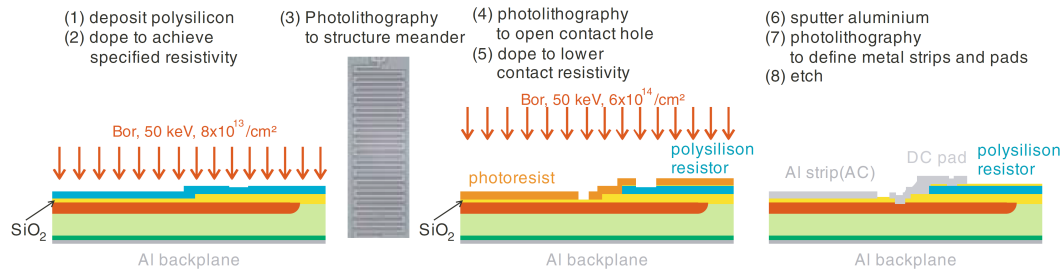


Figure 2.12.: Production of the polysilicon bias resistor for sensor biasing [Har09]. First the polysilicon is deployed at the whole surface and doped to the required resistivity. Then the surplus material is etched away and only the meandered structure of the resistor is left (3). In the next step openings for the contacts are created and another doping process is used to reduce the contact resistivity. In the last steps aluminium is sputtered on the surface for the strip contact and the contact pads (AC and DC).

polysilicon as well as the length and width of the trace. In another lithography step an opening in the SiO_2 is created to allow the direct contact of the strip implant. The right picture shows the final cross section with the AC coupled aluminium strip above the implant, the DC pad with direct contact to the strip and also to the resistor. All polysilicon resistors are connected to the bias ring, which allows the application of high voltage to deplete the whole device.

The sensors are not produced piece by piece but several on a large wafer. To separate them the wafer is cut by either a diamond saw or laser cutting. Typical wafer sizes are 6 or 8 inch while the sensor size can vary from a few millimetres for small test structures to several centimetres for real applications.

2.3.3. Electric Field and Ramo's Theorem

Figure 2.13 shows the dependence of the depletion width for a strip sensor on the applied bias voltage. The depleted region starts at the pn-junction and the width increases with increasing bias voltage. Electrons and holes, created by an ionizing particle, are separated due to the electric field and drift towards the electrodes in the depleted region (left picture). In the un-depleted region there is no force that separates them so that they can recombine immediately after creation. When the bias voltage is equal to the full depletion voltage (middle picture) the whole sensor is depleted, but the electric field at the backside is very weak. Therefore sensors are usually operated in over-depletion (right picture) so that a minimum electric field strength is available everywhere in the sensor.

In a strip sensor the signal generation, as well as the position determination, depends on the electric field. An ionizing particle, that traverses a depleted silicon

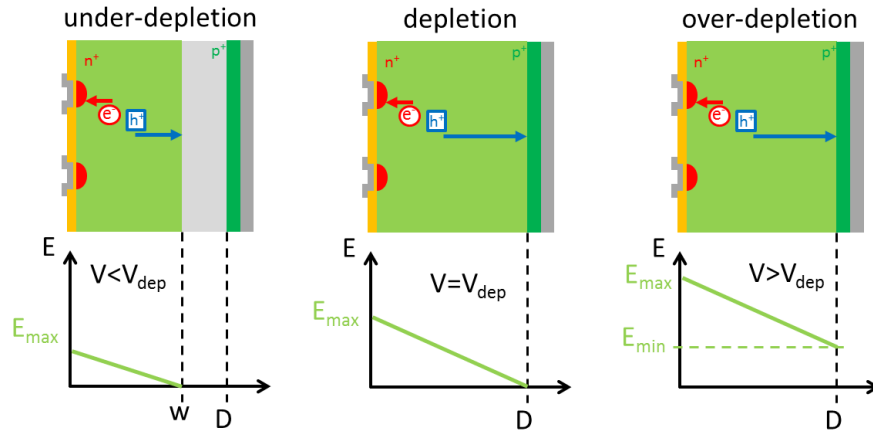


Figure 2.13.: Schematic view of a under-depleted, depleted and over-depleted strip sensor with the electric field strength for different bias voltage values (according to [Har09]).

strip detector, generates electron-hole pairs along its path (see Figure 2.14). Because of the electric field inside the depleted area the pair is separated. In a n-in-p detector the electrons drift towards the strip implants while the holes move towards the backside. Because electric field lines are always perpendicular to the conductive surface and do not cross each other they determine to which strip implant the electrons travel.

The position resolution of a strip sensor can be calculated from geometric consid-

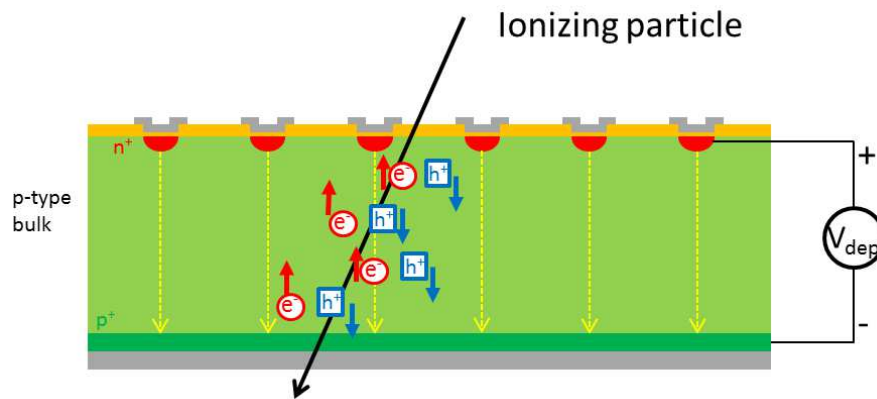


Figure 2.14.: Schematic view of a traversing particle in a depleted strip detector (according to [Har09]). Created electron-hole pairs are separated by the electric field and drift towards the implants (e^- to the strips and h^+ to the backside).

erations to

$$\sigma_x^2 = \langle \Delta x^2 \rangle = \frac{1}{P} \int_{-P/2}^{P/2} x^2 dx = \frac{P^2}{12}$$

where P is the strip pitch. This only considers a signal in a single strip. If the generated charge is distributed among several neighbouring strips the centre of gravity method can be used to improve the resolution. Figure 2.15 shows a sketch for both cases. In the left case a signal is only generated in one channel because the particle has traversed perpendicular to the strip direction. All charge carriers are generated within the electric field of a single strip and can not reach others. If the particle passes with an angle the generated charge is distributed over several strips. While a digital readout chip only indicates if the signal in a certain strip is higher than a set threshold, an analogue chip also provides the amount of collected charge. This can be used as a weight for the position reconstruction. With this the resolution, taking the pulse heights into account, can be calculated to [Har09]

$$\sigma_x \propto \frac{\text{pitch}}{\text{signal/noise}}.$$

In typical applications the signal/noise value is higher than 10, therefore the resolution improves by using the centre of gravity method.

The physical quantity that is called signal is the current in the readout strip.

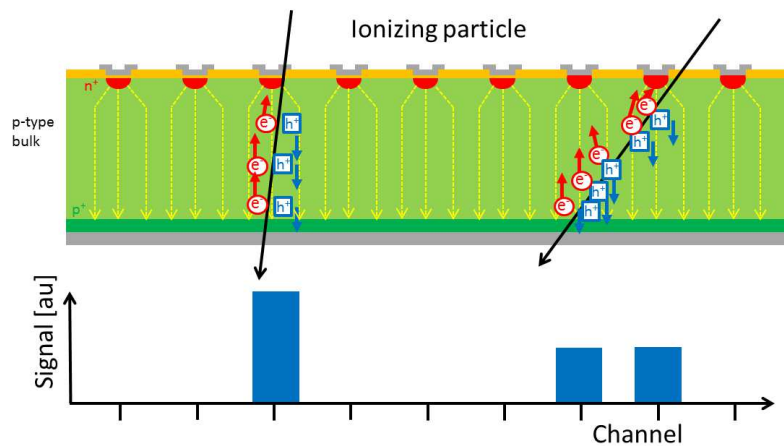


Figure 2.15.: The signal strength in a readout channel depends on the particle trajectory: if the charged particle hits the silicon detector nearly perpendicular to the strip direction (left case) than the produced electron-hole pairs only generate a signal in one particular channel. If the particle passes the electric field of several strips (right case) then a generated signal can be seen in two (or more) channels. The signal strength is given in arbitrary units, like it would be for a analogue readout chip.

When the generated electrons and holes move within the electric field, they induce a current in the strip (see Ramo's theorem below). Two possible methods can be used for reading the signal.

For a **DC** connected readout the channel in the ASIC is directly connected with the doped implant of the strip. This method makes high demands on the ASIC: the strip implants are also used for applying the bias voltage to generate the depletion zone. In general several hundreds volts are used, in extreme situations up to 2000 V. If the sensor suffered from high radiation damage the leakage current is much higher than in an unirradiated sensor. Therefore the readout chip must be able to meet these demands but at the same time be able to reliably measure the signal of the traversing particle. To allow a DC connection of the strips most sensors have allocated pads (see Figure 2.9).

An alternative is the more commonly used **AC** connection. Above each strip implant an aluminium strip is processed, which is separated by a thin SiO₂ layer from the silicon. These aluminium strips are electrically floating and therefore a change in the implant current will induce a current in the aluminium. While the small current change, generated by the traversing particle, is transferred to the aluminium strip, the constant high bias current has no effect. Therefore a readout chip must only be able to withstand the signal current.

Ramo's Theorem Ramo's theorem describes the induced current of an electric charge in an electric field. The current on the electrode i_A is given by [Spi09]:

$$i_A = q \left(\frac{\partial V_{q1}}{\partial x} \frac{dx}{dt} \right) = qv_x \frac{\partial \Phi}{\partial x}$$

with the induced voltage at the electrode V_{q1} . This equation can also be expressed as:

$$i(\vec{r}) = q\vec{v}(\vec{r}) \cdot \vec{E}_w(\vec{r})$$

where Φ is the weighting potential that describes the coupling of a charge at any position to electrode A and v_x the velocity of the charge. The weighting field E_w and the electric field are distinctly different.

- The electric field determines the charge trajectory and velocity.
- The weighting field depends only on geometry and determines how charge motion couples to a specific electrode.
- Only in two-electrode configurations are the electric field and the weighting field of the same form.

An over-biased semiconductor detector can be approximated by a uniform field (like a parallel plate capacitor). Then the electric field is given as $E = V_b/d$ while the weighting field is given as $E_w = 1/d$. For an electron-hole pair, the charge carriers move in opposite directions so they induce current of the same sign at a given electrode (despite their opposite charge). Because the hole moves slower than the electron the total cumulative induced charge depends on the integration time. Integration times larger than the collection time of all charge carriers yield in the full charge while a shorter time yields a fractional charge. Another result from this is that the induced charge begins immediately after the creation of the electron-hole pairs and not only when they reached the electrodes.

These considerations assumed only two electrodes where the current on both electrodes is the same, although of opposite sign. The continuity equation (Kirchhoff's law) must be satisfied. For a strip detector with several electrodes the instantaneous current from one electrode must balance the sum of the currents from the others, so all signal currents can be different. This is the situation in strip detectors.

2.3.4. Noise

Even for a fully depleted silicon sensors there are statistical electron and hole fluctuations, called noise. The quantifiable unit for noise is the Equivalent Noise Charge (ENC), which represents the number of electrons contributing to the noise. Several different sources can be identified and they add up quadratically to the total noise value [Har09]:

$$ENC = \sqrt{ENC_{C_d}^2 + ENC_{I_L}^2 + ENC_{R_P}^2 + ENC_{R_S}^2}$$

The noise sources are the load capacitance C_d , the leakage current I_L , the bias resistor R_P and the metal strip resistance R_S .

Figure 2.16 shows an equivalent electric circuit diagram of the different noise sources in a strip sensor. The contributions depend on the peaking time t_p and the operating temperature T .

The most significant contribution comes from the load capacitance:

$$ENC_{C_d} = a + b \cdot C_d$$

a and b are pre-amplifier specific parameters where b depends on the intrinsic chip voltage noise $u_{n,amp}$ and the peaking time ($b \sim \frac{u_{n,amp}}{t_p}$). Load capacitance and strip capacitance are similar ($C_d = C_{strip}$). The leakage current contributes through the shot noise

$$ENC_{I_L} = \frac{e}{2} \sqrt{\frac{I_L \cdot t_p}{q_e}} \approx 107 \sqrt{I_L / \text{nA} \cdot t_p / \mu\text{s}}$$

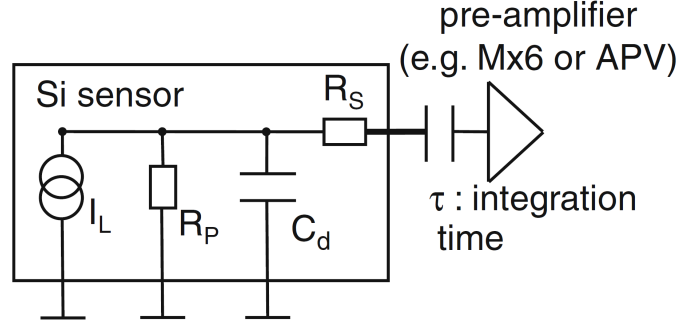


Figure 2.16.: Equivalence diagram of the different noise sources in a strip sensor [Har09]. I_L : leakage current, R_P : bias resistor, C_d : load capacitance and R_S : strip resistance.

with the Euler number e and the electron charge q_e . Two noise contributions are dependent on the temperature, the parallel thermal noise from the bias resistor

$$ENC_{R_P} = \frac{e}{q_e} \sqrt{\frac{k_B \cdot T \cdot t_p}{2 \cdot R_P}} \approx 44.5 \sqrt{\frac{T/\text{K} \cdot t_p/\mu\text{s}}{R_P/\text{M}\Omega}}$$

and the serial thermal noise from the metal strip resistance

$$ENC_{R_S} = C_d \cdot \frac{e}{q_e} \sqrt{\frac{k_B \cdot T \cdot R_S}{6 \cdot t_p}} \approx 0.025 \cdot C_d/\text{pF} \sqrt{\frac{T/\text{K} \cdot R_S/\Omega}{t_p/\mu\text{s}}}$$

To minimize the noise the following sensor criteria have to be fulfilled:

- small load capacitance C_{strip}
- low leakage current I_L
- high parallel resistance R_{bias}
- small series resistance R_{strip}

The peaking time should not be neglected because capacitance tuning is much more relevant for short peaking times, while for larger peaking times noise due to leakage current and bias resistance is more enhanced. For the LHC with very short bunch crossings the noise is maximally affected by the ENC_{C_d} term.

2.4. Radiation Damage

In high energy physics experiments the semiconductor detectors suffer from radiation damages. This section will give a brief overview, more details can be found in

[Wun92] and [Mol99]. The radiation effects can be separated in bulk and surface damage.

2.4.1. Bulk Damage

Displacement of atoms from their position in the lattice is the main source of damages in the bulk material. Figure 2.17 gives an overview of the different damage types. When an atom is removed from its original position it leaves an empty lattice space, a vacancy (V). An atom can also be placed between normal lattice positions and build an interstitial (I). The combination of a vacancy and an interstitial is called Frenkel pair. More complex constructs like di-vacancies V_2 , triple-vacancies V_3 or di-interstitials I_2 are possible, in which several vacancies/interstitials occur in neighbouring lattice places. It is also possible that diffusing Si atoms form combinations with impurity atoms, like oxygen, phosphorus or carbon. Examples in the figure show a carbon-oxygen interstitial pair (C_iO_i) or an interstitial oxygen-vacancy pair (VO_i).

These lattice displacements can form new levels in the band gap with either no beneficial effects or malevolent effects on the detector operation. This includes the increase of the leakage current, the change of the depletion voltage due to creation of mainly additional acceptor levels and the decrease of charge collection efficiency due to defects acting as traps.

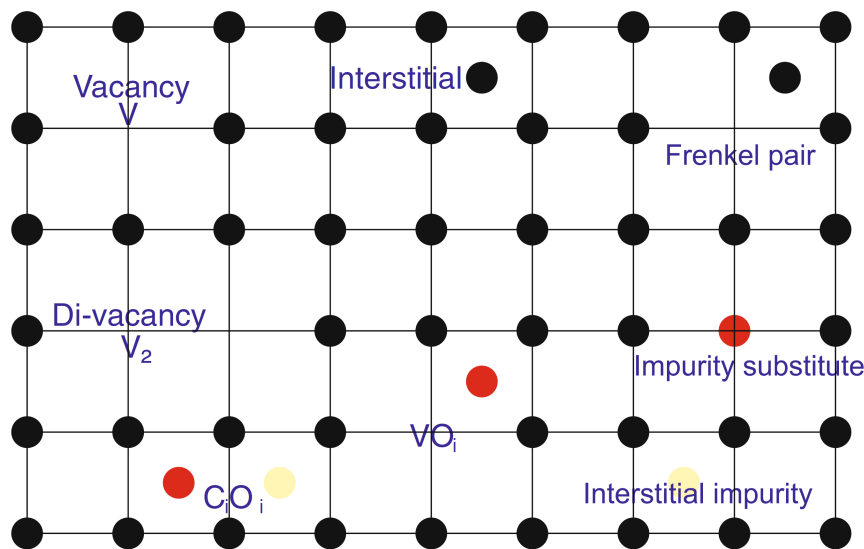


Figure 2.17.: Exemplary selection of bulk damages after irradiation (from [Har09]). Through radiation damages atoms can be removed from their lattice place (vacancy) and are then placed at a random position (interstitial). The combination of a vacancy and an interstitial is called Frenkel pair.

For example a vacancy-phosphorous pair (VP) removes the donor property of single phosphorus and a V_2O combination introduces additional negative space charge due to their new energy levels in the band gap. Figure 2.18 shows the effects of different defect levels in the band gap on the overall detector performance. A defect in the middle of the band gap will increase the leakage current by being an efficient electron-hole pair generator. Defect levels close to the valence band or conduction band will increase the depletion voltage by acting as donor/acceptor levels and affecting the effective space charge N_{eff} .

Deep levels can influence the charge collection by trapping electrons and holes. If the trapping time is larger then the charge collection time the charge carriers are ‘lost’ and the signal decreases. Because of the different mobilities electrons are less affected than holes, which supports the use of n-in-p detectors that collect electrons at the strips. The inter-centre charge transfer model says that combinations of the different defects in defect clusters additionally enhances the malevolent effects.

Figure 2.19 shows some example defect levels, found by the CERN RD50 collaboration, with their corresponding effects on the detector properties. They are categorized in point defects and extended defects (for example in defect pairs).

Donor removal (VP) together with acceptor-like levels (V_2O) shift the space charge towards p-like semiconductors. This can result in the unwanted type inversion of n-type silicon, which after a sufficient irradiation fluence shows p-like properties. In a p-in-n detector this result in the shift of the effective pn-junction from the strip side to the back-side. To operate such a detector it needs to be fully depleted, which might require very high bias voltages. An n-in-p detector can be

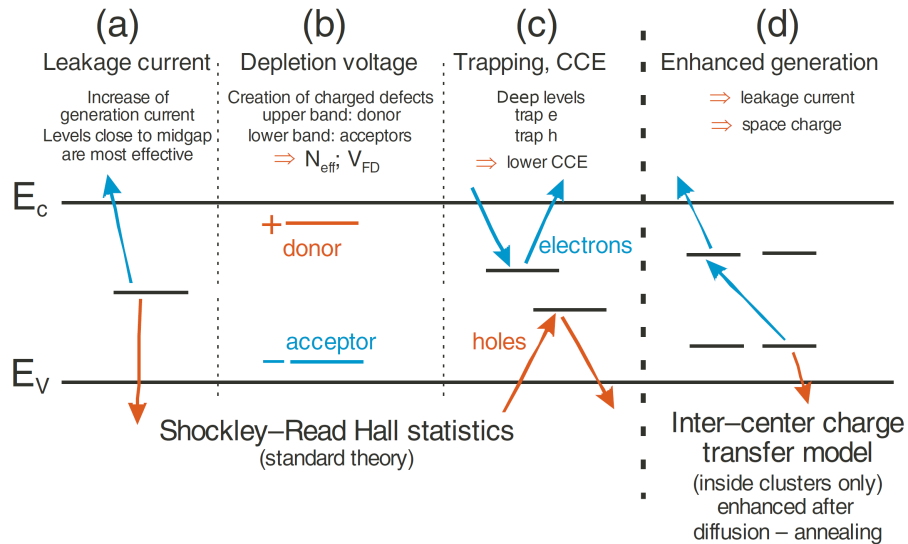


Figure 2.18.: Effects of different defect levels in the band gap on the detector performance [Har09].

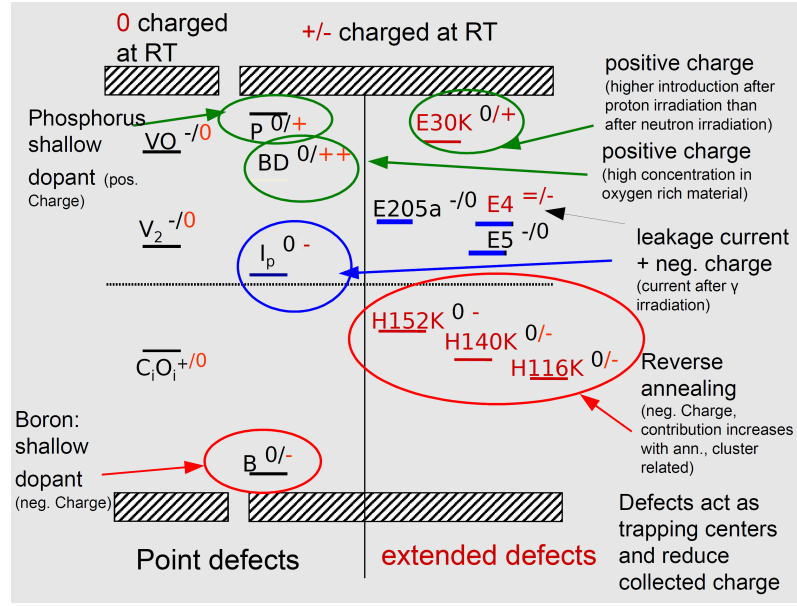


Figure 2.19.: Band-gap overview of some defect levels in silicon [Küh15]. Some of the defect level names are based on the measurement method that allowed the determination of their properties, but a detailed description is outside the scope of this thesis.

operated under-depleted because the depletion region always starts at the strip side and therefore guarantees a good position resolution². The change in the effective space charge can be parametrized according to [Wun92]:

$$N_{eff} = N_{D,0}e^{-c_D\Phi_{eq}} - N_{A,0}e^{-c_A\Phi_{eq}} - b\Phi_{eq} \quad (2.18)$$

with the irradiation fluence Φ_{eq} , the initial donor/acceptor concentration ($N_{D,0}/N_{A,0}$), the donor and acceptor removal rates c_D and c_A and the acceptor creation term $b\Phi_{eff}$.

The silicon damage depends strongly on the incident particle and its energy. For the creation of a Frenkel pair an energy loss of approximately 25 eV is needed, while the production of a cluster (local accumulation of defects) requires approximately 5 keV. 10 MeV protons produce a quite homogeneous vacancy distribution while more energetic protons with 24 GeV form more clusters and discrete defects. Neutrons interact only due to strong interaction and produce isolated clustered defects already at low energies (1 MeV). For irradiation damage in the lattice from electrons high kinetic energies are required.

To compare the damages of different particles and energies the NIEL scaling hy-

²If the strip region is not depleted the charge carriers move through diffusion in all directions, while in a depleted semiconductor they drift along the electric field lines towards a specific strip implant.

pothesis (Non Ionizing Energy Loss) is used: it allows a first order normalization of radiation damage with respect to different particles with different energies. As a standard the 1 MeV neutron equivalent fluence with the unit $[n_{\text{eq}}/\text{cm}^2]$ or $[n_{1\text{ MeV}}/\text{cm}^2]$ is used and abbreviated with Φ_{eq} . It can be calculated from the irradiation fluence Φ by [Har09]

$$\Phi_{\text{eq}} = \kappa\Phi \quad (2.19)$$

with κ being the numerical hardness factor, which has to be determined for each irradiation particle and particle energy. Table 2.1 lists the κ values for the irradiation facilities used for the irradiation of the samples investigated in this thesis.

Institute	Irradiation particle	Hardness factor	Reference
CERN	24 GeV/c protons	0.51	[Mol99]
TRIGA mark III (Ljubljana)	thermal neutrons	0.90	[Mol99]
Birmingham cyclotron	23 MeV/c protons	2.2	[Gon16]
KIT cyclotron	23 MeV/c protons	2.0	[Gon16]

Table 2.1.: Hardness factor for different irradiation centres

The main detector operation limiting effects of radiation bulk damages arise at different fluences:

- $1 \times 10^{14} n_{\text{eq}}/\text{cm}^2$: main problem from increased leakage current
- $1 \times 10^{15} n_{\text{eq}}/\text{cm}^2$: additional high depletion voltage might result in the under-depleted operation of the device
- $1 \times 10^{16} n_{\text{eq}}/\text{cm}^2$: additional charge collection degradation, mainly due to trapping

After irradiation the signal in a silicon detector is in general lower than for an unirradiated device. One reason is the change in the effective doping concentration, which has a direct impact on the depletion width (Equation 2.14). Additionally at higher fluences trapping reduces the signal. Charge multiplication through impact ionization can be beneficial. If the multiplication factor is not too high then a few electrons / holes can create a reasonable amount of secondary particles to create a signal of measurable size. But if the multiplication factor is too high it will result in avalanche breakdown.

2.4.2. Annealing

Interstitials and vacancies are very mobile at temperatures larger than 150 K. There is the possibility that Frenkel pairs recombine, vacancies or interstitials combine

($V+V \rightarrow V_2$) or the combination of more complex defects ($C_i+O_i \rightarrow C_iO_i$). This whole process is called annealing and the effects are time dependent. While the first two have a short time constant, the last happens with a longer time constant. Macroscopically a distinction between the short term beneficial annealing, in which the damages are reduced, and the long term reverse annealing, in which the sensor properties degrade further, can be made. Because of the temperature dependence some effects can be frozen out at temperatures below 0°C .

The different parts can be seen very clearly in the evolution of N_{eff} according to the Hamburg model [Mol99], which depends on the annealing time t and the annealing temperature T_a :

$$\Delta N_{eff}(\Phi_{eq}, t, T_a) = N_C(\Phi_{eq}) + N_A(\Phi_{eq}, t, T_a) + N_Y(\Phi_{eq}, t, T_a) \quad (2.20)$$

with the stable term N_C , the short-term annealing term N_A and the second-order long term annealing term N_Y . Figure 2.20 shows the different parts as function of the annealing time. The full depletion voltage directly depends on the effective doping concentration and can be measured to quantify the different annealing processes in this model. The stable term N_C consists of a donor removal and an acceptor creation rate. It depends on the oxygen concentration because oxygen could bind vacancies, which would otherwise combine with phosphorus ($V+O \rightarrow VO$ instead of $V+P \rightarrow VP$). Both are not time dependent as there are no evolutionary diffusion processes. N_A takes the decay of the introduced acceptors into account which can be seen as an increase of the effective doping concentration (p-type material becomes more positive), which is time and temperature dependent. After longer times more

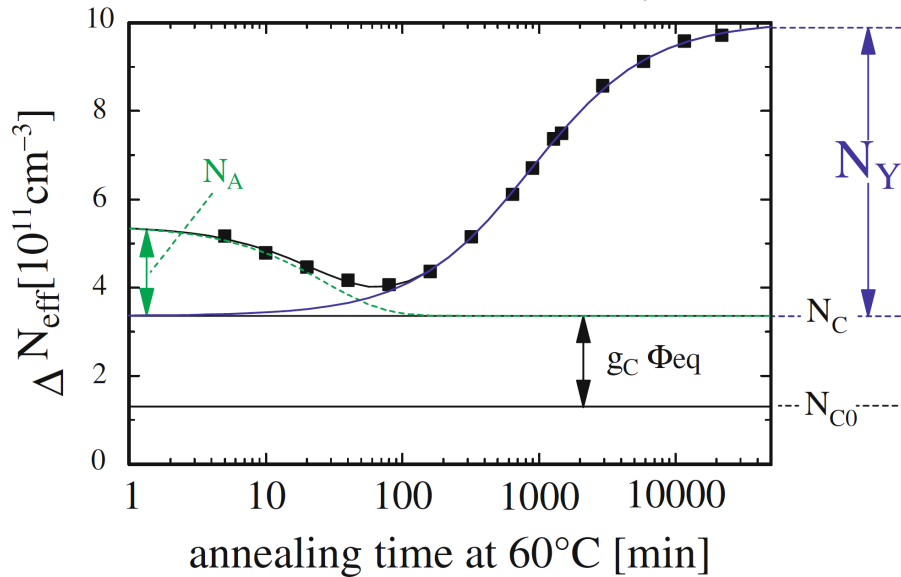


Figure 2.20.: N_{eff} evolution with annealing time for a n-type sensor [Har09], parametrized according to the Hamburg model.

acceptor levels form, which is expressed by the long-term part N_Y .

Macroscopic changes deriving from diffusion (annealing) are highly temperature dependent. They can be frozen out at temperatures below 0°C while they are dominant at higher temperatures. Charge collection efficiency increases for electrons and decreases for holes. Acceptor levels, created through radiation damages, decay in the beneficial annealing phase and increase later in the reverse annealing phase which affects the full depletion voltage. Effects on the leakage current will be discussed in more details in section 2.4.3 because of its importance for some aspects of this thesis, but it should be mentioned that the leakage current always decreases with increasing annealing time.

Usually the values of annealing effects are given at room temperature (21°C), but the effects can be accelerated by annealing the device at higher temperatures. Table 2.2 shows the acceleration factors for different annealing times, as given in [Mol99]. The factors differ for beneficial and reverse annealing, but in both cases room temperature annealing is chosen to be the standard. A common step is the annealing of an irradiated device for 80 minutes at 60°C. At this point the beneficial annealing stops and the reverse annealing is beginning, as can be seen in Figure 2.20. Applying the acceleration factor for beneficial annealing a device would have to anneal for 13920 minutes at room temperature, which is equivalent to approximately 10 days.

annealing temperature	-10°C	0°C	10°C	20°C	40°C	60°C	80°C
acceleration factor for:							
beneficial annealing	1/134	1/23	1/5	1	16	174	1490
reverse annealing	1/396	1/47	1/6	1	29	544	7430

Table 2.2.: Time factors for accelerated annealing from [Mol99]. The factors differ for beneficial annealing and reverse annealing.

2.4.3. Surface Damage

The main source of radiation damage in the surface is damage in the SiO₂ layer and the SiO₂-Si interface. They are introduced by ionization, not by atomic displacement. Electron-hole pair creation is not fully reversible in the insulator and they can be captured by existing defects where the emission is suppressed by the larger band gap. Because the mobility of electrons is several orders of magnitude higher than that of holes, the created pairs separate quickly. The holes drift towards the SiO₂-Si interface and in addition the defect concentration is higher at the interface. This results in the accumulation of positive static charge at the interface. Negative charge from the bulk is attracted to the interface and produces an electron accumulation layer. This reduces the interstrip resistance and increases the capacitance (increased

polarisability). The decreased resistance increase the cross talk between the strips while the increased capacitance result in an higher noise. These effects only occur for n-in-p detectors.

The left picture in Figure 2.21 shows a schematic cross section of the strip region where the strips are short-circuited due to the electron accumulation layer. This can be prevented by repelling the electrons from the surface area. One method is the use of a p^+ implant between the n-type strips, called p-stop (shown in the picture). It is also possible to cover the whole surface with a diffuse layer of p-dopants (p-spray). A combination of both can be used as well. In a third method the overhang of the aluminium strips is increased and set to a slightly negative potential to repel the electrons, acting as field plates (right picture in Figure 2.21).

Reverse Bias Current after Irradiation

Temperature Dependence The temperature dependence of the current becomes important because of the increased current due to irradiation damages. In irradiated diodes the generation current dominates the current saturation value (even after rather low fluences) so that the temperature dependence of the reverse bias current I_R is given by [Spi09]:

$$I_R(T) \propto T^2 \exp\left(-\frac{E_{eff}}{2k_B T}\right) \quad (2.21)$$

with the effective energy $E_{eff} \approx E_g$ and the temperature T , given in Kelvin. The value for the effective energy for irradiated devices was determined by measurements to (1.214 ± 0.014) eV [Chi13] for irradiation fluences up to 1×10^{15} n_{eq}/cm^2 .

This relation can be used to scale the current $I(T_1)$ measured at the temperature T_1 to a different temperature T_2 by:

$$I(T_2) = I(T_1) \cdot \left(\frac{T_2}{T_1}\right)^2 \exp\left(-\frac{E_{eff}}{2k_B} \left(\frac{1}{T_2} - \frac{1}{T_1}\right)\right). \quad (2.22)$$

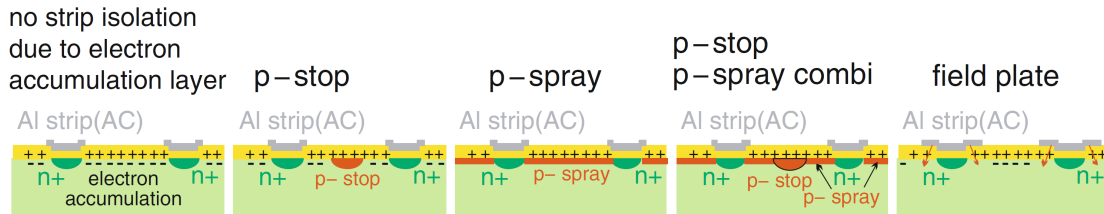


Figure 2.21.: Schematic view of the different strip isolation methods for n-in-p sensors to prevent the effects of the surface radiation damages [Har09].

The uncertainty of the scaled current depends on the uncertainties of the measured current, the measured temperature and the effective energy.

$$\sigma_{I(T_2)}^2 = \left(\frac{\partial I(T_2)}{\partial I(T_1)}\right)^2 \sigma_{I(T_1)}^2 + \left(\frac{\partial I(T_2)}{\partial T_1}\right)^2 \sigma_{T_1}^2 + \left(\frac{\partial I(T_2)}{\partial T_2}\right)^2 \sigma_{T_2}^2 + \left(\frac{\partial I(T_2)}{\partial E_{eff}}\right)^2 \sigma_{E_{eff}}^2$$

Because this equation is used to scale the current measured at T_1 to the temperature T_2 there is no uncertainty on the scaling temperature which means $\sigma_{T_2} = 0$. Calculating the derivatives compute to

$$\sigma_{I(T_2)}^2 = I(T_2)^2 \left[\left(\frac{\sigma_{I(T_1)}}{I(T_1)}\right)^2 + \left(2 + \frac{E_{eff}}{2k_B T_1}\right)^2 \left(\frac{\sigma_{T_1}}{T_1}\right)^2 + \left(\frac{1}{2k_B} \left(\frac{1}{T_2} - \frac{1}{T_1}\right)\right)^2 \sigma_{E_{eff}}^2 \right]. \quad (2.23)$$

The quadratic summands contribute in different orders of magnitude to the total uncertainty. Looking at the values from a single measurement of a highly irradiated sensor used in chapter 6 allows a qualitative comparison. The used values are: $I(T_1) = 3.429432 \times 10^2 \mu\text{A}$, $\sigma_{I(T_1)} = 8.506112 \times 10^{-2} \mu\text{A}$, $E_{eff} = (1.214 \pm 0.014) \text{eV}$ and $T_1 = (-14.7 \pm 0.01)^\circ\text{C} = (258.45 \pm 0.01) \text{K}$. The contribution of the relative current uncertainty (first term) is approximately 6×10^{-8} , the contribution from the second term (measured temperature) 1.3×10^{-6} and the contribution from the relative effective energy uncertainty 3.8×10^{-5} for a scaling temperature T_2 of 253.45 K ($T_1 - 5 \text{K}$). This last term strongly depends on the temperature difference because the uncertainty of the effective energy can be assumed to be a constant. Table 2.3 shows some example values for temperature difference $\Delta T = T_1 - T_2$ starting at 1 K up to 50 K. With increasing ΔT the uncertainty increases up to approximately 0.6×10^{-2} for a difference of 50 K. This term clearly dominates the uncertainty of the scaled current.

$\Delta T = T_1 - T_2$ [K]	$\left(\frac{1}{2k_B} \left(\frac{1}{T_2} - \frac{1}{T_1}\right)\right)^2$ [1/eV ²]	$\left(\frac{1}{2k_B} \left(\frac{1}{T_2} - \frac{1}{T_1}\right)\right)^2 \sigma_{E_{eff}}^2$
1	0.0076	0.149×10^{-5}
2	0.0307	0.601×10^{-5}
5	0.1962	3.845×10^{-5}
10	0.8165	16.00×10^{-5}
20	3.5457	69.50×10^{-5}
50	28.9986	568.37×10^{-5}

Table 2.3.: Impact of the temperature difference $\Delta T = T_1 - T_2$ on the effective energy uncertainty term in Equation 2.23.

Fluence Dependence It has been experimentally shown in [Mol99, Wun92] that the current of an irradiated silicon sensor depends on the irradiation fluence and follows the following equation:

$$\frac{I(\Phi_{eq}) - I(\Phi_0)}{V} = \frac{\Delta I}{V} = \alpha \Phi_{eq}. \quad (2.24)$$

Here $I(\Phi_0)$ represents the current of the unirradiated sensor and $I(\Phi_{eq})$ the current at fluence Φ_{eq} . V labels the depleted sensor volume and α the current related damage rate. Figure 2.22 shows the plot which led to this equation and is used to determine the value of α by a straight line fit.

This relation can also be used to determine the effective fluence due to the good linearity by measuring the current. It allows the experimental determination of the hardness factor by measuring the current of a known silicon detector at different irradiation fluences and insert Equation 2.19 in Equation 2.24 to determine κ from the straight line fit.

Current Related Damage Rate

The current decreases with annealing time and therefore the current related damage rate has to change as well, to include the annealing time dependence in Equation 2.24. The annealing behaviour of α has been experimentally determined in [Mol99, Wun92]

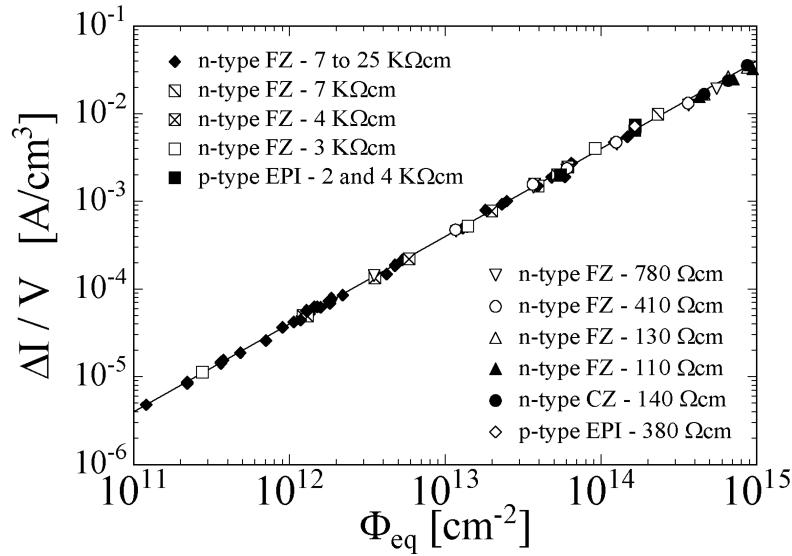


Figure 2.22.: $\Delta I/V$ as function of the irradiation fluence shows a linear behaviour [Mol99]. For this figure the irradiated samples were measured after annealing for 80 min at 60°C , which results in an expected slope (α) of $(3.99 \pm 0.03) \times 10^{-17}$ A/cm.

and result in equations for short term and long term annealing.

Short term annealing The annealing of the current related damage rate can be seen as a sum of exponential terms, where each term represents a radiation defect that contributes to the leakage current and anneals out with its own time constant τ_i . This results in an equation for the current related damage rate $\alpha(t, T_a)$, depending on the annealing time t and the annealing temperature T_a [Mol99, Wun92]

$$\begin{aligned}\alpha(t, T_a) &= \frac{\Delta I(t, T_a)}{\Phi_{eq} \cdot V} \\ &= \alpha_\infty \sum_i \frac{b_i}{b_\infty} \exp\left(-\frac{t}{\tau_i(T_a)}\right)\end{aligned}\quad (2.25)$$

with the relative amplitude b_i which fulfils the condition $\sum_i b_i = 1$. Numeric values for the parameters are given in Table 2.4. The parameter $\alpha_\infty = (2.86 \pm 0.18) \times 10^{-17}$ A/cm [Chi95] describes the saturation value that is reached at several months of room temperature annealing, when no further annealing takes place³.

Term	$i = 1$	$i = 2$	$i = 3$	$i = 4$	$i = 5$	$i = \infty$
τ_i [min]	1.78×10^1	1.19×10^2	1.09×10^3	1.48×10^4	8.92×10^4	∞
σ_{τ_i} [min]	0.17×10^1	0.03×10^2	0.01×10^3	0.01×10^4	0.59×10^4	
b_i	0.156	0.116	0.131	0.201	0.093	0.303
σ_{b_i}	0.038	0.003	0.002	0.002	0.007	0.006

Table 2.4.: Parameters of leakage current annealing at room temperature (21°C) [Mol99, Wun92] .

Long term annealing For long term annealing times ($t > 1$ year at room temperature) Equation 2.25 does not describe the observed behaviour. The alpha value does not saturate, but follows a logarithmic function in time [Mol99]:

$$\alpha(t) = \alpha_0 + \alpha_I \exp\left(-\frac{t}{\tau_I}\right) - \beta \ln\left(\frac{t}{t_0}\right)\quad (2.26)$$

with the t_0 was set to 1 min and the other parameters were obtained from fits at different annealing temperatures (see Table 2.5). The weighted average value of the amplitude α_I for all annealing temperatures, shown in the table, was found to be

$$\alpha_I = (1.23 \pm 0.06) \times 10^{-17} \text{ A/cm},\quad (2.27)$$

³This is a historic notation where no measurements after very long annealing times were done and long term annealing was not observed. Therefore it was assumed that α reaches a saturation value after long annealing times of α_∞ .

T_a [°C]	α_I 10^{-17} A/cm	τ_I [min]	α_0 10^{-17} A/cm	β 10^{-18} A/cm
21	1.23	14000	7.07	3.29
49	1.28	260	5.36	3.11
60	1.26	94	4.87	3.16
80	1.13	9	4.23	2.83
106	—	—	3.38	2.97

Table 2.5.: Parameter for longterm annealing of α [Mol99].

and the Arrhenius plot of the time constant τ_I showed

$$\frac{1}{\tau_I} = k_{oI} \times \exp\left(-\frac{E_I}{k_B T_a}\right) \quad \text{with} \quad \begin{array}{l} k_{oI} = 1.2_{-1.0}^{+5.3} \times 10^{13} \text{ s}^{-1} \\ E_I = (1.11 \pm 0.05) \text{ eV} \end{array} .$$

The average value of the parameter β is given as

$$\beta = (3.07 \pm 0.18) \times 10^{-18} \text{ A/cm} \quad (2.28)$$

and α_0 was found to be

$$\alpha_0 = -(8.9 \pm 1.3) \times 10^{-17} \text{ A/cm} + (4.6 \pm 0.4) \times 10^{-14} \text{ AK/cm} \times \frac{1}{T_a}, \quad (2.29)$$

which result in a α_0 value for annealing at 21 °C of $(6.74 \pm 0.06) \times 10^{-17}$ A/cm.

This parametrization is not based on any physical model. It is not valid for annealing times shorter than one minute nor for times and annealing temperatures that result in α values larger then 6×10^{17} A/cm.

3. Measurement Setups

In this chapter the different measurement systems which have been used for this thesis are described. These are the probe station in the Oliver Lodge Building (Liverpool Semiconductor Detector Centre) of the University of Liverpool for current (IV) and capacitance (CV) measurements at room temperature (subsection 3.1.1), the 'old' cold IV system (subsection 3.1.2) as well as the 'new' cold IV box (subsection 3.1.3). For comparison some cold IV measurements have been performed with the CERN system (SSD laboratory in the ED-DT group), which is described in subsection 3.1.4. For charge collection measurements the ALiBaVa system has been used (section 3.2).

3.1. IV-CV

The silicon test facilities in Liverpool are located in the clean room of the Oliver Lodge Building. It is separated in two parts, the ISO 14644-1 class 5 and the ISO class 7 area. These classifications refer to the number of particles with the size of $0.5\ \mu\text{m}$ or larger per cubic metre of air. ISO class 7 allows 352 000 particles/ m^3 , while in ISO class 5 allows 3 520 [POR16]. Room air (ISO class 9) for comparison has approximately 35 200 000 particles/ m^3 . The ISO class 5 area is used, amongst others, for the wire bonding machines. With these machines the connection of silicon sensors with the readout electronic is made by the use of $25\ \mu\text{m}$ thick aluminium wires. Setups which require less emphasis on environmental particles, like the probe station or the ALiBaVa system, are located in the ISO class 7 area.

3.1.1. Probe Station

Measurements of the current and capacitance of silicon sensors at room temperature are done with the probe station, which is located in a light-tight box. Figure 3.1 shows on the left side an overview of the system. Located in the centre is a vacuum chuck, which holds the silicon samples in position by use of a hole in the centre which is connected to vacuum. The chuck is surrounded by a platform which allows to place several probe needles. A microscope with a built-in light source allows the precise positioning of the needles. A detailed picture (bottom right) shows a silicon sensor placed on the chuck with a probe needle at the right side. The surface of

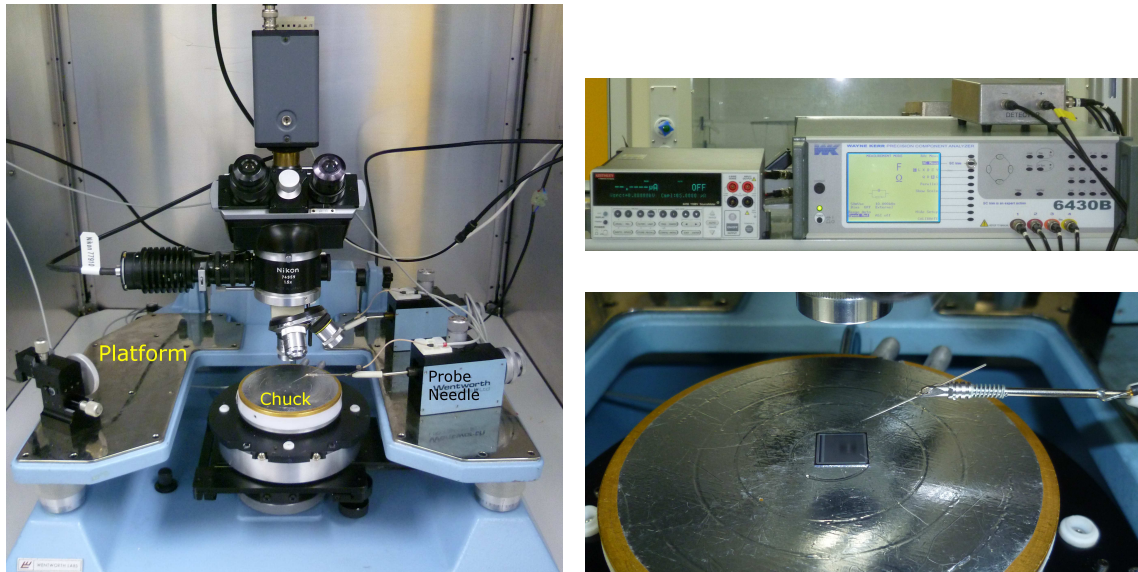


Figure 3.1.: [left] Interior view of the probe station with the microscope to position the probe needles. [bottom right] Detailed view with a silicon sample in the centre, the microscope at the top and the probe needle at the right. [top right] Keithley 2410 high voltage power supply (left), Wayne Kerr 6430B LCR meter (right) and LCR-HV coupling box (top right).

the chuck is covered by a conducting metal to implement the backside contact to the silicon sensor. The test circuit is closed by the needle, which can contact any pad on the sensor, like the bias rail bond pad. In the top right picture the Keithley 2410 [Kei16a] high voltage power supply, the Wayne Kerr 6430B LCR meter and the LCR-HV coupling box are shown. The LCR meter allows measurement of the inductance (L), capacitance (C) and resistance (R), but usually is only used for the capacitance measurement. This is done by adding a sinusoidal voltage to the bias voltage. The LCR meter provides the alternating voltage with adjustable frequency and amplitude and the LCR-HV coupling box combines it with the direct high voltage from the Keithley 2410. This is necessary because the Keithley 2410 can provide up to 1100 V which would destroy the LCR meter if this voltage would be directly connected to its input. The CV measurements in this thesis are taken in serial mode (resistance in series with capacitance).

The measurements are controlled by a LabVIEW [Nat16] program with a graphical user interface shown in Figure 3.2. The program changes the voltage from the start voltage to the final voltage in predefined steps with a chosen ramping speed. Before measuring current and capacitance at each step the software waits some time for stabilization (settling time). For the visualization and analysis of the data from the text file several programs can be used. All results shown in this thesis are generated by a ROOT script [ROO16] which has several features, including the analysis of CV data to obtain the full depletion voltage.

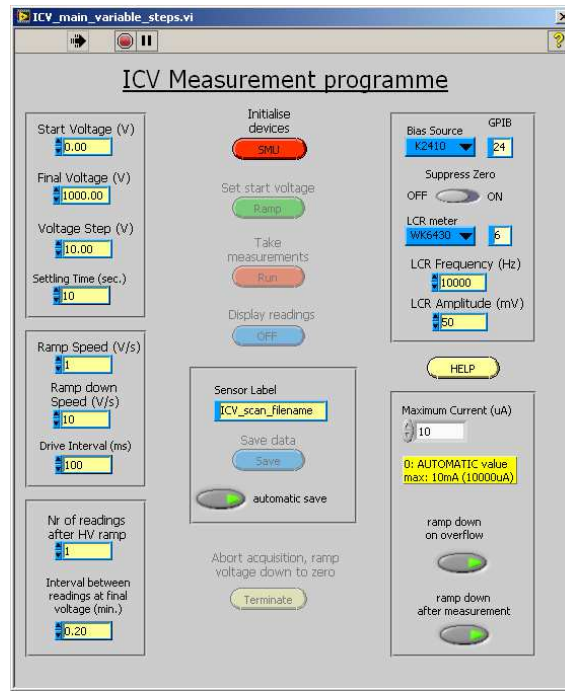


Figure 3.2.: User interface of the probe station LabVIEW program for CV and IV measurements.

3.1.2. Cold IV (old)

The original cold IV setup in Liverpool is basically a commercial freezer. Inside is a mount for the test PCBs (Figure 3.3). The temperature of the freezer is measured and an external regulator controls the power (on or off) to get the set temperature. A fan, covered in a copper housing, blows the cold air of the freezer towards the PCB for passive cooling. This setup has several disadvantages: While it is possible to get a stable temperature of about -23°C , this is only achieved by the freezer running constantly to a lower temperature which can not be reached. Setting a higher temperature will result in the freezer switching off and on which results in an oscillating temperature, as can be seen in Figure 3.4. The response time of the freezer to temperature changes with the controller is approximately 1 to 2 hours for several degrees. During the time the freezer is open, for example to change the sample, the internal temperature increases approximately 10°C , which results in having to wait several hours for the temperature to reach the set value. Another disadvantage is the necessity of a PCB. For this setup the sample needs to be attached to the test PCB. This can either be done by permanently glueing the sensor to the PCB with silver conducting glue, or by temporary clamping. While the permanent way is advantageous in terms of heat transfer, it is not possible to use the sample for other measurements later on.

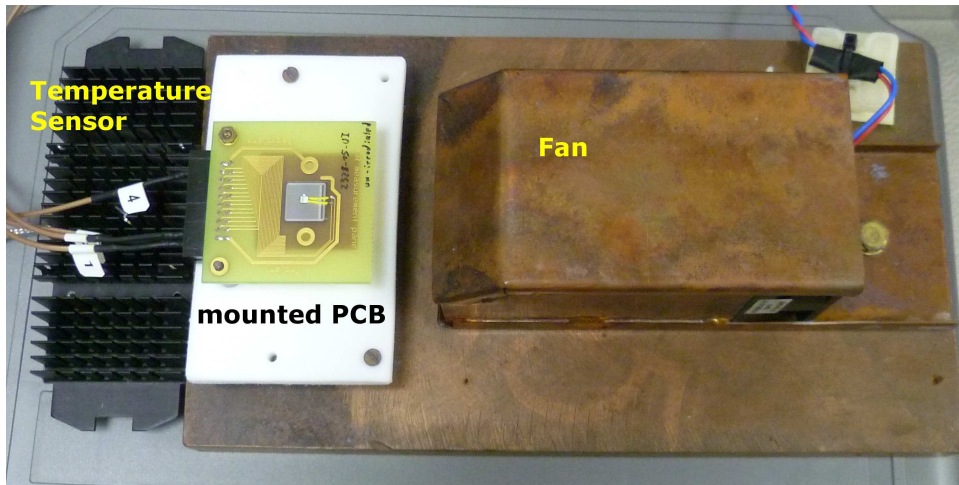


Figure 3.3.: Old cold IV setup, consisting of a freezer with the PCB mount. A fan is used for air circulation while a temperature sensor is connected with the freezer controller.

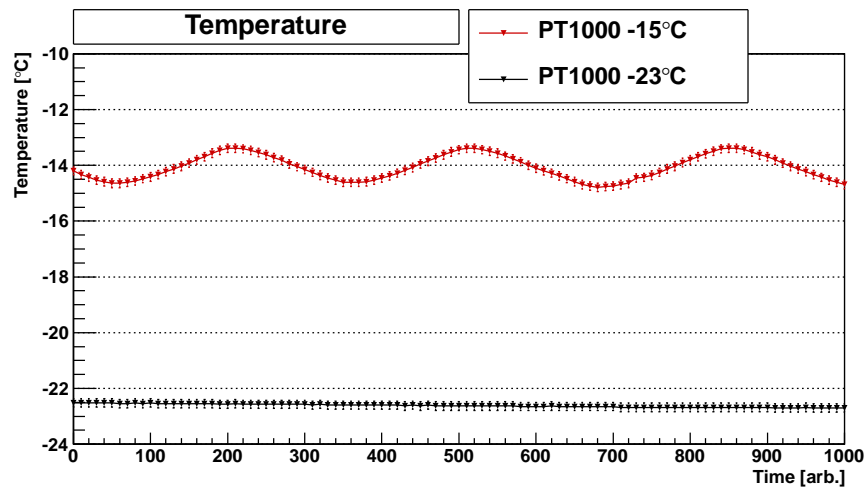


Figure 3.4.: Measured temperature in the freezer for cold IV for two chosen temperatures (-15°C and -23°C). While the lower temperature is stable, the higher temperature oscillates due to the duty cycle of the freezer to maintain the set temperature.

3.1.3. Cold IV (new)

For the IV study presented in chapter 6 a new cold IV system has been developed by the author of this thesis. The aim for the new cold IV setup is better temperature control. This is achieved using a Peltier element [Pel16, Act16] for cooling. Figure 3.5 shows a picture of the new system. The cold block at the bottom is connected to a chiller, which removes the heat of the warm side of the Peltier element. The cold Peltier side is attached to the PCB mounting plate. Heat conducting paste facilitates the temperature transfer. To reduce temperature bridges between cold and warm side, nylon screws have been used for the assembly. A PT1000 temperature sensor for the temperature control is attached to the mounting plate.

The Peltier element transfers heat from the cold side to the hot by applying power to it. For the cold IV system the Peltier power is regulated by a PR-59 Proportional-Integral-Derivative (PID) controller [PID16]. The output of the controller is affected by the deviation of the measured temperature and the set temperature according to the following equation [Wik16, Ara16]:

$$u(t) = K_P e(t) + K_I \int_0^t e(\tau) d\tau + K_D \frac{de(t)}{dt}$$

with the output value u , the error value e (deviation of measured value from set value), the time t , the proportional gain K_P , the integral gain K_I and the derivative gain K_D . These three gain values are tuning parameters, which have to be set by the user. The proportional term produces an output value that is proportional to the current error. A too small gain makes the controller less sensitive while a too high value results in an unstable system. The integral term takes into account the magnitude of the error as well as the duration. Because it is affected by the accumulated errors from the past it can cause to overshoot the set value. The

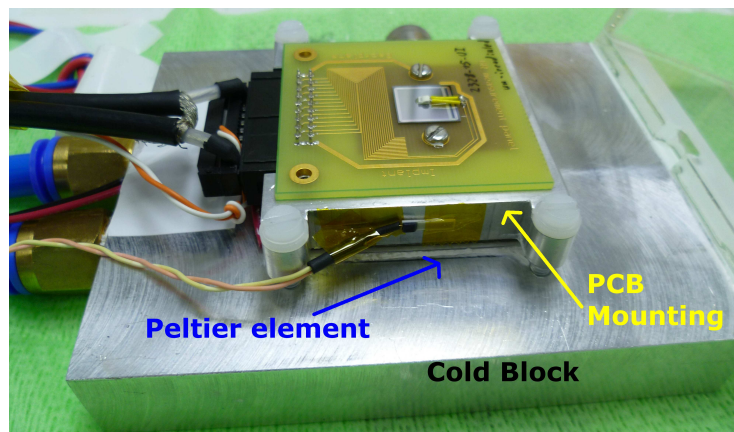


Figure 3.5.: New cold IV system, consisting of a cold block, a Peltier element and the PCB mounting plate.

derivative term predicts the behaviour of the system and thus improves settling time and stability. The PR-59 requires at least 12 V as input, but also applies the same voltage as output. Therefore an appropriate Peltier element has to be chosen (here 112.7 W / 6 A) as well as a compatible power supply.

The whole assembly is covered by a perspex box with a nitrogen inlet. This is necessary when using temperatures below 0°C. Condensed water will accumulate at the cold test device and freeze, which can be prevented by the nitrogen.

Figure 3.6 shows the temperature of a silicon sensor measured in the freezer setup and the new PID controlled setup. The oscillations from the freezer (seen in the red curve) disappear with the Peltier cooling. A deviation in the PID controlled system between set temperature and measured temperature is caused by the inaccurate calibration of the system. This also explains the changes in temperature because the PID system has not reached the equilibrium state.

3.1.4. CERN IV

Some measurements have been performed with the CERN IV setup, shown in Figure 3.7. This system is a combination of the probe station and the cold IV: it is built up of a chuck with a vacuum connection, which is cooled by a Peltier-chiller system. The sample is contacted by probe needles (seen on the right hand side in the picture). Instead of using the Keithley 2410 power supply for the current measurement as well, a Keithley 6487 Picoammeter is used in series to improve the resolution. The whole system is covered by a movable metal box to ensure it is

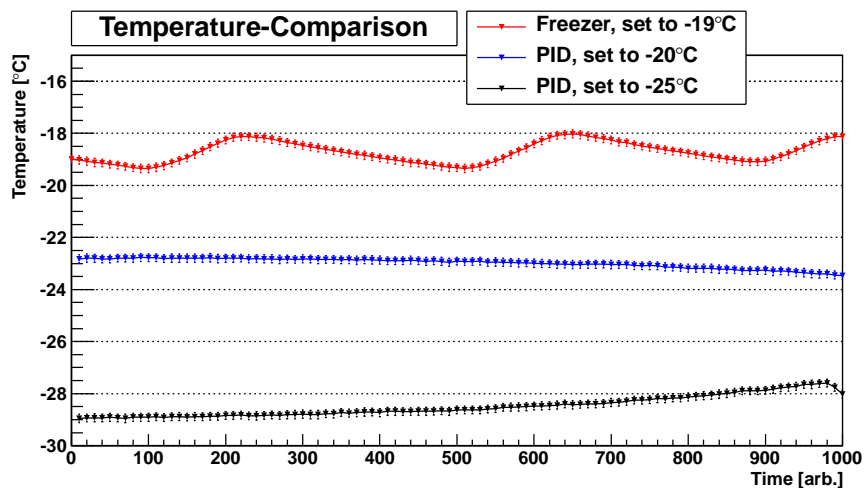


Figure 3.6.: Measured temperature with the Peltier setup in comparison with the freezer setup. The measured temperatures of the PID controlled system deviate from the set temperature because the system is not calibrated properly. With the Peltier system the temperature oscillations of the freezer disappear.

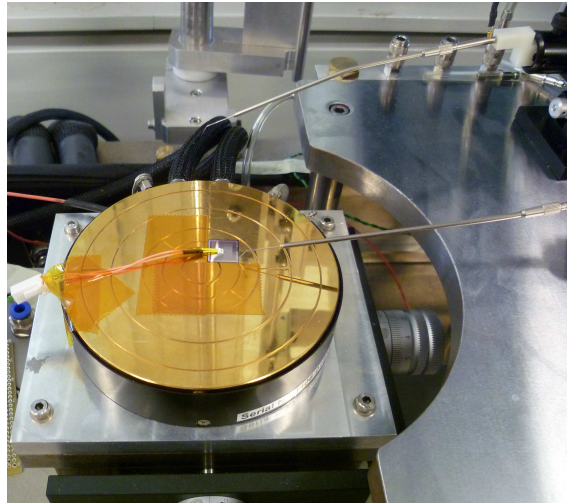


Figure 3.7.: Picture of the CERN IV setup with the cold chuck in the centre and probe needles at the right hand side.

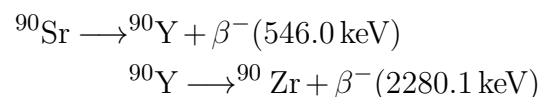
light-tight and flushed with dry air to prevent condensation on the sample.

There are some advantages of this measurement setup: by using probe needles, instead of wire bonds, the sample can be easily used for further experiments without occupying space on the bias bond pads by old wire feet. By using a cold chuck it is not necessary to attach the sensor to a PCB, which improves heat transfer as well as re-usability. The cold chuck also allows measurements of large sensors, which would be too large for the PCBs.

3.2. Charge Collection

A common method for charge collection measurements in laboratories is the use of a β -setup, like it is illustrated in Figure 3.8.

Strontium-90 source is an electron-emitter with the following decay chain:



Strontium-90 has a half life time of 28.8 years [Chu16a] and decays purely to yttrium-90 by emitting an electron of 546.0 keV. Yttrium-90 itself is not stable (64 hours half life time) and decays to zirconium-90 and an electron of 2280.1 keV [Chu16b]. The high energy electron can be assumed to be a Minimum Ionizing Particle (MIP) and therefore the energy loss in silicon is well known. For a certain silicon thickness d in μm , the number of electron-hole pairs ($N_{e/h}$) can be calculated according to [Bic88]

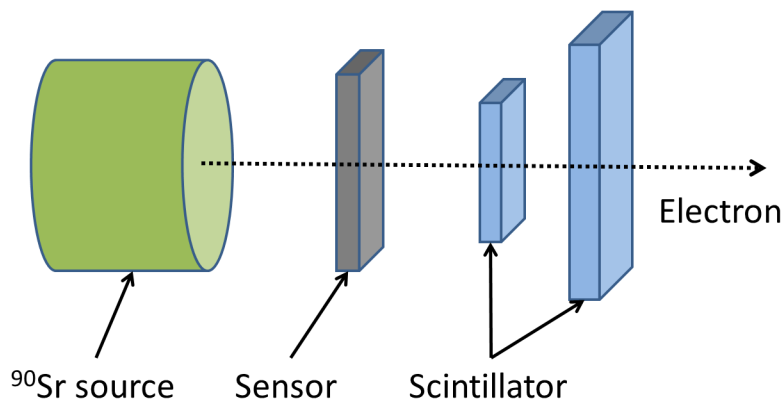


Figure 3.8.: Schematic drawing of a β -system.

with d being the sensor thickness given in μm :

$$N_{e/h} = \begin{cases} \frac{d}{3.68} \cdot (100.6 + 35.35 \cdot \ln(d)) & \text{for } 13\ \mu\text{m} < d < 110\ \mu\text{m} , \\ \frac{d}{3.68} \cdot (190.0 + 16.30 \cdot \ln(d)) & \text{for } 110\ \mu\text{m} < d < 3000\ \mu\text{m} , \end{cases} \quad (3.1)$$

Figure 3.9 shows $N_{e/h}$ as function of the device thickness d for a typical sensor thickness of up to $350\ \mu\text{m}$. The bottom graph shows the difference between the calculation for thin sensors and thick sensors if the values would have been calculated for the full thickness range. For thin sensors the highest difference was calculated for a sensor thickness of $40\ \mu\text{m}$ with a difference of approximately $200\ e^-$ and for thick sensors the difference increases with increasing thickness.

After passing the silicon sensor and thereby creating electron-hole pairs, the β -particle is detected by the scintillator, which triggers the readout electronics. The low-energy electron is absorbed in the first scintillator (approximately $5\ \text{mm}$ thick¹) while the high energetic one can reach the second. Using both scintillators in a coincidence circuit will result in triggering only the high-energy β -particles. If only one scintillator is available, the low energy β -particle can be absorbed by a piece of perspex (thickness variable, here used $1\ \text{mm}$). This method is applied in the ALiBaVa system for charge collection measurements.

3.2.1. ALiBaVa System

The ALiBaVa system (Analogue Liverpool Barcelona Valencia system, [Ali16a]) was developed from the demand of having a measurement system for microstrip sensors that is close to real detector applications and utilizes an analogue front-end readout chip [Her12]. It can be used for laser measurements, as well as for radioactive source

¹Only approximate value known because the scintillator is wrapped light-tight and no more information are given.

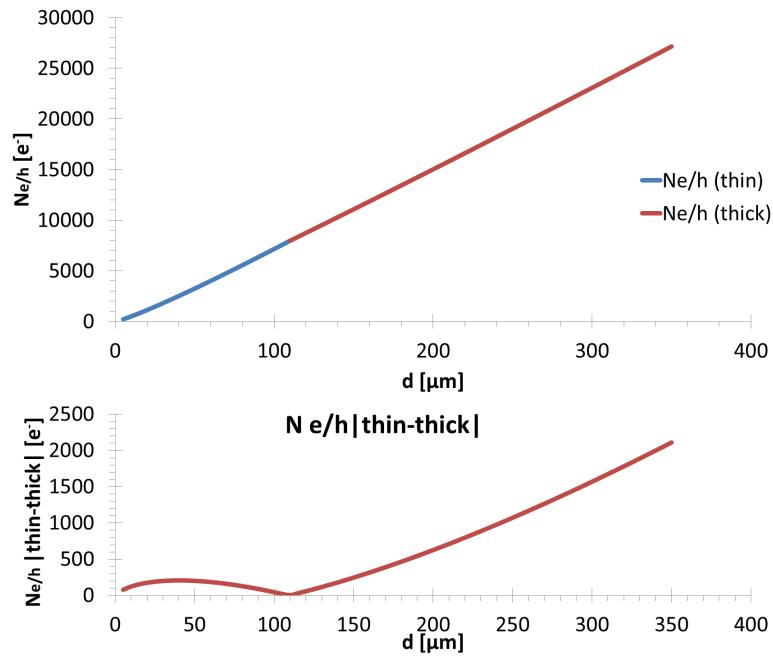


Figure 3.9.: Expected collected charge in silicon as function of the device thickness according to Equation 3.1. The bottom plot shows the absolute value of the difference where $N_{e/h}$ has been calculated with both equations for the full thickness range.

measurements with the method described in the previous subsection. The system allows to read out all channels of a microstrip silicon sensor at the same time with the analogue front-end Beetle chip that is used in the LHCb experiment [Löc06a].

The ALiBaVa system is widely used within the RD50 collaboration [Mol16] for charge collection measurements. A silicon sensor is attached to the daughterboard (Figure 3.10). It is then wire-bonded to the pitch adaptor which is connected to the Beetle chip [Löc06b], an analogue readout ASIC (Application Specific Integrated Circuit) with 128 channels, which was designed for the LHCb experiment. Each channel has its own low-noise charge-sensitive preamplifier, an active CR-RC pulse shaper and a storage/pipeline (Figure 3.12). The shaper is used for pile-up prevention and signal-to-noise optimization. This also allows adjustment of the pulse shape to specific requirements by changing certain parameters (see [Her12]). The input signal from the sensor can either be positive or negative, which allows measurement of n- and p-type sensors. After shaping, the signal is stored in the pipeline, a 168 capacitors long ring storage (it starts to overwrite entries from the start when the end is reached).

Each daughterboard has two readout chips, which are mounted opposite of each other, but only one is connected with a silicon sensor. The sensor itself is either glued or strapped to a heat sink, which is screwed to the daughterboard. The sensor backside is contacted by the aluminium heat sink, which is contacted via the screws, while the bias rail is wire-bonded to a circuit on the PCB. Glueing the silicon sensor with silver-epoxy ensures a good electrical backside contact and is done for sensors that will not be used in other systems in the future. On the other hand, if further procedures, like irradiations, are planned for the sensor it will only be temporary

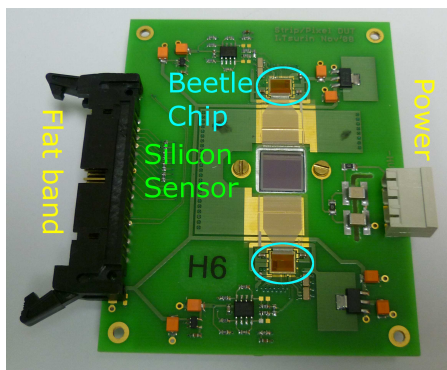


Figure 3.10.: Picture of the ALiBaVa daughterboard.

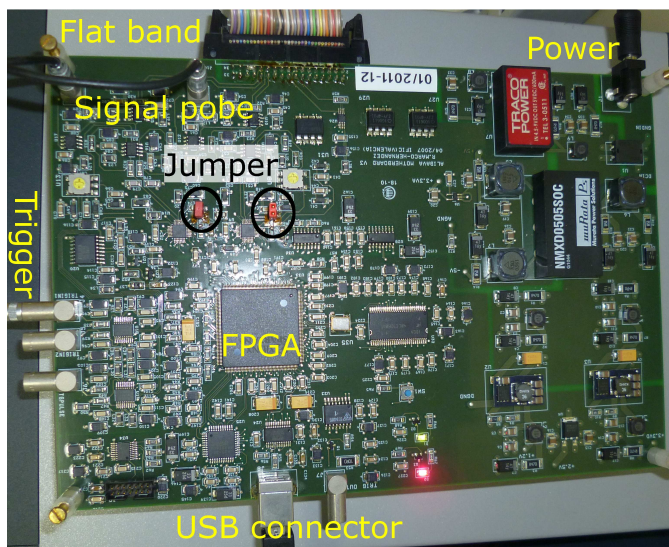


Figure 3.11.: Picture of the ALiBaVa motherboard.

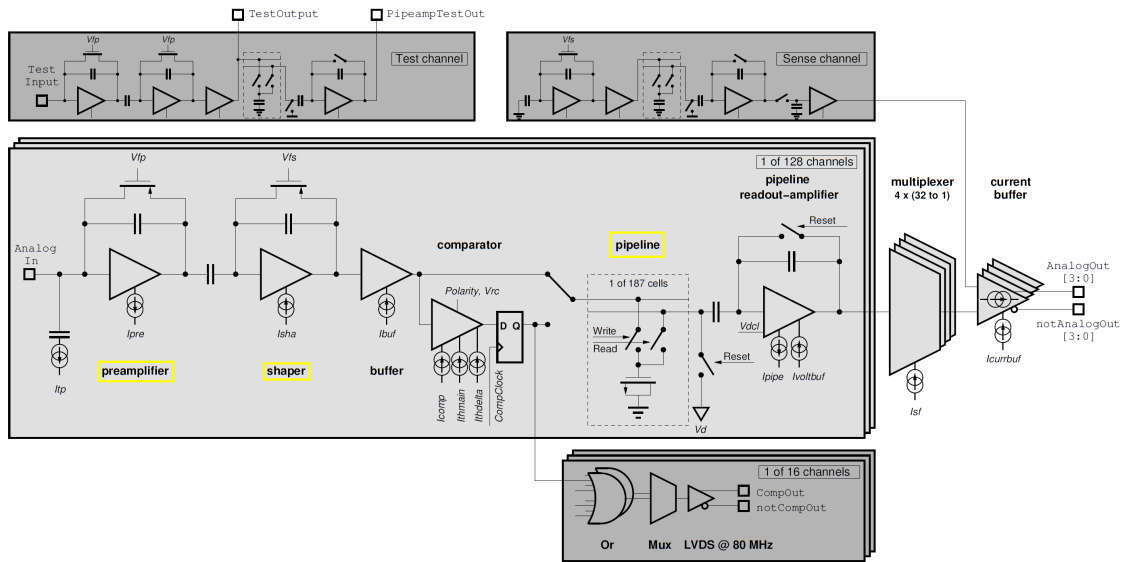


Figure 3.12.: Schematic block diagram of the Beetle readout chip [Löc06a].

attached by strapping it down.

The board has connectors for silicon high voltage and a flat cable connector which links it to the motherboard (Figure 3.11). A Field Programmable Gate Array (FPGA) in the centre regulates the functions and is controlled by a computer which is connected via USB with the motherboard. Two Lemo connectors, one for each Beetle chip, allow to probe the raw data signals from the daughterboard with an oscilloscope. The readout is triggered by a scintillator in the test box (Figure 3.13). The whole box is flushed with nitrogen and located in a freezer. Two fans provide a constant air flow in the box to cool the sensor. A lid covers the box and has a support for the radioactive source. The source is housed in a brass cylinder with

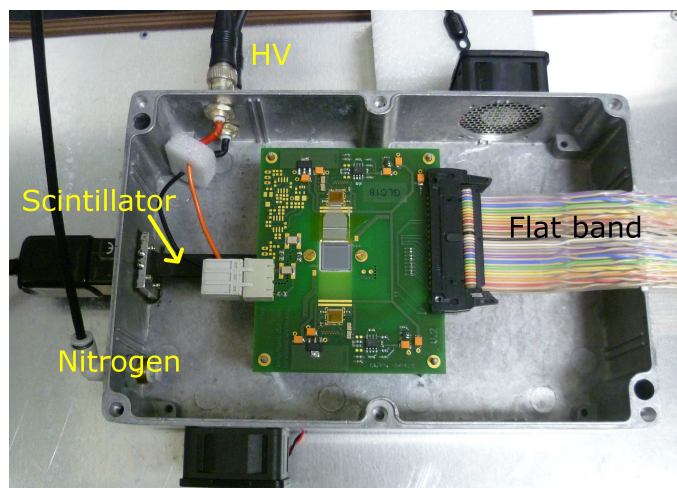


Figure 3.13.: Picture of the ALiBaVa test-box.

a small hole pointing downwards, to collimate the β -particles in one direction and shield the environment from unwanted radiation. For the high voltage an Iseg SHQ 222M [ISE16] power supply is used which can provide up to 2000 V.

The whole ALiBaVa system is controlled by a C++ program, which provides a graphical user interface (GUI). The Liverpool system uses software version 0.1.5-1. When starting the GUI a specific set of Beetle settings is loaded, the ‘kazu’ settings (see Table A.2). These settings, which define amongst others the pulse shape, are chosen because they create an optimal SNR and are used in LHCb test measurements.

Full Gain and Half Gain Two jumpers on the motherboard (Figure 3.11) allow the choice between two different measurement modes, full gain and half gain. With this self-made change of the motherboard at Liverpool it is possible to improve the measurement range. Full gain refers to the jumper connecting the two pins while for half gain the jumper is not set. This affects the Analogue-to-Digital Converter (ADC, Figure 3.14): the used ADC on the motherboard has 511 channels. For converting the signal from the daughterboard a reference voltage ($V_{ref,in}$) is used to define the voltage increments of the channels ($511 \text{ channels}/V_{ref,in}$). In the full gain configuration the jumper closes a voltage divider and therefore $V_{ref,in} = V_{ref,out}/2$, with the constant voltage $V_{ref,out}$. If the jumper is not set (half gain), it is simply $V_{ref,in} = V_{ref,out}$. Assuming a signal of 100 mV from an irradiated sensor and $V_{ref,out} = 500 \text{ mV}$, for full gain it would be in channel 204 whereas for half gain only in 102. Half gain is good for high signals (unirradiated sensors) and full gain allows a better measurement of small signals (irradiated sensors). The original motherboard without jumper is always in half gain mode.

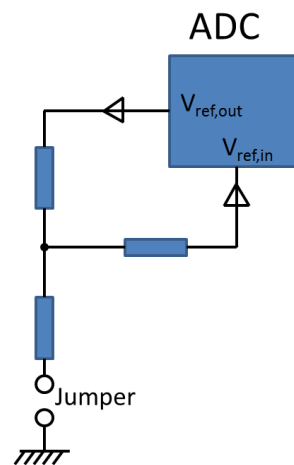


Figure 3.14.: Schematic overview for jumper position for full gain (jumper set) or half gain (jumper not set).

3.2.2. ALiBaVa Data Analysis

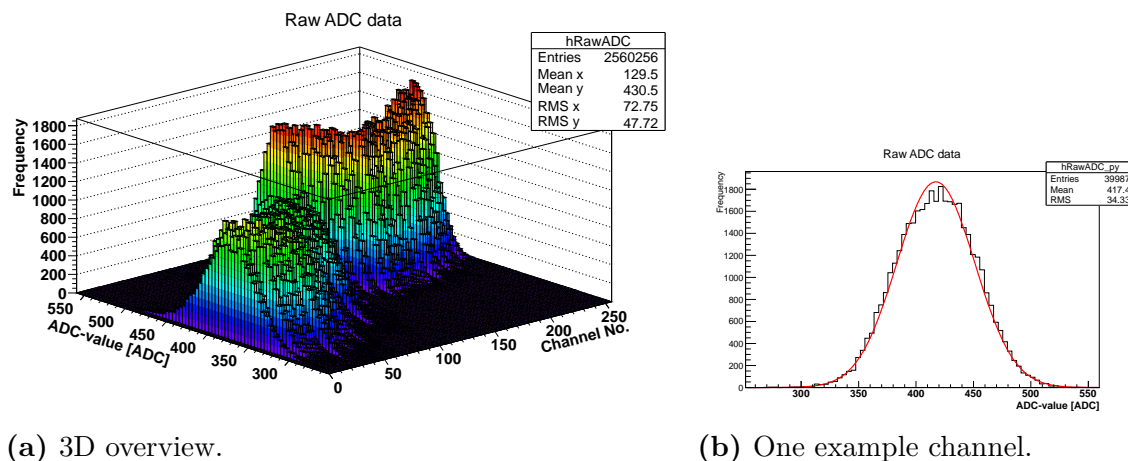
The raw data from the ALiBaVa system is saved to binary files. These are analysed by ROOT scripts, developed in Liverpool, but are based on the code provided by Alibavasystems [Ali16a].

Charge collection measurements are usually performed at different voltages to see the evolution of the collected charge with increasing bias voltage. At each voltage two measurements are performed: the pedestal measurement records 10 000 events

with random trigger input, while the radioactive source run (RS run) collects 100 000 events triggered by the scintillator. Although the pedestal run should be done without the source, it can be done with it because the events are randomly triggered and source hits are ignored by the software.

The analysis is also performed in two steps. First the pedestal run has to be analysed because the results are required for the source run analysis. With the ALiBaVa system it is possible to measure positive and negative signals, depending on the doping type of the silicon bulk. Because the saved ADC value can only be positive the signal is recorded in the way that negative signals get ADC values from 0 to ~ 500 and positive signals go from ~ 500 to 1023 ADC. By analysing the data the exact position of the base line, the so called pedestal value, is obtained. This is done for each channel individually by averaging the signals over all events. Figure 3.15 shows that the distribution is Gaussian for each channel. The mean corresponds to the pedestal value while the width σ is associated with the noise. For a quick analysis the RMS (root mean square) can be calculated and if the distribution does not deviate too much from the Gaussian shape the RMS is equal to the Gaussian width σ . Because ROOT is used for the analysis the RMS values from the analysis are equal to the standard deviation [ROO17] while the name is kept for consistency with old versions.

While the pedestal value is unique for each channel and calculated from all events, it can happen that there is a shift of the measured data of a group of channels from one event to the next. This is called common mode noise and can be caused by exter-



(a) 3D overview.

(b) One example channel.

Figure 3.15.: The left picture shows the raw data signals of a pedestal run with all channels having a Gaussian shape. A silicon sensor is connected to the channels 1 to 127 (first Beetle chip). For a better illustration number of bins for the channel number and the ADC-value were reduced. An example channel can be seen in the right picture, where the raw data were fitted with a Gaussian to demonstrate that the signal follows this distribution.

nal interferences. The simple case scenario is that all channels are equally affected. After the pedestal subtraction the signal of each channel should be approximately 0, taking the Gaussian noise into account. The shift is computed by calculating the average value of all channels (connected and unconnected separately) and is then subtracted from the signal value of each channel. This has to be done for each event individually and channels with considerably higher signal (due to charge generation from β -particles) are discarded. To improve pedestal and noise correction, these steps can be done more than once.

Figure 3.16 shows on the left side the raw ADC values after a pedestal run for each channel where the frequency is colour coded for all events. The channels 1 to 128 are connected to a silicon sensor which results in higher noise. It can be seen as well that some of these channels show single hits with lower ADC values which are caused by charge deposition from the source in single events. These events are ignored in the analysis. On the right hand side of the picture the signals are shown after pedestal correction and common mode subtraction (CMS). All signals are centred at 0 ADC and show an overall uniform appearance.

While the pedestal analysis will be performed for all channels, it is important to distinguish between channels which are connected to the sensor and those which are not. The Liverpool ROOT scripts use an options file to set certain parameters in the analysis (see Table 3.1). These are among others the SENSOR-CHANNEL-RANGE (the channels which are connected to the silicon sensor) and MASKED-CHANNELS. It can happen that some channels show significantly higher noise than their neighbours, which can be caused by missing or touching wirebonds or by faulty strips. These channels should not be used in the analysis and are therefore masked.

Pedestal values for each channel are written to a file, which is used in the source run analysis. Figure 3.17 shows the noise distribution before (black) and after pedestal and CMS correction (red). The total noise value is obtained by calculating the average of all connected channels and is used as uncertainty of the collected

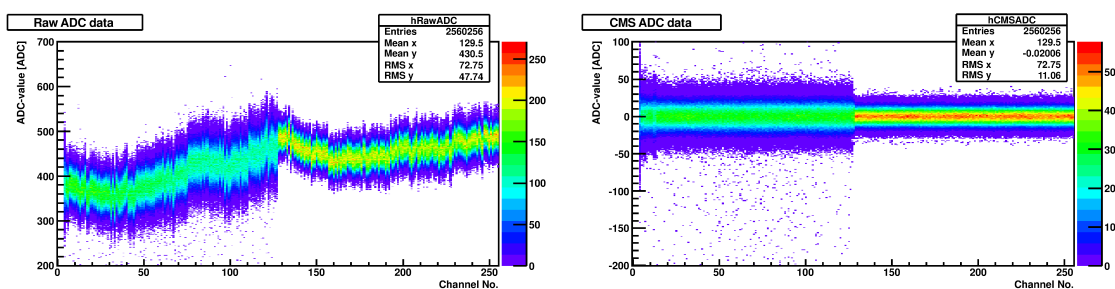


Figure 3.16.: Signal in all channels from pedestal measurement. Left: raw signal, Right: signal after pedestal correction and common mode subtraction. The channels 1 to 128 are connected to a silicon sensor, while the channels 129 to 256 are not.

Variable	Value	Description
SEED-THRESHOLD	3.5	Seed cut
LOW-THRESHOD	1.8	Neighbour cut
TIME-CUT-LOW	12	Time cut start
TIME-CUT-HIGH	22	Time cut end
POLARITY	-1	-1 for p-type, +1 for n-type
FIT-RANGE-LOW	300	Landau-Gauss fit start
FIT-RANGE-HIGH	800	Landau-Gauss fit end
NUMBER-OF-BINS	400	Bins in histogram
SENSOR-CHANNEL-RANGE	10 100	Channels used in analysis (connected to sensor)
MASKED-CHANNELS	0 50 90	Masked channels
PLOT-ADC-VS-EVENT	0	Default setting
CMS-MODE	SLOPE32	Default setting
GLOBAL-GAIN-ELECTRONS -PER-ADC	1	Conversion factor, default 1

Table 3.1.: Values for certain variables used in the ALiBaVa data analysis.

charge.

The first step of the radioactive source run analysis is to correct for the pedestal values and subtract the common mode noise. Further restrictions on the data are required: the time cut and the seed cut.

The time cut is necessary due to the way the ALiBaVa system records the data. Figure 3.18 shows the detailed process. The front end signal height from the Beetle chip is sampled every 25 ns and stored in the ring storage. Due to electronics and the cable the motherboard receives the trigger signal from the scintillators with a short delay. Furthermore a longer delay of 128 'bunch crossings' is implemented in the firmware of the motherboard to allow the complete sampling of the signal. Therefore it is not the current storage entry that is required, but one which was previously recorded. The time delay between received trigger signal and actual particle transit in the sensor is compensated by the LATENCY value (also in units of 'bunch crossings', see Table A.2), a constant which is set in the Beetle settings. Together with the Beetle signal value the time between the trigger signal and an internal 10 MHz clock is written into the output file. As can be seen in Figure 3.19, this time difference, recorded by the Time-to-Digital Converter (TDC), is uniformly distributed within the 100 ns period because the radioactive decay occurs randomly. Based on the random nature of the radioactive decay it may happen that the recorded signal value is not the actual maximum of the signal curve. While the signal value at the maximum is proportional to the generated charge in the silicon sensor, smaller values would lead to false charge values. This is where the time cut is used to improve the analysis. The cluster charge of the channel with the highest SNR is

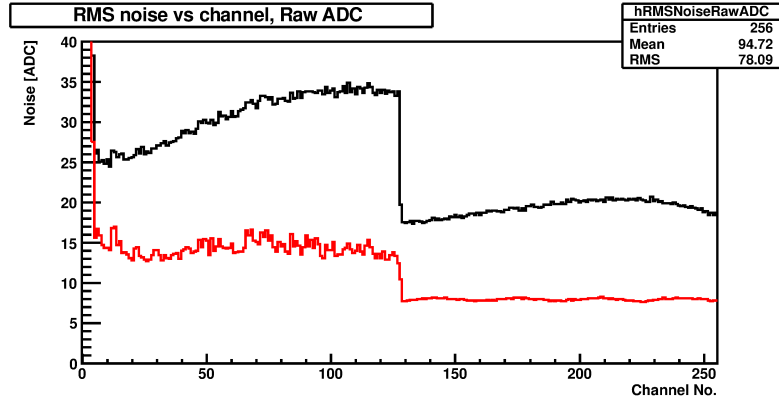


Figure 3.17.: Noise in all channels from pedestal measurement with a silicon strip sensor connected to the channels 1 to 127. Black: raw noise values, Red: noise after pedestal and common mode subtraction. This example shows the noise of a sensor irradiate to $5 \times 10^{15} \text{ n}_{\text{eq}}/\text{cm}^2$ and measured at a bias voltage of 1300 V.

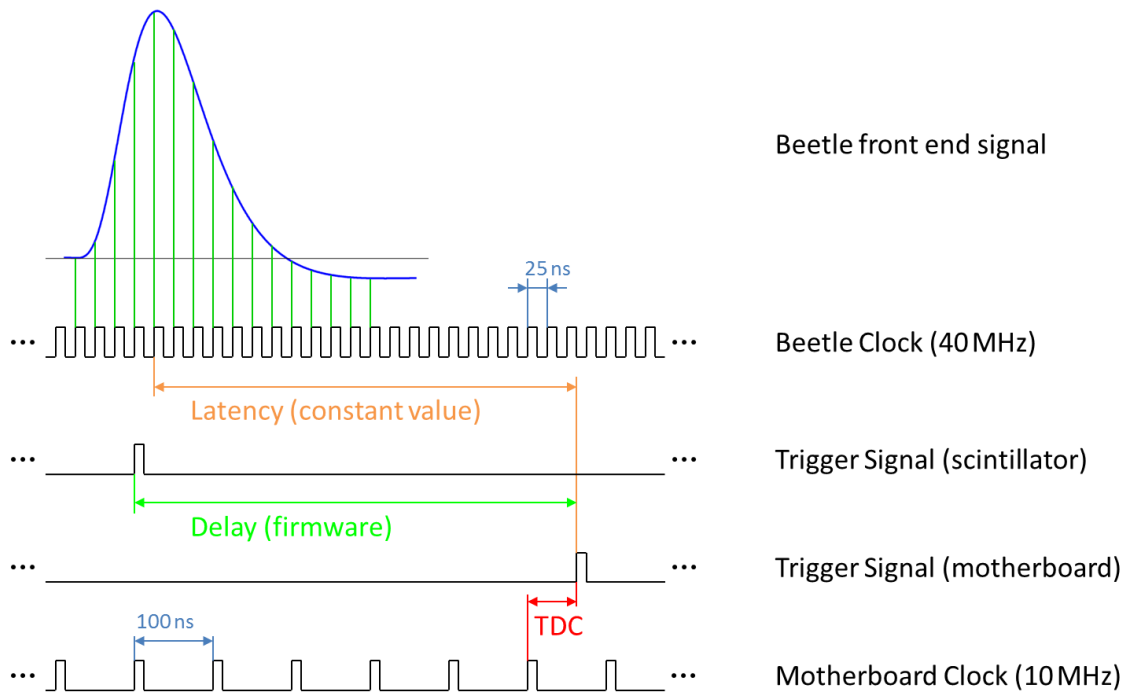


Figure 3.18.: Sketch of ALiBaVa timing. The front-end signal of the Beetle chip is sampled every 25 ns and written in a ring storage. When the random trigger signal arrives (after a hardware delay), the ring storage entry which is a fixed value (Latency) in the past will be read and further processed. The time between the trigger signal and a 10 MHz clock is recorded by the TDC.

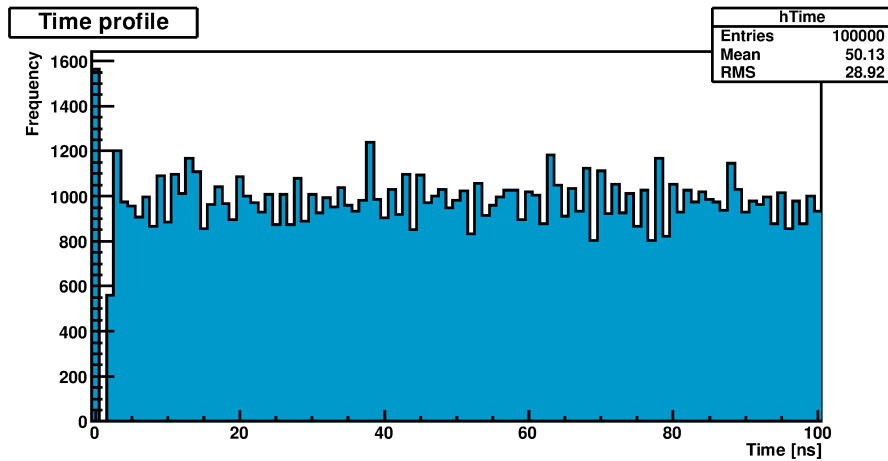


Figure 3.19.: Time profile of RS-run: histogram of all TDC values, evenly distributed. The TDC has a resolution of at least 100 ps and the binning in the histogram is purely driven by the analysis.

plotted as function of the TDC value (Figure 3.20). A maximum can be seen at approximately 15 ns. The position of the maximum can vary for different systems but by changing the LATENCY parameter is possible to get a similar graph. Ideally the TDC value with the highest charge will be used, but this would reduce the data too much. Instead a time cut of 10 ns around the maximum is applied to get

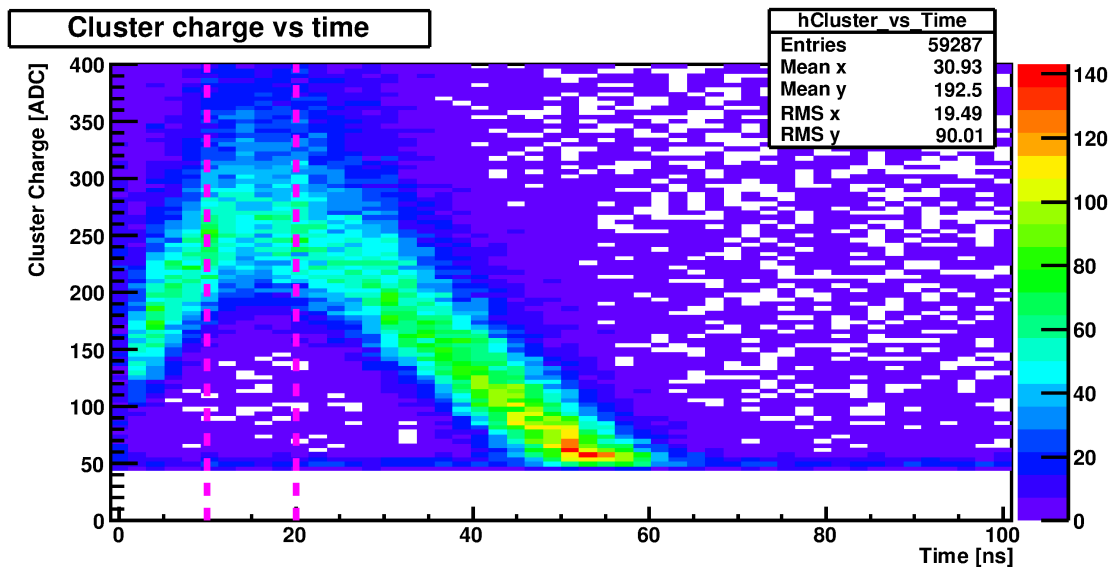


Figure 3.20.: Cluster charge as function of time, measured by the TDC, with a maximum approximately at 15 ns. The time cut (10 ns window, dashed lines) is applied to cover the maximum.

enough statistics for the further analysis (TIME-CUT-LOW and TIME-CUT-HIGH in Table 3.1). The exact position of the time window is obtained by looking at the final collected charge for different positions in the area of the maximum and choosing the parameters which results in the highest signal. It is usually not necessary to change the time cut during a voltage scan of a sensor. With a time window of 10 ns 90 % of all events will be discarded; therefore it is important to record enough data.

The time-bin 0 in Figure 3.19 shows more events, because times less than 2 ns can not be recorded (seen as gap in the histogram) and are all added to this bin. Additionally a known error of the TDC can occur occasionally: instead of recording the correct time difference the value is set to 0. If too many events are affected by this so called ‘time-bin-0 problem’ then there are not enough good events available after the time cut for a reasonable analysis. This effect can be recognized during data taking by looking at the GUI window which displays the TDC values. The TDC unit needs a reset and therefore the measurement has to be repeated.

After restricting the events with the time cut, the seed cut is applied. For all events within the time window the strips with the highest signal-to-noise ratio are compared with the seed cut value (SEED-THRESHOLD, Table 3.1). If the SNR is higher, the event is used otherwise it is rejected. Due to charge sharing and tracks that are not perpendicular to the surface also neighbour strips will collect some charge and form a cluster. This is taken into account by comparing the neighbour strips with the neighbour cut value (LOW-THRESHOD) and if the SNR is higher, the charge is added to the cluster charge.

In the final step, the cluster charge is plotted (Figure 3.21) and fitted with a convoluted Landau-Gauss distribution. The x-position of the maximum (Most Probable Value MPV) corresponds to the collected charge in the silicon device. The energy loss of electrons in matter follows the Landau distribution rather than a Gauss distribution, because δ -electrons are responsible for a high energy transfer creating the tail. This Landau distribution has to be convoluted with a Gauss distribution to take the detector noise into account.

By looking at the cluster position (Figure 3.22) it is possible to estimate the position of the radioactive source. In this graph only the events which have passed the time cut and seed cut are used as well as only the channels which are used in the analysis. A Gauss-like shape would be expected as the source is collimated by its housing. If it is placed properly above the centre of the sensor this can also be seen. In this example figure the first beetle chip with the channel numbers 1 to 128 was used and the cluster position shows a maximum at approximately 60 which indicates that the source is positioned centrally above the sensor. The shown channels are restricted by the SENSOR-CHANNEL-RANGE and take noisy channels at the sensor edge into account by ignoring them for the analysis. It is also possible to identify faulty channels in this plot and add them to the masked channels. Figure 3.23 shows an example where channel 142 shows an excess in hits and channels 185 and 194 show a shortage. For the final cluster charge fit these

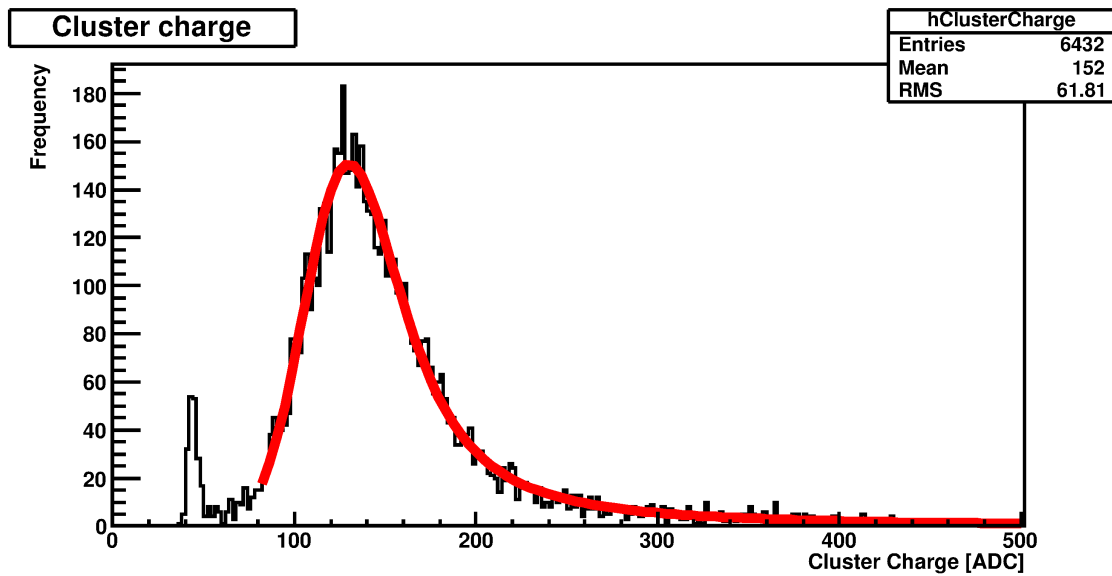


Figure 3.21.: Fit of the final cluster charge spectrum with a convoluted Landau-Gauss distribution. The maximum value (MPV) corresponds to the collected charge. This example shows a strip sensor irradiated to $5 \times 10^{15} \text{ n}_{\text{eq}}/\text{cm}^2$ and measured at a bias voltage of 800 V.

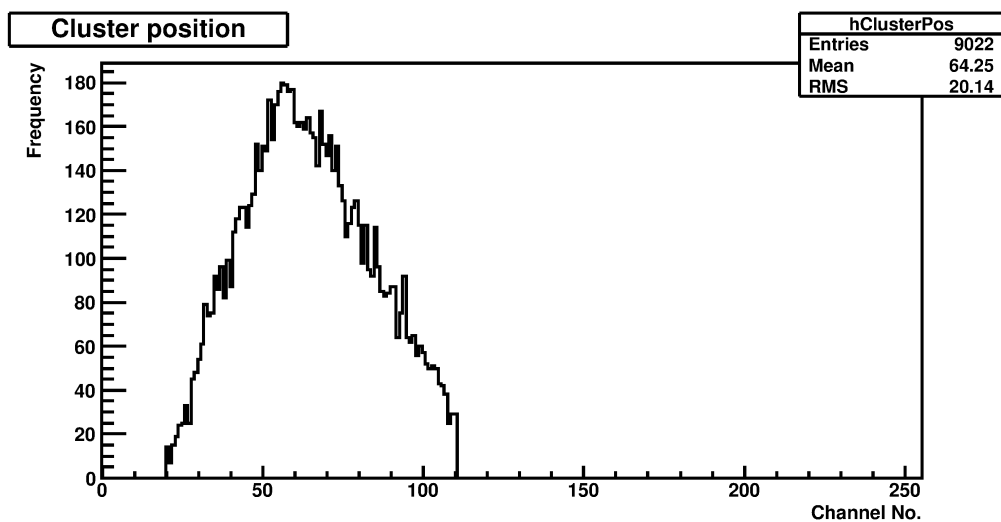


Figure 3.22.: Cluster position of source run allows to see the position of the source.

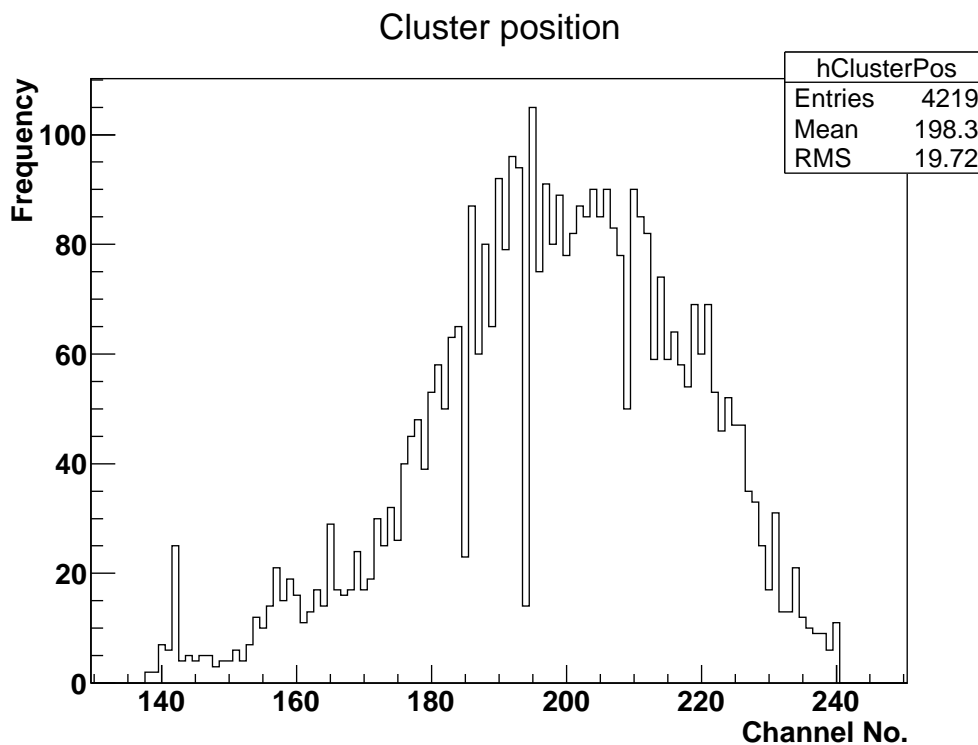


Figure 3.23.: Cluster position of source run allows with bad channels. Channel 142 shows an excess in hits compared to the surrounding channels and should be excluded from the charge fit. The channels 185 and 194 show a smaller signal and have to be masked as well.

channels have to be excluded by masking them.

3.2.3. Calibration

From the data analysis the collected charge is given in ADC units. This needs to be converted into the number of electrons, which is done with the calibration measurement. Each daughterboard has a unique calibration factor because of the small deviations in the used components as well as the Beetle chip itself. Additionally for the custom made Liverpool motherboards the calibration has to be done for full gain and half gain respectively.

An unirradiated strip sensor with well known thickness is measured with the ALiBaVa system. It is important to use voltages well above the full depletion voltage, preferably a full voltage scan. This will result in a graph like in Figure 3.24. In this example of an ATLAS12 mini sensor the collected charge increases approximately linearly with bias voltage until the sensor is fully depleted at ~ 350 V. Increasing the bias voltage beyond this value does not increase the collected charge further.

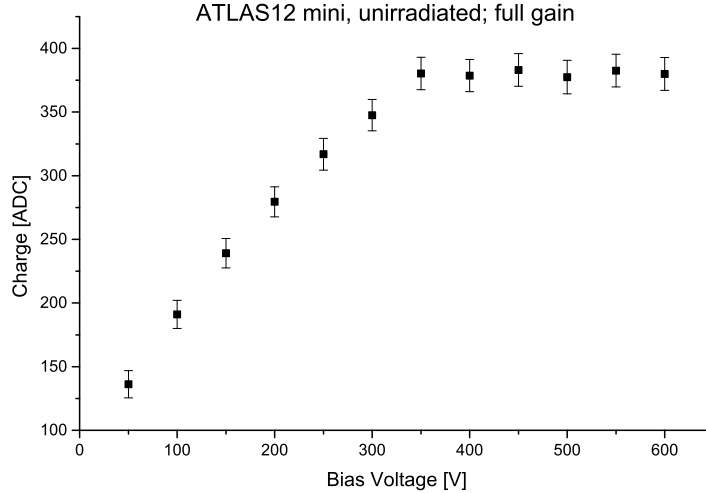


Figure 3.24.: Full gain ALiBaVa measurement of unirradiated ATLAS12 mini sensor with full depletion voltage of approximately 350V. The errors of the charge are the noise values from the pedestal analysis.

For a fully depleted silicon sensor the number of electron-hole pairs produced by a traversing MIP through silicon can be calculated using Equation 3.1. To get the conversion factor the average of all charge values after full depletion is used. In this example the values from 350 V to 600 V compute to a average signal of (380.4 ± 0.9) ADC for the full gain measurement. The active thickness of the ATLAS12 mini sensors is (302 ± 1) μm in which (23231 ± 81) electron-hole pairs are generated. Using these values and

$$Cal = \frac{N_{e/h}}{\langle \text{Charge} \rangle} \quad (3.2)$$

a calibration factor of $(61.1 \pm 0.3) e^-/\text{ADC}$ was calculated for this specific daughterboard. Table A.1 in section A.1 shows all calibration values which have been measured for the presented work.

One well known fact of the Beetle chip has not been taken into account so far. The charge collection depends on the temperature. An example measurement has been done with a 300 μm thick Micron sensor. Figure 3.25 shows the collected charge as function of the temperature. A distinct linear correlation is visible. Fitting the data with a straight line result in a slope of $(-1.42 \pm 0.09) \text{ADC}/^\circ\text{C}$ and an intercept of $(243.8 \pm 1.6) \text{ADC}$. For each set temperature the calibration factor has been plotted as function of the average temperature in Figure 3.26. The straight line fit of this graph results in values for gradient and intercept shown in Table 3.2. A similar measurement from [Wal10] is included for comparison. It can be seen that the values obtained in Liverpool are approximately half the values from [Wal10]. This is in good agreement with the fact that in Liverpool the full gain configuration

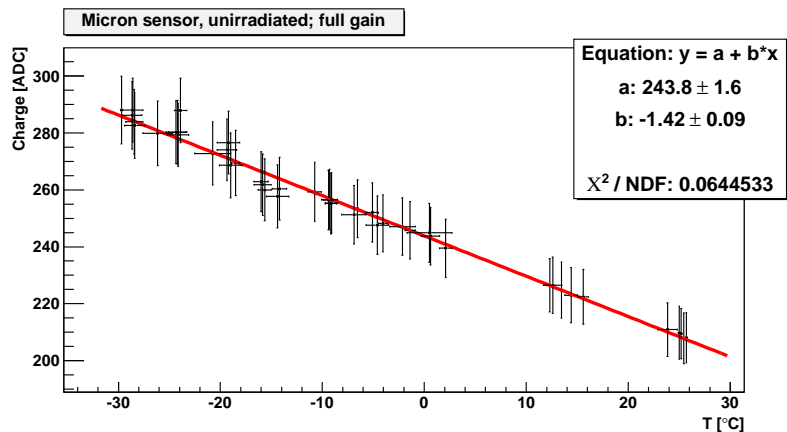


Figure 3.25.: Collected charge of a 300 μm Micron strip sensor for different temperatures. The errors of the charge are the noise values from the pedestal analysis. A linear fit was performed with ROOT.

	Gradient $\left[\frac{e^-}{\text{ADC} \cdot ^\circ\text{C}}\right]$		Intercept $\left[\frac{e^-}{\text{ADC}}\right]$		Gain Setting
	Value	Uncertainty	Value	Uncertainty	
Liverpool	0.54	0.01	95.4	0.2	half
[Wal10]	1.08	0.07	183.3	1.8	full

Table 3.2.: Parameter of the linear fit, describing the temperature dependence of the ALiBaVa calibration.

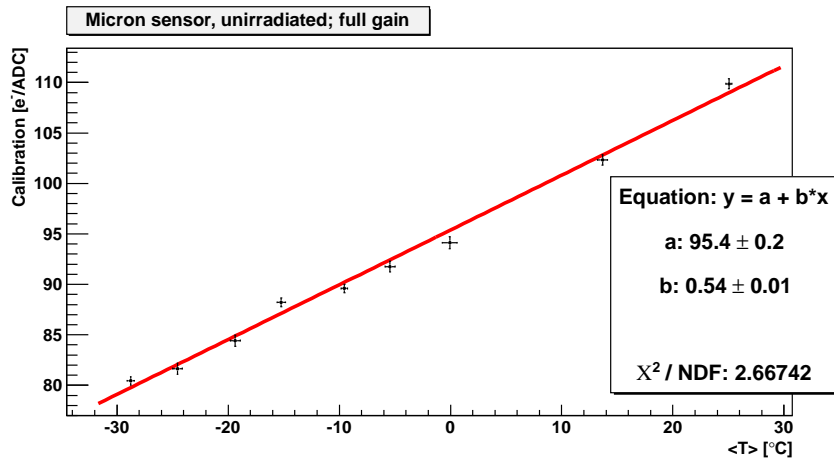


Figure 3.26.: Calibration value of a 300 μm Micron strip sensor for different temperatures. The Linear fit was performed with ROOT.

has been used, while the unchanged motherboard in [Wal10] uses half gain, which reduced the signal by a factor of approximately two.

4. Charge Multiplication Study

With increasing irradiation damage the collected charge in silicon sensors decreases. Therefore charge multiplication can be beneficial. It has been observed in irradiated sensors, resulting in more collected charge than expected. In some cases even more charge has been collected than in fully depleted unirradiated sensors (see Figure 4.1). The sensors used for the study shown in this chapter have been designed to enhance charge multiplication by changing the strip properties or the sensor properties. In section 4.1 the measurements after irradiation are shown. Some of these devices have been used for an extensive room temperature annealing study, shown in section 4.2. To investigate the stability of the observed charge multiplication a constant bias voltage has been applied to some sensors up to several weeks and the results are presented in section 4.3.

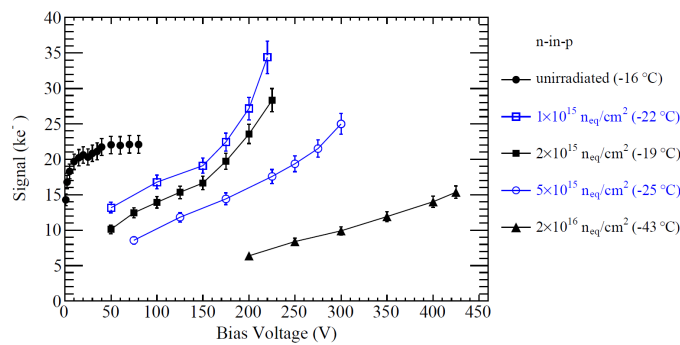


Figure 4.1.: Example of sensors that show charge multiplication from [Köh11]. N-in-p 3D sensors have been measured before and after irradiation. It can be seen that some sensors show more collected charge after irradiation than unirradiated sensors. This is called charge multiplication.

4.1. Charge Collection Measurements

The effect of charge multiplication (CM), where the collected charge exceeds the expected value, is thought to be caused by impact ionization in the high electric fields at the strips' edges. To investigate this effect further, dedicated silicon micro-strip sensors ($\sim 1 \times 1 \text{ cm}^2$) have been produced by Micron Semiconductor Ltd. [Mic16] within the RD50 framework. These are n-in-p FZ strip sensors, produced with different production methods, various strip geometries and different thicknesses.

Beside the standard production method, in some of the wafers the implant energy, or the diffusion time, has been doubled. The standard thickness for silicon strip sensors is approximately 300 μm but for this study also thin (150 μm) and thick (675 μm) sensors have been produced. It has to be mentioned that the physical thickness of the thick sensors is not the designed value of 75 μm but the standard thickness of 300 μm . Nevertheless these samples show a different behaviour than the standard samples and therefore they are treated as an own group. Table 4.1 shows a list of the different wafer types with their labels, which are used within this thesis.

The strip geometry has a huge impact on the electric field; therefore several combinations of strip pitch (distance between two readout strips) and strip width (width of the n-type implant) have been tested. Additionally intermediate strips have been implemented (see Figure 4.2), which are either connected to the bias ring or are floating. Biased intermediate strips contribute to the electric field geometry but in both cases they contribute to the signal by capacitive coupling to the readout strips¹. For the sensor labels in this thesis, the following convention is used: First the letter ‘P’ for the strip pitch with the value in μm , followed by ‘W’ for the strip width in μm . If intermediate strips are implemented then they are either biased (I) or floating (F) followed by the intermediate strip width in μm . For example the sensor ‘P80-W25-I10, extra diff’ has a strip pitch of 80 μm , a strip width of 25 μm , the biased intermediate strips are 10 μm wide and the diffusion time was doubled.

Figure 4.3 shows the simulated electrical field of a strip sensor with a strip pitch of 80 μm and strip widths of 6, 25 and 60 μm [Buc16]. These geometries were chosen to match existing detectors of this study. For the simulation the bias voltage was

Wafer Serial No.	Thickness [μm]	Resistivity [$\text{k}\Omega\text{cm}$]	Implant Detail	Label
2935-(2,4,5,6,7,8,9)	305	13	standard	std
2912-(2,3)	300	10 - 13	standard, double implant energy	2E imp
2935-10	305	13	standard, double diffusion time	extra diff
2885-5	150	10	thin	thin
2488-(6,7)	675	8	thick	thick

Table 4.1.: Details of the different charge multiplication wafers. Although the thick sensors are supposed to have a physical thickness of 675 μm , in reality they are only 305 μm thick. The column ‘Label’ refers to the used notation in this thesis. Here the label for the wafers 2488-(6,7) was kept as ‘thick’ to distinguish them from the ‘std’ sensors with the same thickness but different resistivity.

¹An intermediate strip distributes the signal of a particle traversing between two read-out strips more evenly than a wide read-out strip geometry would.

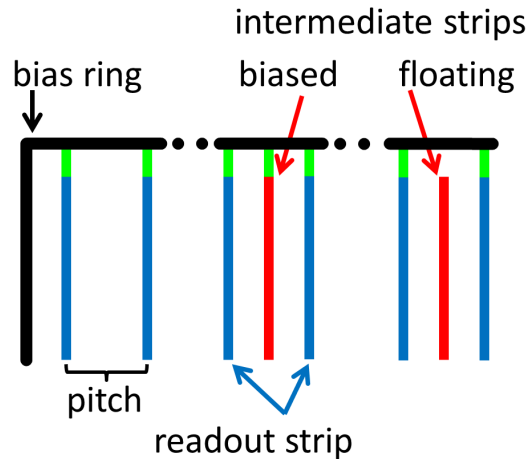


Figure 4.2.: Different strip geometries for the dedicated charge multiplication sensors. The standard design (left) is extended by including an intermediate strip. This strip is not read out and could either be biased (middle) or floating (right).

set to 500 V so that the sensor is fully depleted. It can be seen that the electric field is highest at the corners of the strip implants. With decreasing strip width the field strength at the corners increase and the sensor with a strip width of $6\ \mu\text{m}$ has the largest absolute field value. It is expected that charge multiplication will happen in these areas.

To study the effect of irradiation on the collected charge of these silicon sensors, samples were irradiated with protons at the cyclotron at the Karlsruhe Institute of Technology in Germany [KIT16b, KIT16a] to a fluence of $1 \times 10^{15}\ \text{n}_{\text{eq}}/\text{cm}^2$ and with thermal neutrons at the TRIGA mark III reactor at the Jožef Stefan Institute in Slovenia [JSI16a, JSI16b] to fluences of $1 \times 10^{15}\ \text{n}_{\text{eq}}/\text{cm}^2$ and $5 \times 10^{15}\ \text{n}_{\text{eq}}/\text{cm}^2$.

Charge collection measurements were performed before and after irradiation with the ALiBaVa system (see section 3.2). A large amount of sensors had to be measured for this study so that samples were shared with Freiburg. Measurements in Freiburg were carried out mainly by Christopher Betancourt and most Liverpool sensors were measured by the author of this thesis. Table A.3 in the appendix shows a list of all sensors and the contribution from the author is indicated. While the measurements before irradiation and after proton irradiation were only done at Freiburg, Liverpool contributed to the measurements after neutron irradiation. The results shown here have been partially published in talks [Bet12b, Won13a, Bet13b, Won14c] and papers [Bet12a, Bet13a]

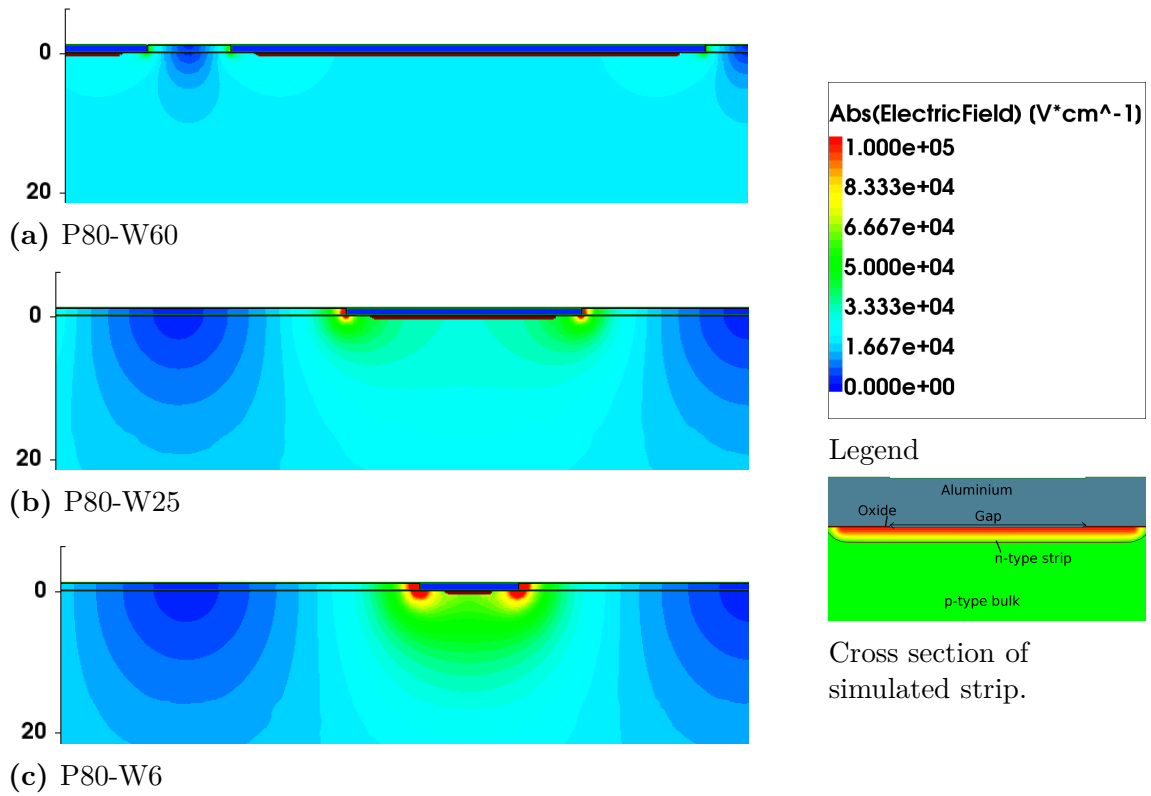


Figure 4.3.: TCAD electrical field simulations of different strip widths by Matthew Buckland [Buc16], showing the absolute electric field values colour coded. The pitch was set to $80 \mu m$ while widths of 6, 25 and $60 \mu m$ were used to match available detector geometries. For the simulation the bias voltage was set to 500 V so that the detector is fully depleted.

4.1.1. Unirradiated Sensors

Sensors with different strip geometries and from different wafer types have been measured before irradiation. As can be seen in Figure 4.4, it was possible to apply up to 1000 V to most of the sensors. The collected charge saturates for bias voltages higher than 100 V, indicating that the sensors are fully depleted. An approximate charge of 24 ke^- was measured, which is in good agreement with the expectation for $300 \mu\text{m}$ thick sensors ($(23.07 \pm 0.08) \text{ ke}^-$). It can be seen as well that there is a large spread with some sensors even reaching 30 ke^- , but there is no clear correlation with the sensor type. All sensors have in common that after reaching the saturation the collected charge is constant with increasing bias voltage, which signifies that there is no observable charge multiplication up to 1100 V. The noise and the signal-to-noise ratio, displayed in Figure 4.5, show similar behaviour as the collected charge: after reaching full depletion they stay constant.

4.1.2. Proton Irradiation, $1 \times 10^{15} \text{ n}_{\text{eq}}/\text{cm}^2$

Some of the 'std' wafer sensors have been irradiated with protons to a fluence of $1 \times 10^{15} \text{ n}_{\text{eq}}/\text{cm}^2$. By comparing the collected charge after irradiation (Figure 4.6) with the unirradiated sensors it can be seen that the values are lower and they also increase with increasing bias voltage, which indicates that the sensors are not fully depleted. Additionally no difference between the distinct strip types can be seen. Two sensors ('P80-W6, std' and 'P100-W10, std') show slightly higher charge from approximately 500 V to 700 V, but the shape of the curve is comparable with sensors

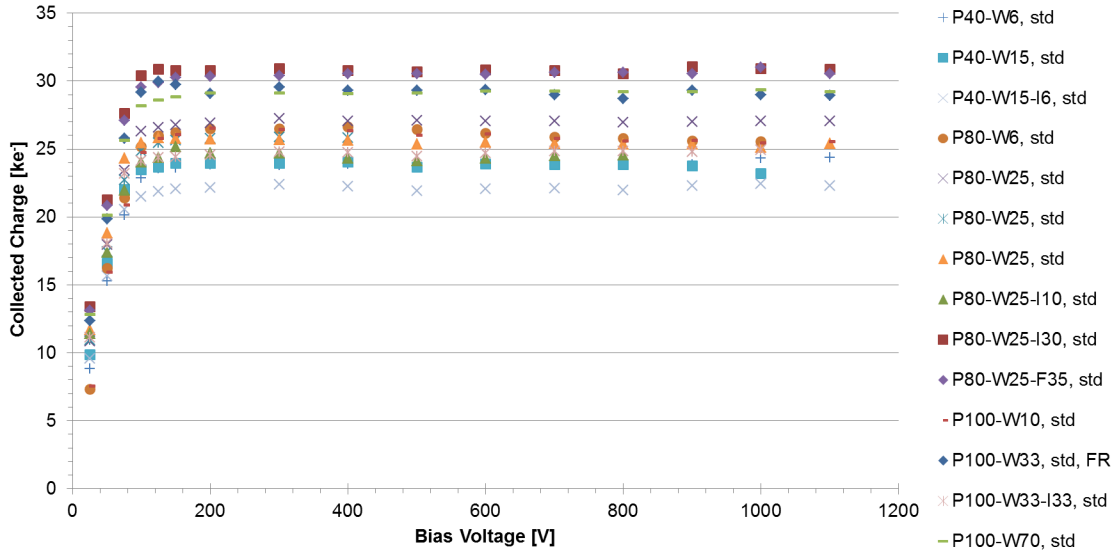


Figure 4.4.: Collected charge of unirradiated charge multiplication sensors, measured at Freiburg.

4. Charge Multiplication Study

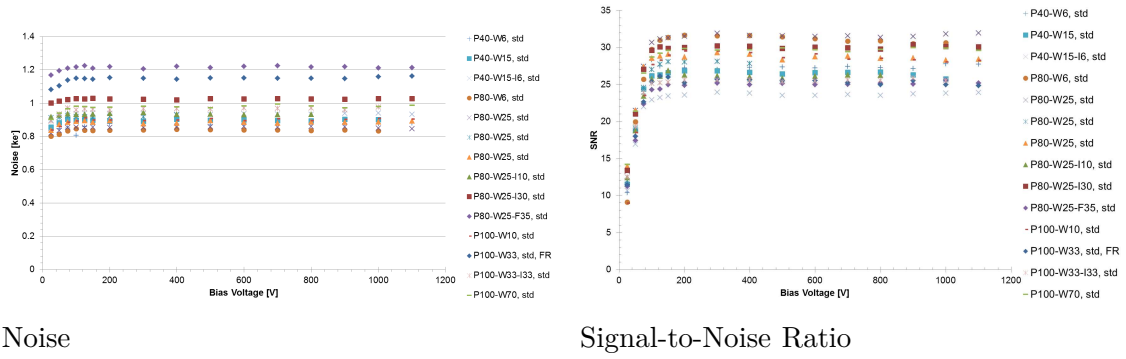


Figure 4.5.: Noise and Signal-to-Noise Ratio of unirradiated charge multiplication sensors.

that have been annealed. The noise distribution (Figure 4.7) is fairly uniform and in total even smaller than for the unirradiated sensors. There are no indications for charge multiplication.

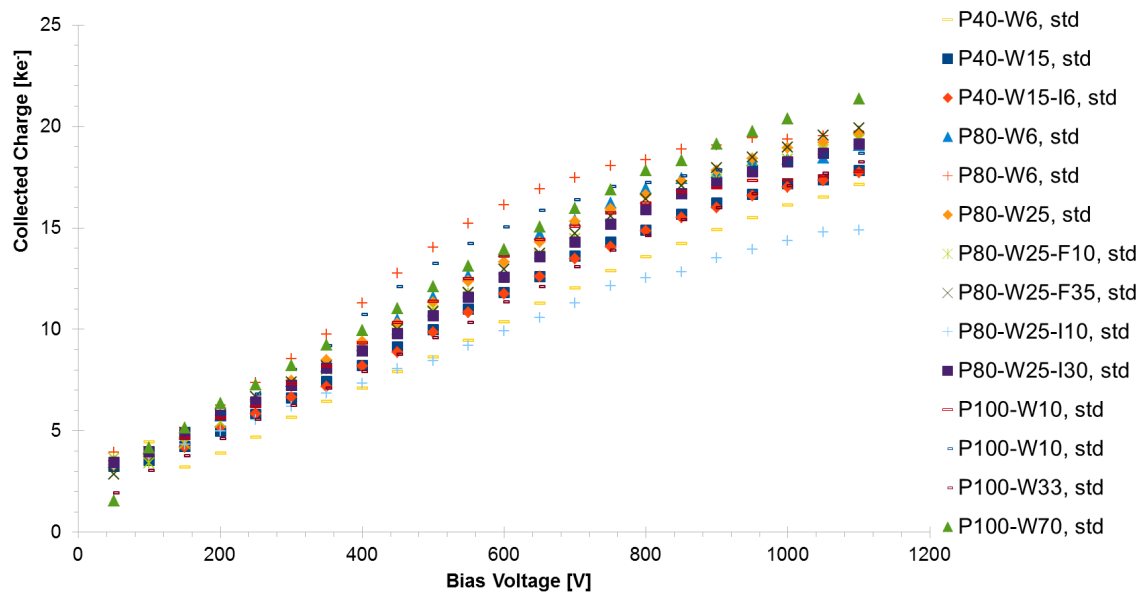


Figure 4.6.: Collected charge of charge multiplication sensors after $1 \times 10^{15} \text{ neq/cm}^2$ proton irradiation.

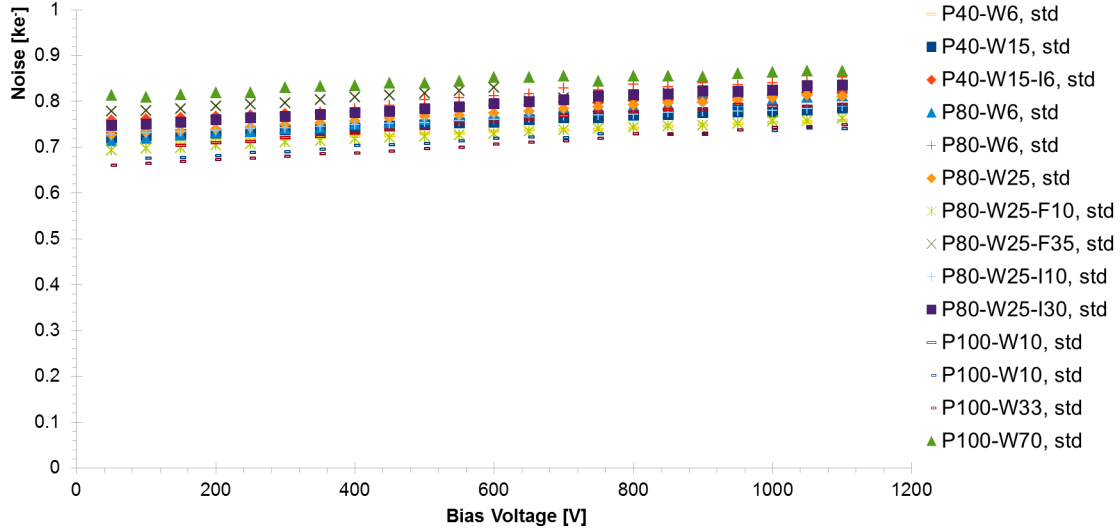


Figure 4.7.: Noise of charge multiplication sensors after $1 \times 10^{15} \text{ n}_{\text{eq}}/\text{cm}^2$ proton irradiation.

4.1.3. Neutron Irradiation, $1 \times 10^{15} \text{ n}_{\text{eq}}/\text{cm}^2$

While the measurements of the unirradiated and the proton irradiated sensors have been performed only at Freiburg, the samples which were irradiated with neutrons have been measured at Liverpool as well. It is important first to validate that the results are comparable. This can be done by looking at sensors with the same properties, but measured at both sites.

The results of this comparison are shown in Figure 4.8. The four examples show a very good agreement, which allows the conclusion that all measurements presented in this section are comparable, independent of the sensor geometry. It can also be seen that some measurements at Liverpool reach higher voltages than at Freiburg. The reason is that different power supplies were used: the Keithley 2410 (Freiburg) has a limit of 1100 V while the Iseg SHQ 222M at Liverpool can reach 2000 V.

Figure 4.9 shows the collected charge of all sensors irradiated with neutrons to $1 \times 10^{15} \text{ n}_{\text{eq}}/\text{cm}^2$. For this fluence, only the 'std' wafer type sensors were available. Up to 1000 V the values are in accordance with each other and no sensor geometry has clear benefits. The collected charge of the sensors which had been biased up to 2000 V increases as expected. At very high voltages first signs of saturation at approximately 25 ke^- can be seen. One sensor clearly shows a different behaviour than the other: 'P80-W25, std' shows a steeper increase. However the noise of this sensor (see Figure 4.10) does not show this strong increase in comparison with the other sensors. Some of the other samples² stand out because of their extreme

²'P40-W15-I15, std', 'P80-W25-I35, std' and 'P80-W25-F35, std'

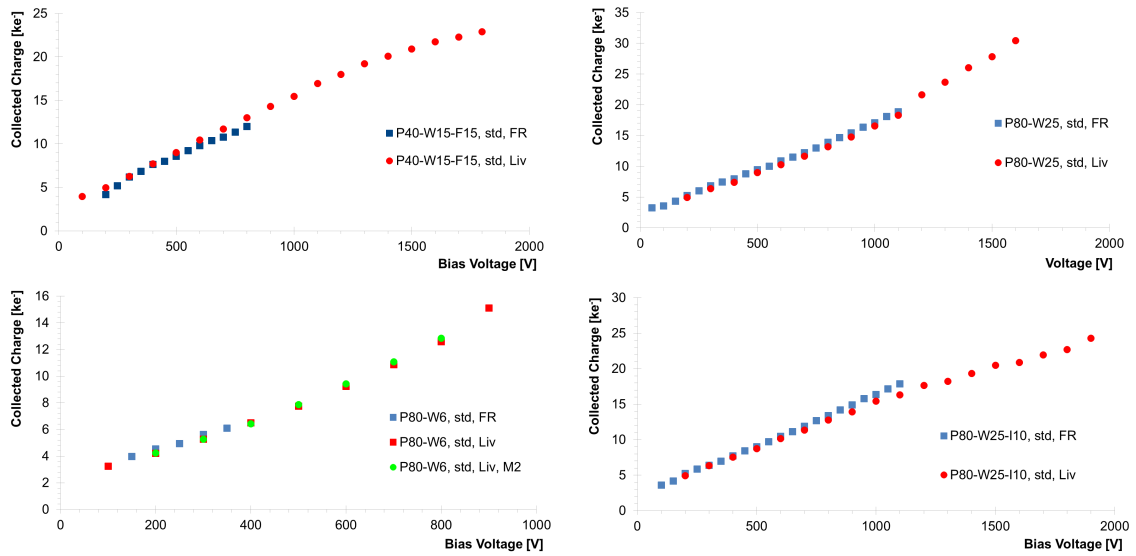


Figure 4.8.: Comparison of charge collection measurements between Freiburg and Liverpool for sensors with same properties, irradiated with neutrons to $1 \times 10^{15} \text{ n}_{\text{eq}}/\text{cm}^2$.

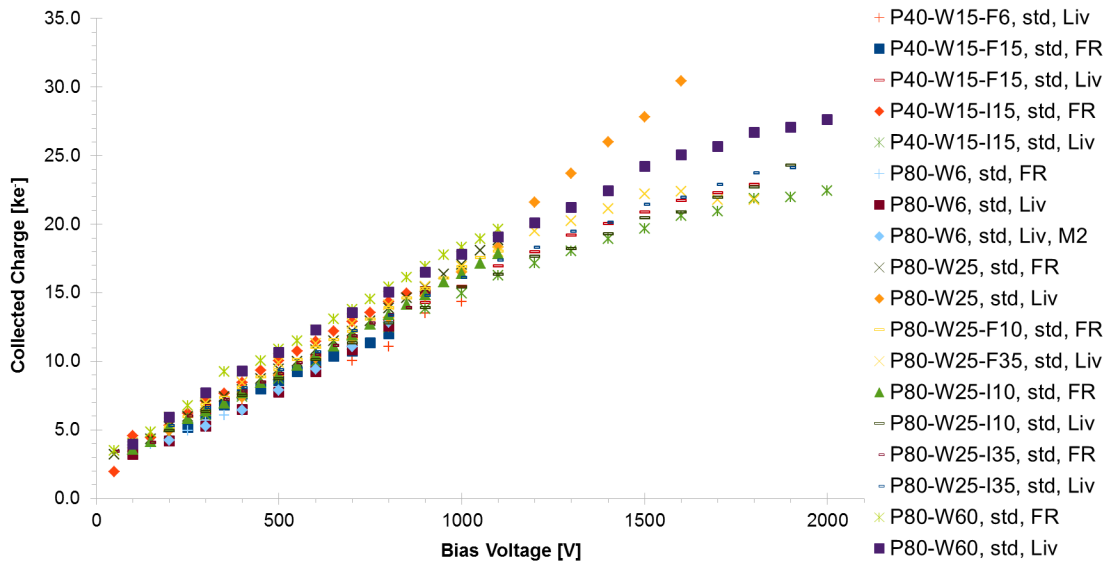


Figure 4.9.: Collected charge of charge multiplication sensor after neutron irradiation to $1 \times 10^{15} \text{ n}_{\text{eq}}/\text{cm}^2$, measured at Freiburg (FR) and Liverpool (Liv).

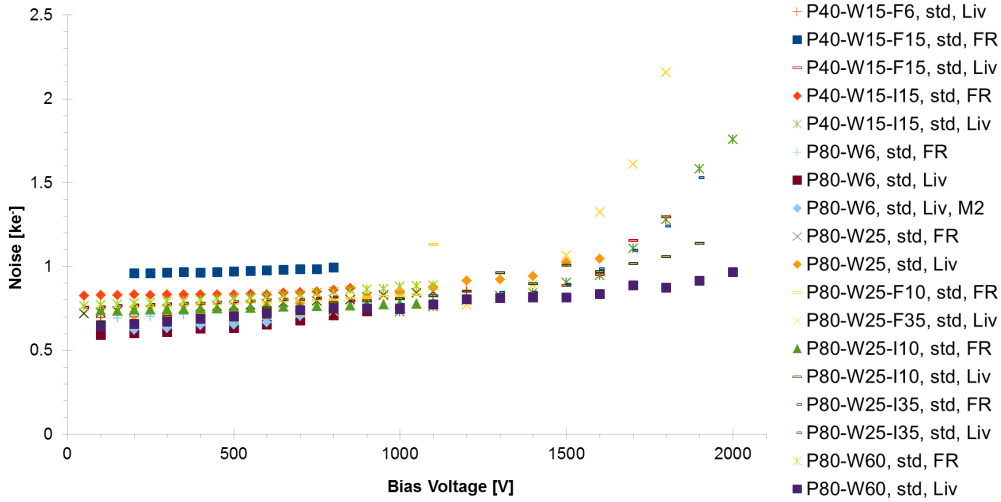


Figure 4.10.: Noise of charge multiplication sensor after neutron irradiation to $1 \times 10^{15} \text{ n}_{\text{eq}}/\text{cm}^2$, measured at Freiburg (FR) and Liverpool (Liv).

increase in noise at high voltages.

The reverse bias currents of these devices (see Figure 4.11) increase as well, indicating the breakdown of the sensors. Sample ‘P80-W25, std’ has a high current as well. The breakdown process could explain the high signal and high noise values. In the avalanche breakdown, the electrons from the MIP could be multiplied. This would affect signal and noise at the same time. For ‘P80-W25, std’ the signal is clearly enhanced while the noise increase is not very prominent. For ‘P40-W15-I15, std’ and ‘P80-W25-F35, std’ on the other hand the noise is enhanced while the signal is not.

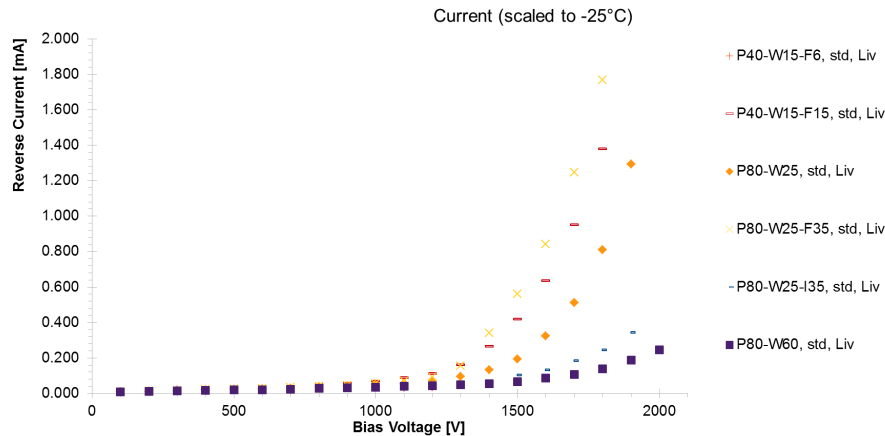


Figure 4.11.: Reverse bias current of charge multiplication sensor after neutron irradiation to $1 \times 10^{15} \text{ n}_{\text{eq}}/\text{cm}^2$, scaled to -25°C .

4.1.4. Neutron Irradiation, $5 \times 10^{15} \text{ n}_{\text{eq}}/\text{cm}^2$

The largest quantity of samples were irradiated with neutrons to a fluence of $5 \times 10^{15} \text{ n}_{\text{eq}}/\text{cm}^2$, including different wafer types and strip geometries. While measurements for sensors with the same wafer type and same geometry with a fluence of $1 \times 10^{15} \text{ n}_{\text{eq}}/\text{cm}^2$ have shown good agreement between Freiburg and Liverpool, this is not clear after the $5 \times 10^{15} \text{ n}_{\text{eq}}/\text{cm}^2$ irradiation. In Figure 4.12 there is good agreement for the sensors in the left hand graph, while in the right hand graph the values measured at Liverpool are smaller. By comparing the sensor names with Table A.3 it can be seen that the Liverpool sensor was not measured by the author and therefore the used daughterboard is unknown. By using the standard calibration value of $61.2 \text{ e}^-/\text{ADC}$ the collected charge is too small compared to the Freiburg value. If the calibration value is adjusted to get the same charge, $77.2 \text{ e}^-/\text{ADC}$ should be used. With this value the agreement between Freiburg and Liverpool is good also for other sensor types (see Figure 4.13), therefore it is applied to all Liverpool measurements in this section, that were not done by the author. This issue has not been seen for the $1 \times 10^{15} \text{ n}_{\text{eq}}/\text{cm}^2$ samples because all Liverpool data were collected by the author, including calibration measurements for each daughterboard.

The collected charge for all sensors is shown in Figure 4.14. Because there are 41 different sensors, it is not easy to identify individual features. For a better overview different colours have been used for different wafer types. The standard sensors in blue show similar behaviour and in comparison with the others have the lowest collected charge. They also show a wide spread which can be caused by measurement uncertainties or fluence uncertainties during the irradiation. The thin sensors (orange) show higher collected charge then the standard, but they start to saturate at higher voltages. The saturation charge is in good agreement with the expected charge of $(11.07 \pm 0.08) \text{ ke}^-$ for $150 \mu\text{m}$ thick fully depleted sensors

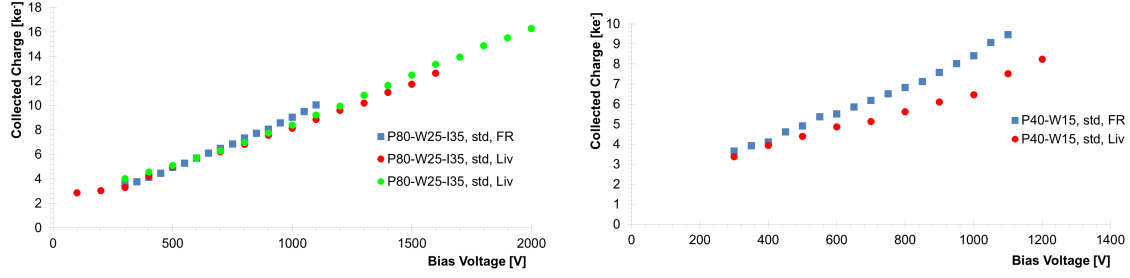


Figure 4.12.: Comparison of Freiburg and Liverpool after $5 \times 10^{15} \text{ n}_{\text{eq}}/\text{cm}^2$ neutron irradiation.

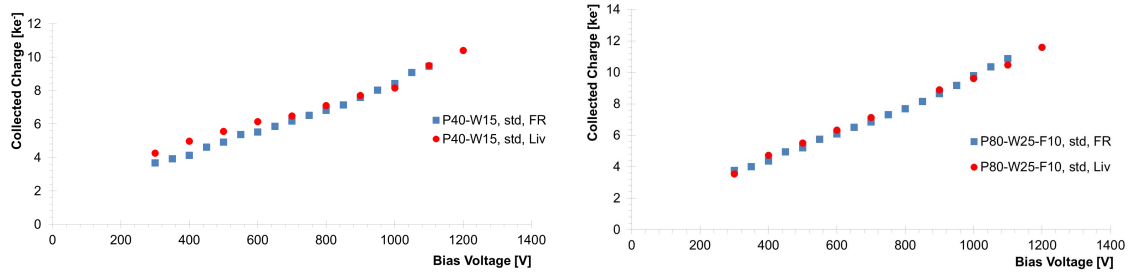


Figure 4.13.: Comparison of Freiburg and Liverpool after $5 \times 10^{15} \text{ n}_{\text{eq}}/\text{cm}^2$, using a calibration value of $77.2 \text{ e}^-/\text{ADC}$

(Equation 3.1). It can be seen as well that the collected charge of sensors with double diffusion time is in the same region as the medium to high standard sensors. Double implant energy and thick sensors show the highest collected charge for bias voltages above 700 V. This can either be the result of the production method or an effect of the strip configuration (width, pitch or intermediate strips).

Figure 4.15 shows the repeated measurement of one of the samples. While the first measurement was done using the 'full gain' configuration, the second measurement was performed several days later using 'half-gain'. This shows that the measurements are in general reproducible and the small difference shown in the Figure is well within the measurement uncertainty.

By choosing sensors with the same wafer type and same strip pitch and width, but additional biased or floating intermediate strips it is possible to examine the effect of intermediate strips. Only two sample types ('P40-W15, std' and 'P80-W25, std') are available for this comparison. In Figure 4.16 the left graph shows 'P40-W15, std': the biased intermediate strips (red) show less collected charge then the standard sensor (blue). It can be seen as well that the wider intermediate strips (I15) collects more charge at high voltages then the narrow (I6). The sensor with floating intermediate strips (orange) clearly has a higher signal for all voltages. But the 'P80-W25, std' sensors (right graph) show a slightly different performance. The sensors with biased intermediate strips still have less signal, but the sensor with floating intermediate strips shows also less collected charge. While the biased intermediate

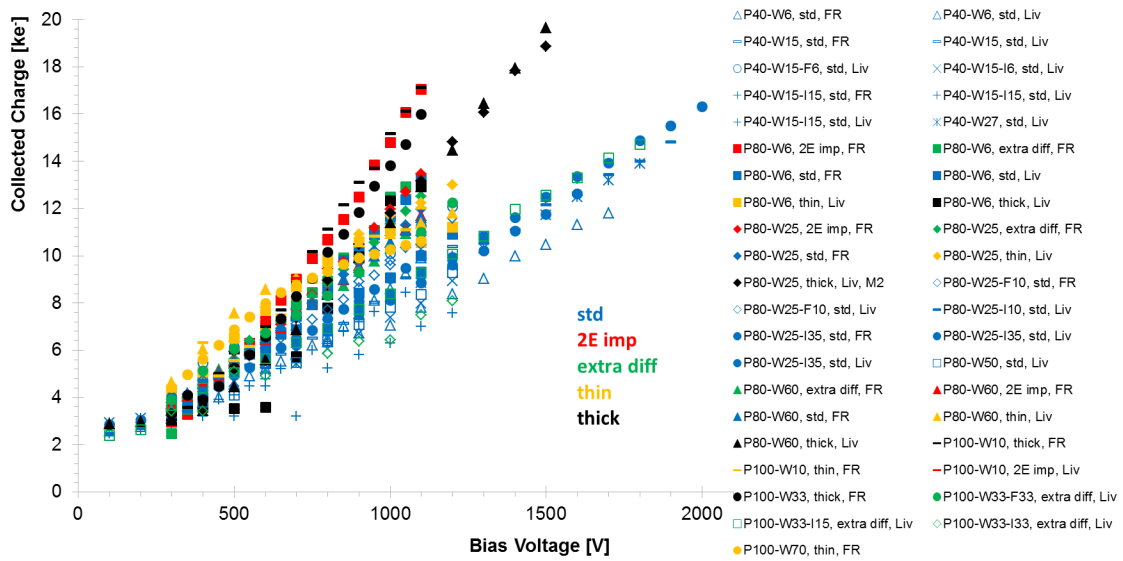


Figure 4.14.: Collected Charge after $5 \times 10^{15} \text{ n}_{\text{eq}}/\text{cm}^2$ neutron irradiation, measured at Freiburg (FR) and Liverpool (Liv). The wafer type is colour coded: ‘std’ in blue, ‘2E imp’ in red, ‘extra diff’ in green, ‘thin’ in orange and ‘thick’ in black.

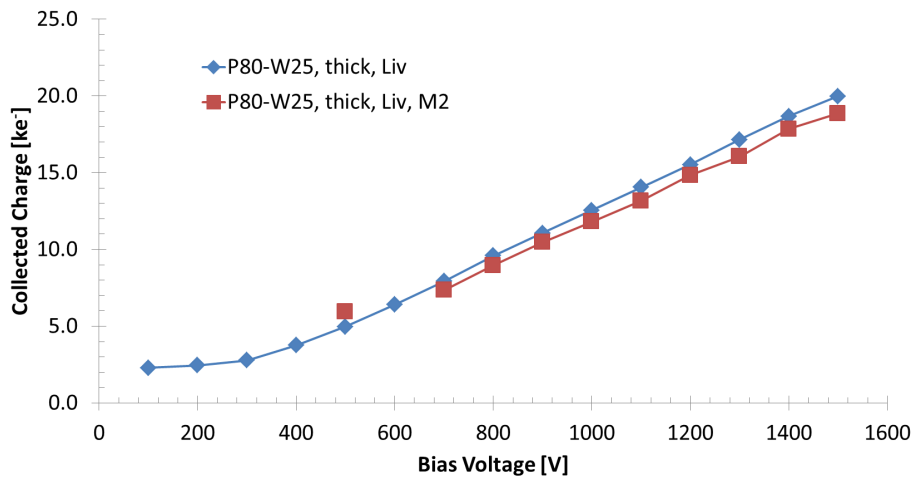


Figure 4.15.: Repeated measurement of ‘P80-W25, thick’ sensor. The second measurement in red is labelled with the addition ‘M2’ and was done several days after the first. While for the first measurement the ‘full gain’ configuration was used, the second was done using ‘half gain’.

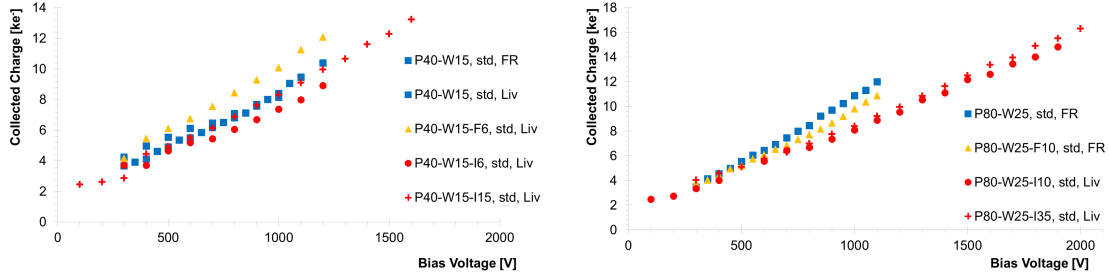


Figure 4.16.: Examination of intermediate strips after $5 \times 10^{15} \text{ n}_{\text{eq}}/\text{cm}^2$. Left: P40-W15; Right: P80-W25.

strips have no benefits with respect to the standard sensors, the measurements for the floating intermediate strips are inconclusive.

Another property to investigate is the strip width and pitch. To do this, sensors from the different wafer types, but without intermediate strips are compared. The used samples all have a pitch of $80 \mu\text{m}$, but different strip widths ($6 \mu\text{m}$, $25 \mu\text{m}$ and $60 \mu\text{m}$). For the categorisation the width-over-pitch ratio (W/P) has been used and the values can be found in Table 4.2. The corresponding graphs, shown in Figure 4.17, depict the collected charge at 600 V (top), 800 V (middle) and 1000 V (bottom). It can be seen that at 600 V the collected charge for all wafer types is similar for all W/P values, except the thin sensor, which has a higher signal, especially for ‘P80-W60’. At 800 V the standard and double diffusion time sensors have a nearly constant collected charge for all W/P values. The double implant energy sensors show an increased signal with decreased W/P ratio, while thin sensors collect the most charge for ‘P80-W25’ and ‘P80-W60’. When increasing the voltage further to 1000 V the change for the thin sensors is smaller than for other types, resulting in values comparable with the standard type. The measured collected charge is comparable with a fully depleted thin sensor. A lower W/P ratio seems to improve the collected charge for all other wafer types. The highest collected charge was measured with the ‘P80-W6’ sensor with double implant energy. It can be expected that the lowest W/P ratio is better in terms of charge collection because the electric field strength at the strips is higher due to the smaller strip cross section, which has been shown in the simulations (Figure 4.3). Double diffusion time, double implant energy and thick sensors show more collected charge than the standard wafer.

Sensor type	W/P ratio
P80-W6	0.075
P80-W25	0.313
P80-W60	0.750

Table 4.2.: Width-over-pitch ratio (W/P) for sensor comparison.

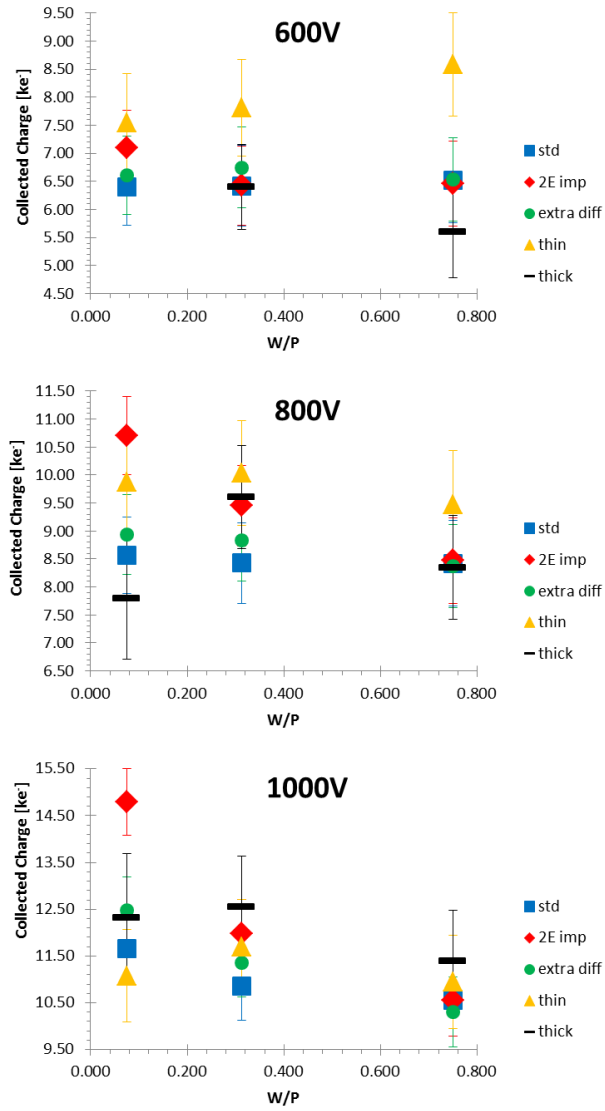


Figure 4.17.: Collected charge versus width-over-pitch ratio (W/P) ratio for different wafer types, plotted at 600 V (top), 800 V (middle) and 1000 V (bottom) for sensors irradiated to $5 \times 10^{15} \text{ n}_{\text{eq}}/\text{cm}^2$.

4.2. Annealing Study

When used in large high energy physics experiments, silicon sensors have to be cooled to temperatures below 0°C, especially after being irradiated to significant fluences. Occasionally they will undergo annealing due to maintenance requirements or cooling failures, or they could be warmed deliberately to exploit beneficial annealing. Some of the CM sensors have been used for an extensive annealing study to look into the device behaviour. The annealing was performed at room temperature (21°C) in a nitrogen cabinet. Selected results have been presented in talks [Won13b, Won14b].

For better comparison, sensors with an irradiation fluence of $1 \times 10^{15} \text{ n}_{\text{eq}}/\text{cm}^2$ and $5 \times 10^{15} \text{ n}_{\text{eq}}/\text{cm}^2$ were chosen in pairs with the same strip geometry. Thick sensors were chosen, as they showed enhanced collected charge, to see if this effect is stable after annealing. For the comparison there were only standard wafer types available at the lower fluence. Table 4.3 shows the sensors used for this study. The total number of tests was limited due to the number of available daughterboards. Due to the confined space on the wirebond pads on the sensor they needed to be bonded to the boards the whole time. Removing the bond wires between sensor and daughterboard always leaves the bond feet on the sensors, which is a limitation because it is not possible to place a wire-bond on top of a bond foot. For a better overview in the graphs only every other measured voltage is shown and the measurement points are connected by a line to guide the eye.

Sensor label	Fluence [$\text{n}_{\text{eq}}/\text{cm}^2$]	Total annealing time [d]
P80-W25-I35, std	1×10^{15}	785
P80-W25-I35, std	5×10^{15}	726
P80-W60, std	1×10^{15}	446
P80-W60, thick	5×10^{15}	46 (Beetle broken)
P80-W25, std	1×10^{15}	417
P80-W25, thick	5×10^{15}	416

Table 4.3.: List of sensors for the annealing study. ‘P80-W60, thick’ could not be annealed further than 46 days because the Beetle chip on the daughterboard stopped working.

‘P80-W25-I35’ Figure 4.18 depicts the collected charge versus annealing time for the ‘P80-W25-I35, std’ sensors. The top graph displays the sensor with a fluence of $1 \times 10^{15} \text{ n}_{\text{eq}}/\text{cm}^2$ and the measurements are in good agreement with the expectation: Up to approximately 30 days the collected charge increases due to beneficial annealing. For further annealing the charge decreases as an effect of the reverse annealing. After about 40 days the measurements at very high voltages start to fail. With increasing annealing time the maximum voltage at which measurements were possible

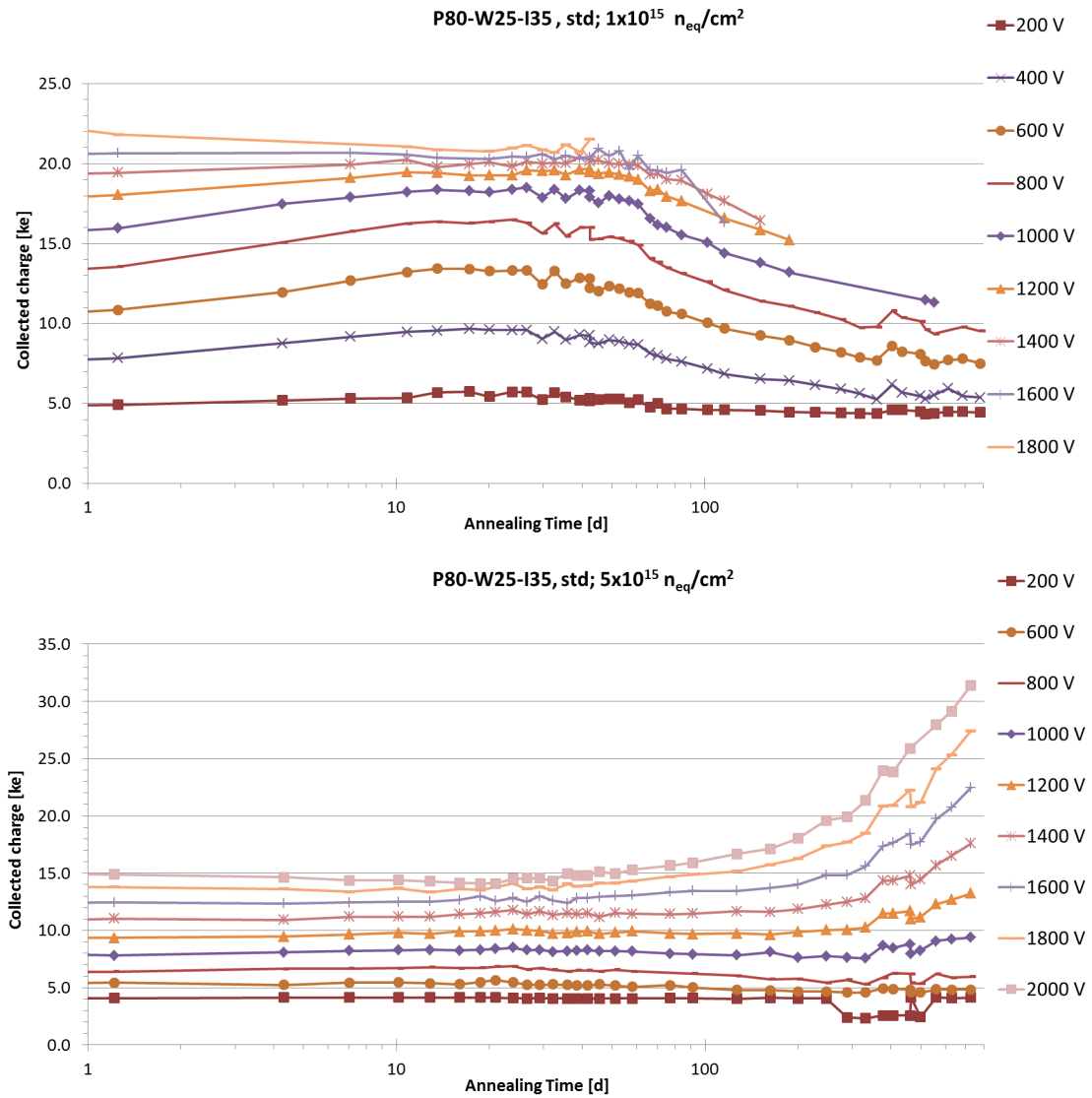


Figure 4.18.: Collected charge for ‘P80-W25-I35, std’ after room temperature annealing. Top: $1 \times 10^{15} n_{eq}/cm^2$; Bottom: $5 \times 10^{15} n_{eq}/cm^2$. Lines are used to guide the eye.

decreases further. While it was possible to apply even higher bias voltages without reaching the current compliance level, it was not possible to run measurements with the ALiBaVa system. This misbehaviour has been observed with other samples as well, without any indication of what was causing it.

The same sensor geometry and wafer type, but irradiated up to $5 \times 10^{15} \text{ n}_{\text{eq}}/\text{cm}^2$ shows a different behaviour (Figure 4.18 bottom). While there is little to no increase in the collected charge within the first 100 days of annealing, afterwards the signal increase is unexpectedly high, in particular for voltages above 1000 V. Not only is this contrary to reverse annealing, but the collected charge at voltages above 1700 V even exceeds the charge of a fully depleted unirradiated sensor. At approximately 450 days of annealing a small drop in the collected charge can be seen. This is caused by the longterm bias test with this sensor, described in section 4.3.

If this increased signal is caused by charge multiplication, it is expected that the noise increases at the same time. Figure 4.19 shows the signal-to-noise ratio for this sample. In the region of 5 to 40 days the SNR values at high voltages fluctuate significantly. This is caused by random noise fluctuations and was observed as well with other sensors that were measured at the same time with the setup. Flushing the test-box with nitrogen solved this issue. For measurements after more than 100 days of annealing the SNR increases. The rise is not as steep as that of the collected charge which is caused by slowly increasing noise. A spike after 450 days is caused by the afore mentioned longterm test. This fairly flat distribution with a slow increase at high annealing times is a good indicator for charge multiplication. For charge multiplication an increase in signal and noise is expected which results in a flat or small increase in the signal-to-noise ratio.

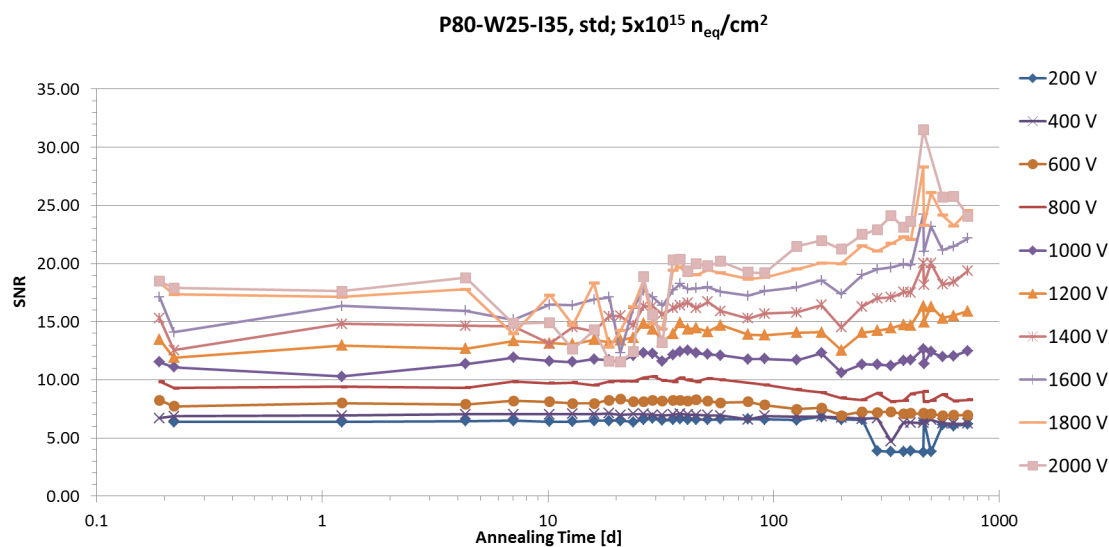


Figure 4.19.: Signal-to-noise ratio versus annealing time for P80-W25-I35 after $5 \times 10^{15} \text{ n}_{\text{eq}}/\text{cm}^2$ irradiation.

‘P80-W60’ Sensors with the strip geometry ‘P80-W60’ have been annealed as well. The results, shown in Figure 4.20, confirm the standard behaviour for the sensor irradiated to a fluence of $1 \times 10^{15} \text{ n}_{\text{eq}}/\text{cm}^2$. For voltages below 1000 V the collected charge increases with short annealing times until reaching a maximum after approximately 40 days, followed by decreasing collected charge. The sensor has been removed from the daughterboard after 30 days and reconnected to a different one at 40 days which can be seen as discontinuities in the graph, but this has not affected the overall trend.

A sensor with the same strip geometry, but from the thick wafer and irradiated to $5 \times 10^{15} \text{ n}_{\text{eq}}/\text{cm}^2$ has been annealed as counterpart (Figure 4.20, bottom). The acquired collected charge is comparable with the previously shown ‘P80-W25-I35’ sample. Unfortunately the Beetle chip on the daughterboard has stopped working after approximately 47 days of annealing. Even after changing the chip it was not possible to perform further measurements. This also happened with a different daughterboard, which indicates that the sensor was damaged in such a way that further measurements are not possible.

‘P80-W25’ The third tested geometry were sensors with ‘P80-W25’. As for the ‘P80-W60’ the sensor irradiated to $1 \times 10^{15} \text{ n}_{\text{eq}}/\text{cm}^2$ was processed in the standard way while the sensor with $5 \times 10^{15} \text{ n}_{\text{eq}}/\text{cm}^2$ was from the thick wafer. The collected charge for the standard sensor (Figure 4.21, top) clearly shows the expected increase due to beneficial annealing and the decrease after approximately 40 days due to reverse annealing.

While it was not possible to apply bias voltages higher than 1400 V to the thick sensor irradiated to $5 \times 10^{15} \text{ n}_{\text{eq}}/\text{cm}^2$, the previously observed increase of the collected charge for a total annealing time of more than 100 days is clearly visible. As well as the ‘P80-W25-I35’ sample, it was possible to collect more charge than with an unirradiated sensor for bias voltages higher than 1000 V. The signal-to-noise ratio, shown in Figure 4.22, decreases at the same time as the collected charge increases, which means that the noise increases as well. This is in accordance with the expected charge multiplication effect which multiplies the signal but at the same time also the noise.

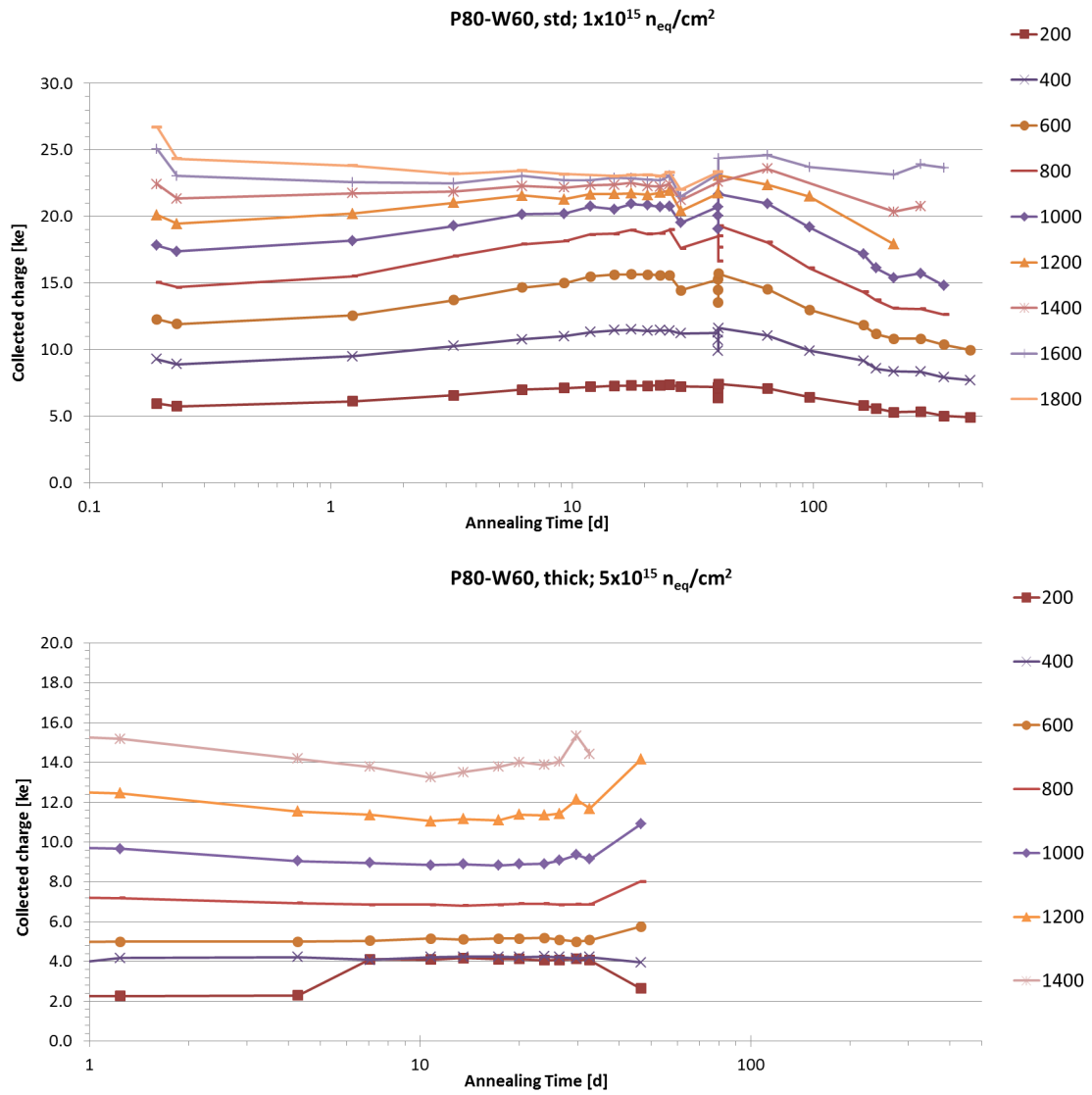


Figure 4.20.: Collected charge for ‘P80-W60’ after room temperature annealing. Top: 1×10^{15} n_{eq}/cm², std; Bottom: 5×10^{15} n_{eq}/cm², thick.

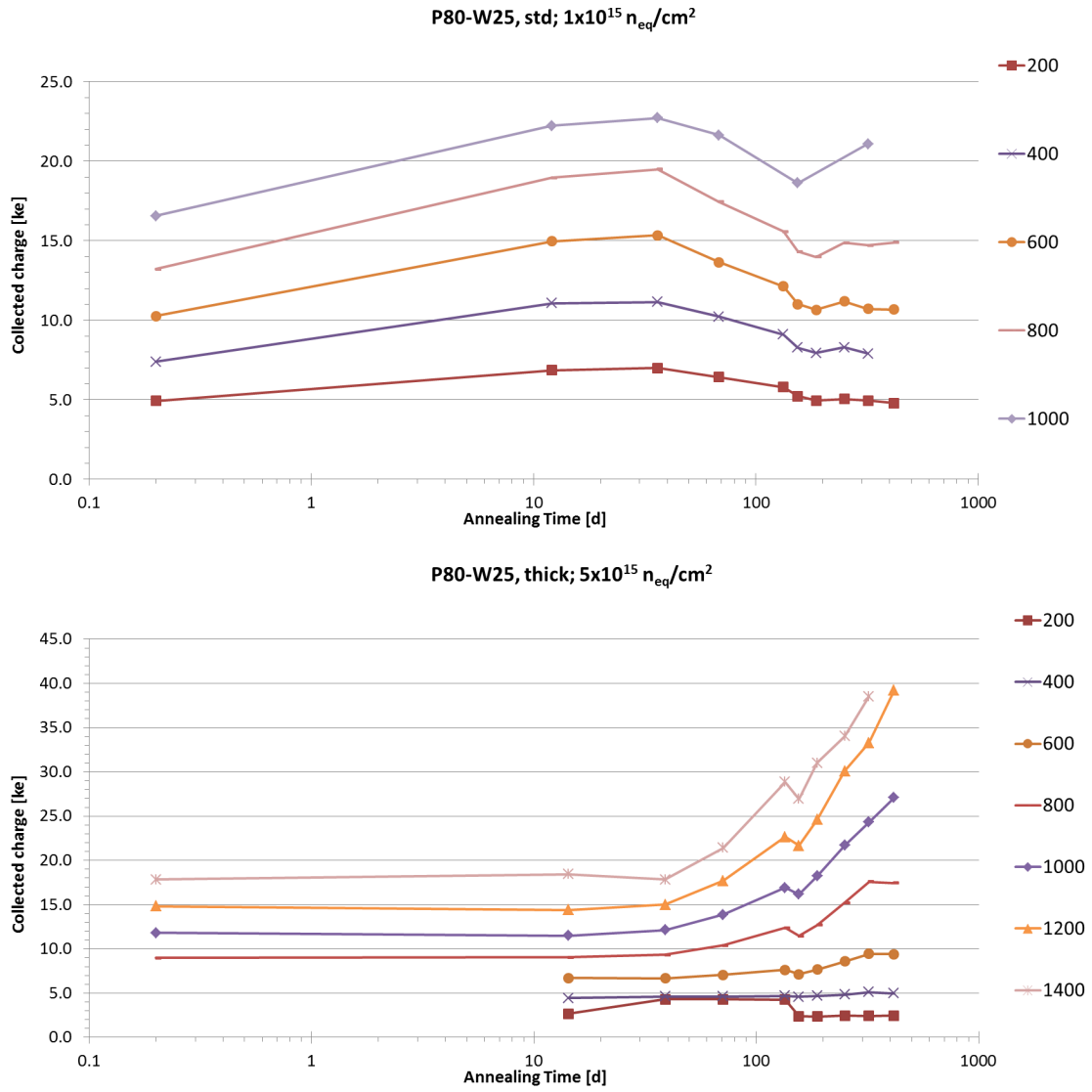


Figure 4.21.: Collected charge for ‘P80-W25’ after room temperature annealing. Top: $1 \times 10^{15} n_{eq}/cm^2$, std; Bottom: $5 \times 10^{15} n_{eq}/cm^2$, thick

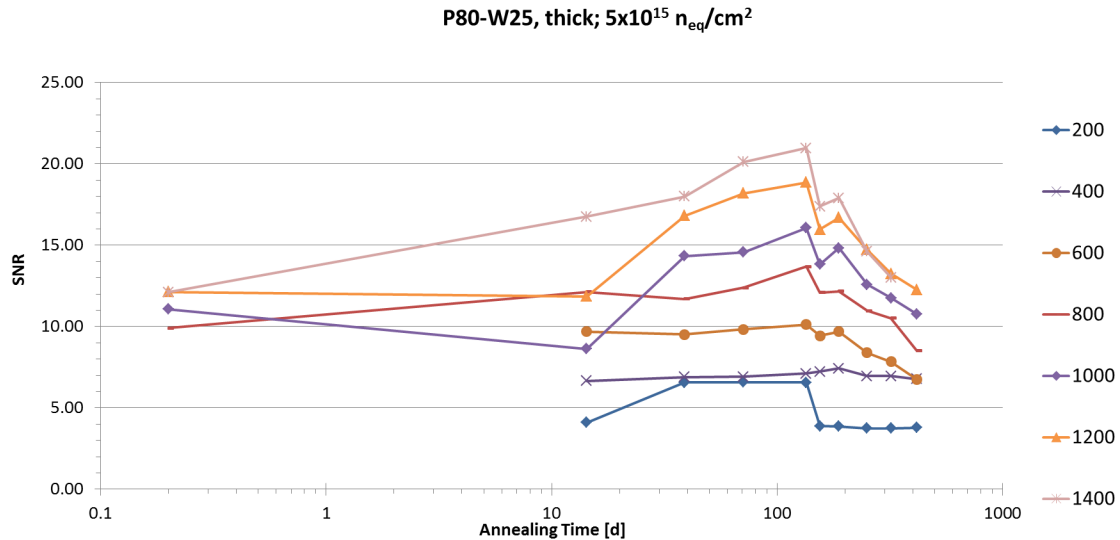


Figure 4.22.: ‘P80-W25, thick’ irradiated to $5 \times 10^{15} \text{ n}_{\text{eq}}/\text{cm}^2$: signal-to-noise ratio with annealing time

4.3. Long-term Bias Test

In the previous sections it has been shown that some sensors show enhanced collected charge compared to standard devices. After annealing some samples the collected charge even exceeds the values of unirradiated sensors. These results were obtained in stand-alone measurements where the sensors were only biased for the measurement, which takes not more than 4 hours. In real applications the sensors will be constantly biased for a much longer time. Several sensors have been measured with the ALiBaVa system while applying a constant bias voltage for several days to several weeks, with the radioactive source present for the whole time. The Beetle chip was constantly powered as well to investigate the influence of this heat source in close proximity to the sensor. Selected results from this section have been shown in [Won14b].

‘P80-W60, std’ The first longterm bias test was performed with the ‘P80-W60, std’ sensor, irradiated to $1 \times 10^{15} \text{ n}_{\text{eq}}/\text{cm}^2$, before using it in the annealing study. Initial measurements after irradiation have shown that above 1500 V the collected charge exceeds that of an unirradiated fully depleted sensor. When conducting the longterm measurements the first applied bias voltage was 2000 V, but after approximately 36 h the current was too high so that it was necessary to choose a lower voltage (1600 V). In Figure 4.23 the collected charge is shown versus the measurement time. The signal at 2000 V clearly decreased within the first day. The 1600 V signal also decreases slightly. When the collected charge reaches approximately 23 ke^- it becomes stable with time, which would be the expected collected charge of an unir-

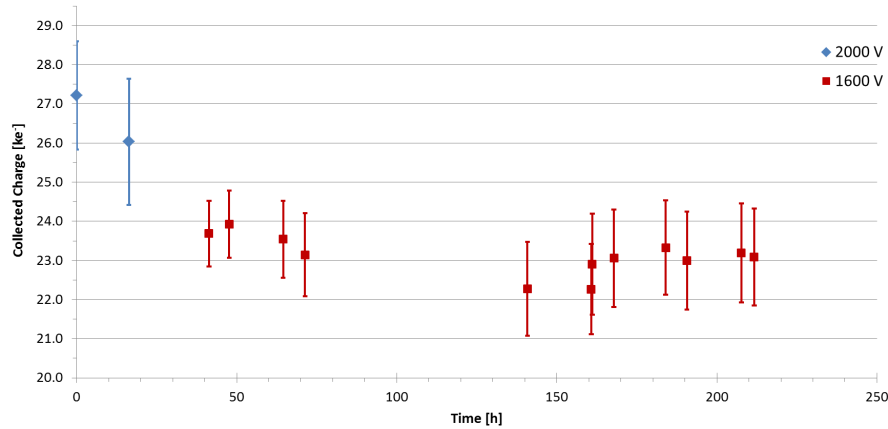


Figure 4.23.: Longterm bias measurement of ‘P80-W60, std’ after irradiation to $1 \times 10^{15} n_{eq}/cm^2$. The errors of the collected charge have been calculated from the pedestal measurements.

radiated fully depleted sensor. The large gap between 70 h and 140 h is caused by the weekend, at which measurements were not possible, but the high voltage was continually applied. This sensor was used again for a longterm test after one year, in which the sensor was annealed to a total annealing time of 40 days. The collected charge, shown in Figure 4.24, for an applied bias voltage of 1600 V, is fairly constant with measurement time at approximately $23 ke^-$.

In these two measurements it has been shown that if the initial collected charge exceeded the total expected collected charge for a fully depleted $300 \mu m$ thick sensor of approximately $23 ke^-$, the collected charge decreases with continuous application of bias voltage. But if the initially measured charge was smaller then it stayed

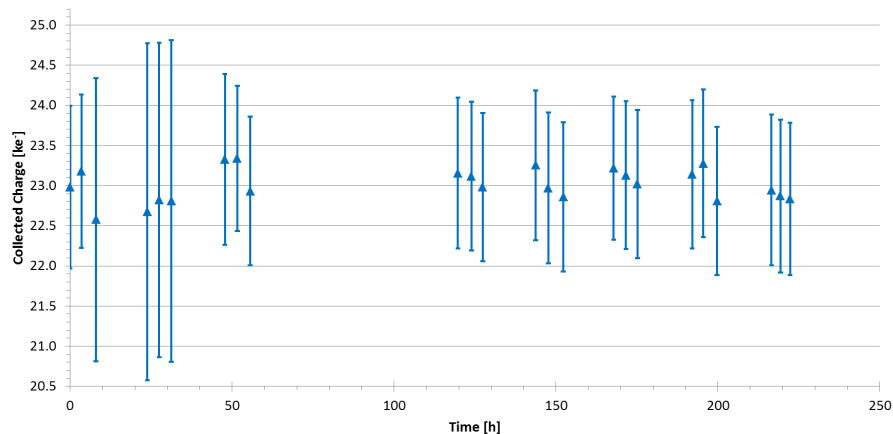


Figure 4.24.: Longterm bias measurement of ‘P80-W60, std’ after irradiation to $1 \times 10^{15} n_{eq}/cm^2$ and 40 days annealing with an applied bias voltage of 1600 V.

constant for the whole duration of the measurement campaign.

‘P80-W25-I10, std’ The sensor ‘P80-W25-I10, std’ irradiated to $5 \times 10^{15} \text{ n}_{\text{eq}}/\text{cm}^2$ was used for the second longterm test with a constant bias voltage of 1500 V for 30 days. The results shown in Figure 4.25 indicate no significant change in the collected charge for the whole measurement time. Larger gaps without measurements are caused by the weekends. The noise in the bottom graph of the Figure shows an increase of the noise of up to 500 e^- within the first 200 hours, which drops back to the value at the start of the measurement.

The temperature was monitored at the start and end of each ALiBaVa measurement and is shown in Figure 4.26. It can be seen that there is a temperature variation of more than 3°C which is caused by the measurement setup. The sample is cooled in a commercial freezer which can’t provide a better temperature stability. Measurements were started arbitrarily with respect to the freezer cycle and one run takes approximately 6 minutes which explains the random distribution of the temperature points. The general trend indicates no temperature change for the whole measurement time. The large reverse bias current spread of up to 40 mA can be caused by the temperature uncertainty of the freezer. The temperature is not measured directly at the silicon sensors but by a sensor with a resolution of 0.1°C loosely attached to the heat sink of the daughterboard. Therefore there is a temperature difference between silicon and temperature sensor. Additionally the freezer cycle has a negative influence: while the freezer is cooling the air temperature inside of the freezer changes at a different rate than the silicon temperature. With the current system it is not possible to accurately measure the silicon sensor temperature, but the measured values should give a rough estimate of the silicon temperature change.

In addition to the temperature, the current was recorded at the start and end of each measurement and scaled to -25°C (Figure 4.27). Within the first 300 hours the current increases slightly ($\approx 10 - 20 \text{ mA}$) and stays at this level until the end of the measurement. By scaling the current with the inaccurate temperature the obtained current graph reflects the temperature uncertainty by having a large spread.

‘P80-W25-F35, std’; annealed For the third measurement a sensor from the annealing study was chosen: ‘P80-W25-F35, std’ irradiated to $5 \times 10^{15} \text{ n}_{\text{eq}}/\text{cm}^2$ and annealed for approximately 460 days. At 1700 V, which was used for the longterm test, the collected charge had increased with increasing annealing time, which makes this sensor the ideal device to study the longterm stability of enhanced charge.

The collected charge at 1700 V during the longterm test is shown in Figure 4.28. Within the first 100 hours the higher charge decrease from approximately 20 ke^- to 18.5 ke^- . After this initial drop the collected charge stays fairly constant until approximately 480 hours. The temperature as well as the current, scaled to -25°C ,

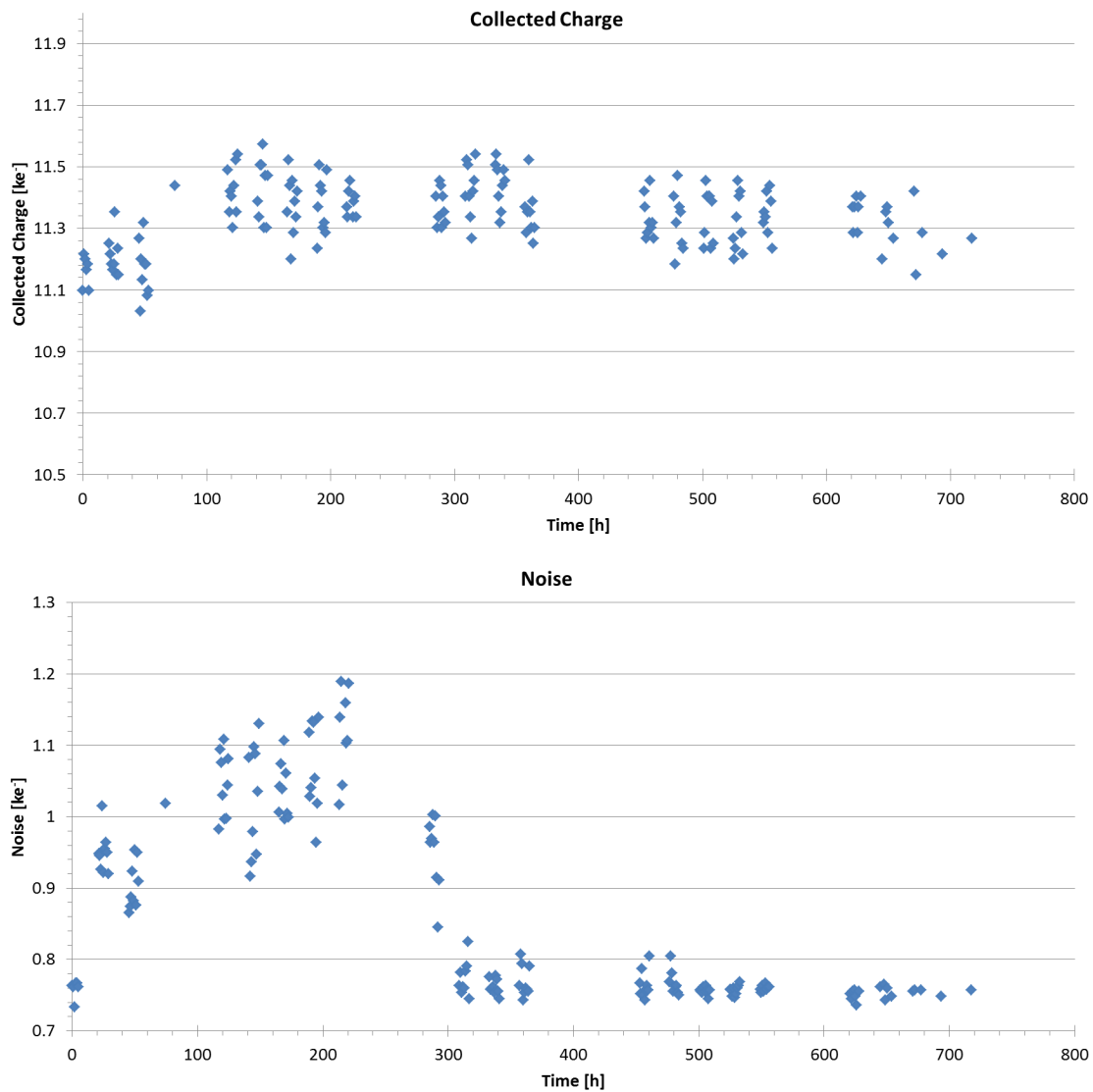


Figure 4.25.: Longterm bias measurement at 1500 V of ‘P80-W25-I10, std’ after neutron irradiation to $5 \times 10^{15} \text{ n}_{\text{eq}}/\text{cm}^2$. The top graph shows the collected charge and the bottom one the noise.

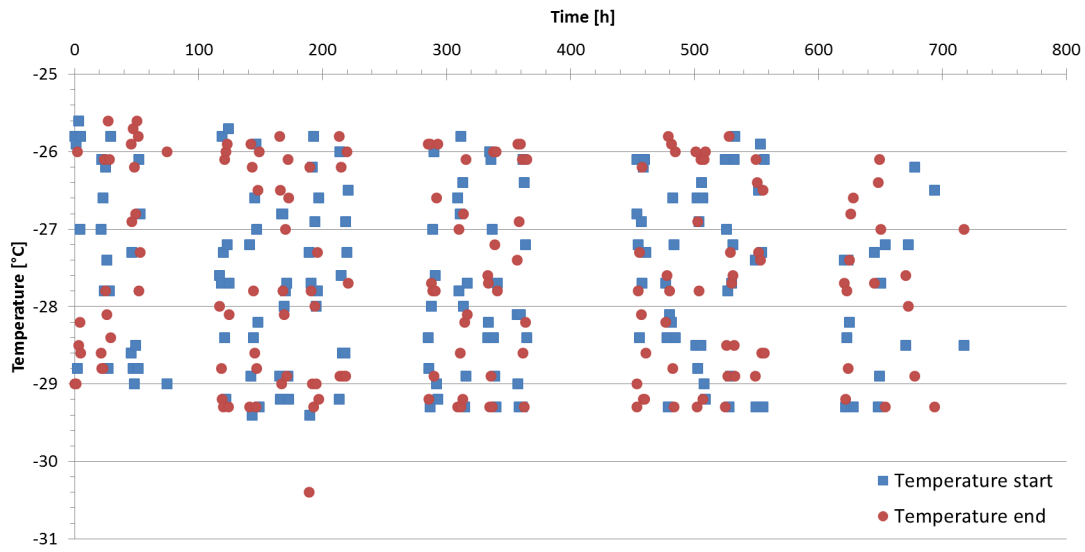


Figure 4.26.: Temperature during longterm test of 'P80-W25-I10, std'.

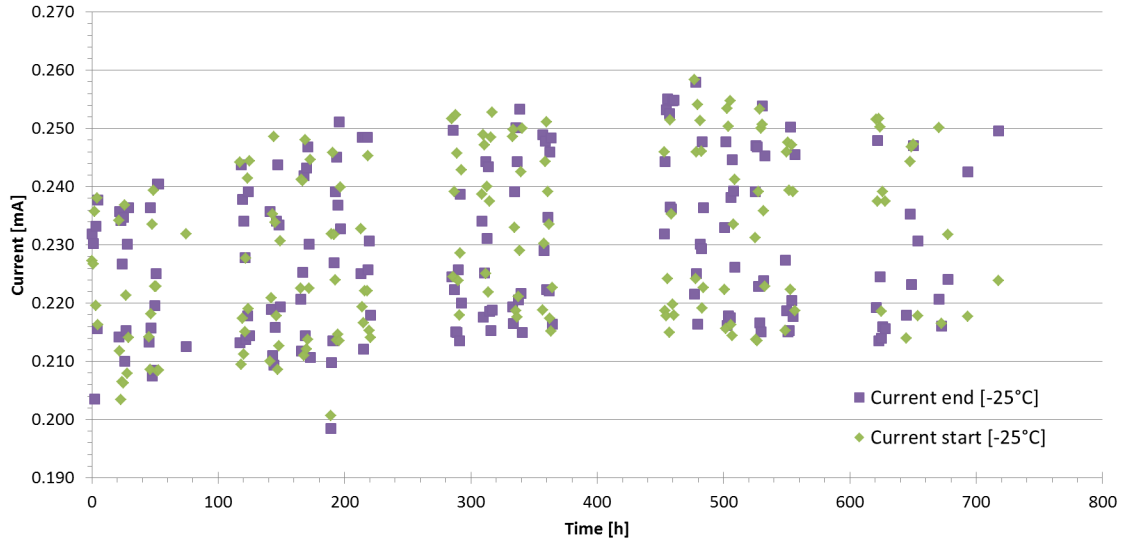


Figure 4.27.: Reverse bias current during longterm test of 'P80-W25-I10, std', scaled to -25°C.

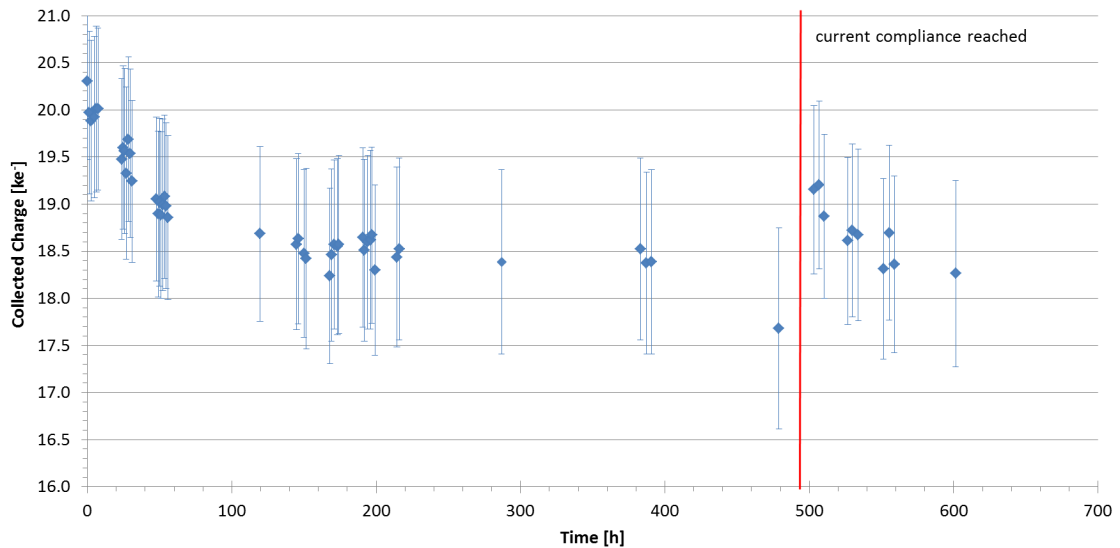


Figure 4.28.: Collected charge during longterm test of ‘P80-W25-F35, std’, irradiated to $5 \times 10^{15} \text{ n}_{\text{eq}}/\text{cm}^2$ and annealed for approximately 460 days, at 1700 V. Collected charge uncertainties were obtained from the pedestal run analysis. The red line indicates the break in the test which was caused by too high current.

increase within the first 200 hours (see Figure 4.29) with the largest change within the first 100 h.

After 480 hours of measurement the current compliance level was reached, which resulted in a voltage drop of the power supply. Because of this the bias voltage was reduced to 0 V and the sensor was left unbiased for 24 h. The collected charge afterwards was higher than before the interruption, but has not reached the value at the start of the longterm test. The same behaviour can be seen in the temperature and current graphs. While the charge decreased with increasing measurement time, the temperature and the current increased. After 610 hours the current compliance level was reached again which resulted in the end of the longterm test for this sensor.

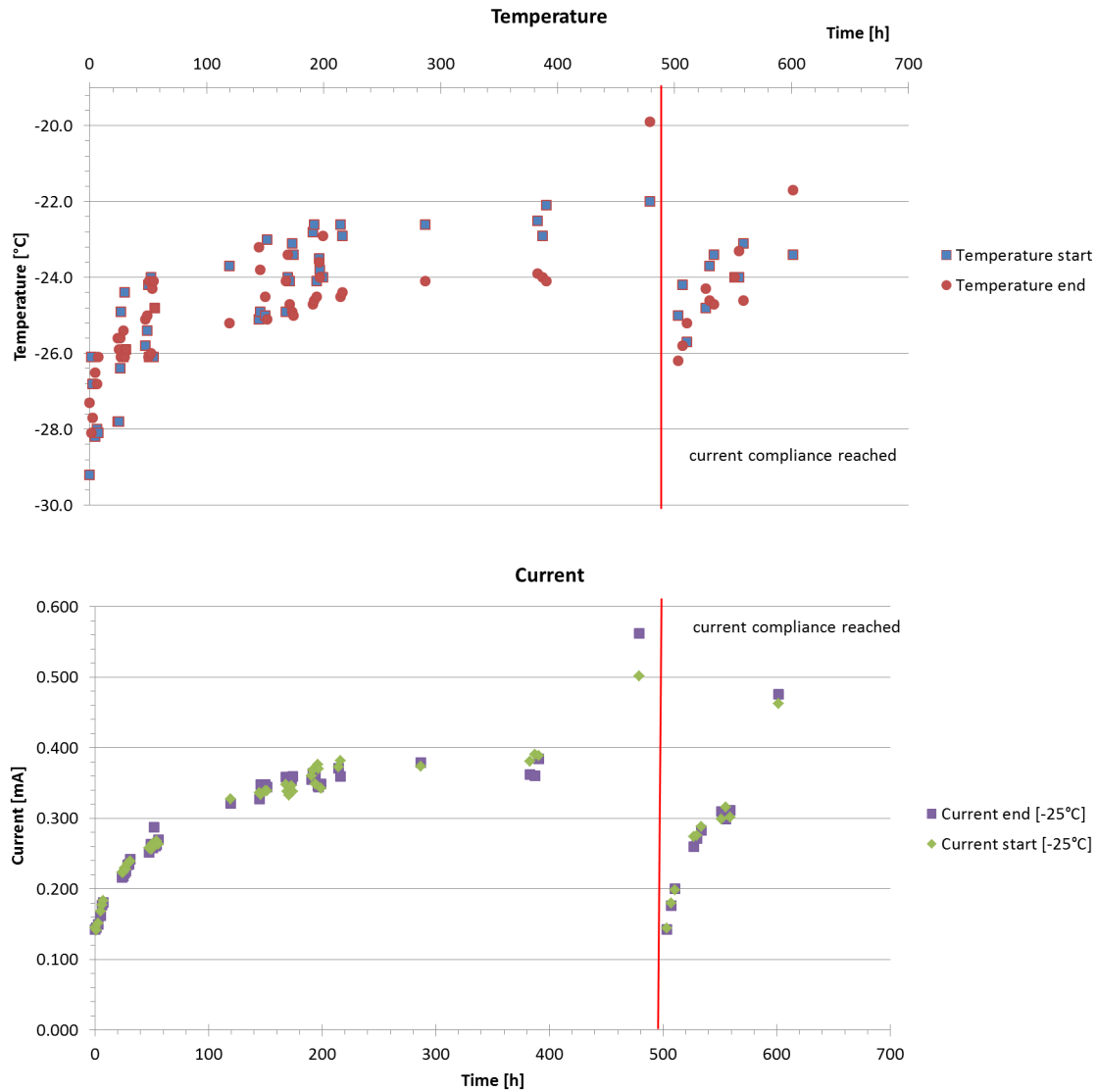


Figure 4.29.: Temperature (top) and Current (bottom), scaled to -25°C , during longterm test of ‘P80-W25-F35, std’, irradiated to $5 \times 10^{15} \text{ n}_{\text{eq}}/\text{cm}^2$ and annealed for approximately 460 days. The red line indicates the interruption in the test which was caused by too high current.

4.4. Summary

Dedicated charge multiplication sensors have been used to investigate different strip geometries and sensor manufacturing steps to produce detectors which benefit from charge multiplication. Charge collection measurements have been done with the ALiBaVa system before and after irradiation. The samples were irradiated with protons to $1 \times 10^{15} \text{ n}_{\text{eq}}/\text{cm}^2$ and with neutrons to $1 \times 10^{15} \text{ n}_{\text{eq}}/\text{cm}^2$ and $5 \times 10^{15} \text{ n}_{\text{eq}}/\text{cm}^2$. Measurement results shown in this chapter were obtained at Freiburg and Liverpool. It has been shown that the measurement values from both institutes are comparable.

The unirradiated sensors have not shown any signs of charge multiplication. They were fully depleted for voltages higher than 100 V and it was possible to bias them up to 1000 V for all measured devices. After the proton irradiation there were no indicators for charge multiplication as well.

From the samples irradiated with neutrons to $1 \times 10^{15} \text{ n}_{\text{eq}}/\text{cm}^2$, ‘P80-W25, std’ showed higher collected charge for voltages higher than 1000 V, but without an increase of the noise. Only standard wafer sensors were available at this fluence which allowed no investigation of different wafer types. Most sensors were available from the neutron irradiation to $5 \times 10^{15} \text{ n}_{\text{eq}}/\text{cm}^2$. The sensors from the standard wafer have shown the lowest collected charge, compared with other wafer types. Thin sensors had the highest charge at lower voltages and saturated at higher voltages to charge values expected for fully depleted unirradiated sensors with the same thickness. At voltages above 800 V the sensors with double diffusion energy as well as the thick sensors had the highest collected charge. The comparison of sensors with and without intermediate strips has demonstrated that biased intermediate strips always collect less charge. For floating intermediate strips the results were not conclusive. Sensors were produced with different strip pitch and strip width values. A comparison of different width-over-pitch ratios for different wafers has shown that a lower W/P ratio is better at high voltages, especially for double implant energy wafers. At lower voltages the thin sensors collected more charge irrespective of the W/P ratio.

Annealing sensors at room temperature demonstrated that the sensors irradiated with neutrons to $1 \times 10^{15} \text{ n}_{\text{eq}}/\text{cm}^2$ behave as expected: the collected charge increased up to a total annealing time of approximately 40 days in accordance with beneficial annealing. After further annealing the charge decreased, which can be explained by reverse annealing. The sensors irradiate to $5 \times 10^{15} \text{ n}_{\text{eq}}/\text{cm}^2$ showed an increased collected charge for voltages well above 1000 V after approximately 100 days of annealing. For the highest voltages the charge even exceeded the values obtained by an unirradiated fully depleted sensor. The noise increased at the same time which is a good indicator for charge multiplication.

Some sensors were tested for longterm charge collection stability by applying high bias voltage for several days. The voltage was chosen to be higher than 1000 V

to investigate the observed charge multiplication from the annealing study. If the collected charge exceeded the value for an unirradiated depleted device, than the charge decreased with increasing longterm measurement time to a value expected for an unirradiated fully depleted device at of the same thickness. For one sample the bias voltage was switched off for 1 day during the longterm test. After starting the measurement again, the collected charge was higher than before the interruption, but decreased again with increasing measurement time. One possible explanation for this could be surface charge induced by the radioactive beta source. This could be excluded by measurements with an α -source, pointing to the backside of the sensor. Due to the complete metallisation of the backside no surface charge can accumulate. The ALiBaVa system is triggered by scintillators therefore it is not possible to do the measurements with the standard setup. A special self-triggering daughterboard is required, which was not available at Liverpool within the scope of this thesis.

5. Thin Sensors

When building large particle physics detector systems two properties are required of the silicon sensors: a high Signal-to-Noise ratio (because a clear separation between signal and noise has to be possible at the end of the detector lifetime, when the radiation damage is highest) and a low material budget to reduce multiple scattering (and for low energy experiment also to minimize the energy loss in the detector). These requirements are contrary to each other. The number of electron-hole pairs created by an ionizing particle increases with increasing active silicon thickness (see Equation 3.1); therefore an easy way of increasing the signal strength is to increase the sensor thickness. But increasing the thickness also increases the material budget. In the case of large LHC experiments, the silicon sensors are located closest to the interaction point and therefore it is important to have as little material as possible to minimize multiple scattering, which would affect tracking. The calorimeters are used to determine the energy of the particles; therefore it is preferable that the energy loss in other detectors is as small as possible. It is necessary to find a compromise for the sensor thickness which has a sufficient SNR but also a low material budget. The currently used silicon strip sensors in the ATLAS experiment have a thickness of approximately 300 μm , which is an acceptable compromise.

Other factors might have to be considered. The reverse bias current depends on the sensor thickness and is lower for thinner sensors. When space for cooling is limited the power consumption of the sensors can be a decisive factor, especially for irradiated sensors where the reverse bias current increases with increasing irradiation fluence. Production cost and sensor handling need to be considered. Thinner sensors are harder to produce and therefore more expensive than sensors with the standard thickness of 300 μm . And because they are thinner they are also more fragile and special care is required when building large detector structures. Since the construction of the LHC the technology to fabricate thin silicon devices has improved and strip sensors up to a thickness of 50 μm are available.

This chapter focuses on the measurement results of 50 μm thin silicon strip sensors. In section 5.1 the charge collection measurements of irradiated sensors will be presented. Measuring the charge collection of highly irradiated thin sensors with the ALiBaVa system has proven to be challenging. Because of the radiation damage the charge decreased to a level where it is difficult to distinguish between signal and noise. Results obtained with different analysis methods will be shown and compared in section 5.2. Two sensors have been annealed with the results shown in section 5.3. Some material in this chapter has been presented in talks [Won15d, Won15c].

5.1. Charge Collection Measurement

The n-in-p strip sensors, used in this study, were produced by Micron Semiconductor Ltd. in the standard process. They are 50 μm thick with outer dimensions of (12.4 \times 12.4) mm^2 and 131 strips with a pitch of 80 μm . The sensors were irradiated together with the samples for the IV study (see chapter 6) to fluences from $1 \times 10^{15} \text{ n}_{\text{eq}}/\text{cm}^2$ to $2 \times 10^{16} \text{ n}_{\text{eq}}/\text{cm}^2$ at the Triga mark III reactor at Ljubljana. Table 5.1 lists all sensors and the received irradiation fluence, including an unirradiated reference sample.

Sensor Label	Fluence [$\text{n}_{\text{eq}}/\text{cm}^2$]
3107-6-1	unirradiated
3107-3-13	1×10^{15}
3107-3-19	2×10^{15}
3107-6-12	5×10^{15}
3107-6-15	1×10^{16}
3107-6-20	2×10^{16}

Table 5.1.: List of 50 μm thick sensors, irradiated at Ljubljana.

The collected charge has been measured with the ALiBaVa system directly after irradiation and it is shown in Figure 5.1. From Equation 3.1, the expected collected charge can be calculated to $(3.24 \pm 0.07) \text{ ke}^-$. A comparison with the data from the unirradiated sample shows good agreement with this value, as well as the sensors irradiated to $1 \times 10^{15} \text{ n}_{\text{eq}}/\text{cm}^2$ and $2 \times 10^{15} \text{ n}_{\text{eq}}/\text{cm}^2$. For higher fluences it can be seen that at low voltages they show a similar collected charge of approximately

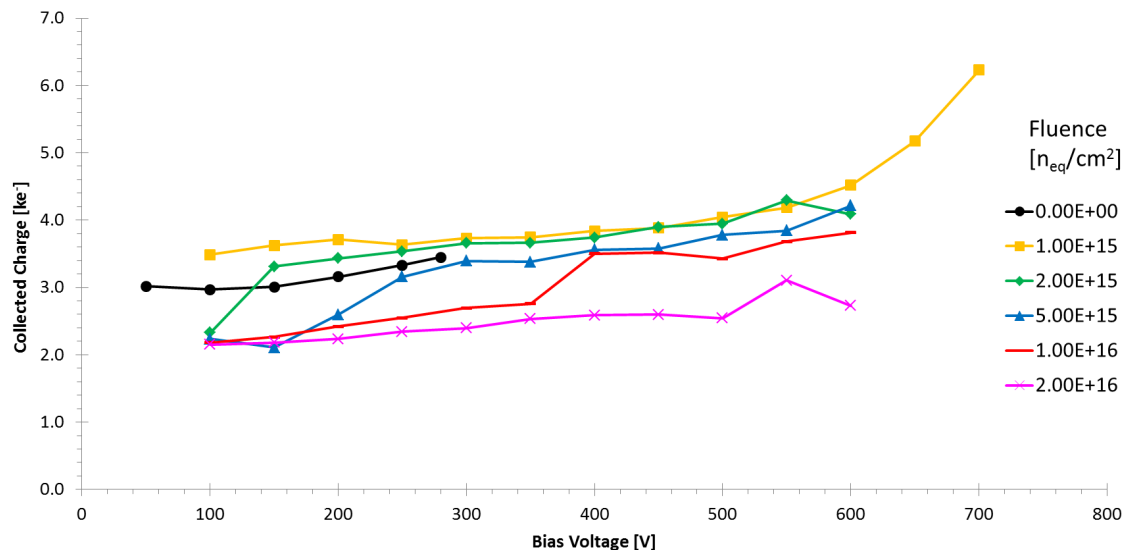


Figure 5.1.: Collected charge of all 50 μm thick samples directly after irradiation.

2.2 ke^- . While the sample irradiated to $5 \times 10^{15}\text{ n}_{\text{eq}}/\text{cm}^2$ reaches the full value at 250 V, the collected charge of the device irradiated to $1 \times 10^{16}\text{ n}_{\text{eq}}/\text{cm}^2$ reaches this level at 400 V. For the highest fluence the charge is stably low with the exception of the value at 550 V. The highest bias voltage that could be applied safely for all devices was 600 V. Only for the lowest fluence it was possible to measure it up to 700 V with a steep increase in the collected charge at the highest voltages. This can be explained by the beginning breakdown of the sensor, accompanied by a steep increase in the measured current.

Figure 5.2 shows the noise of the devices. Most samples are in good agreement with each other at a noise value of approximately 0.6 ke^- . For the unirradiated sample the last two measurements are significantly higher, which is caused by higher current and the beginning breakdown of the sensor (shot noise). The sensor irradiated to $2 \times 10^{16}\text{ n}_{\text{eq}}/\text{cm}^2$ shows higher noise values than the other sensors, whereas the value at 550 V is closer to the results for the other devices.

The reason that the collected charge of highly irradiated thin sensors is at a constant level is that the analysis fails to distinguish between signal and noise. In the ALiBaVa analysis the signal is separated from the background by comparing the channel with the highest signal with the seed cut. But for thin sensors after high irradiation the signal itself is small due to the radiation damages. It can happen that the value of a random channel exceeds the seed cut, even if there was no passing beta particle. In this case an additional noise peak appears in the cluster charge histogram. One characteristic of this peak is that it has a low cluster charge which is independent of the applied bias voltage. The true signal emerges from the noise peak with increasing bias voltage because the increased depleted area increases the signal strength and therefore it is less likely that a random

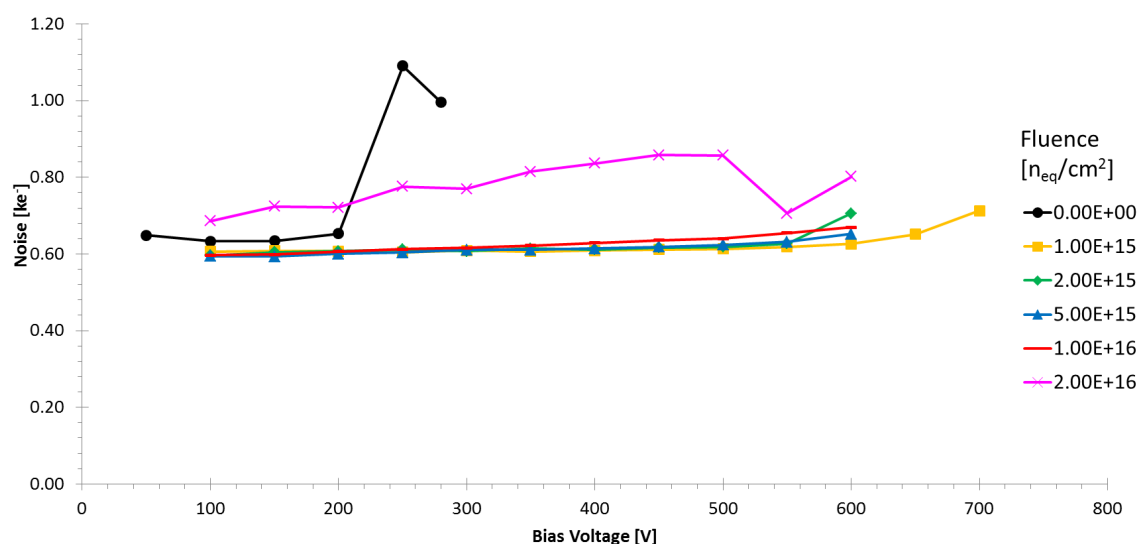


Figure 5.2.: Noise of all $50\text{ }\mu\text{m}$ thick samples after irradiation.

fluctuation creates the channel with the highest signal. Figure 5.3 shows this for the sensor irradiated to $5 \times 10^{15} \text{ n}_{\text{eq}}/\text{cm}^2$. The graphs have been scaled so that the highest bin is equal to 100. At 100 V a narrow peak with a MPV of approximately 36 ADC can be seen (black). With increasing bias voltage the distribution broadens. At approximately 300 V a double peak structure can be recognized. While the noise peak is still at approximately 36 ADC, the signal peak starts to emerge at approximately 55 ADC. For higher voltages it can be seen as well that the relative height of the noise peak decreases with respect to the signal peak, which can now clearly be separated from the noise. To make sure that this peak is not the signal a measurement has been done. The daughterboard with the irradiated thin sensor was in one test box with connections to the ALiBaVa motherboard and the HV power supply. The radioactive source was placed in a second box. The beta particles had to pass a dummy daughterboard with a silicon sensor to reach the scintillator used for triggering.

Figure 5.4 shows the cluster charge of the thin sensor irradiated to $2 \times 10^{16} \text{ n}_{\text{eq}}/\text{cm}^2$ measured with and without the radioactive source pointing at the device. On the left hand side the results from the measurement without the radioactive source prove that there is a noise peak at approximately 40 ADC for low and high voltages. On the right hand side the histograms from the full measurement with the radioactive source are displayed. It can be seen that at 200 V the number of events in the noise peak is lower than that in the full data. This could be explained by the signal being at the same position as the noise peak so that the total number of events add together. At 600 V the noise only peak is slightly higher than the full data peak. Because of the higher bias voltage the signal peak starts to migrate from the noise peak which is indicated by the broader distribution. In addition with a higher signal the seed cut should reject more random noise events because the channel with the highest signal is that of the traversing beta particle.

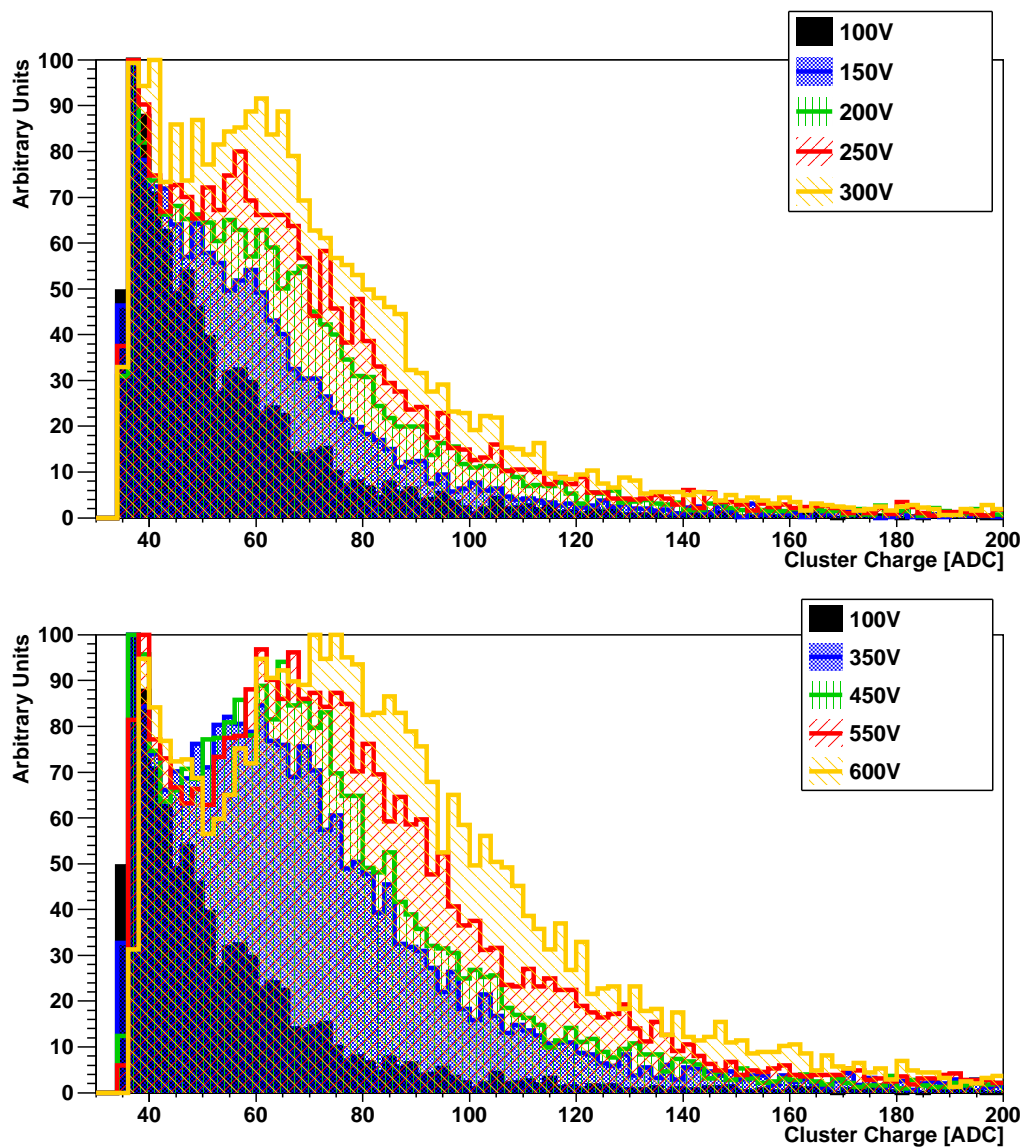


Figure 5.3.: Signal peak emerges from noise peak with increasing bias voltage. Real measurements ($5 \times 10^{15} \text{ n}_{\text{eq}}/\text{cm}^2$) are used but scaled to have a maximum of 100. The top graph shows the shift for bias voltages up to 300 V, while in the bottom graph the voltages go up to 600 V.

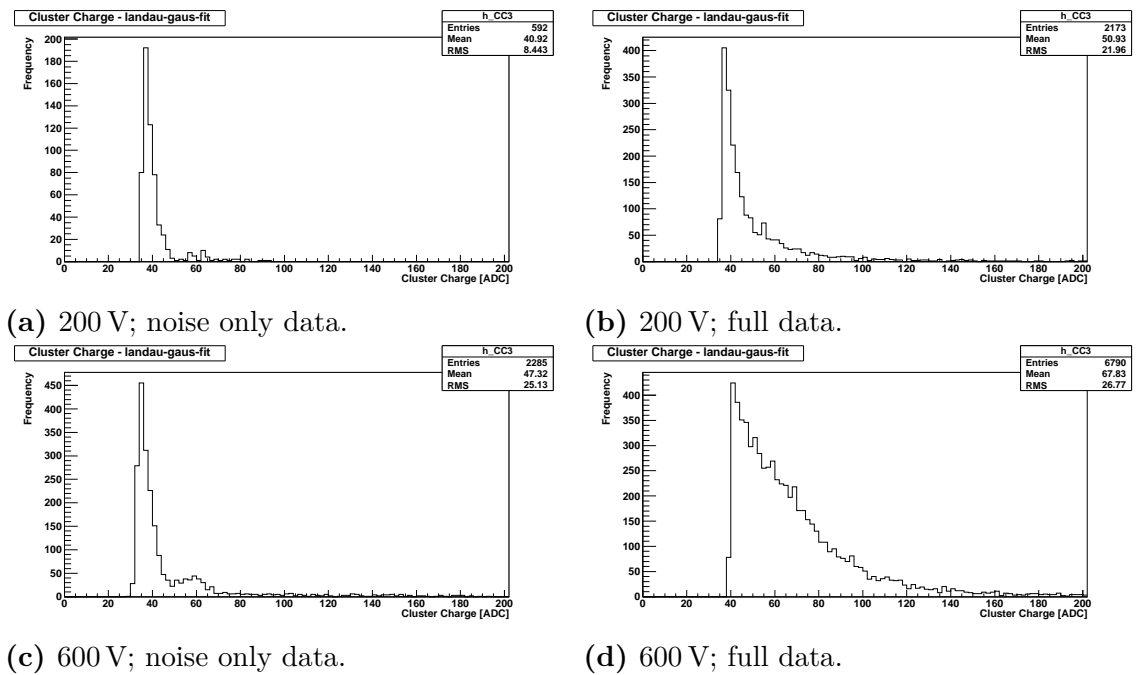


Figure 5.4.: Comparison of noise only data, obtained without a radioactive source, and real data at 200 V and 600 V for the thin sensor irradiated to $2 \times 10^{16} \text{ n}_{\text{eq}}/\text{cm}^2$.

5.2. Data Analysis

It has been shown that the analysis of highly irradiated thin silicon strip sensors is challenging. Different methods were used to improve the result and tested with simulated and real data.

5.2.1. Analysis Methods

Three different methods were used to analyse the data for thin irradiated silicon strip sensors with the aim to find one that allows the reconstruction of the signal at low bias voltages.

Method 1 In the standard analysis method (here referred to as Method 1), as described in section 3.2, the cluster charge distribution is fitted with a convoluted Landau-Gauss function (Figure 5.5). This works well for sensors with the standard thickness, but it requires a clear signal peak where the maximum is clearly separated from the noise peak. If not, the obtained signal MPV is lower than the true signal because the noise is misidentified as signal.

Method 2 For Method 2 the convoluted Landau-Gauss is again used as fit function for the signal. To reduce the noise contribution this method uses an iterative approach. The first step is to fit the noise peak in the total data set with a Gauss function (Figure 5.6a). Then this fit function is subtracted from the total data set, leaving only the signal fraction, which is fitted with the Landau-Gauss distribution (Figure 5.6b). A second iteration is implemented to improve the results. The obtained signal peak is subtracted from the total data set and the remaining noise peak is fitted again with a Gauss function (Figure 5.6c). Subtracting once again the fitted noise from the total data set the remaining distribution should resemble the true signal and is fitted with the convoluted Landau-Gauss to obtain the final MPV

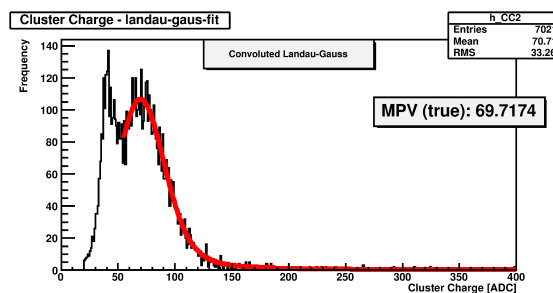


Figure 5.5.: Fit of cluster charge distribution with convoluted Landau-Gauss function according to Method 1.

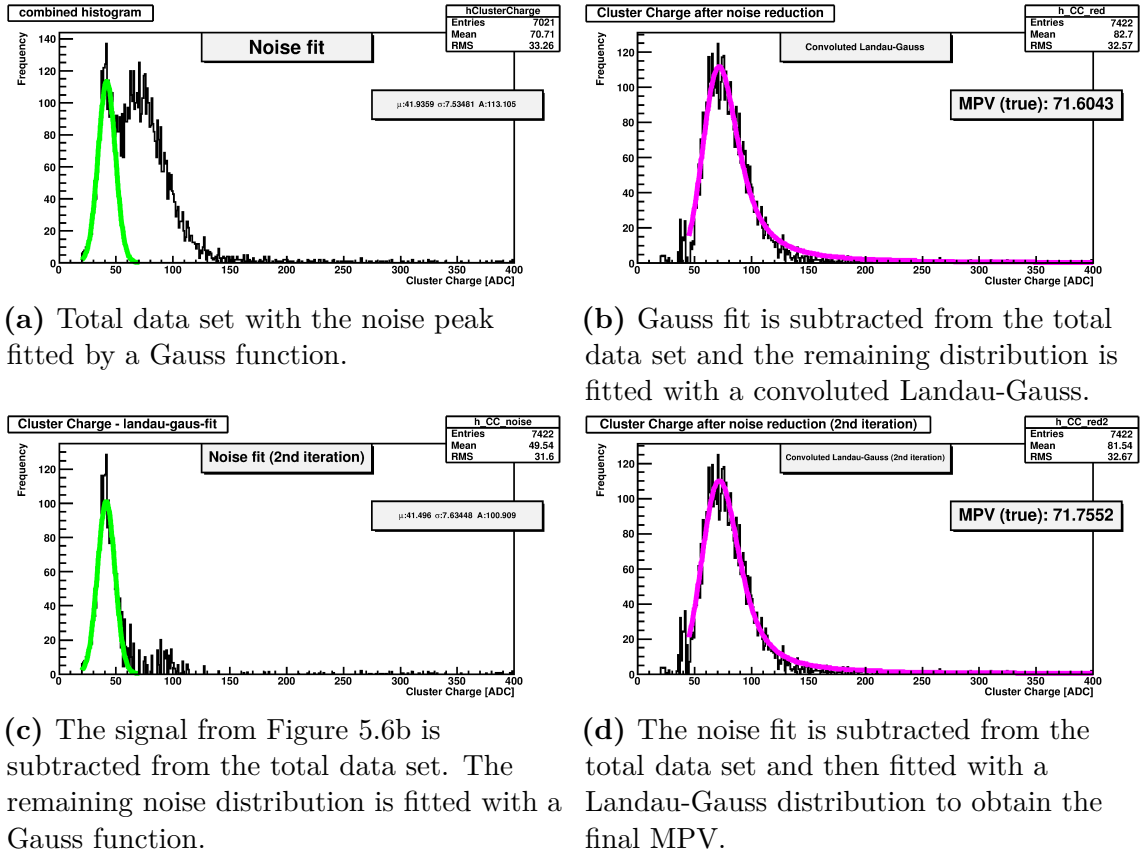


Figure 5.6.: Different steps of data analysis Method 2.

(Figure 5.6d). The disadvantage of this method is that if the signal MPV is close to the noise MPV it might be misidentified as noise and subtracted from the total data set. This would result in a final signal MPV that is larger than the true MPV.

Method 3 For Method 3 the fit function itself has been changed. Instead of trying to subtract the noise as in Method 2, the Gauss function is included into the fit. The final fit function is a combination of a Gauss and a Landau-Gauss (see Figure 5.7), where the signal MPV is obtained as maximum of the Landau-Gauss only. Like Method 1 this method is not very reliable when the signal and noise peak are at the same position, however it is better at obtaining the signal MPV when the signal starts to emerge from the noise. Even when the signal MPV is within the noise peak as long as a sufficient part of the Landau tail can be fitted the final MPV is closer to the real MPV.

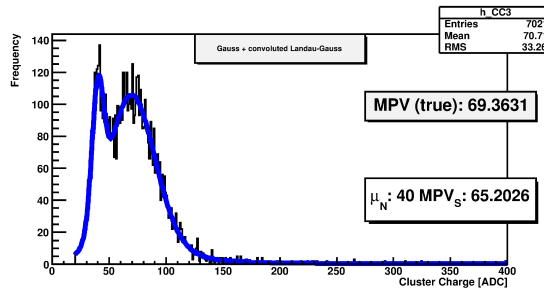


Figure 5.7.: Fit of cluster charge distribution with Gauss + convoluted Landau-Gauss according to Method3. With this method it is possible to fit the double peak distribution.

5.2.2. Simulated Data

Tests with simulated data have been done to compare the different fit methods. The simulations were done with ROOT and use a Gauss-distributed noise peak and a Landau-Gauss distributed signal peak. Figure 5.8 shows an example picture. The Gauss distribution in the top right graph is parametrized by the mean μ_N , the standard deviation σ_N and multiplied by a constant A_N . For the convoluted Landau-Gauss (top left) the standard definition in ROOT is used with the Landau width w_S , the Landau most probable MPV_S , the total area A_S and the width of the convoluted Gaussian function σ_S . Both histogram were filled randomly according to the signal and noise distribution with a predefined number of events (N_N for the Gaussian noise and N_S for the signal). Then they were fitted with the appropriate function to get clean fit results, including the true MPV from the Landau-Gauss fit of the pure signal peak. Afterwards they were added to get one single histogram. The first 20 ADC were removed to simulate the seed cut and the histogram was saved as a ‘.root’ file. This ‘.root’ file could then be read by the analysis ROOT script. The reason for using two scripts is that it is possible to analyse real data ‘.root’ files from the ALiBaVa analysis as well, which required a specific file structure for the simulated data. Three different test series were used to compare the diverse fit methods.

Test 1 In the first test series the only parameter that changed was the number of events in the noise peak. All other variables in the distributions have been kept the same (see Table 5.2). This test series simulates the case of low bias voltage when the signal peak is masked by a large noise peak. Figure 5.9 shows two example histograms from the simulation for a small and a large noise peak.

In Figure 5.10 the analysis results of this test series are shown. To analyse the quality of the different methods, the true MPV (from the raw signal Landau-Gauss fit) has been subtracted from the MPV obtained by the fits. For Method2 the two results are obtained from the two iteration steps (first iteration: Method2_1, second iteration: Method2_2). It can be seen that the results from Method1 are

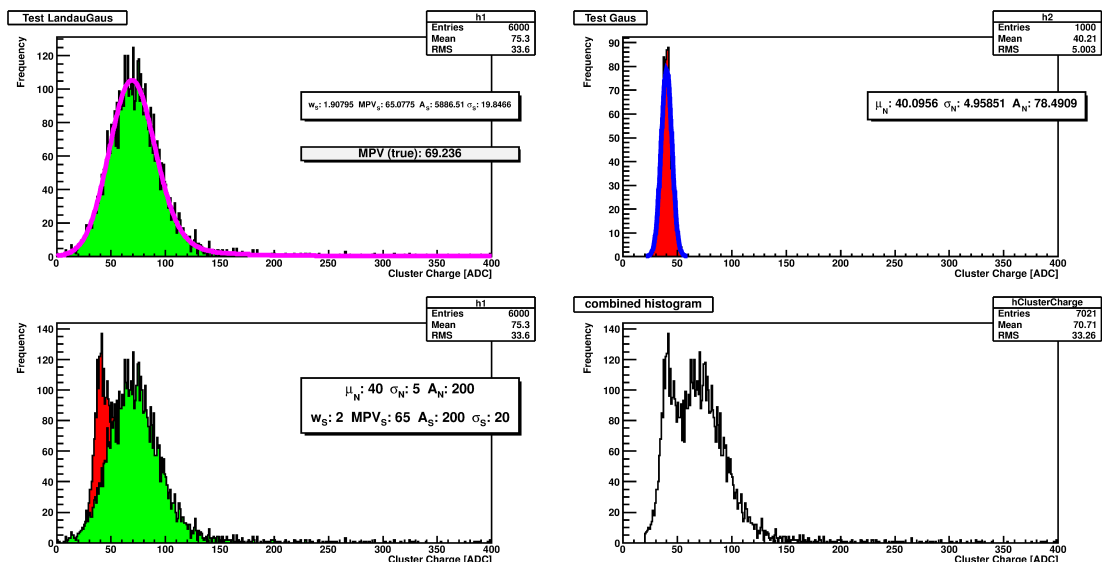


Figure 5.8.: Example graphs for one simulation. The top left graph shows the simulated signal (Landau-Gauss distribution) with the fit result that is used as true MPV. In the top right graphs the noise peak is shown, whereas the bottom left graph shows a stacked histogram with both graphs. The final raw data histogram can be seen in the bottom right graph.

Function	Parameter	Value	
		Test 1	Test 2
Gauss (Noise)	μ_N	40	40
	σ_N	5	5
	A_N	200	200
	N_N	variable	1000
Landau-Gauss (Signal)	w_S	2	2
	MPV_S	45	variable
	A_S	200	200
	σ_S	20	20
	N_S	6000	6000

Table 5.2.: Parameter for simulated noise and signal for Test 1 and Test 2.

negative which means that the obtained MPV value is smaller than the true MPV. The difference of 10 ADC is equivalent to the difference of the Gauss MPV (40 ADC) and the true signal MPV (50 ADC) which shows that this method is not suitable for cases in which a large noise peak masks the signal peak. In contrast, Method 2 obtains an MPV that is higher than the true MPV. The reason is that in the process of subtracting the noise from the total signal also the lower part of the signal is removed, resulting in a false signal peak with a too high MPV. The best results are

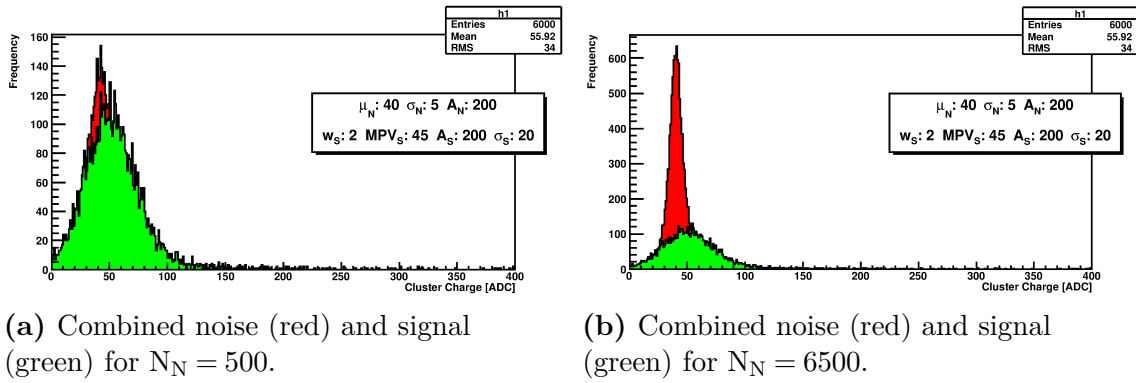


Figure 5.9.: Combined noise (red) and signal (green) histogram for Test 1 with 500 (left) and 6500 (right) entries in the noise peak.

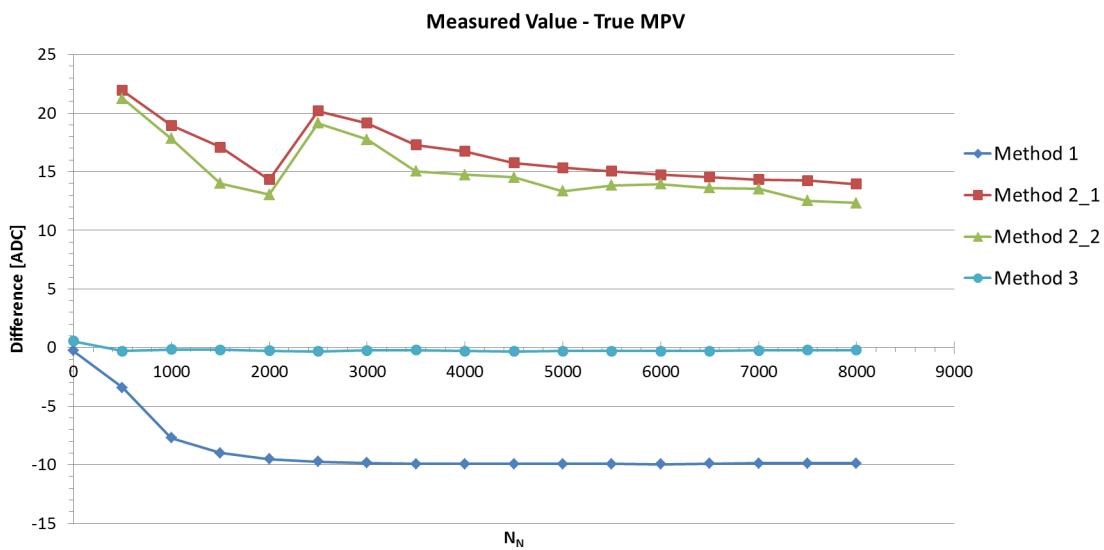


Figure 5.10.: Test 1 results: The true MPV is subtracted from the fitted MPV.

obtained with Method 3, which acquires a MPV that is nearly similar to the true MPV.

Test 2 In the second test series the number of events in the signal and the noise peak were kept constant, while the position of the signal was changed (see Table 5.2 for parameter values). This resembles a real test series in which the signal increases with increasing bias voltage. Figure 5.11 shows two examples where in the left picture the position of noise and signal peak are nearly identical, whereas in the right picture the signal is clearly separated.

Figure 5.12 shows the analysis results for this test series, where again the true MPV was subtracted from the value obtained by the fits. It can be seen that for

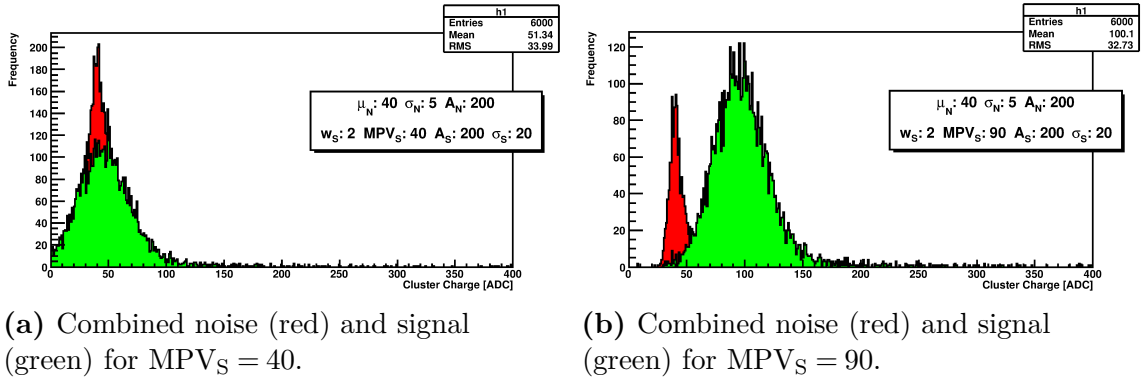


Figure 5.11.: Combined noise (red) and signal (green) histogram for Test 2 with the signal peak close to the noise peak (left) or clearly separated (right).

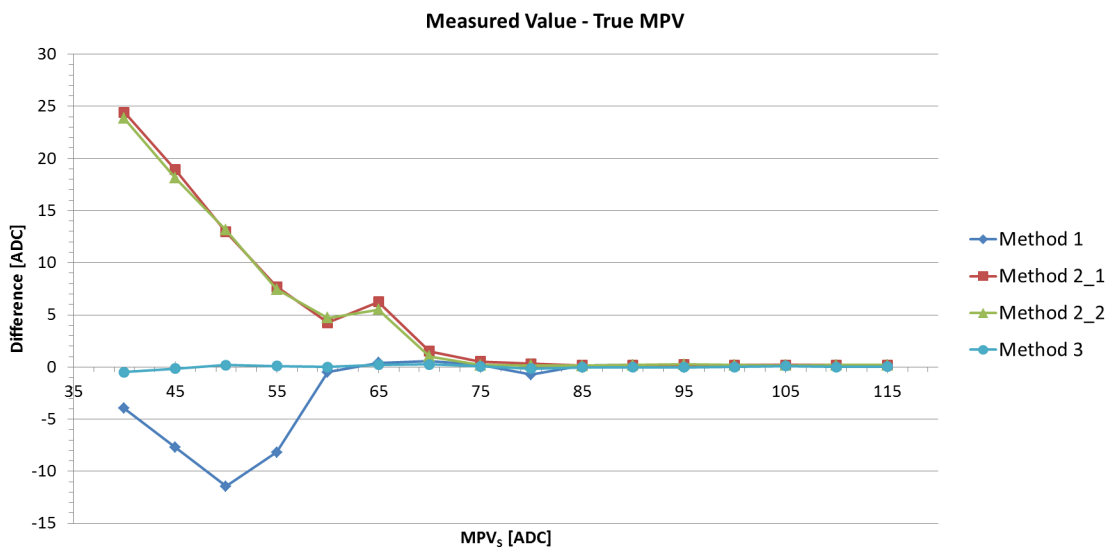


Figure 5.12.: Test 2 results: The true MPV is subtracted from the fitted MPV.

low signal positions Method 1 as well as Method 2 deviate from the true MPV, as it was observed in Test 1. With increasing signal strength (higher MPV_S) the values from Method 2 get closer to the true MPV. In Method 1 the difference first increases because the fitted noise peak stays constant. When the signal peak becomes fitable the difference to the true MPV decreases. For signal MPVs higher than approximately 70 ADC the acquired values for each fit method are in good agreement with the true value. As in the previous test series the results from Method 3 are close to the true value for all signal MPVs.

Physical Test The two shown test series were intended to resemble real data, but the start parameter for the fits were chosen to be close to the parameters from the simulation to make sure that the fits work. Five simulated histograms were

fitted for the Physical Test with various intentions. The parameters are shown in Table 5.3. In Physical1 and Physical2, two cases from test series 1 were repeated, but the start parameters of Method3 have not been optimized. This was done to investigate if the method still obtains the true MPV, even when the fit started from an unsuitable point. In the third simulation the number of events in the noise peak was much larger than that of the signal peak. Physical4 and Physical5 simulate a larger signal value with little to no noise.

Parameter	Value				
	Physical 1	Physical 2	Physical 3	Physical 4	Physical 5
μ_N	40	40	40	40	40
σ_N	5	5	5	5	5
A_N	200	200	200	200	200
N_N	500	1000	3000	0	500
w_S	2	2	2	2	2
MPV_S	45	45	45	140	65
A_S	200	200	200	200	200
σ_S	20	20	20	20	20
N_S	6000	6000	1000	10000	6000

Table 5.3.: Parameter for physical simulation for noise and signal.

The results of the physical tests are shown in Figure 5.13 in the same way as for Test 1 and Test 2. It can be seen that for the fourth simulation all fit methods result in the same MPV value. Because there was no noise in this test, this can be expected. For the other tests, the results from Method2 are higher than the true MPV. The best results are obtained with Method3, which shows the smallest difference from the true MPV. For lower noise values the MPV from Method1 shows as well good results, while for higher noise the obtained value is too small.

5.2.3. Real Data

With the simulated data it could be seen that Method3 works best for all tests. This could be expected since the method of generating the simulated histograms results in a distribution that is equal to the fit function of Method3. It is therefore important to compare the different methods with real data. The disadvantage is that by using real data the true MPV is unknown. From the simulations it can be seen that this is no issue for large signals, but especially for small signals and large noise, where the standard fit method is not reliable, it is hard to prove that the other methods work well.

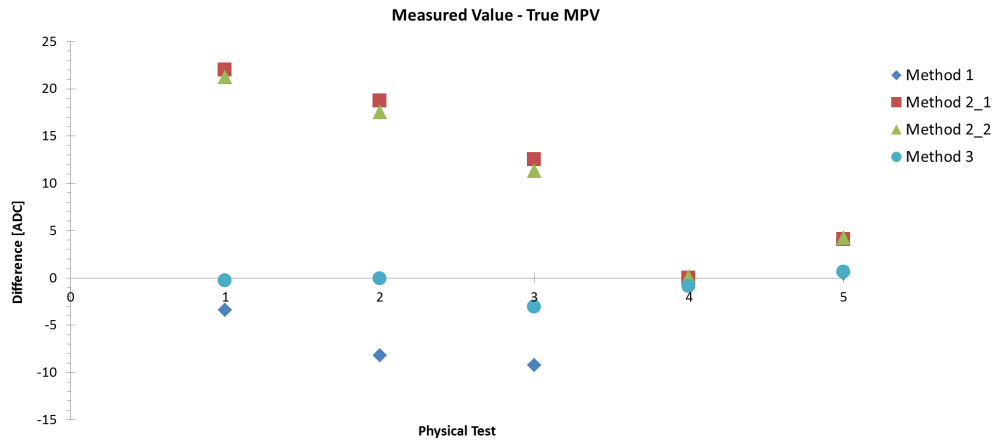


Figure 5.13.: Results of the physical tests. Test 1 to 3 have a low signal ADC with a large noise contribution where the number of noise events increase from 500 to 3000. In test 4 and 5 the signal is clearly higher than the noise with very few noise events. In all tests the start parameters of the fits were chosen to be not optimal to examine the fit quality.

Seed Cut One way of improving the data quality could be to change the seed cut. In the analysis a signal channel has to exceed the seed cut value to be identified as primary channel of the hit cluster (seed). This might help to reject random noise peaks. Two sensors were used to compare different seed cut values: the thin sensor irradiated to $1 \times 10^{15} \text{ n}_{\text{eq}}/\text{cm}^2$ was tested at 700 V, where there is a clear separation between signal and noise. For a higher irradiation fluence the thin sensor irradiated to $2 \times 10^{16} \text{ n}_{\text{eq}}/\text{cm}^2$, tested at 550 V, has proven to be hard to analyse because of the small signal and the large number of noise events. For the analysis Method 3 was used because it worked best in the simulations and the results shown in Figure 5.1 have already shown that Method 1 is not fully suitable for a highly irradiated sensor. Method 2 has been excluded because the overall performance in the simulations was not satisfactory.

The results of the MPVs are shown in Figure 5.14. For the sensor irradiated to $1 \times 10^{15} \text{ n}_{\text{eq}}/\text{cm}^2$ it can be seen that a higher seed cut increases the collected charge. For low seed cut values too many of the random noise hits pass the filter which distort the fit result. The standard seed cut of 3.5 result in an acceptable MPV value. Increasing the cut would only improve the result slightly. While the initial increase can also be observed at the sample irradiated to $2 \times 10^{16} \text{ n}_{\text{eq}}/\text{cm}^2$, it shows that after reaching a maximal MPV at 3.0 further increasing of the seed cut reduces the signal. One possible reason could be that some real events are rejected because the signal strength is too small. Another reason can be seen when looking at the number of events that passed the cut (Figure 5.15). While the number is fairly constant for a seed cut larger than 3.0 for the lower fluence, it decreases further for the higher fluence sensor. The lower number of events has a negative influence on

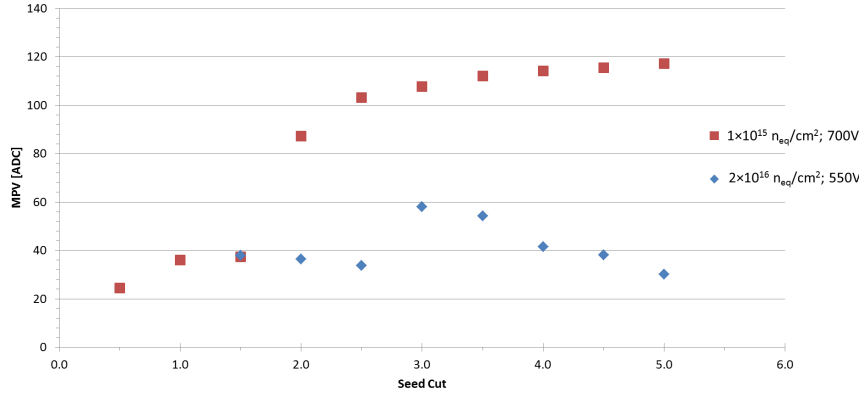


Figure 5.14.: Collected charge MPV for different seed cut values (standard is 3.5).

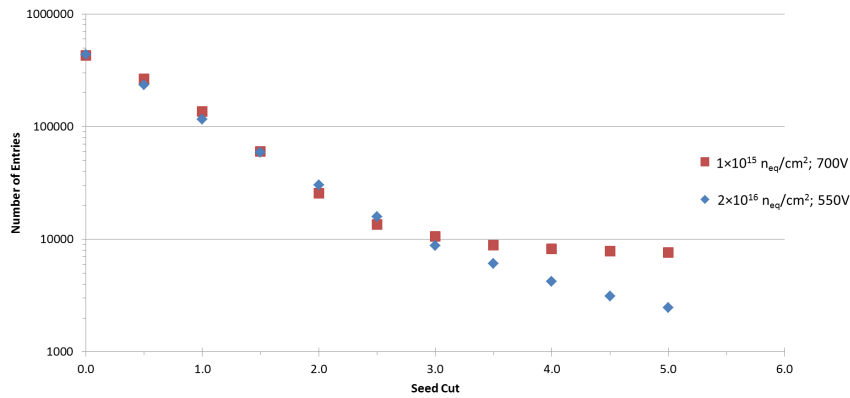


Figure 5.15.: Number of entries in cluster charge histogram for different seed cut values.

the quality of the fit. Both tests show that the standard seed cut of 3.5 results in a reasonable MPV.

Analysis Method Comparison To compare the analysis methods the measurements of the 50 μm thin sensors have been re-analysed. Figure 5.16 shows the comparison of the different methods with real data from each measured sensor. It can be seen that for the lower fluences the results from all methods agree well with each other. They start to deviate at a fluence of $5 \times 10^{15} \text{ n}_{\text{eq}}/\text{cm}^2$ at low voltages. The lowest values are obtained by Method 1, which is not able to distinguish between signal and noise. Method 3 results in higher signal values while the largest collected charge is obtained by Method 2. The reason for this could be that while it is not possible to get a clear discrimination between noise and signal, some of the signal is misidentified as noise and subtracted prior to the fit. With higher bias voltages the signal strength increases which results in better fit results. While the bias voltage at which all methods agree is at 250 V, for the next higher fluence of $1 \times 10^{16} \text{ n}_{\text{eq}}/\text{cm}^2$

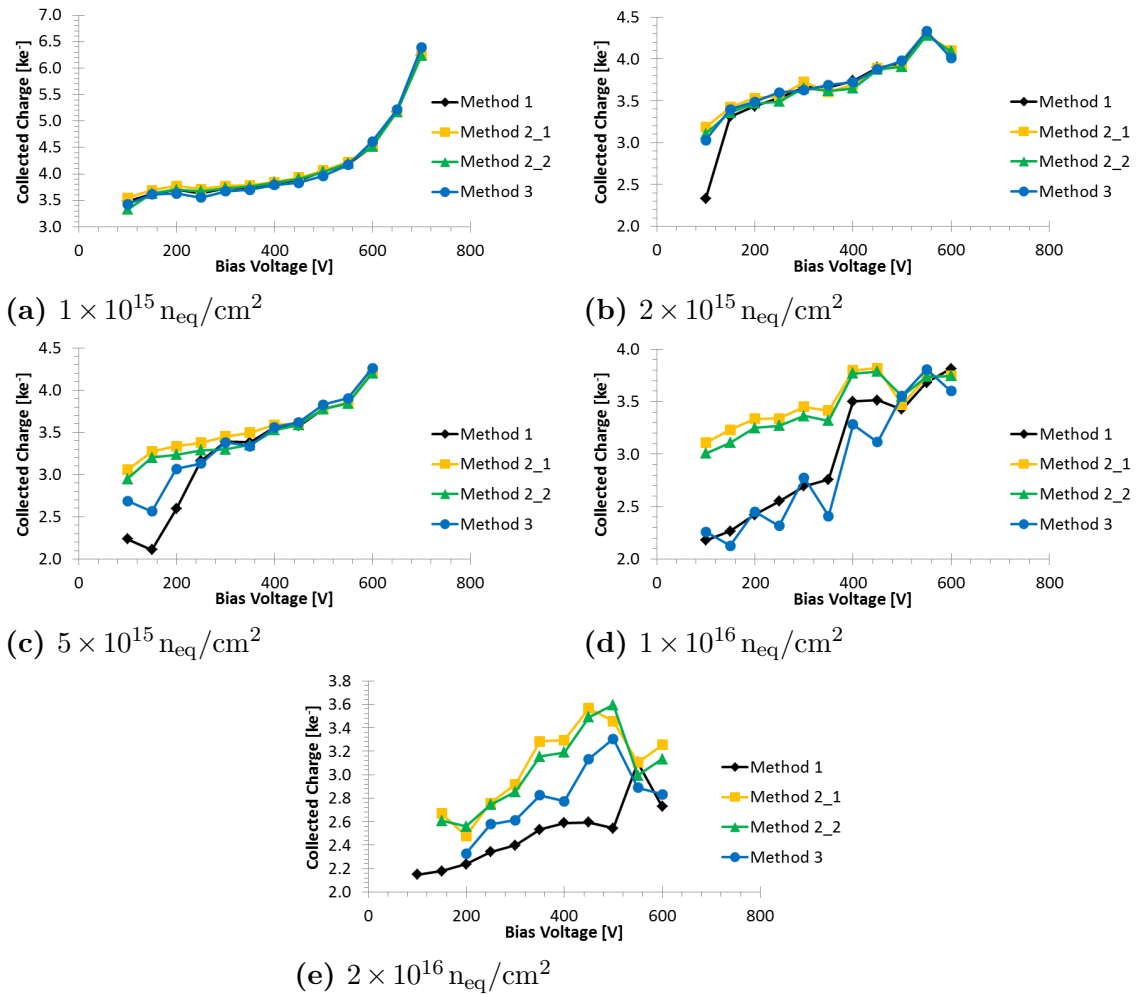


Figure 5.16.: Comparison of analysis methods with $50 \mu\text{m}$ sensors after irradiation with neutrons to different fluences.

this increases to 500 V. The difference between Method 1 and Method 3 are negligible for this fluence and it can be seen that the values of Method 2 are higher than those of the other methods. At the highest fluence ($2 \times 10^{16} \text{ n}_{\text{eq}}/\text{cm}^2$) the only agreement can be seen at 550 V. For the other bias voltages the collected charge from Method 3 is between that of Method 1 and Method 2, but the difference to Method 2 decreases with increasing bias voltage.

To estimate the quality of the fit methods the difference with respect to 'Method 1' was calculated and is shown in Figure 5.17. Because the largest deviation in the collected charge was seen after the irradiation fluence of $2 \times 10^{16} \text{ n}_{\text{eq}}/\text{cm}^2$ these data were used. These differences can be used as a measure of the systematic uncertainty. It shows that beside the values at 550 V the best agreement to 'Method 1' can be achieved with 'Method 3'. Compared to the electronic noise from the pedestal measurement the systematic uncertainties of the different fit methods are smaller.

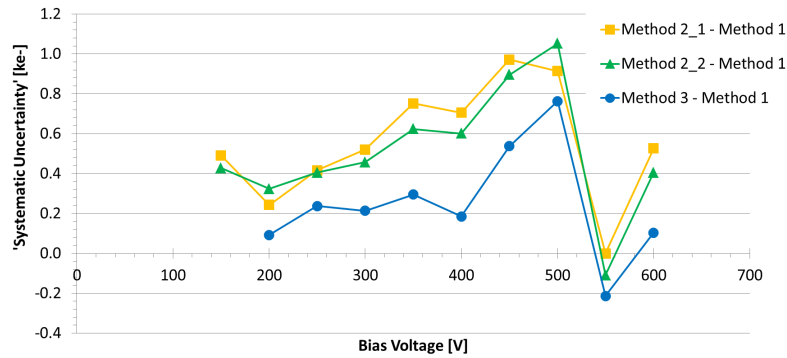


Figure 5.17.: Difference of the collected charge for the fit methods compared to 'Method 1'. The data for the samples irradiated to $2 \times 10^{16} \text{ n}_{\text{eq}}/\text{cm}^2$ directly after irradiation were used.

5.3. Annealing

Two sensors have been used to study the annealing behaviour of $50 \mu\text{m}$ thick sensors: 2922-1 was irradiated at CERN [Gla16] with protons to $3.19 \times 10^{16} \text{ p}/\text{cm}^2$. With the hardness factor of 0.62 and the NIEL scaling hypothesis ([Har09]) this corresponds to $1.98 \times 10^{16} \text{ n}_{\text{eq}}/\text{cm}^2$. The second device is 3107-6-20 irradiated to $2 \times 10^{16} \text{ n}_{\text{eq}}/\text{cm}^2$ with neutrons at Ljubljana. The annealing was done at room temperature in a nitrogen cabinet.

2922-1 Figure 5.18 shows the collected charge after annealing of the sensor 2922-1, analysed with Method 1. It can be seen that the collected charge is highest for the first measurements and decreases with increasing annealing time. While an unirradiated thin sensor has a maximum charge of approximately 3.2 ke^- , the charge for voltages higher than 400 V exceed this value. Taking the noise into account (Figure 5.19) this can be explained by charge multiplication which enhances the signal as well as the noise. The shape of the annealing curve deviates from the expectation by not displaying the initial increase of signal due to beneficial annealing. This can be explained by the setup at the irradiation site: In the old CERN facility (up to 2012) the irradiation was done at room temperature. To reach the planned fluence the sample needed to be irradiated for more than 50 days. In section 4.2 it has been shown that the maximum of the collected charge was reached after approximately 40 days of room temperature annealing, which means that the measurements of the sensor 2922-1 only show the signal decrease of reverse annealing.

3107-6-20 The sensor 3107-6-20 was only annealed for up to 30 days and therefore only a small increase in signal due to beneficial annealing is expected. Additionally

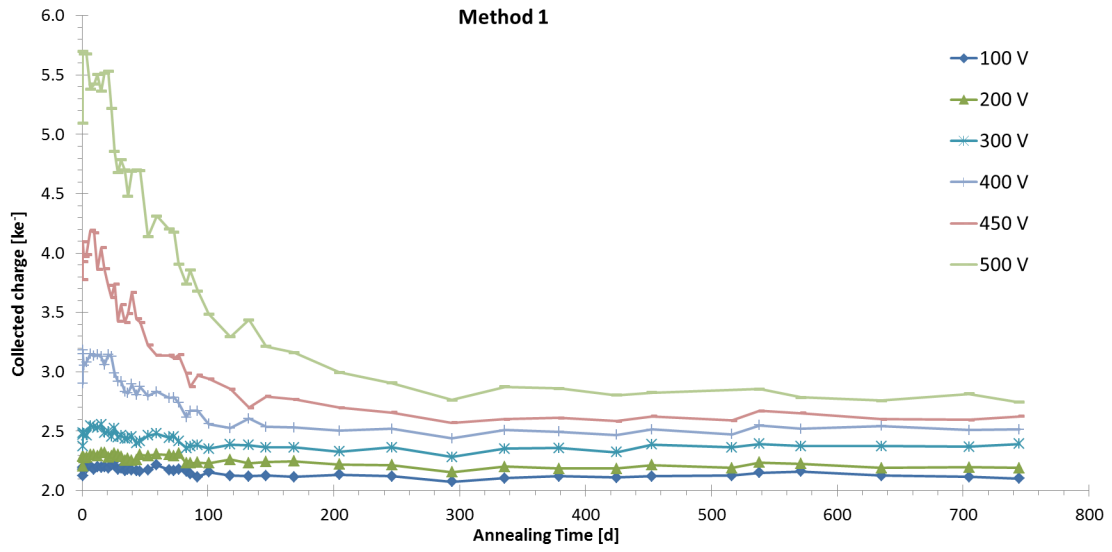


Figure 5.18.: Collected charge after room temperature annealing for 2922-1 ($1.98 \times 10^{16} \text{ n}_{\text{eq}}/\text{cm}^2$).

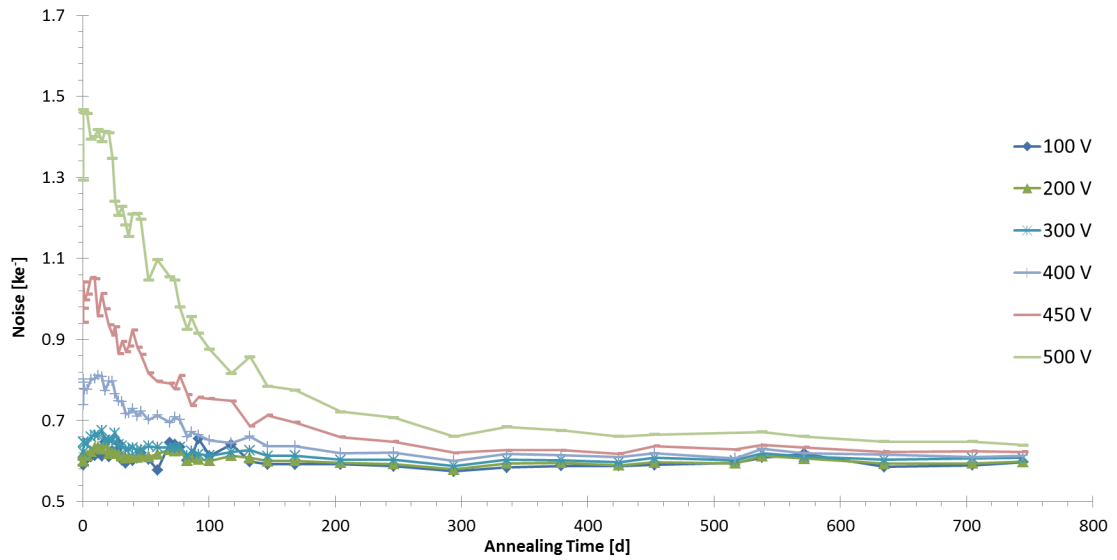
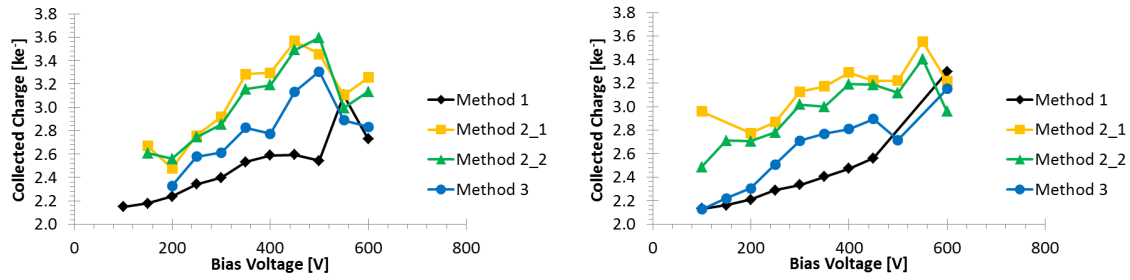
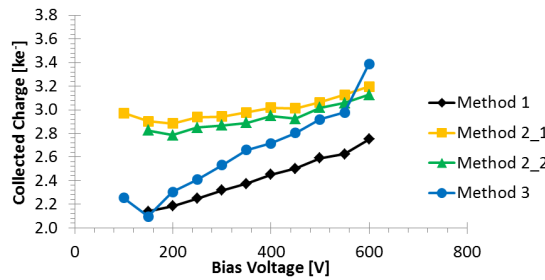


Figure 5.19.: Noise after room temperature annealing for 2922-1 ($1.98 \times 10^{16} \text{ n}_{\text{eq}}/\text{cm}^2$).



(a) After irradiation (1 day annealing).

(b) After 10 days of annealing.



(c) After 30 days of annealing.

Figure 5.20.: Collected charge of 3107-6-20 ($2 \times 10^{16} \text{ n}_{\text{eq}}/\text{cm}^2$) after irradiation, 10 days and 30 days of room temperature annealing, obtained by the different analysis methods.

the initial signal strength was smaller without the observed charge multiplication of the 2922-1 device.

Figure 5.20 shows a comparison of the three analysis methods at each annealing step. It can be seen that the collected charge directly after irradiation does not follow a smooth increase for Method 2 and Method 3. This improves with increasing annealing time with the best shape after 30 days of annealing. Like in the previous comparisons the values from Method 2 are the highest and Method 1 the lowest, whereas Method 3 is in between.

As expected, the collected charge versus annealing time for this sample, shown in Figure 5.21 and analysed with Method 1, shows a small increase with increasing annealing time.

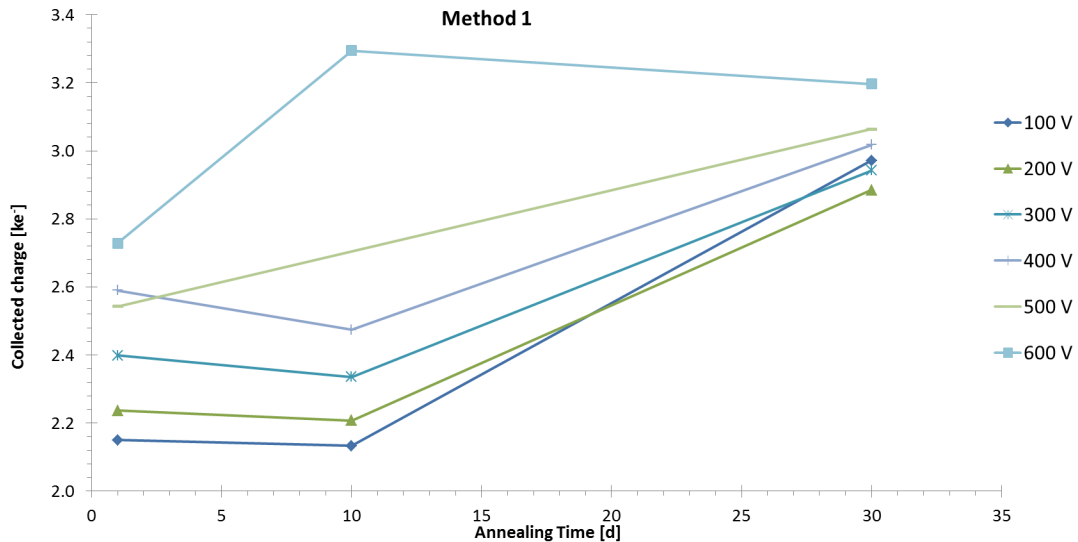


Figure 5.21.: Collected charge versus annealing time for 3107-6-20 ($2 \times 10^{16} \text{ n}_{\text{eq}}/\text{cm}^2$).

5.4. Summary

Several $50 \mu\text{m}$ thick silicon strip sensors, produced by Micron Semiconductor Ltd., have been irradiated up to $2 \times 10^{16} \text{ n}_{\text{eq}}/\text{cm}^2$ and tested with the ALiBaVa system. It has been shown that up to $5 \times 10^{15} \text{ n}_{\text{eq}}/\text{cm}^2$ the collected charge for all voltages shows no excess in collected charge compared to an unirradiated sensor. For the highest fluences the analysis was challenging because the small signal peak can be covered by fake signals from random noise. Only for high bias voltages the signal peak emerges clearly from the noise peak.

Three different analysis methods have been used to tackle this issue: Method 1 represents the standard fit with a convoluted Landau-Gauss distribution. Method 2 uses an iterative approach in which the noise peak is first fitted with a Gauss function and subtracted from the total data set. Then the signal peak is fitted with a Landau-Gauss. In the second iteration this signal is subtracted from the total data and a Gauss fit of the noise is performed. After subtracting this new noise from the total data the signal is fitted again. For Method 3 the fit-function is a Gauss added to a Landau-Gauss. The idea is to use the Gauss part to fit the noise peak and at the same time use the Landau-Gauss to fit the signal peak, which might only appear as landau-tail in the noise peak.

To investigate the quality of these analysis methods they were tested with simulated data. For the first test series the number of noise events was changed and it has been shown that Method 3 shows the best agreement with the true MPV while Method 2 result in too high signals and Method 1 in too small values. This can be

seen in the second test series as well, in which the signal MPV was increased. With increasing signal MPV the values of the methods converge towards the true MPV and there was no difference for signals larger than 70 ADC. Method 3 has shown the best agreement between fit result and true MPV in all test series.

The analysis methods were used with real data. While all methods result in the same values for low fluences ($1 \times 10^{15} \text{ n}_{\text{eq}}/\text{cm}^2$ to $5 \times 10^{15} \text{ n}_{\text{eq}}/\text{cm}^2$) they differ for higher fluences. For the sample irradiated to $1 \times 10^{16} \text{ n}_{\text{eq}}/\text{cm}^2$ the values deviate up to a bias voltage of 500 V with Method 2 having the highest value. For the highest fluence of $2 \times 10^{16} \text{ n}_{\text{eq}}/\text{cm}^2$ only one acceptable agreement can be seen at 550 V whereas at all other voltages Method 2 result in the highest and Method 1 in the lowest collected charge. While the obtained values follow a smooth curve for low fluences, the shape is irregular for high fluences.

Annealing the device irradiated to $2 \times 10^{16} \text{ n}_{\text{eq}}/\text{cm}^2$ shows that the curves become smoother with increasing annealing time. The observed difference between the three methods can be seen in all annealing steps. When looking at the collected charge (Method 1) it has been shown that it increases with increasing annealing time. This is expected due to beneficial annealing. For an other device, irradiated to $1.98 \times 10^{16} \text{ n}_{\text{eq}}/\text{cm}^2$ with protons at CERN, the initial collected charge decreases with increasing annealing time most likely due to reverse annealing. The initial charge for high voltages ($>400 \text{ V}$) exceeded the expected charge for a fully depleted unirradiated sensor. By taking the increased noise into account it can be concluded that this is due to charge multiplication. This has also been observed with $300 \mu\text{m}$ thick sensors (see chapter 4).

6. Study on Leakage Current

The study, presented in this chapter, is aimed to deepen the understanding of highly irradiated silicon strip sensors, especially of the reverse bias current. Equation 2.22 is used to scale the current, measured at one temperature, to another temperature. The scaling depends on the effective energy, a parameter that is obtained from measurements to fluences up to $1 \times 10^{15} \text{ n}_{\text{eq}}/\text{cm}^2$ [Chi13]. For future high energy experiments the expected irradiation fluence exceeds this range and it is therefore essential to investigate whether the effective energy changes at high fluences. Another aspect is to look into the fluence dependence of the current (Equation 2.24). This parametrization is not based on any physical theory and it is therefore crucial to investigate if it is still valid at high fluences.

Sensors with different thicknesses from 50 μm to 293 μm have been irradiated with fluences from $1 \times 10^{12} \text{ n}_{\text{eq}}/\text{cm}^2$ to $2 \times 10^{16} \text{ n}_{\text{eq}}/\text{cm}^2$. In section 6.1 some more details of the measurement systems and the methodology are discussed. The reverse bias current has been measured for the unirradiated sensors (section 6.2) as well as after irradiation (section 6.3). Measuring the current at several temperatures allows the calculation of the effective energy. The results are shown in section 6.4. With the different presented methods it is possible to determine the current related damage rate, shown in section 6.5. Some sensors were measured at CERN and compared to the results from Liverpool (section 6.6). The new Peltier cooled system was used as well and compared with the freezer cooling in section 6.7. To validate the results a second set of sensors has been irradiated and measured by the Freiburg group (Physikalisches Institut, Abteilung Prof. K. Jakobs [Uni16a]). The results including a detailed comparison are shown in section 6.8.

Results from the Liverpool measurements have been shown at RD50 workshops [Won13b, Won14a, Won14b, Won15b], at the 11th Trento workshop [Won16a] and first results have been published in a paper [Won15a].

6.1. Measurement Setup

The measurements of the reverse bias currents were done with the probe station at room temperature for the unirradiated devices and with the cold IV system for the irradiated samples (see section 3.1). To investigate the temperature dependence of the current an accurate temperature measurement of the silicon sensor is crucial.

In standard measurements the temperature sensor is placed as close to the silicon device as possible, but there is usually no direct contact. For this study a new measurement PCB has been designed at Liverpool [Tsu14], which is compatible with the cold IV system and can be seen in Figure 6.1. The irradiated silicon sensor was glued with silver conductive glue (TraDuct [Hen16]) on to the PCB to establish the backside contact. The bias ring was connected with a wire-bond to one circuit path to apply high voltage to the sensor. For a good temperature measurement a PT1000 temperature sensor was glued directly on to the silicon surface with a non-conductive glue (Araldite [RS 16]). Four holes in the PCB were used to attach it to the cold IV measurement systems.

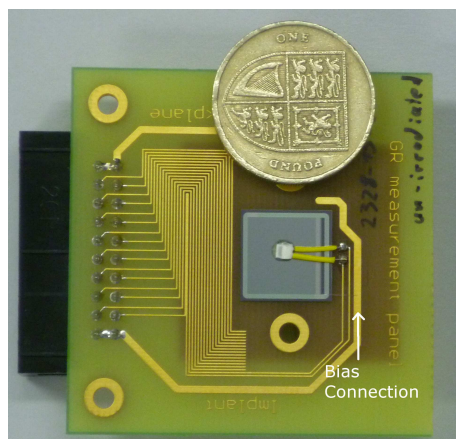


Figure 6.1.: Cold IV measurement PCB with the silicon sensor in the centre. A PT1000 temperature sensor (white) was glued directly on to the silicon to get precise temperature measurements. Yellow plastic tubes were used to protect the silicon from the wires of the temperature sensor and electrically isolate them.

PT1000 For temperature measurements a platinum temperature sensor PT1000 was used (P1K0.232.6W.A.010, [Far16]). This sensor has a resistance of $1000\ \Omega$ at 0°C , is rated from -200°C to $+600^\circ\text{C}$ and has the outer dimensions of $(2.3 \times 2.0)\ \text{mm}^2$. The following equation describes the temperature (T) dependence of the resistance R [Sch16]:

$$R = \begin{cases} R_0 \cdot \left(1 + a \cdot T + b \cdot T^2 + c \cdot (T - 100^\circ\text{C}) \cdot T^3\right) & \text{for } -200^\circ\text{C} \leq T \leq 0^\circ\text{C} \\ R_0 \cdot \left(1 + a \cdot T + b \cdot T^2\right) & \text{for } 0^\circ\text{C} \leq T \leq 850^\circ\text{C} \end{cases} \quad (6.1)$$

with $R_0 = 1000\ \Omega$, $a = 3.90802 \times 10^{-3}/^\circ\text{C}$, $b = -5.7750 \times 10^{-7}/^\circ\text{C}^2$ and $c = -4.1830 \times 10^{-12}/^\circ\text{C}^4$. The temperature has to be in $^\circ\text{C}$ and the resistance R is given in Ω .

For temperatures higher than 0°C it is easy to convert the measured resistance to a temperature value because the quadratic equation 6.1 can be converted, but for the use in the cold IV system the temperature is always below the freezing point and

that equation can not be reversed analytically. When accuracy is not so important, it is possible to use the same equation as for positive temperatures. Figure 6.2 shows the difference between the full equation and the quadratic approximation where the approximation is subtracted from the full equation. For lower temperatures the values from the approximation are higher and the temperature difference increases with decreasing temperature. Only temperatures down to approximately -50°C are used due to the limit of the cooling system in this study. The detailed temperature difference for this range is enlarged in the graph and it can be seen that the largest difference is reached at -50°C with a value of approximately $0.08\ \Omega$.

To get a more accurate temperature value a different method was used for the work presented here: The resistance was calculated for temperatures in 0.01°C steps. This leads to resistance steps of approximately $0.04\ \Omega$. The calculated resistance values were then compared to the measured value and when the difference was less than $0.03\ \Omega$ the corresponding temperature was used. With this method the temperature uncertainty depends on the step size and is in this case 0.01°C . Assuming a resistance uncertainty that is smaller than the step size, the temperature uncertainty is dominated by this conversion method and therefore this uncertainty is used for the uncertainty on the temperature.

Measurement uncertainty The LabVIEW program which was used for current, capacitance and resistance measurements also calculates the uncertainty for each of these measured quantities by measuring each more than once and as fast as possible. The following equations are implemented to calculate the average value and the

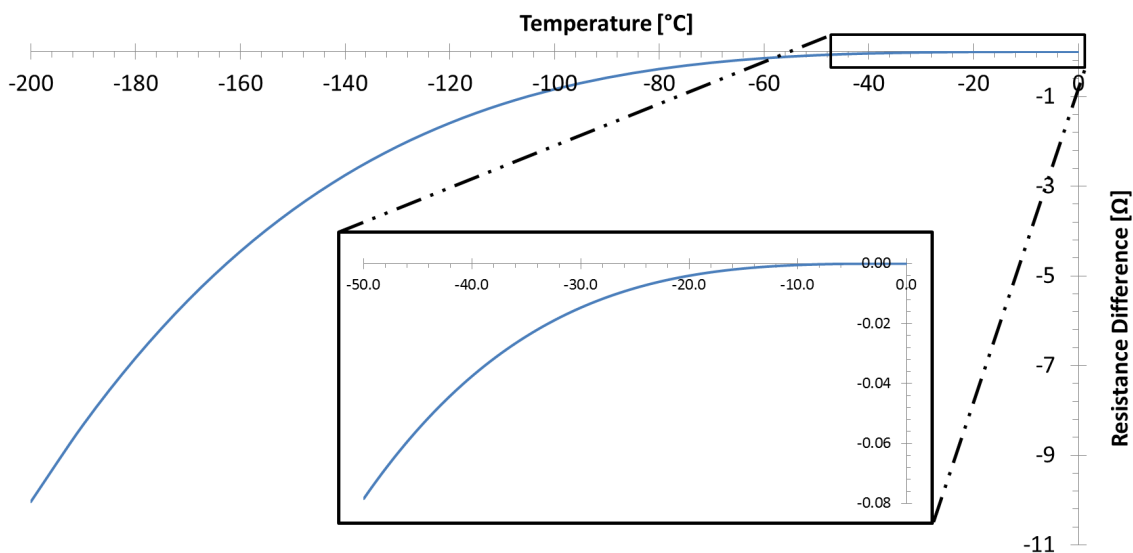


Figure 6.2.: PT1000 temperature difference between full equation and quadratic approximation, where the quadratic is subtracted from the full. The temperature range used in this thesis (0°C to -50°C) is enlarged.

corresponding uncertainty:

$$\begin{aligned} \text{Average: } \bar{x} &= \frac{\sum_{i=1}^N x_i}{N} \\ \text{Uncertainty: } \sigma_{\bar{x}} &= \frac{\sigma_x}{\sqrt{N}} \cdot 3 \\ \text{with } \sigma_x &= \sqrt{\frac{1}{N} \sum_{i=1}^N (x_i - \bar{x})^2} \end{aligned} \tag{6.2}$$

where N is the number of measurements and x_i being the i^{th} measured value. The factor 3 in the uncertainty arises from the Student's t-distribution and is chosen so that for the small number of samples at 99% confidence the measured values are within the uncertainty interval. 30 samples are used for the current measurements while for capacitance and resistance only 10 samples were taken.

6.1.1. Methodology

A Keithley 2410 power supply was used to apply high voltage to the silicon strip sensor and at the same time it also measured the current. The resistance measurements were done with a Keithley 2000 Multimeter [Kei16b].

In the first measurements the standard IV LabVIEW program was used while the resistance was read out by hand. The acquired precision was 0.1Ω for a single measurement per voltage step. After an upgrade the resistance measurement was included into the LabVIEW program, which results in smaller uncertainties because the values were readout electronically rather than by eye. The voltage was set from 0 V up to 1000 V in 10 V steps. To get accurate current measurements it is important to change the voltage slowly and let it settle for some time before the measurement. The chosen voltage ramping speed was 1 V/s with 10 s settling time. Because the sensors were irradiated to different fluences the current compliance value had to be chosen for each sample separately so that the highest possible voltage could be reached without seeing a breakdown. The PT1000 was only connected with two wires to the Multimeter so the cable resistance needed to be taken into account. This was done by measuring it and subtracting it from the measured resistance. In Liverpool the measured cable resistance was 1.3Ω while it was 0.5Ω for the measurements at CERN.

6.2. Measurements of Unirradiated Sensors

Sensors with different thicknesses (50, 108, 143 and 293 μm) from Hamamatsu Photonics K.K. (HPK, [Ham16]) and Micron Semiconductor Ltd. were irradiated for this study with protons at Birmingham (low fluence HPK sensors) and neutrons at

Ljubljana. Table A.4 in the appendix lists all measured sensors with their fluences, the irradiation source and their thickness. Selected details of the sensors from the two manufactureres are summarized in Table A.5.

All sensors have been measured at room temperature before the irradiation to make sure that they can reach 1000 V (500 V for the 50 μm thick sensors). In Figure 6.3 the currents are shown with different colours for the different sensor types. It can be seen that the thickest Micron sensors (143 μm , red) have the highest current. On the other hand the 293 μm thick HPK sensors have the lowest current despite being the thickest sensors. A possible explanation could be a difference in the sensor resistivity. This can also be seen when looking at the capacitance (Figure 6.4). The full depletion voltage was computed with the method described in 2.2.2. While V_{dep} for the Micron sensors is in the range of 20 V to 40 V, for the HPK sensors it is between 200 V and 300 V depending on the wafer type. It can also be seen that the sensor with the largest thickness has the smallest capacitance (graph shows $1/C^2$) which is in good agreement with the theoretical expectation. Because the capacitance is inverse proportional to the resistivity the high $1/C^2$ value of the HPK sensors indicates a higher resistivity value compared to the Micron sensors.

None of the 50 μm sensors in the current graph reaches 500 V, they all break down for voltages higher than approximately 300 V. Previous experiences with thin sensors have shown that this improves after irradiation, so they can be used for this study.

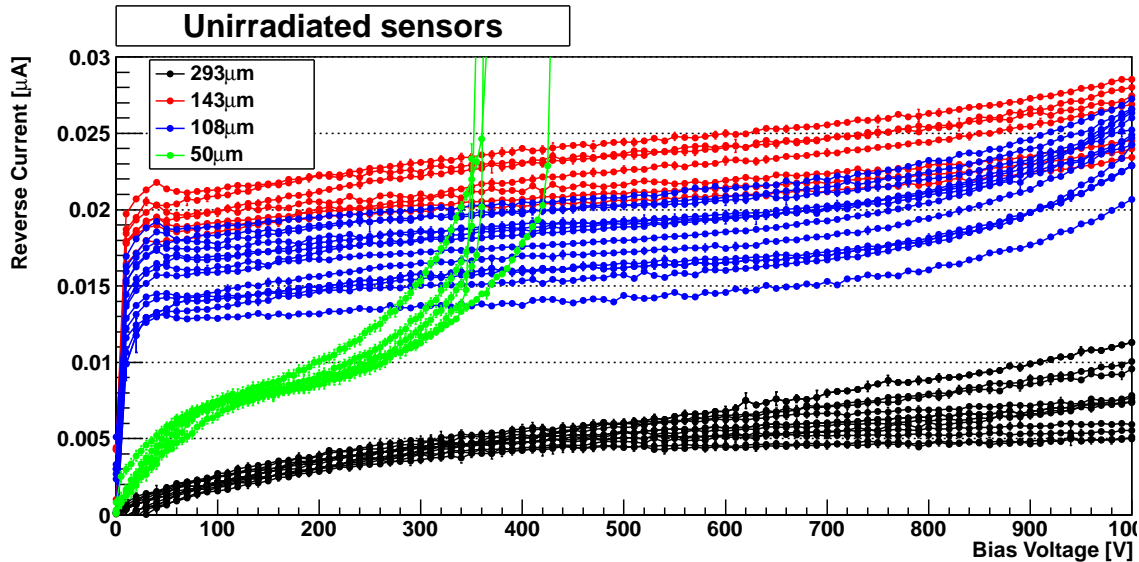


Figure 6.3.: Reverse bias current of the unirradiated sensors measured at room temperature. Different colours are used for the different sensor types: black for the 293 μm thick HPK sensors, red for 143 μm , blue for 108 μm and green for 50 μm thick Micron sensors.

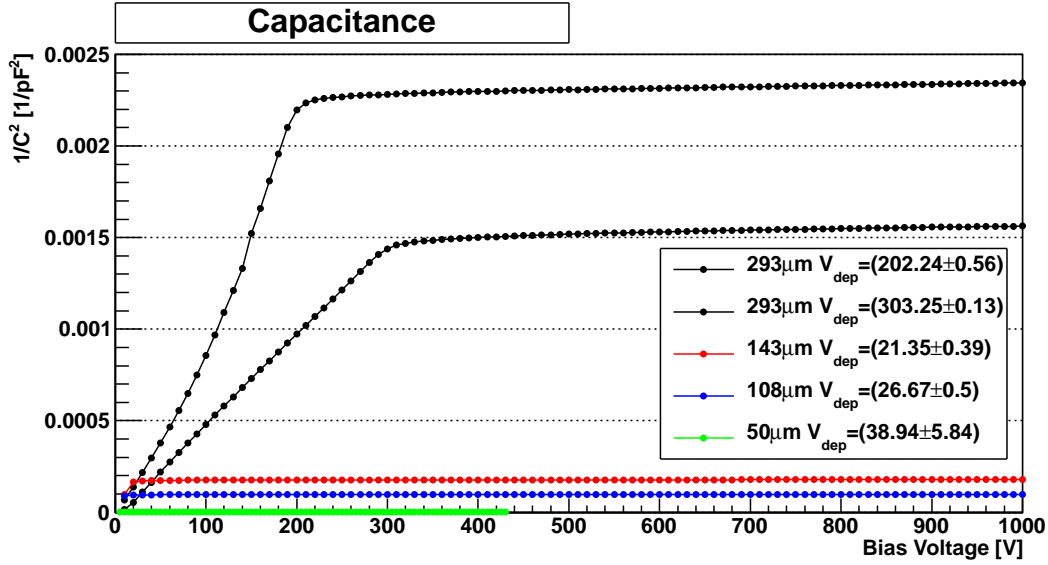


Figure 6.4.: Capacitance graph which was used to determine the full depletion voltage by fitting the increasing slope and the constant part with straight lines. The intersection of the two fit lines computes to the full depletion voltage. One sample of each type is shown as example. The two 293 μm samples are from different wafers therefore a different resistivity could explain the disagreement.

6.3. Measurements after Irradiation

The sensors have been irradiated with protons and neutrons to fluences from $1 \times 10^{12} \text{ n}_{\text{eq}}/\text{cm}^2$ to $2 \times 10^{16} \text{ n}_{\text{eq}}/\text{cm}^2$ (see Table A.4). The initial IV measurements of the HPK sensors after irradiation, shown in Figure 6.5, are as expected: with increasing fluence the reverse bias current increases. It can be seen as well that three sensors did not reach 1000 V because they have shown an early breakdown. The currents have been measured with the old cold IV setup with the freezer set to -23°C and then scaled to -25°C with Equation 2.22. Although not shown, all other sensor types as well show the increase in current with increasing irradiation fluence.

In Figure 6.6 the reverse bias current, divided by the active area (see Table A.5), is shown for the four different sensor thicknesses after the irradiation to a fluence of $1 \times 10^{15} \text{ n}_{\text{eq}}/\text{cm}^2$. The current depends on the sensor thickness with the 50 μm thin sensor having the lowest current and the 293 μm thick sensor the highest. All curves have the typical square-root shape, but some show the beginning of a breakdown at higher voltages, indicated by an increasing current. At a fluence of $2 \times 10^{16} \text{ n}_{\text{eq}}/\text{cm}^2$ the currents, shown in Figure 6.7, are nearly linear with a good agreement for all thicknesses. Only the 50 μm sensor shows a beginning deviation for voltages higher than 400 V which is caused by the beginning breakdown. First indications of this have been observed at $1 \times 10^{16} \text{ n}_{\text{eq}}/\text{cm}^2$. This suggests that at very high fluences larger than approximately $1 \times 10^{16} \text{ n}_{\text{eq}}/\text{cm}^2$ the reverse current becomes independent

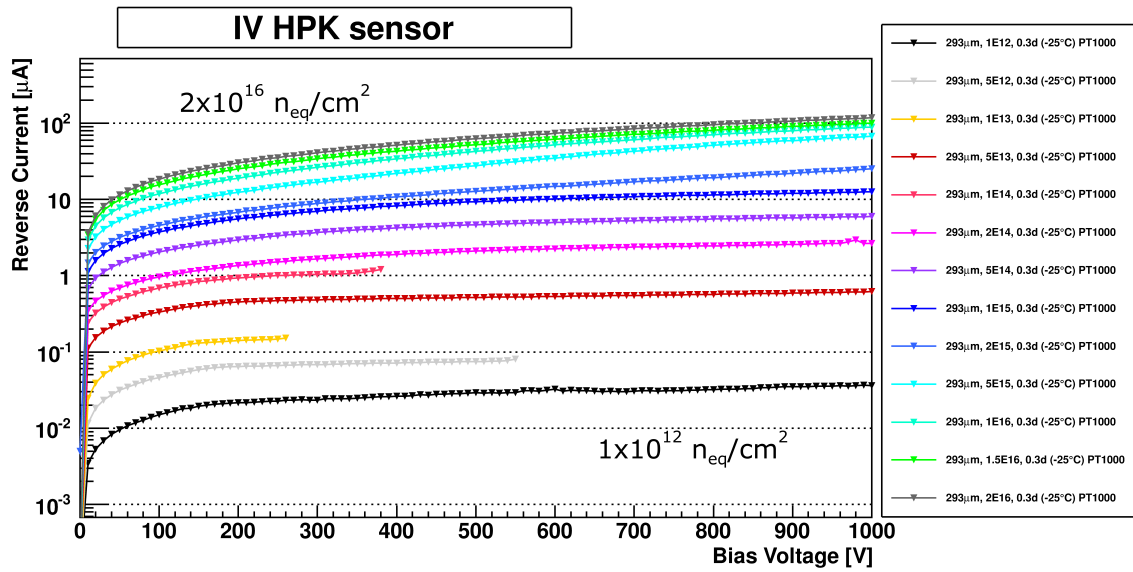


Figure 6.5.: Reverse bias current for HPK sensors after irradiation, scaled to -25°C . For three sensors (5×10^{12} , 1×10^{13} and $1 \times 10^{14} n_{\text{eq}}/\text{cm}^2$) a lower maximum bias voltage has been used due to the onset of breakdown. The sensors were measured after 0.3 d room temperature annealing.

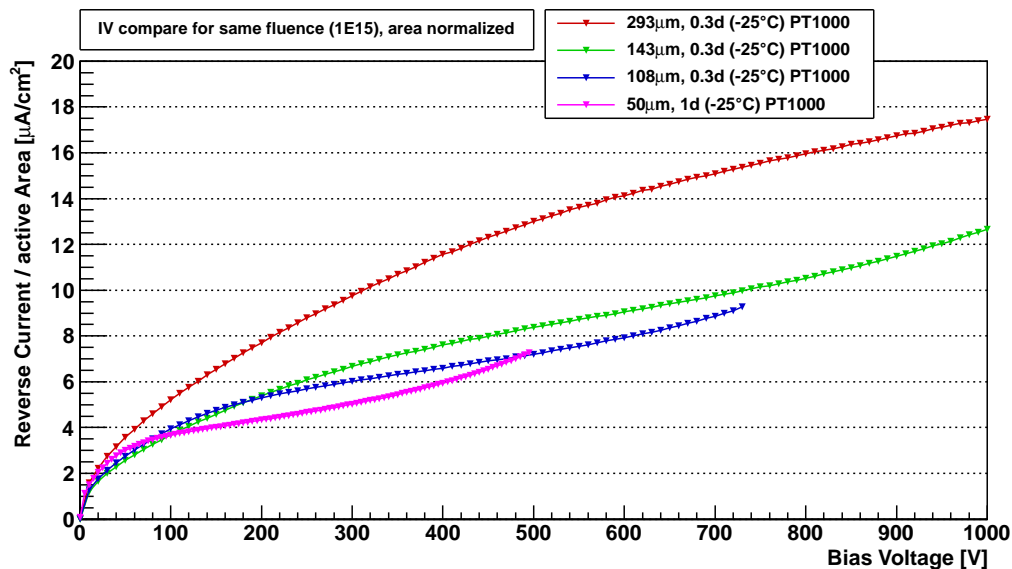


Figure 6.6.: Comparison of the reverse bias current per active sensor area after $1 \times 10^{15} n_{\text{eq}}/\text{cm}^2$ irradiation for different sensor thicknesses.

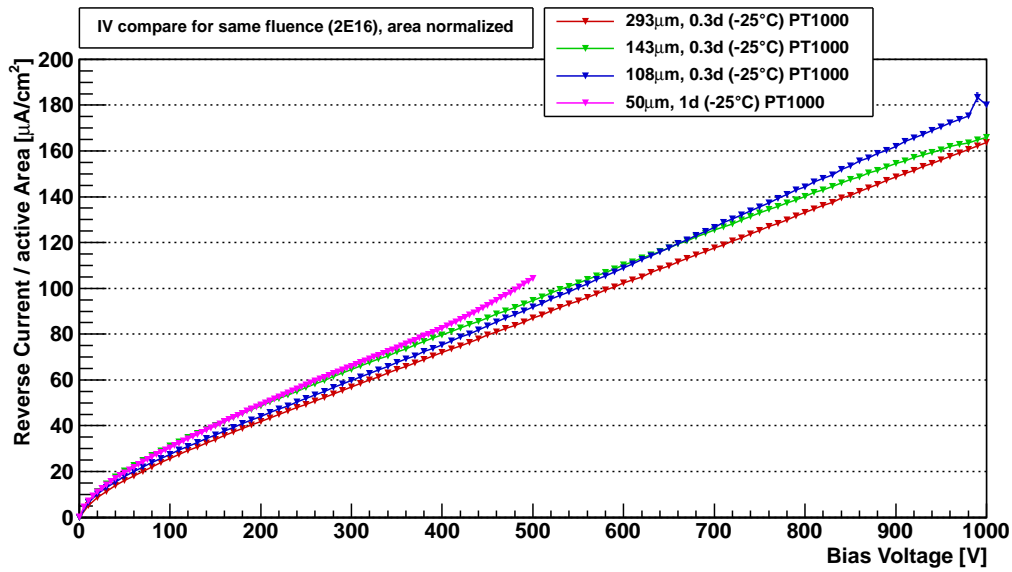


Figure 6.7.: Comparison of the reverse bias current per active sensor area after $2 \times 10^{16} \text{ n}_{\text{eq}}/\text{cm}^2$ irradiation for different sensor thicknesses.

of the sensor thickness for the observed voltage range.

The measurements after irradiation were done at an annealing time of 0.3 days and 1 day respectively at room temperature. This time was needed to attach the sensors to the PCBs. Further annealing at room temperature in a nitrogen cabinet has been done to total annealing times of 10 days and 30 days. After each annealing step the sensors have been measured in the cold IV system. Figure 6.8 shows as an example of the reverse bias current for the Hamamatsu sensor, irradiated to $1 \times 10^{15} \text{ n}_{\text{eq}}/\text{cm}^2$ at all annealing steps. It can be seen that the current decreases with increasing annealing time. This is expected from the theory and will be discussed in detail in section 6.5.

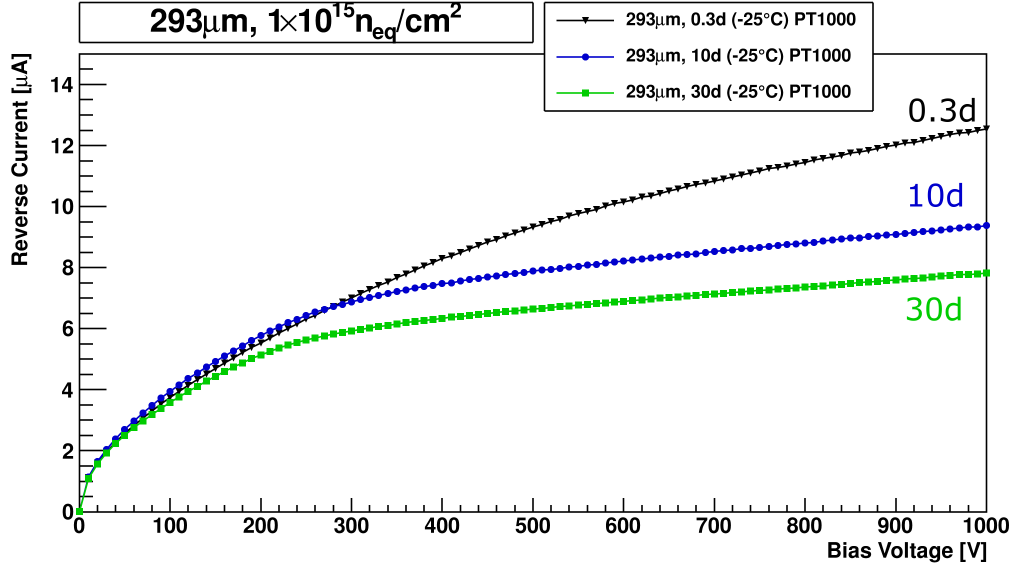


Figure 6.8.: Reverse bias current for the 293 μm thick Hamamatsu sensor, irradiated to $1 \times 10^{15} \text{ n}_{\text{eq}}/\text{cm}^2$ at all room temperature annealing steps (black: 0.3 d; blue: 10 d; green: 30 d).

6.4. Effective Energy

One of the main aims of this study was the calculation of the effective energy at highly irradiated silicon sensors. The best way would be to measure the current at several temperatures and use Equation 2.21 for a fit. This was not possible for the measurements with the old cold IV system. With the commercial freezer the temperature range was limited as well as the number of measurements. The coldest possible temperature was approximately -23°C . A second measurement was done at -19°C ¹, but higher temperatures would increase the risk of thermal runaway, especially for highly irradiated devices. Additionally the freezer needs a long time to change the temperature and taking more than two measurements would be unreasonable.

With only two measurements at two different temperatures it is possible to solve Equation 2.22 to get the effective energy. This leads to the following equations for the effective energy and its uncertainty:

$$E_{eff} = \frac{T_1 T_2 2k_B}{T_2 - T_1} \cdot [\ln(I(T_2)) - \ln(I(T_1)) + 2\ln(T_1) - 2\ln(T_2)],$$

$$\sigma_{E_{eff}}^2 = \left(\frac{T_1 T_2 2k_B}{T_2 - T_1} \right)^2 \cdot \left[\left(\frac{E_{eff}}{2k_B T_1} - 2 \right)^2 \frac{\sigma_{T_1}^2}{T_1^2} + \left(\frac{E_{eff}}{2k_B T_2} - 2 \right)^2 \frac{\sigma_{T_2}^2}{T_2^2} + \frac{\sigma_{I(T_1)}^2}{I(T_1)^2} + \frac{\sigma_{I(T_2)}^2}{I(T_2)^2} \right].$$

¹For low fluences ($< 1 \times 10^{15} \text{ n}_{\text{eq}}/\text{cm}^2$) measurements were done at -15°C as well, but only for the proton irradiated HPK sensors after 0.3 d annealing.

σ_{T_1} and σ_{T_2} (temperature uncertainties) are set to 0.01 K because of the temperature measurement method², while the current uncertainties are obtained from the measurements with the LabVIEW program. The uncertainty of the Boltzmann constant has been neglected because the relative uncertainty is much smaller in comparison with the other values.

Figure 6.9 shows two graphs from the effective energy analysis. For each voltage step of the measurement the E_{eff} value was calculated and plotted (left). Two horizontal lines are used as reference, with the green line at the literature value of 1.214 eV [Chi13] and the blue line at 1.0 eV. This example shows the HPK sensor irradiated to $5 \times 10^{13} \text{ n}_{eq}/\text{cm}^2$ after irradiation and it can be seen that the effective energy is in good agreement with the literature value. The voltage range can be limited by applying a minimum and maximum value where only the voltages in-between were used for the analysis. This is necessary for some samples which showed increases or decreases at low or high voltages. For example at high voltages a beginning thermal runaway at the higher temperature could cause divergent effective energy values. The average E_{eff} value and its uncertainty were calculated for all valid data-points according to the following equations:

$$\overline{E_{eff}} = \frac{1}{N} \sum_{i=1}^N E_{eff,i} \quad \text{and} \quad \sigma_{\overline{E_{eff}}} = \sqrt{\frac{1}{N \cdot (N-1)} \sum_{i=1}^N (E_{eff,i} - \overline{E_{eff}})^2}$$

where $E_{eff,i}$ being the effective energy at the i^{th} valid voltage step and N the number of valid data-points. Some fluctuations can be seen in the effective energy. By comparing the shape with the temperature graph (centre) it can be seen that there is a correlation. The lowest temperature is stable, while the higher temperature fluctuates due to the freezer being switched off and on to reach the desired temperature

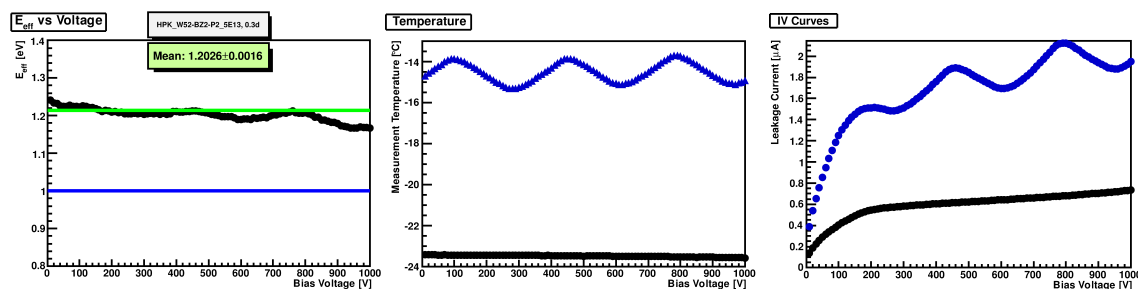


Figure 6.9.: Example of the effective energy calculation for the HPK sensor irradiated to $5 \times 10^{13} \text{ n}_{eq}/\text{cm}^2$ after 0.3 d annealing. The left graph shows E_{eff} for each voltage while the central graph shows the temperature measurements for the two set values (-23°C in black and -15°C in blue). The oscillations of the blue curve are caused by the temperature controller of the freezer. This can also be seen in the reverse bias graph on the right side.

²Measurement of PT1000 resistance and conversion to temperature value, see section 6.1).

value. These fluctuations are also visible in the effective energy graph because of the temperature induced current change, as can be seen in the right graph which shows the measured reverse bias current.

In a second analysis step all E_{eff} values are filled into a histogram (Figure 6.10) and fitted with a Gaussian distribution using ROOT:

$$f(x) = \frac{A}{\sqrt{2\pi}\sigma} \cdot \exp\left(-\frac{(x-\mu)^2}{2\sigma^2}\right) \quad (6.3)$$

with the mean value μ , the standard deviation σ and a scaling constant A . This method has been implemented to take small changes in the effective energy into account. Comparing the values from this example it can be seen that the uncertainty of the average ((1.2026 ± 0.0016) eV) is much smaller than that of the Gaussian fit³ ((1.205 ± 0.012) eV). Also with this fit, it was possible to incorporate a fast increase at small voltages before the minimum cut was implemented. Both effective energy values were stored to be used in further analysis steps.

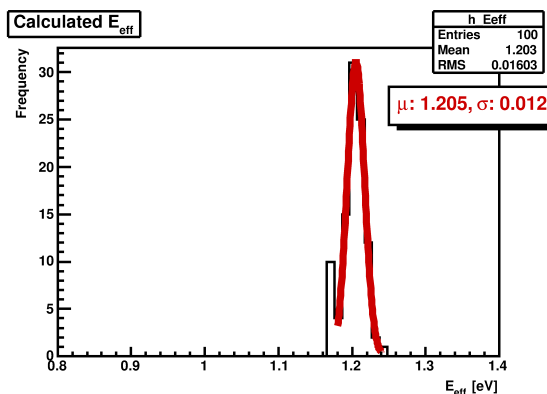


Figure 6.10.: For the example analysis all E_{eff} values are filled into a histogram and fitted with a Gaussian distribution.

The shown example represents one of the ‘well-behaved’ graphs, but this was not always the case. Figure 6.11 shows an example with an ‘ill-behaved’ effective energy graph. In this case the Gaussian fit has not worked. If the fit does not result in an effective energy value between 0.5 eV and 1.5 eV the average value was stored instead.

In the next analysis step all effective energy values for one sensor type are plotted against the irradiation fluence. Figure 6.12 shows the graphs directly after irradiation with a fluence uncertainty of 10%. For each of the two E_{eff} values per fluence a separate graph is used: the pictures on the left side show the average E_{eff} values

³This is caused by the definition of the two uncertainties: For N measurement values $\sigma_{\overline{E_{eff}}} = \sigma_{\text{Gauss}}/\sqrt{N}$.

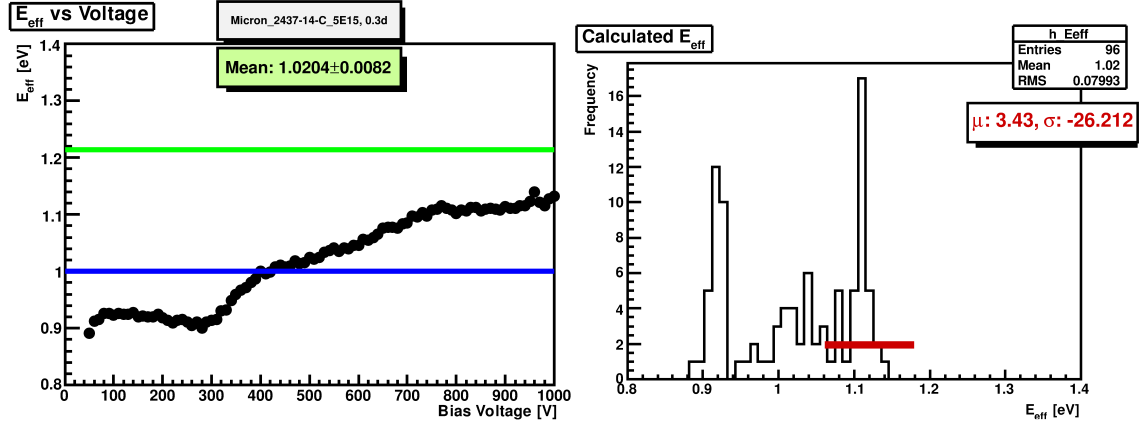


Figure 6.11.: ‘Ill-behaved’ example for an effective energy plot for a Micron sensor irradiated to $5 \times 10^{15} \text{ n}_{\text{eq}}/\text{cm}^2$ and annealed to 0.3 d. The histogram on the right side shows a random distribution where the Gaussian fit has not worked (horizontal red line).

and on the right side the Gaussian fit results are used. Each sensor thickness is shown in a separate figure. From previously published measurements of irradiated samples it has been shown that the effective energy is independent of the irradiation fluence at a constant value of $(1.214 \pm 0.014) \text{ eV}$ [Chi13] up to approximately $1 \times 10^{15} \text{ n}_{\text{eq}}/\text{cm}^2$, but the graphs here show that E_{eff} decreases at higher fluences.

The graphs were then fitted with straight lines for the constant part up to approximately $1 \times 10^{15} \text{ n}_{\text{eq}}/\text{cm}^2$ and the decreasing part at higher fluences. Because the x-axis was plotted logarithmically the following function has been used for the fit:

$$E_{\text{eff}}(\Phi) = a - b \cdot \log_{10}(\Phi)$$

The intersection of the two lines has been calculated to determine the point at which the decreasing part starts. For each graph the fit range has been chosen by hand to get the best results. Additionally the weighted mean has been calculated according to:

$$\overline{E_{\text{eff},w}} = \frac{\sum_i E_{\text{eff},i} / \sigma_{E_{\text{eff},i}}^2}{\sum_i 1 / \sigma_{E_{\text{eff},i}}^2} \quad \text{and} \quad \sigma_{\overline{E_{\text{eff},w}}} = \frac{1}{\sqrt{\sum_i 1 / \sigma_{E_{\text{eff},i}}^2}}.$$

and is shown as dashed horizontal line in the figures. While the fit results have been used in the later analysis, the weighted mean was only calculated for these graphs because it does not represent the measurement results for the full fluence range.

The plots in Figure 6.13 contain all effective energy values after irradiation, separated by the analysis method Average and Gaussian. For completeness the $50 \mu\text{m}$ thick sensors have been added to the graphs, but not been included in the analysis. As the graphs for only one detector type they have been fitted with the two straight

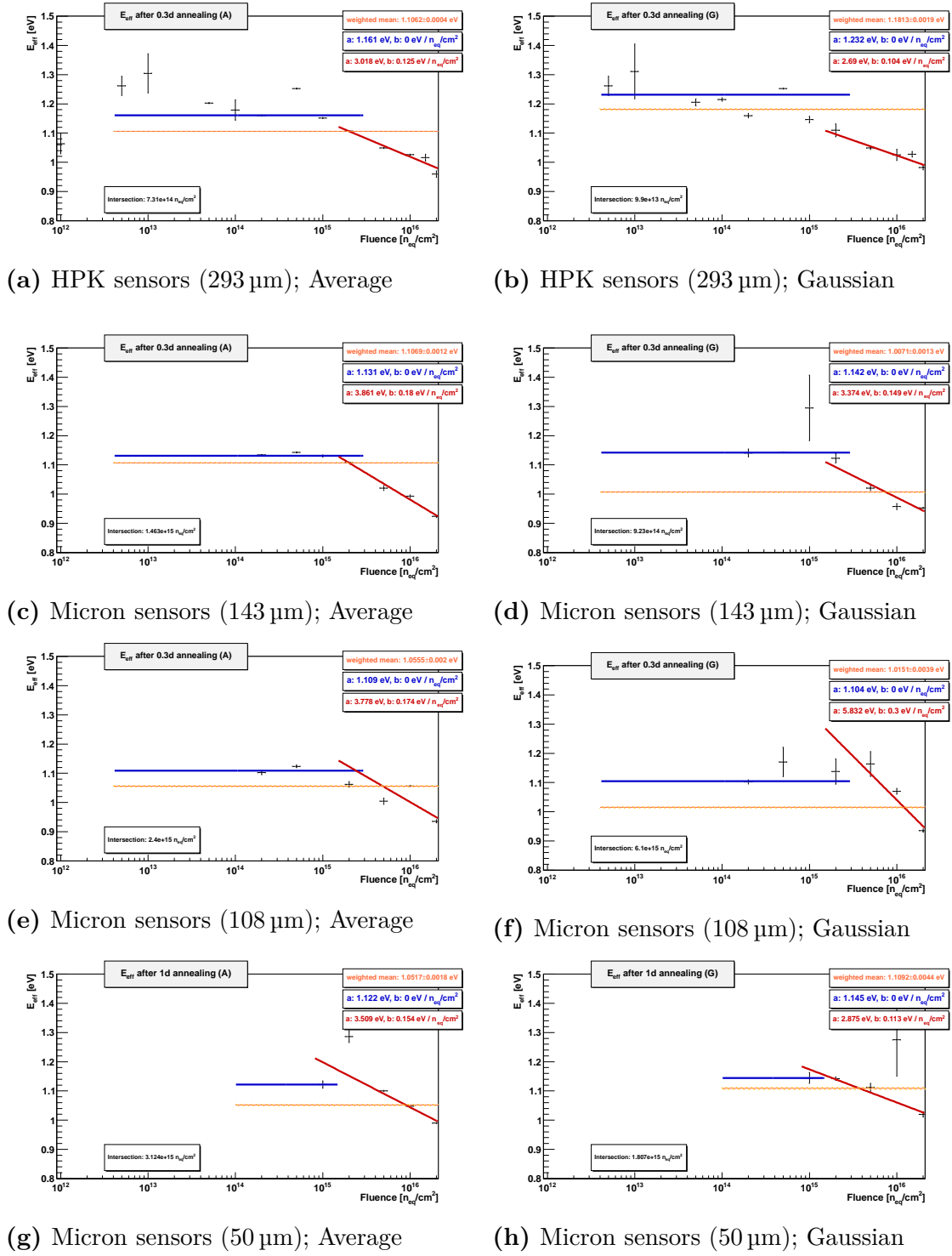


Figure 6.12.: Effective energy values plotted against irradiation fluence for each sensor type and the two E_{eff} values from the analysis (Average and Gaussian) after 0.3d room temperature annealing. The data points are fitted with a constant value for low fluences and a straight line for high fluences. The dashed horizontal line represents the weighted mean.

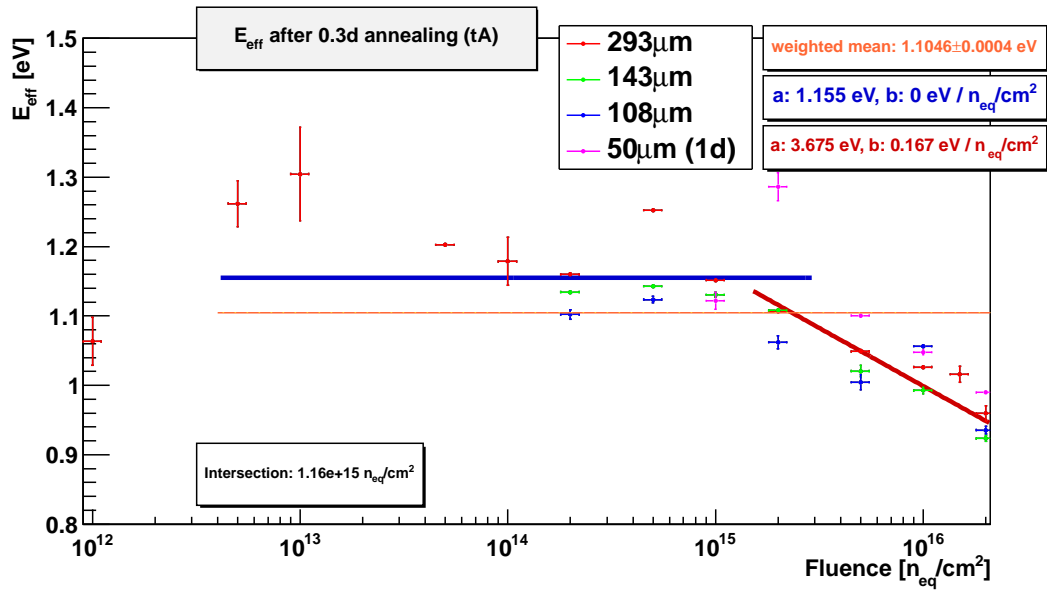
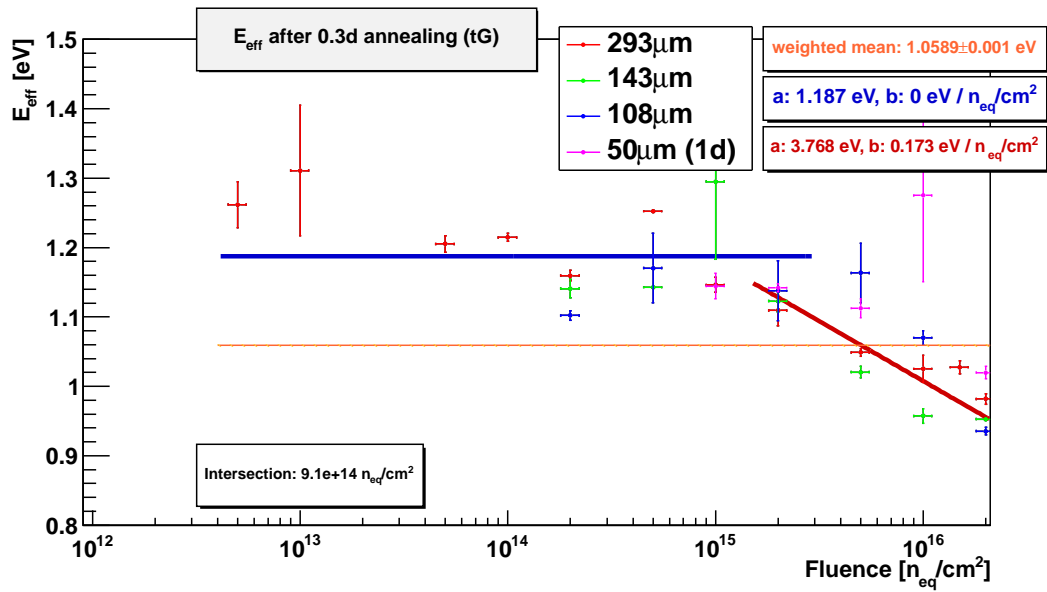
lines. It can be seen that the decrease of the effective energy at high fluences follows the same trend for all samples and there is in general a reasonable agreement.

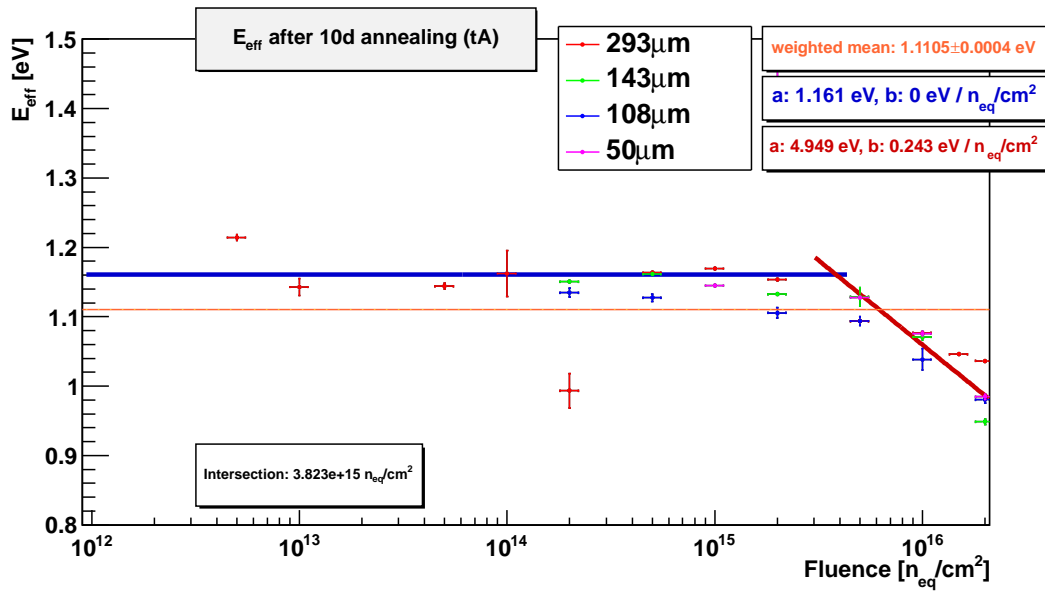
This behaviour is consistent for all annealing steps, as can be seen in Figure 6.14. Table A.6 in the appendix summarizes the fit results for all annealing times. The average E_{eff} values all follow the same trend. With increasing annealing time the effective energy of the high fluence sensors increase slightly from approximately 0.94 eV at 0.3 d to approximately 1.1 eV at 30 d. In general the spread of the different thicknesses at one fluence is smaller after annealing. The sensor thickness appears to have no influence on the calculated effective energy.

One possible explanation for the decrease of the effective energy could be a wrong temperature measurement. The temperature sensor is glued to the silicon sensor to measure this temperature as precisely as possible. By applying a high bias voltage with a significant current the generated power increases the sensor temperature. The cold air in the freezer is blown at the PCB to cool it. Especially at high fluences and high voltages the generated electrical power results in a measurable temperature increase. Because the temperature sensor is exposed to the cooler air at the same time this might result in a measured temperature that is lower than the silicon temperature.

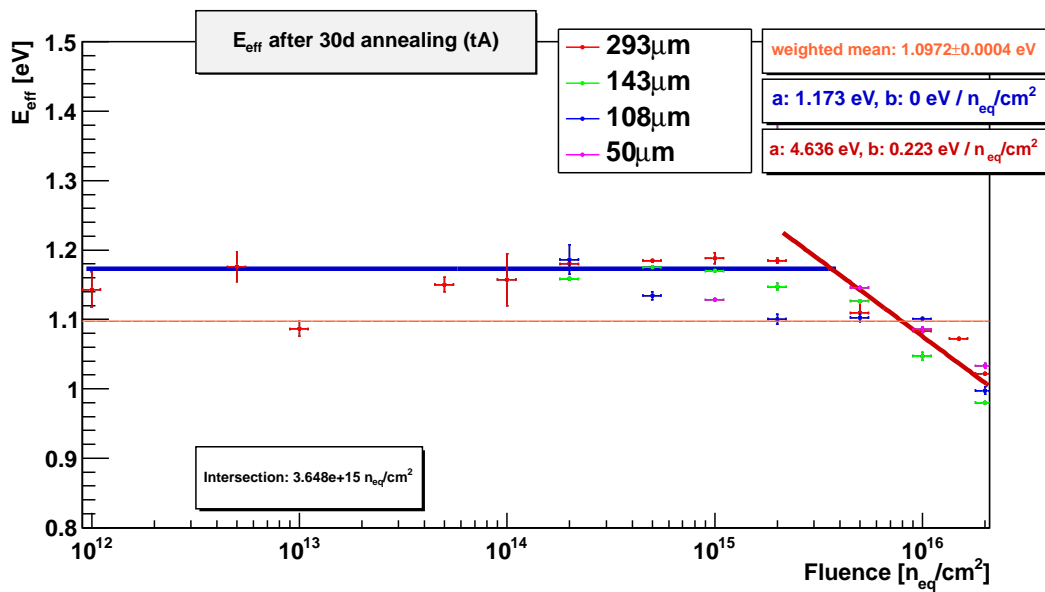
To look into this in detail a contour plot has been generated in which the deviation of the effective energy is shown for deviations from the measured temperatures. This is done by using Equation 2.22. With the fixed values for $T_1 = -20^\circ\text{C}$, $T_2 = -23^\circ\text{C}$ and $I_1 = 20 \mu\text{A}$ the current I_2 has been calculated to $13.987 \mu\text{A}$ assuming an effective energy of 1.214 eV. Then the temperatures have been varied up to $\pm 2^\circ\text{C}$ in small steps for each axis to get a smooth contour plot, shown in Figure 6.15. Assuming a calculated effective energy of approximately 1 eV this would be represented in the graph by the transition region between green and cyan. If for example the measured temperature T_1 was -20°C due to the freezer environment but the real sensor temperature is higher, this would decrease the effective energy even further (indicated by the arrow pointing to the right). Furthermore if T_2 is too cold as well an increase would increase E_{eff} (upwards pointing arrow). To reach the literature value of 1.214 eV the temperature difference between measurement and sensor temperature of T_2 has to be much larger than the difference of T_1 . In the shown example a increase of T_1 of approximately 0.6°C would require an increase of T_2 of approximately 1°C to get the literature effective energy. But the current is lower at the lower temperature which result in less electric power generated in the silicon sensor and therefore less self-heating. The intuitive assumption would be that at the higher temperature more power is generated and therefore the temperature difference between environment and silicon is higher, resulting in a larger measurement difference. As stated in this example, this would decrease the calculated effective energy even further.

An additional factor has to be taken into account: the freezer temperature. While it is stable for the lowest temperature, it has been shown that the temperature oscillates for higher temperatures due to the control system, as discussed in subsection 3.1.2.

(a) Average E_{eff} values.(b) Gaussian E_{eff} values.**Figure 6.13.:** E_{eff} values after 0.3 d annealing for all sensor thicknesses.



(a) Average E_{eff} values after 10 days annealing.



(b) Average E_{eff} values after 30 days annealing.

Figure 6.14.: Average effective energy for all sensor types after 10 and 30 days of room temperature annealing.

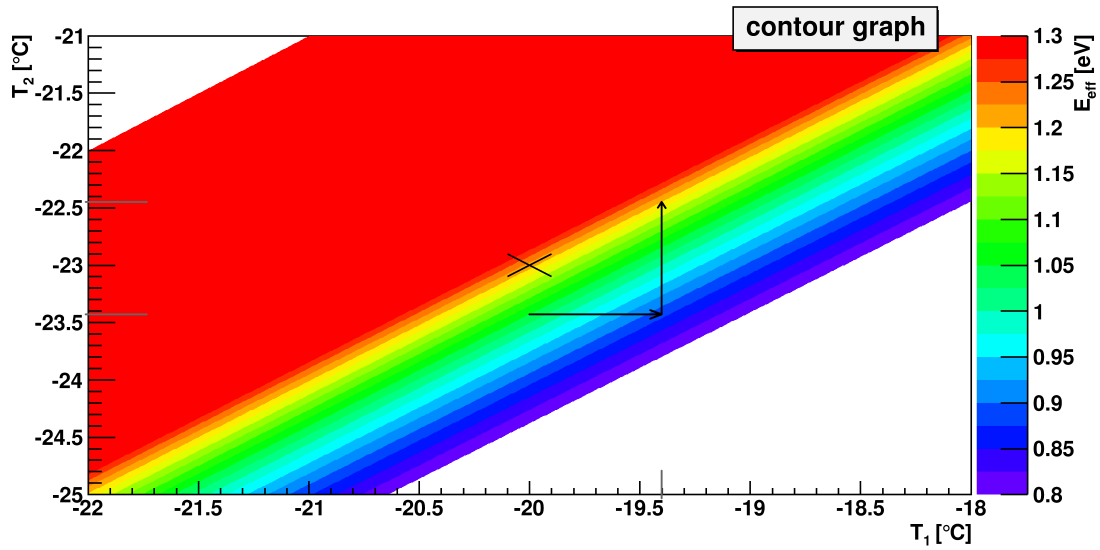


Figure 6.15.: Contour plot to show effective energy variations for temperature variations. The cross marks the initial values where $E_{eff} = 1.214$ eV. For this figure I_1 and I_2 are fixed.

An example is shown in Figure 6.16 for the $293\mu\text{m}$ thick sensor irradiated to $1 \times 10^{16} \text{ n}_{eq}/\text{cm}^2$ and annealed for 0.3 days. The effective energy is fairly constant with an average value of (1.026 ± 0.001) eV, only a small decrease with increasing bias voltage can be seen. While the lower temperature only shows a small increase with increasing voltage due to self heating, the temperature graph for the higher set value shows the oscillations from the freezer and a large decrease from 800 V onward. The temperature has a clear structure, but this has no visible effect on the effective energy which indicates that the value is not, or not only, caused by a wrong temperature measurement. In a previous case (Figure 6.9) changes in the effective energy have corresponded to temperature changes, but the changes were less than 0.05 eV.

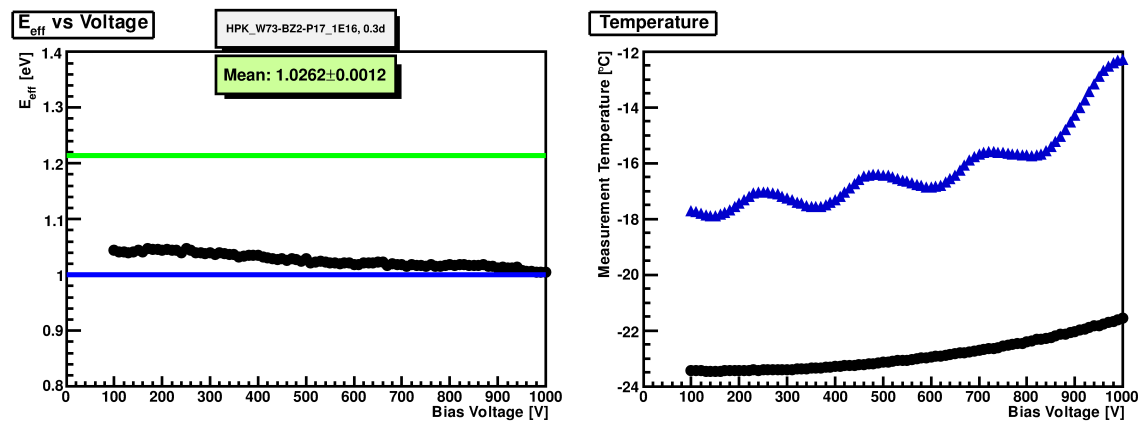


Figure 6.16.: Effective energy (left) and temperature (right) for the $293\ \mu\text{m}$ thick sensor, irradiated to $1 \times 10^{16}\ \text{n}_{\text{eq}}/\text{cm}^2$ and annealed to 0.3 days.

6.5. Current Related Damage Rate

The fluence dependence of the reverse bias current, parametrized in Equation 2.24, requires the knowledge of the depleted volume. For a fully depleted sensor this can be calculated from the thickness and the area. But the area, that has to be used in this case, is not the one defined by the bias ring. The capacitance of large size HPK sensors ($\approx 10 \times 10\ \text{cm}^2$) and mini sensors ($\approx 1 \times 1\ \text{cm}^2$) from the same wafer have been measured. This allowed the comparison of the capacitance per area for both samples. For the large sensor the difference between the physical area and the area defined by the bias ring is small, therefore the effect on the capacitance-per-area value is negligible. But for the small sensor this is significant. It has been shown that the the capacitance-per-area value for the bias ring area is too small compared with the large sensor, but the physical area is too large. Calculating the required area and comparing it with the sensor structure has shown that the active area is enclosed by the guard ring. These results have been used to calculate the active area for the Micron sensors as well. Table 6.1 summarizes the sensor properties of the used devices.

An unknown parameter is the depleted depth. The full depletion voltage can be determined from CV measurements (2.2.2), but it increases with increasing irradiation fluence. For very high fluences the expected full depletion voltage exceeds 1000 V, which is the limit of the power supply. To calculate the current related

Manufacturer	Sensor Thickness [μm]	Active Area [cm^2]
Micron	50, 108, 143	1.0985×1.0973
HPK	293	0.8348×0.8600

Table 6.1.: Active Area for all sensor types.

damage rate α only the currents should be used for voltages higher than the full depletion voltage. Furthermore another fact needs to be taken into account: in a partially depleted sensor the depleted region is defined as the region with an electric field. From edge TCT measurements it has been shown that this definition can not be used for highly irradiated silicon sensors because there is a measurable electric field in the whole sensor [Kra14]. Instead of using the full depleted volume in the following analysis, the geometric volume, calculated from the sensor thickness and the active area, has been used to calculate the geometric current related damage rate α^* . If the depleted volume is equal to the geometric volume (sensor fully depleted) then α should be equal to α^* .

To compare the measurement values with the literature value it is necessary to scale the currents to 21 °C. By plotting $\Delta I/V$ as function of the fluence it is possible to get the geometric current related damage rate from a straight line fit (see Equation 2.24). Because the reverse bias current of the 50 μm thick sensors shows an earlier breakdown before irradiation, this would influence the analysis. Therefore instead of using ΔI only the current after irradiation was used, which has no negative effects as the current before irradiation is at least two orders of magnitude smaller. In the standard literature the fit is done at the full depletion voltage. Because this is not known for high fluences, the α^* value has been calculated for each measured voltage. This allows to plot graphs with α^* as function of the bias voltage and compare the results with the literature values. A discrimination between low(medium) and high fluence has been done as well. The low fluence region was fitted up to $2.1 \times 10^{15} \text{ n}_{\text{eq}}/\text{cm}^2$ to include the values at $2 \times 10^{15} \text{ n}_{\text{eq}}/\text{cm}^2$, whereas the high fluence fit starts at $4 \times 10^{15} \text{ n}_{\text{eq}}/\text{cm}^2$. This separation was based on the HPK overview graph (see Figure 6.17) where a different slope at high fluences can be seen.

The equations in section 2.4.3 allow the calculation of the literature values for the current related damage rate for short-term and long-term annealing. With the known uncertainties of the parameter for the short term current related damage rate (see Equation 2.25), the uncertainty can be calculated with:

$$\sigma_{\alpha}^2 = \alpha^2 \left(\frac{\sigma_{\alpha_{\infty}}}{\alpha_{\infty}} \right)^2 + \sum_i \left[\alpha_{\infty} \frac{b_i}{b_{\infty}} \exp\left(-\frac{t}{\tau_i}\right) \left(\frac{\sigma_{b_i}}{b_i} \right) \right]^2 + \sum_i \left[\alpha_{\infty} \frac{b_i}{b_{\infty}} \exp\left(-\frac{t}{\tau_i}\right) \left(\frac{t}{\tau_i} \right) \left(\frac{\sigma_{\tau_i}}{\tau_i} \right) \right]^2 + \alpha^2 \left(\frac{\sigma_{b_{\infty}}}{b_{\infty}} \right)^2$$

For the long-term value of alpha (Equation 2.26) there are no uncertainties of the given parameters, but it is possible to use the average values of α_I and β as well as

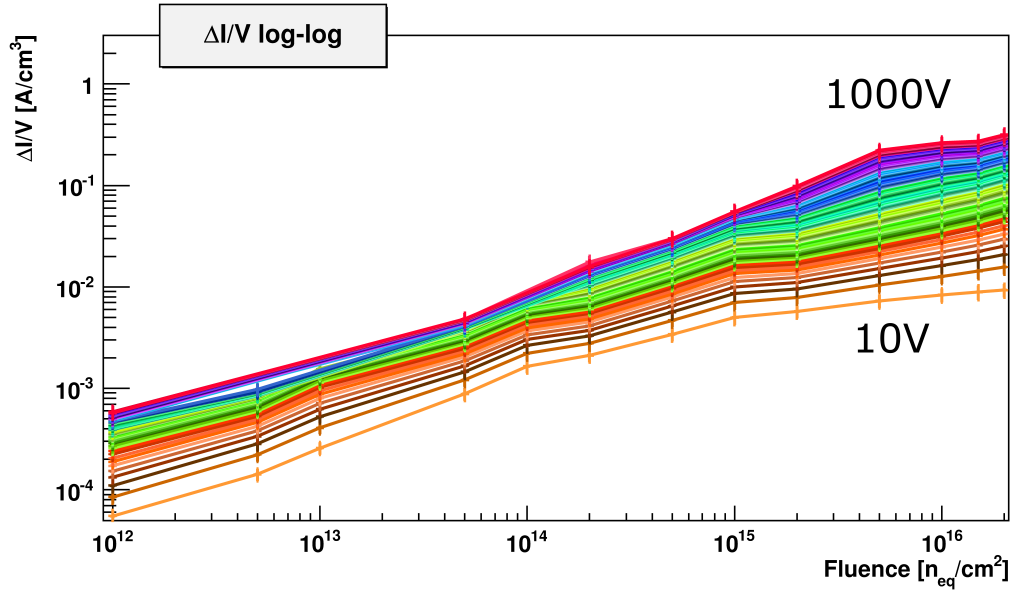


Figure 6.17.: $\Delta I/V$ vs Φ of the HPK sensors (0.3 d annealing) in a double logarithmic plot for a better overview (V is the full volume, not the depleted volume). The voltages are colour coded with the lowest voltage at the bottom and the highest voltage at the top. A difference in slope for low fluences (up to $2 \times 10^{15} \text{ n}_{\text{eq}}/\text{cm}^2$) and high fluences (from $5 \times 10^{15} \text{ n}_{\text{eq}}/\text{cm}^2$) can be seen.

the parametrization of α_0 to get a rough estimate.

$$\sigma_\alpha = \sqrt{\left(\exp\left(-\frac{t}{\tau_I}\right)\sigma_{\alpha_I}\right)^2 + (\sigma_{\alpha_0})^2 + \left(\ln\left(\frac{t}{t_0}\right)\sigma_\beta\right)^2}$$

With these equations and 2.25, 2.26 as well as the parameters given in Table 2.4 the expected literature values for α at different room temperature annealing steps can be calculated (see Table 6.2).

Annealing Time	α short-term [$\times 10^{-17} \text{ A/cm}$]	α long-term [$\times 10^{-17} \text{ A/cm}$]	α long-term (average) [$\times 10^{-17} \text{ A/cm}$]
0.3d	6.42 ± 0.43	6.25	6.06 ± 0.14
1d	5.78 ± 0.39	5.79	5.62 ± 0.15
10d	4.32 ± 0.29	4.36	4.24 ± 0.18
30d	3.50 ± 0.24	3.61	3.52 ± 0.20

Table 6.2.: Expected literature values for α at different room temperature annealing steps.

The values for short-term and long-term annealing agree within the uncertainties

for all annealing stages. Because the long-term parametrization should only be used for room temperature annealing times longer than one year, the short-term literature values were used for the comparison.

In section 6.4 it has been shown that the effective energy can be calculated in different ways from the measurement data. The current has to be scaled to calculate α^* , therefore the choice of E_{eff} affects the result. Different E_{eff} values have been used for the analysis:

- Literature Value (1.214 ± 0.014) eV
- Calculation, individual for each device
 - Average value
 - Gaussian fit value
- Fit of the E_{eff} values for each individual sensor type and all fluences with two straight lines
 - Data from average values
 - Data from Gaussian values
- Fit of all sensors and all fluences at one annealing time
 - Data from average values
 - Data from Gaussian values

All seven combinations have been used to calculate the geometric current related damage rate and will be presented. Using the fitted data allows the effective energy to be calculated at any fluence because the function parameters are known. In the E_{eff} fits a separation between the constant part and the decreasing part has been made. When calculating the effective energy from the fit the intersection point of the two lines has been used to define which fit function represents the data.

0.3 days Figure 6.18 shows the geometric current related damage rate α^* where the current, measured after irradiation, has been scaled with the different effective energy values. For the first graph (Figure 6.18a) the literature value has been used. The low fluence α^* values of the 108 μm and 143 μm thick sensors exceed the expected literature value for voltages higher than approximately 400 V, where as the 293 μm thick high fluence sensors show the lowest α^* values and did not reach the literature value at any voltage. Some curves (293 μm low fluence, 143 μm high fluence and 108 μm high fluence) reach the expected literature value at high voltages. The results of the 293 μm thick sensors is as expected because at low fluences the sensors should be fully depleted while the high fluence sensors would not be and will therefore have a lower α^* . The other sensor geometries do not show the expected behaviour as the low fluence values exceed the literature value with increasing voltage. It could be

assumed that this is based on the usage of an unsuitable effective energy value for the current scaling, especially at high fluences.

The 293 μm graph shows steps at 260 V, 360 V and 560 V. This is based on the current measurements where three sensors reached the voltage limit at these values (see Figure 6.5) due to a breakdown. At each of these steps the total number of sensors reduced by one, which affected the fit and resulted in the steps.

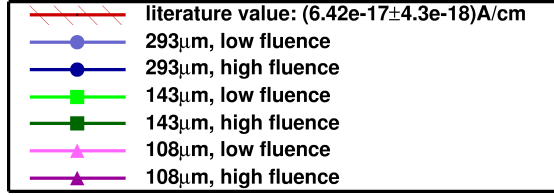
For Figure 6.18b the individual average effective energy from the measurements was used to scale the current. The 293 μm low fluence curve has not changed much in shape, only the steps disappeared and the values are a bit smaller. The high fluence graph for this sensor type decreased by approximately a factor two. A larger difference can be seen for the other sensor types. The low fluence graphs got closer to the 293 μm graph and α^* exceeds the literature value only for voltages higher than 700 V. The high fluence graphs decrease significantly and a clear hierarchy can be seen: with increasing sensor thickness the geometric current related damage rate decreases. A possible explanation is the depleted volume: if the depleted depth is the same for all sensors because of the radiation damages, then the percentage of depleted volume is higher for thinner sensors and therefore α^* should be closer to α .

When using the effective energy from the individual Gaussian fits (Figure 6.18c) some differences can be seen, in particular for the 108 μm thick devices. The low fluence graph has much larger error bars which is caused by the poor Gaussian fits and the values are higher compared to the average method. Additionally the high fluence graph is significantly lower, and at high voltages is between the 293 μm and 143 μm graphs. Using the individual Gaussian values shows no advantage compared to the individual average values. On the contrary, some error bars increase and the high fluence graphs show a counter-intuitive behaviour.

It has been shown in the previous plots (Figure 6.13) that individual effective energy values can differ from the general trend at some fluences. To take this into account the straight line fits were done and the results have been used to generate graphs with the geometric current related damage rate. Because of these fluctuations the uncertainties of the fit parameters are significant and therefore result in large error bars of α^* . To give a better overview the error bars in the graphs, where straight line fit results have been used, were always scaled with a factor 0.2.

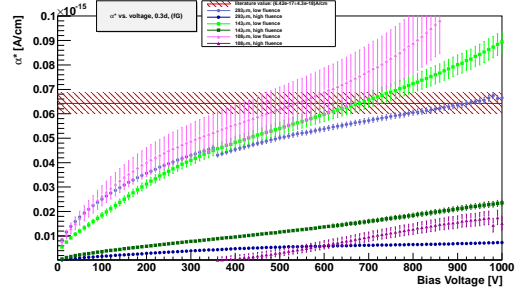
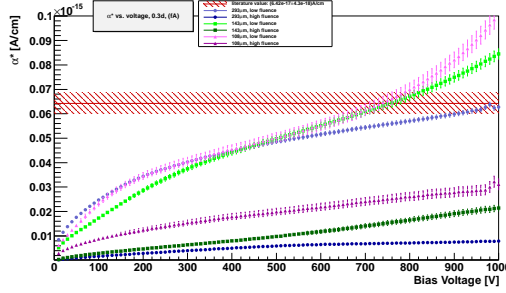
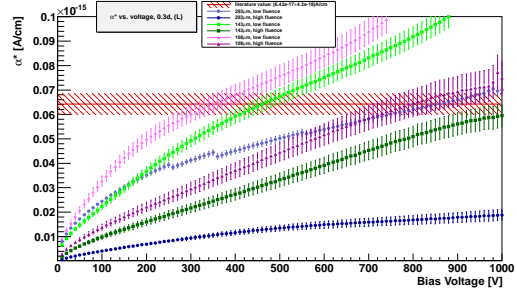
Figure 6.18d shows the graphs when using the fit of the individual average values. Even though the error bars are reduced by a factor of five, they are larger than in the previous graphs. The data follow the previously observed trend, but a slight shift compared to the individual average graph (Figure 6.18b) can be seen. The difference compared to the fit from the Gaussian E_{eff} values (Figure 6.18e) is significant.

The last method to obtain a value for the effective energy was to fit the results from all sensor types. Figure 6.18f shows the results for α^* for the average values: some differences to the graph from the individual average values can be seen, but the



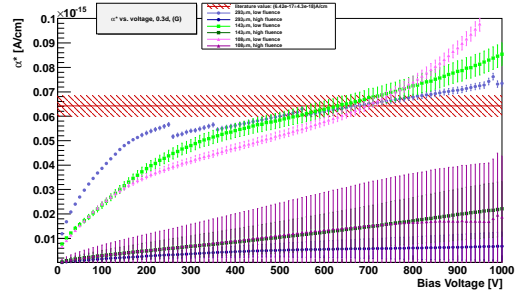
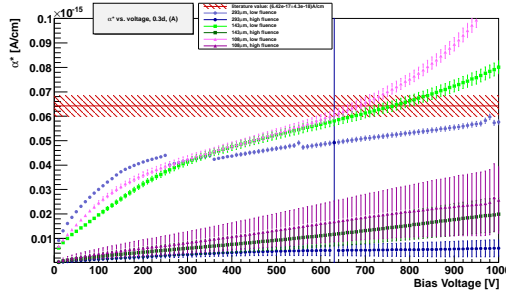
low fluence: $\Phi_{eq} \leq 2 \times 10^{15} \text{ n}_{eq}/\text{cm}^2$
 high fluence: $\Phi_{eq} \geq 5 \times 10^{15} \text{ n}_{eq}/\text{cm}^2$

Legend



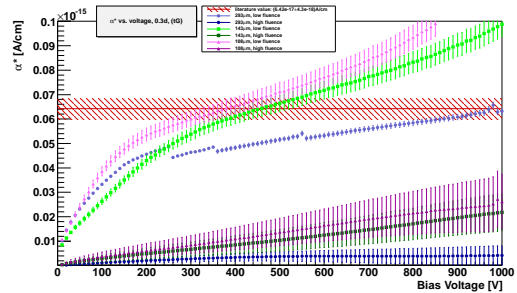
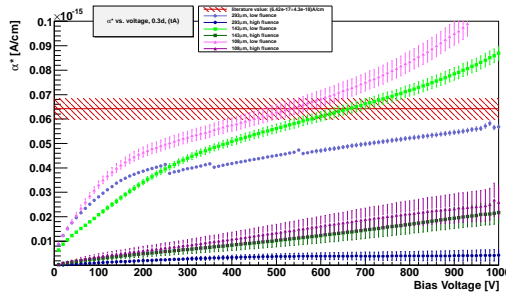
(b) E_{eff} : individual, Average.

(c) E_{eff} : individual, Gaussian.



(d) E_{eff} : fit same sensor types, Average.

(e) E_{eff} : fit same sensor types, Gaussian.



(f) E_{eff} : fit all sensors, Average.

(g) E_{eff} : fit all sensors, Gaussian.

Figure 6.18.: Geometric current related damage rate α^* with the current scaled by different methods, measured directly after irradiation (0.3 d room temperature annealing). For 6.18d and 6.18e the effective energy was obtained by fitting the values at different irradiation steps individually for each sensor type. The E_{eff} values for the graphs 6.18f and 6.18g were obtained by fitting the values of all sensors.

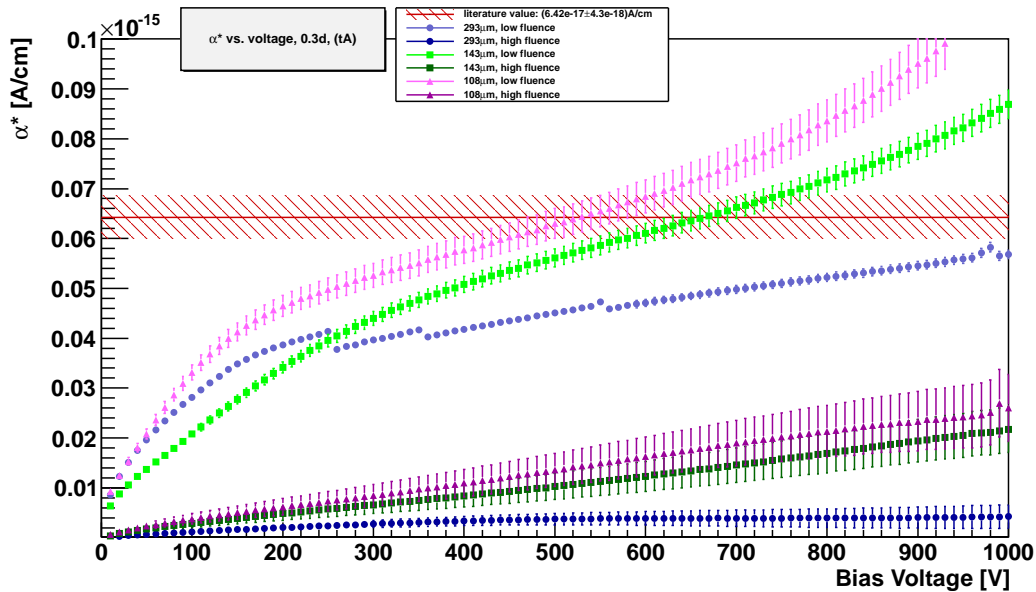


Figure 6.19.: Geometric current related damage rate after 0.3 days annealing with E_{eff} (average) from the fit of all sensors.

general trend is comparable. A comparison with the Gaussian data (Figure 6.18g) shows a good agreement between both graphs.

It has been shown that when using the effective energy values from the data analysis a clear difference between low fluence and high fluence can be seen. While the geometric current related damage rate for low fluences reaches the literature value for higher voltages, the values at high fluences are clearly smaller than expected. In all graphs α^* increases with increasing voltage which would be classically explained by an increasing depletion depth. For the high fluence samples a hierarchy can be seen where the thinnest sensor has the highest geometric current related damage rate. When using the straight line fits to determine the effective energy the results are large error bars of α^* . Using the average E_{eff} values for the IV scaling yield in more consistent results.

For all further comparisons the used effective energy will be the one obtained by fitting all average values. The difference to the other E_{eff} values is small (with the exception of the literature value). Although the uncertainties are larger compared to the individual values, the fit can accommodate outliers of individual sensors better and the results are therefore more significant. Figure 6.19 shows a larger version of Figure 6.18f to see the details better.

1 day The only sensors which had an annealing time of 1 day were the 50 μm samples. In Figure 6.20 the current related damage rate is shown. The high fluence part follows the expected trend and nearly reaches the expected literature value at

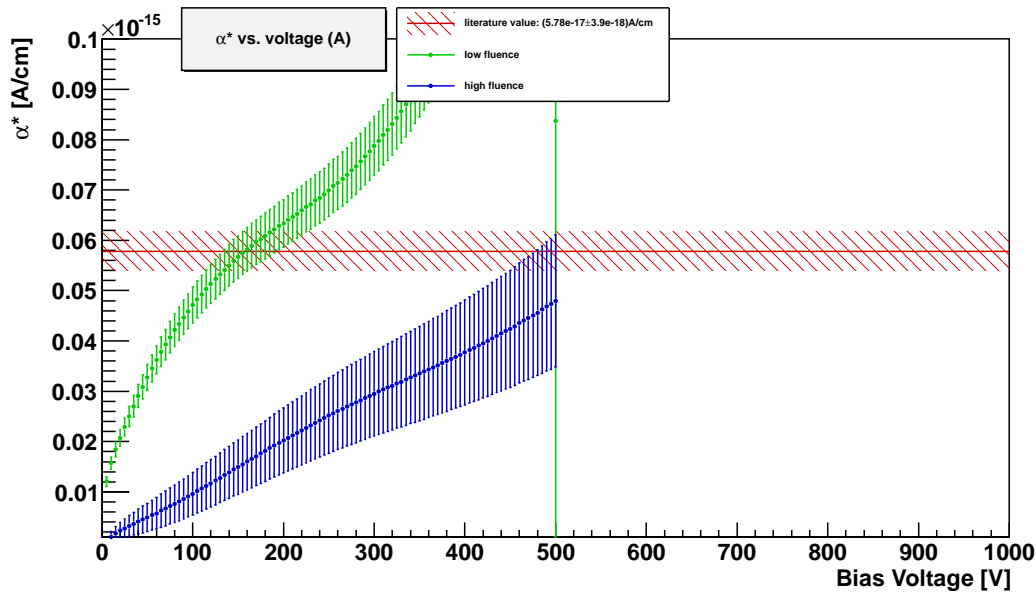


Figure 6.20.: Geometric current related damage rate for 50 μm sensors with current scaled by the fitted average values of the effective energy after 1 day annealing.

the highest voltage. For the low fluence a steep increase is visible, which is calculated from the data points after the irradiation to $1 \times 10^{15} \text{ n}_{\text{eq}}/\text{cm}^2$ and $2 \times 10^{15} \text{ n}_{\text{eq}}/\text{cm}^2$. With only two points, small deviations in the current result in huge deviations in α^* . In this case the currents at $2 \times 10^{15} \text{ n}_{\text{eq}}/\text{cm}^2$ are much higher than for the next higher and next lower fluence.

10 days All sensors have been annealed to a total annealing time of 10 days at room temperature and the geometric current related damage rate is shown in Figure 6.21. The low fluence graphs reach the literature value for all sensor thicknesses and even exceed them. Looking at the shape, it can be seen that after a steep increase for low voltages the gradient decreases which would indicate a plateau with only a small increase for increasing voltage. While the 108 μm and 143 μm sensors exceed the literature value, the 293 μm sensors show a development that would be expected: at low voltages most of the sensors are not fully depleted and therefore with increasing depletion depth α^* increases highly. When most sensors are fully depleted α^* drops and to the observed plateau. The resumed increase of the 108 μm graph could indicate a beginning breakdown, which could also explain the shape of the 50 μm graph.

Furthermore, the high fluence graphs follow the observed hierarchy with the thinnest sensor having the highest geometric current related damage rate. Comparing the absolute values with the previous annealing step it can be noticed that

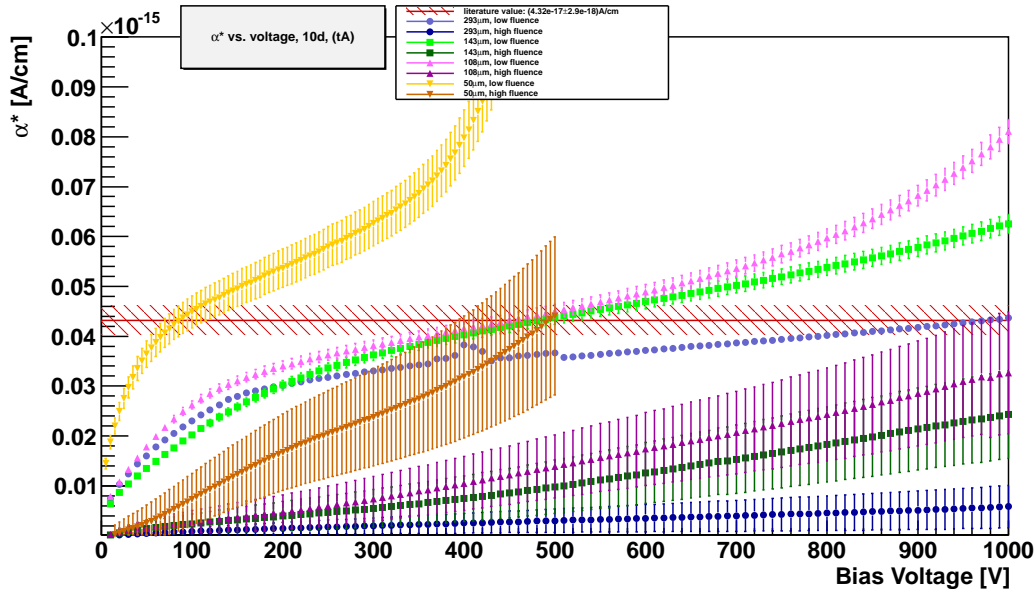


Figure 6.21.: Geometric current related damage rate for all sensors annealed to 10 days at room temperature. The current has been scaled with the fit of all average effective energy values.

they change only slightly. Then again, the values for the low fluences decrease significantly compared to the previous annealing step.

30 days The difference of the geometric current related damage rate after 30 days of room temperature annealing (Figure 6.22), compared to 10 days, is not very high. With the further decreased literature value the 108 μm thick high fluence samples reach the literature value at 1000 V. The reason for exceeding the literature value for the low fluence graphs could be a beginning breakdown or charge multiplication at higher voltages. For the 50 μm devices it is caused by the small number of sensors (only 2) which can result in large errors for the fit and a beginning breakdown at voltages larger than ~ 300 V.

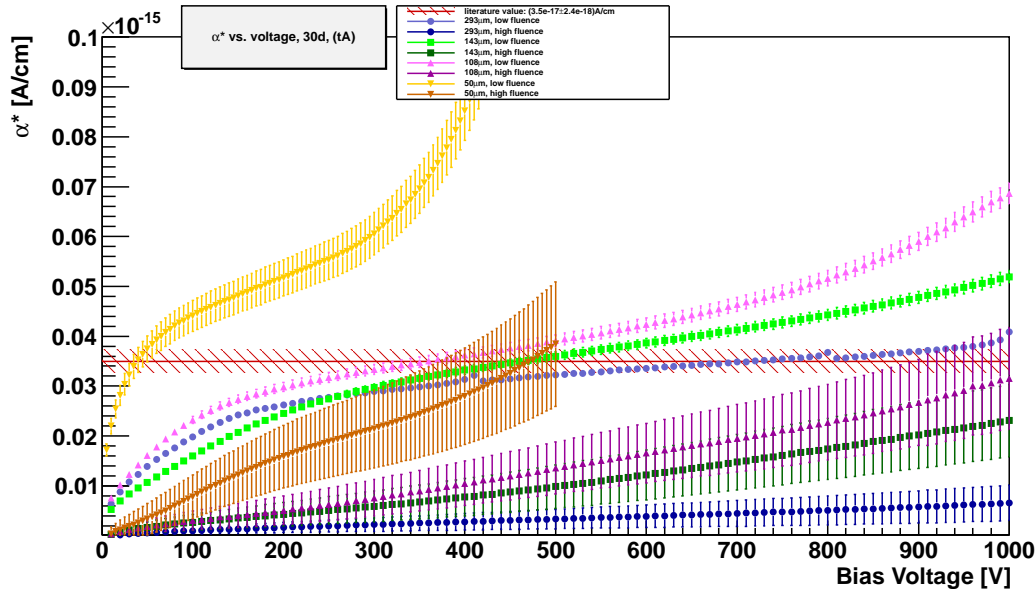


Figure 6.22.: Geometric current related damage rate for all sensors annealed to 30 days at room temperature. The current has been scaled with the fit of all average effective energy values.

6.6. Comparison with Data Measured at CERN

Because the effective energy at high fluences decreased with increasing fluence, a second set of 108 μm thick sensors has been measured at CERN with their cold IV system (subsection 3.1.4) to validate the observations. Figure 6.23 shows the reverse bias current of the samples measured at Liverpool and at CERN, scaled to -25°C . A good agreement can be seen for most fluences, only the lowest fluence of $2 \times 10^{14} \text{ n}_{\text{eq}}/\text{cm}^2$ indicates a significant difference for more than 300 V. At the highest fluences a small deviation at high voltages could be explained by a beginning breakdown or thermal runaway.

The average effective energy for each sample (Figure 6.24) shows a much flatter decrease compared to the Liverpool results (Figure 6.12e). Because the intersection point of the two straight lines is lower than the lowest fluence, an additional condition has been added when using the fit results for current scaling: the decreasing function will be used if the fluence is larger than the intersection point, but only if it is larger than $5 \times 10^{14} \text{ n}_{\text{eq}}/\text{cm}^2$. Otherwise the horizontal fit will be taken.

Figure 6.25 shows the geometric current related damage rate for this sensors. At approximately 600 V the low fluence graph reaches the literature value, but then increases further. The high fluence data series increases as well with increasing bias voltage and reaches the literature value at approximately 750 V. A large drop at 900 V is visible because the sensor irradiated to $2 \times 10^{16} \text{ n}_{\text{eq}}/\text{cm}^2$ could not be

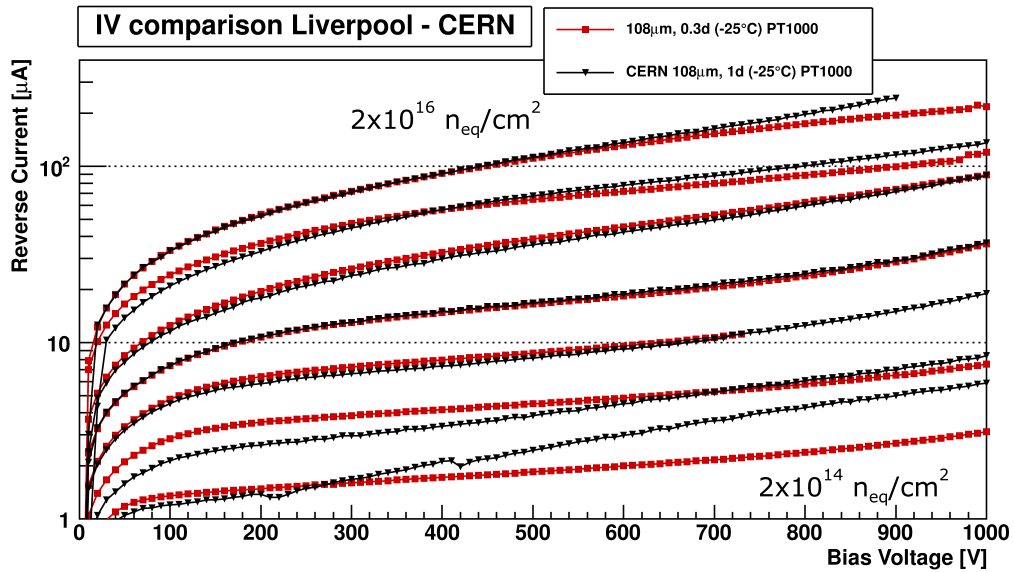


Figure 6.23.: Comparison of reverse bias current of samples measured at Liverpool (red) and CERN (black), scaled to -25°C . The lowest current represents the lowest fluence of $2 \times 10^{14} \text{ n}_{\text{eq}}/\text{cm}^2$ and the highest current the fluence of $2 \times 10^{16} \text{ n}_{\text{eq}}/\text{cm}^2$.

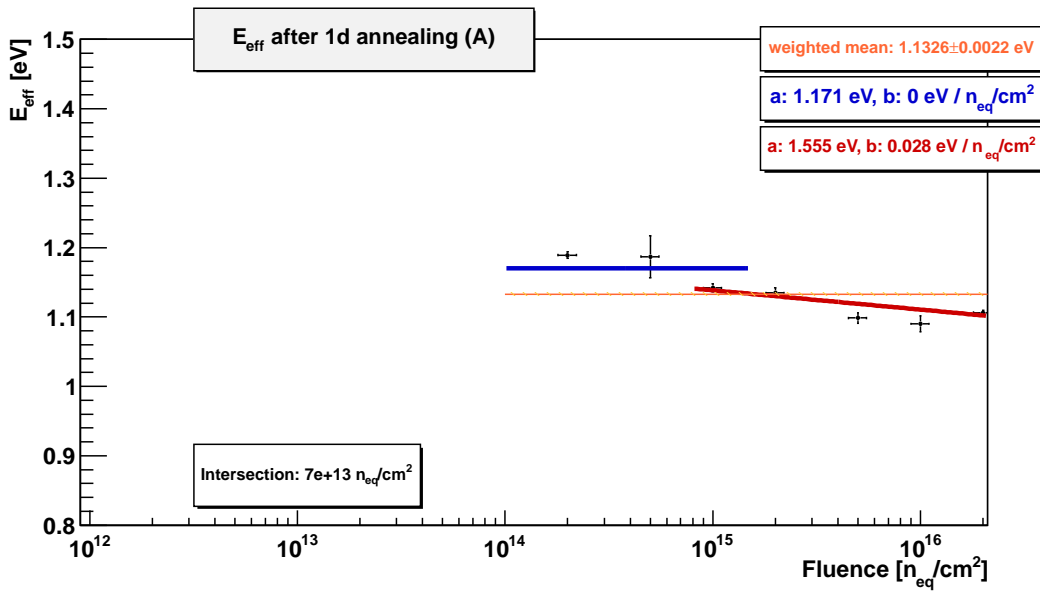


Figure 6.24.: Average effective energy at all fluences of the $108 \mu\text{m}$ samples measured at CERN.

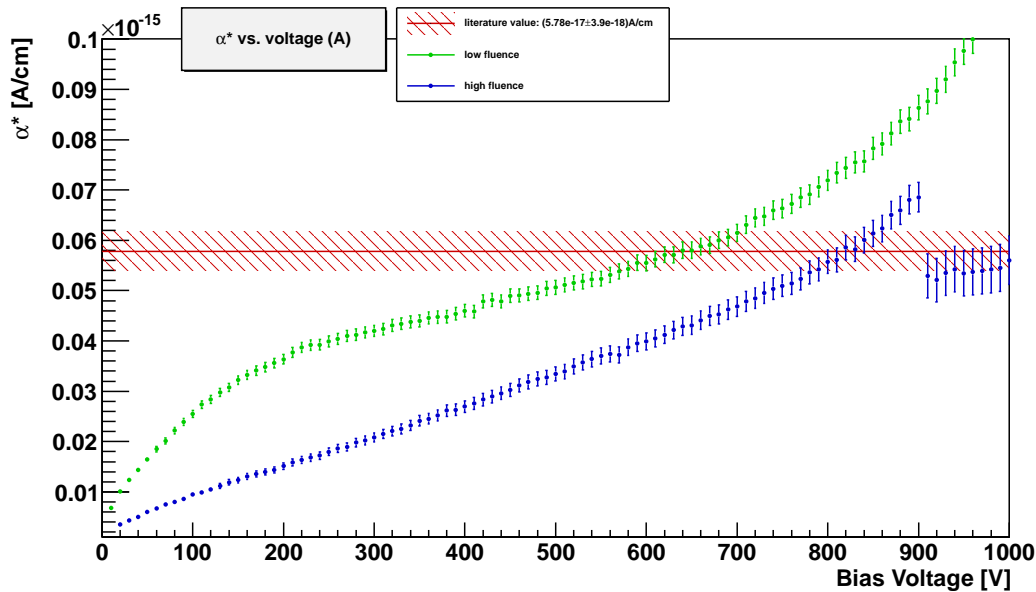


Figure 6.25.: Geometric current related damage rate for the samples measured at CERN (108 μm thick).

measured at higher voltages due to the large current.

The low fluence graph is comparable with the Liverpool measurement (see Figure 6.19), but the high fluence graph is completely different. At Liverpool the gradient is lower and the maximum value is less than half as high as the literature value.

6.7. Comparison with Peltier Setup

All sensors have been measured with the old freezer based cooling system at all annealing steps to get comparable results. The new PID controlled Peltier cooling system was used to measure the devices again after a total annealing time of 30 days. This allows a direct comparison of the two systems.

The measurement method was changed slightly. With the old system the measurements were done during the ramping of the voltage to the maximum value while with the new system the voltage was set to the maximum value and then slowly decreased while performing the measurements. The number of voltage steps and the step size have been kept the same. This has been done to produce results with the same method as used by Freiburg (see section 6.8). Figure 6.26 shows the comparison of the reverse bias current from all Hamamatsu sensors, scaled to -25°C . With the exception of the lowest fluence ($1 \times 10^{12} \text{ n}_{\text{eq}}/\text{cm}^2$) they are in good agreement. Because of the logarithmic scale of the y-axis the difference of the currents looks

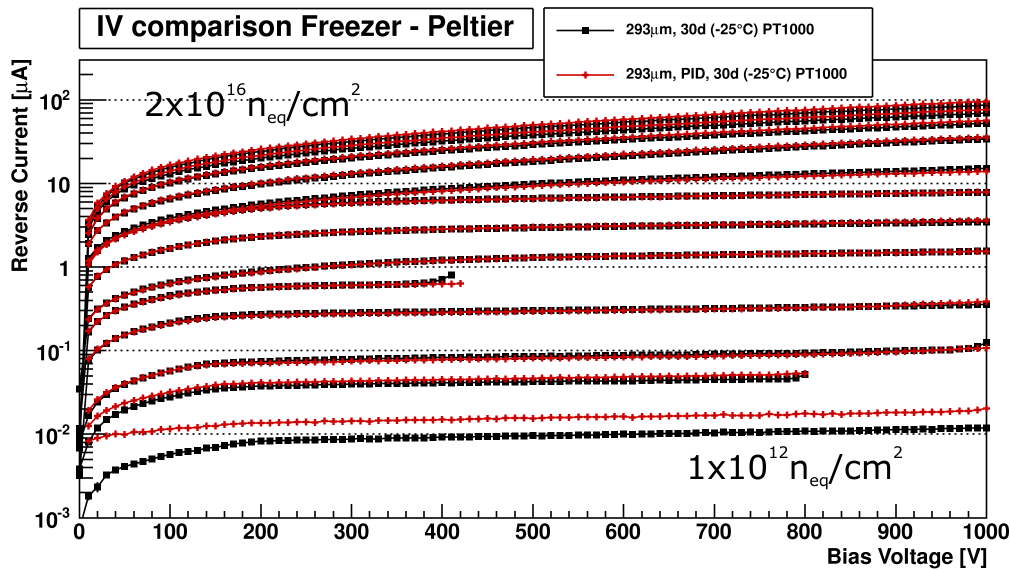


Figure 6.26.: Comparison of IV measurements with freezer cooling (black) or Peltier cooling (red) for all Hamamatsu sensors annealed to 30 days.

large while in reality it is only in the order of 20 nA.

Figure 6.27 shows the effective energy values for the different sensor types, with the exception of the 50 μm devices, because they exceeded the acceptable current range. The comparison with Figure 6.14b shows a good agreement for fluences higher than $1 \times 10^{13} \text{ n}_{\text{eq}}/\text{cm}^2$. At high fluences the decrease of the effective energy with increasing fluence is visible too.

Comparing the graphs for the geometric current related damage rate measured with the old IV system (Figure 6.22) with the Peltier system (Figure 6.28) shows significant differences for some sample types. The low fluence graphs are nearly identical, as well as the high fluence 293 μm graph. Significant changes can be seen in some high fluence graphs. The absolute values of the 143 μm sensors have increased and nearly reach the literature value at 1000 V. For the 108 μm devices the increase is even more prominent with a increasing slope starting at 750 V. Then again the α^* values for the 50 μm low fluence devices decreased and they no more reach the literature value. This is caused by differences in the measured currents with the two setups. One reason could be that with the PID system the measurements started at the highest voltage, at which the sensors had the highest current. Because of the faster ramping the current could not have had enough time to settle.

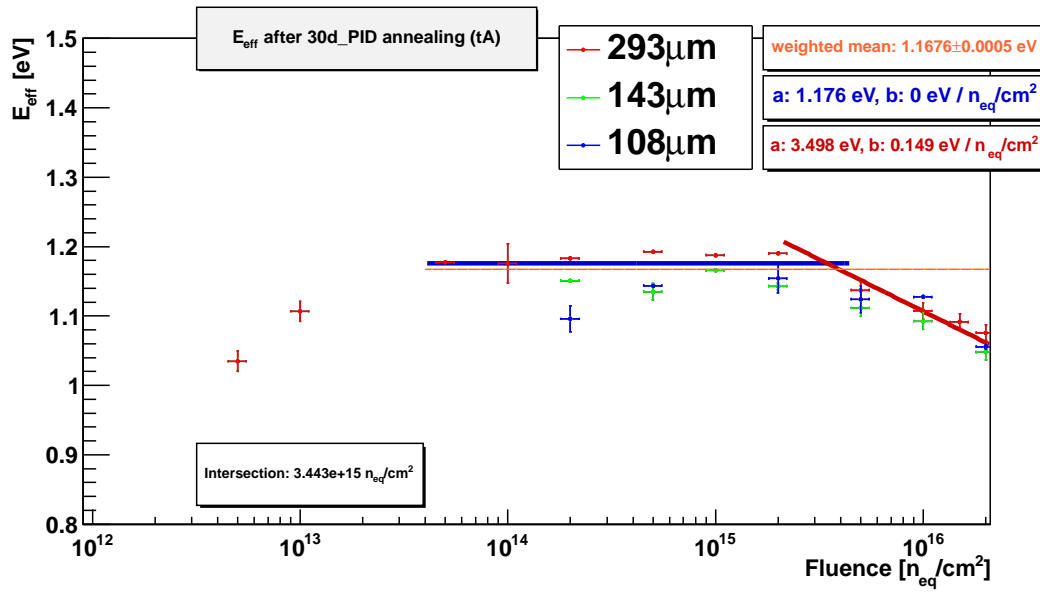


Figure 6.27.: Effective energy for all sensor types measures with the Peltier system.

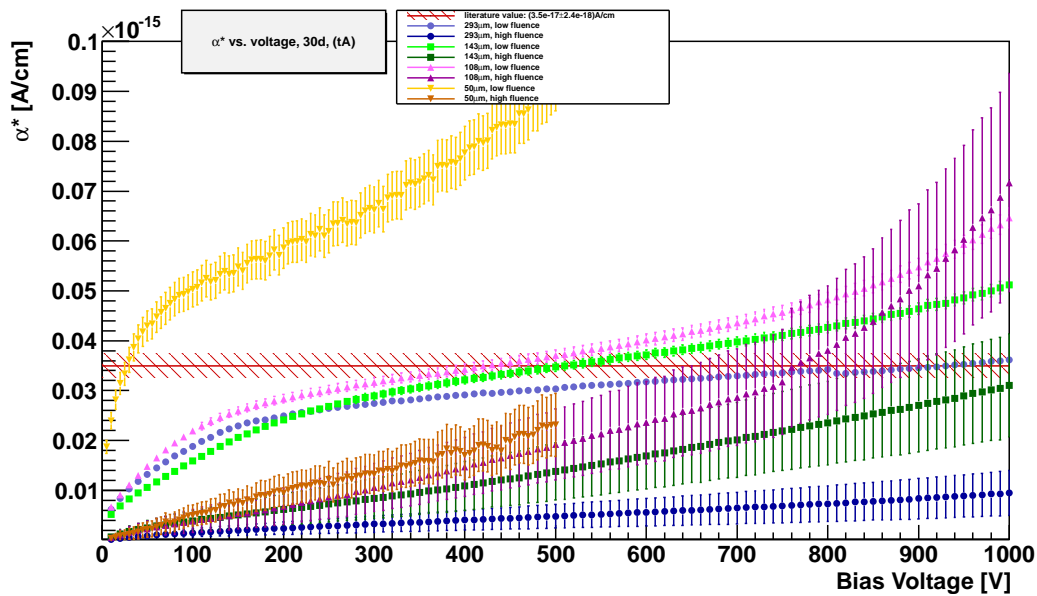


Figure 6.28.: Current related damage rate for the Peltier system.

6.8. Comparison with Freiburg Data

To validate all results, two set of sensors were irradiated. The second set was tested at the Albert-Ludwigs-Universität Freiburg, excluding the proton irradiated samples and the 108 μm sensors, which were tested at CERN. All results from Freiburg have been presented at the DPG spring meeting 2016 [Wie16b] by Moritz Wiehe.

The measurements at Freiburg were done with a Peltier system. Each sample was measured at -23°C , -27°C and -32°C at the same annealing steps as the Liverpool measurements and with the same PCB. Instead of measuring when increasing the voltage to the maximum value, they were measured when ramping the voltage down. Because measurements at three different temperatures were done the effective energy was determined by a fit with

$$I(T) = A \cdot T^2 e^{-\frac{E_{g,eff}}{2k_B T}},$$

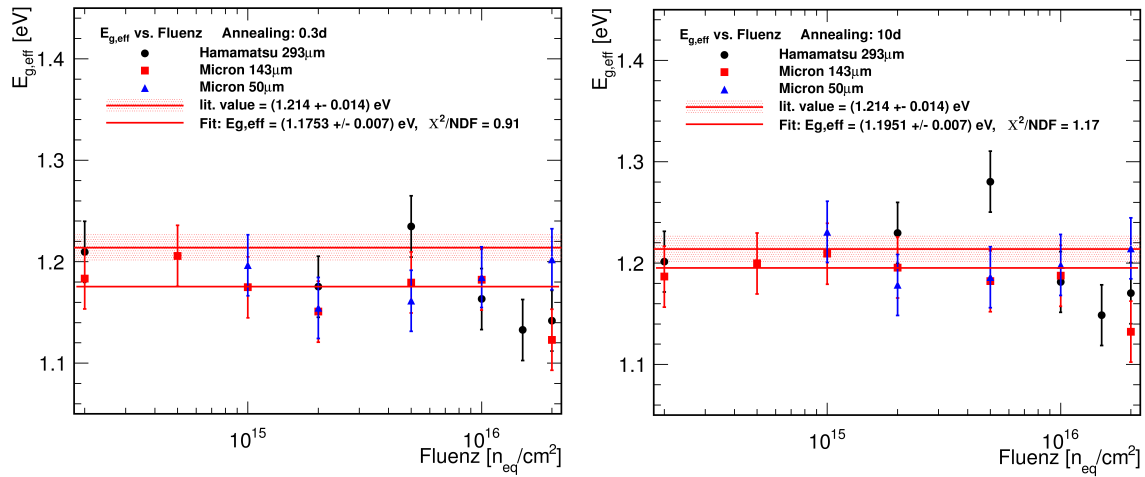
where A is a scaling constant. With this the effective energy at each voltage step was obtained and then fitted with a horizontal line to get E_{eff} for each sensor.

It can be seen in Figure 6.29 that the effective energy values are at the same level for all fluences. Only at very high fluences some data points deviate slightly, but they are within a three σ agreement to the literature value. All values were fitted with a horizontal line and the results are summarized in Table 6.3. Instead of the uncertainty of the fit the significantly larger systematic uncertainty of 0.03 eV was used. This is based on a systematic temperature uncertainty of 0.15°C due to the temperature fluctuations of the PID controlled Peltier element. Regardless it can be seen that the effective energy is fairly stable with annealing and in good agreement with the literature value.

Using these effective energy values the geometric current related damage rate was calculated. The plots in Figure 6.30 show α^* for the different sensor types, separated in low fluence ($\leq 2 \times 10^{15} \text{ n}_{eq}/\text{cm}^2$) and high fluence ($> 2 \times 10^{15} \text{ n}_{eq}/\text{cm}^2$), for the three annealing steps. Comparison with the graphs for the Liverpool results (Figures 6.19, 6.20, 6.21, 6.22) show that the 293 μm sensors follow the same trend with the low fluence reaching the literature value at high voltages. The absolute value for

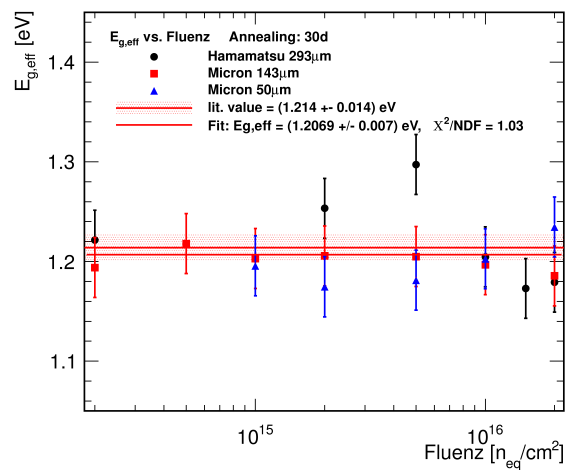
Annealing Time	Effective energy [eV]
0.3 d	1.18 ± 0.03
10 d	1.20 ± 0.03
30 d	1.21 ± 0.03
Literature value	1.214 ± 0.014

Table 6.3.: Effective energy values measured at Freiburg.



(a) 0.3 days annealing.

(b) 10 days annealing.



(c) 30 days annealing.

Figure 6.29.: Effective energy measured at Freiburg [Wie16a].

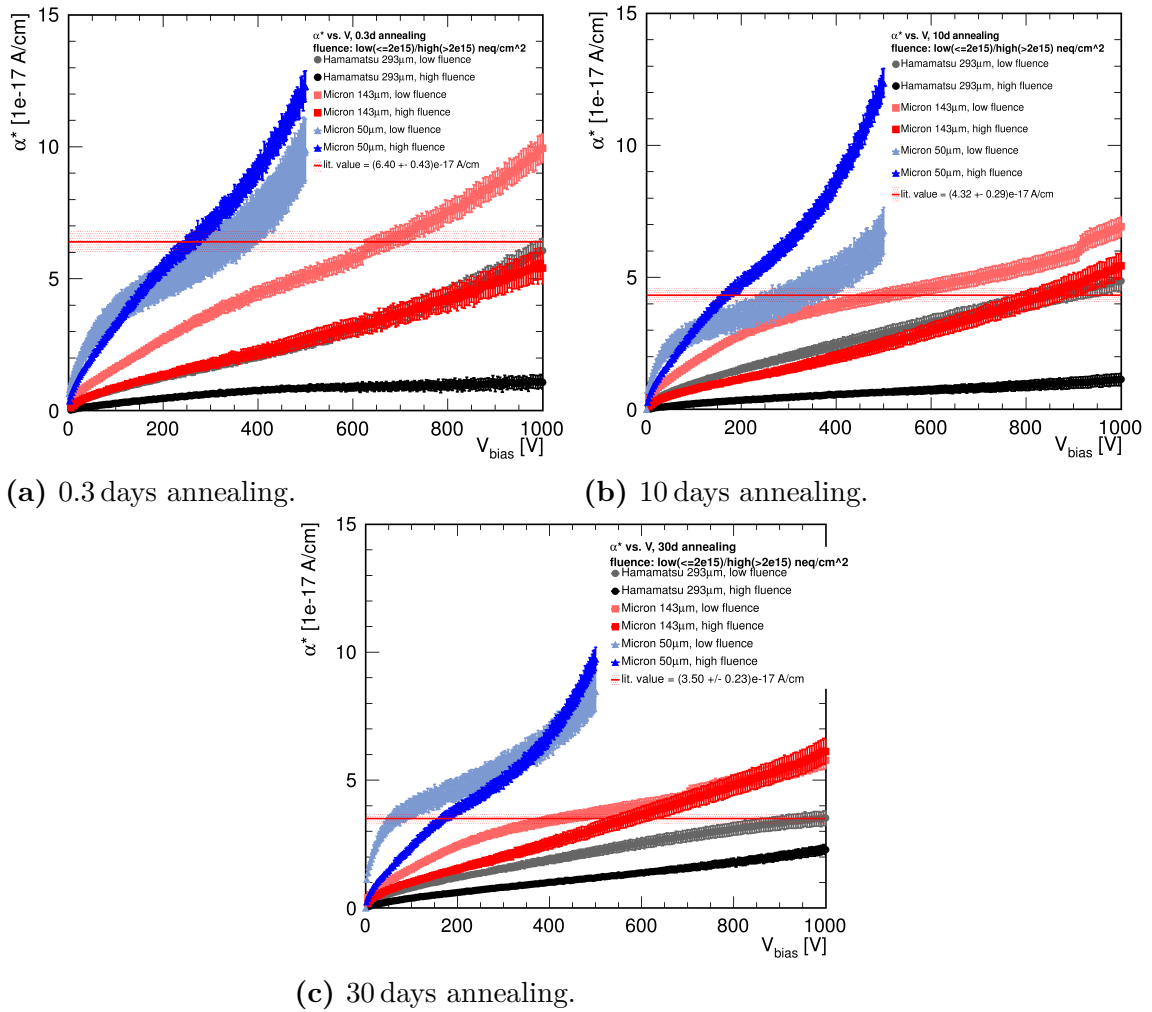


Figure 6.30.: Geometric current related damage rate measured at Freiburg [Wie16a].

the high fluence α^* at Liverpool is smaller than the Freiburg value, especially after 30 days of annealing. For the other device types the difference is even larger but the hierarchy with the low fluence values being higher than the high fluence values is unchanged. While the low fluence values for the 143 μ m thick samples agree well, the high fluence values from Freiburg are significantly higher. They reach the literature value already after 0.3 d annealing and exceed it significantly after 30 d. The largest difference is visible for the 50 μ m samples. The high fluence values at Freiburg are comparable with, or even higher, than the low fluence values. Comparing the graphs with Liverpool, it can be seen that they agree for the low fluences while the high fluence graphs from Liverpool are significantly smaller.

Direct Comparison Differences of the effective energy at high fluences can be seen between the measurements done at Liverpool and at Freiburg. To investigate this

further some direct comparisons have been done.

One possible reason could be the different analysis methods used. To exclude this the raw data files of the HPK sensors (30 days annealing, fluences from $1 \times 10^{14} \text{ n}_{\text{eq}}/\text{cm}^2$ to $2 \times 10^{16} \text{ n}_{\text{eq}}/\text{cm}^2$) have been exchanged: the Liverpool files were analysed at Freiburg with their script and the Freiburg files were analysed at Liverpool. From the good agreement of the low fluence results it was not expected that the different analysis scripts would have a large discrepancy at high fluences and this has been proven. Figure 6.31 shows the comparison for the analysis methods. A good agreement of the analysis methods can be seen, while the deviation of the absolute values at high fluences is clearly visible.

Because the deviation is not based on the analysis method, it could be caused by the sensors themselves. To investigate this further the Liverpool sensors were shipped to Freiburg to be measured with their system while the Freiburg sensors were measured at Liverpool. Figure 6.32 shows the measurements of the the two sets of sensors at Liverpool and Freiburg. While the results at each institute are self-consistent, they deviate between the two sites. This excludes any sensor effects to describe the discrepancy.

After excluding the analysis scripts and the sensors as cause of the difference, only the measurement setups or the measurement method is left. To look into this the current values were directly compared for a common measurement temperature and one specific fluence. The chosen device was the Hamamatsu sensor irradiated

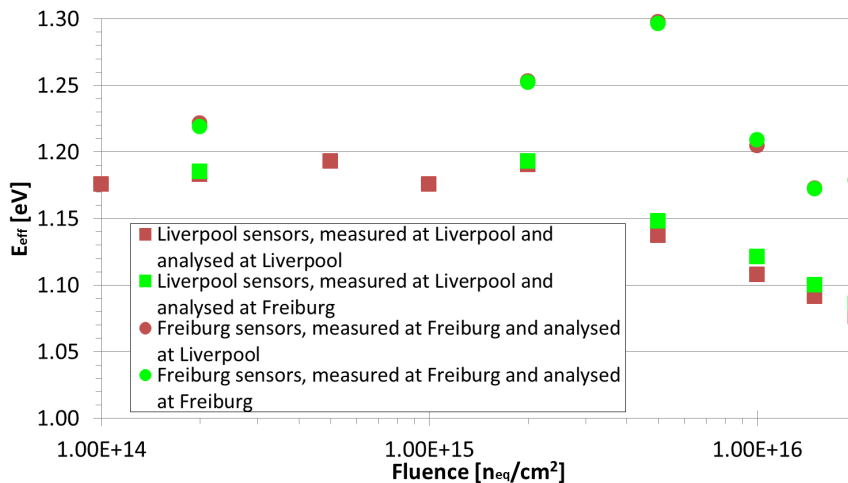


Figure 6.31.: Comparison of Liverpool and Freiburg analysis scripts. The Liverpool sensors are represented in squares while for the Freiburg sensors circles are used. For the Liverpool analysis red is used and for the Freiburg analysis green. A good agreement of the different analysis methods can be seen while the absolute values at high fluences deviate.

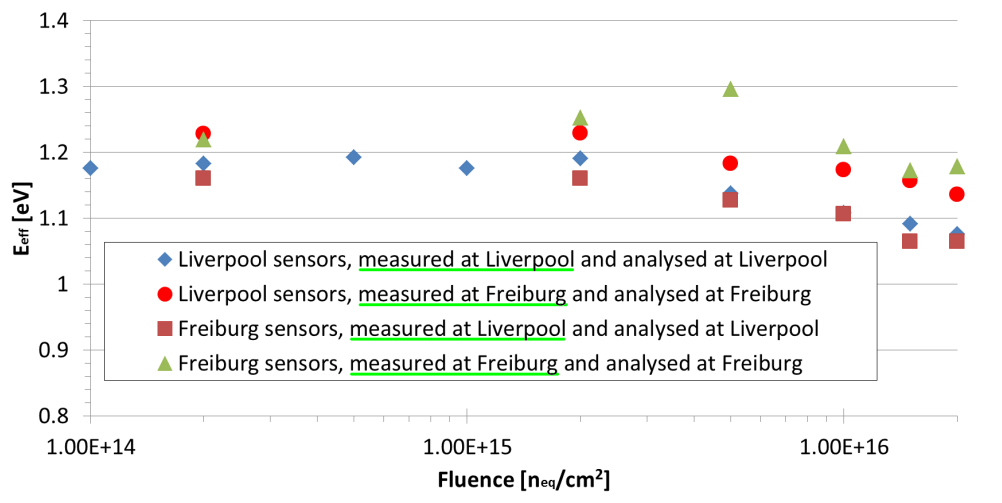


Figure 6.32.: Liverpool and Freiburg sensors swapped and measured: the measurements at each institute are self-consistent, but disagree with each other.

to $2 \times 10^{16} \text{ n}_{\text{eq}}/\text{cm}^2$. Measurements at Liverpool were done in the freezer with a temperature of approximately -23°C while the Freiburg measurements were done with their Peltier cooled system at -23°C as well. Figure 6.33 shows the currents in a direct comparison. They have been scaled to -23°C to eliminate small temperature

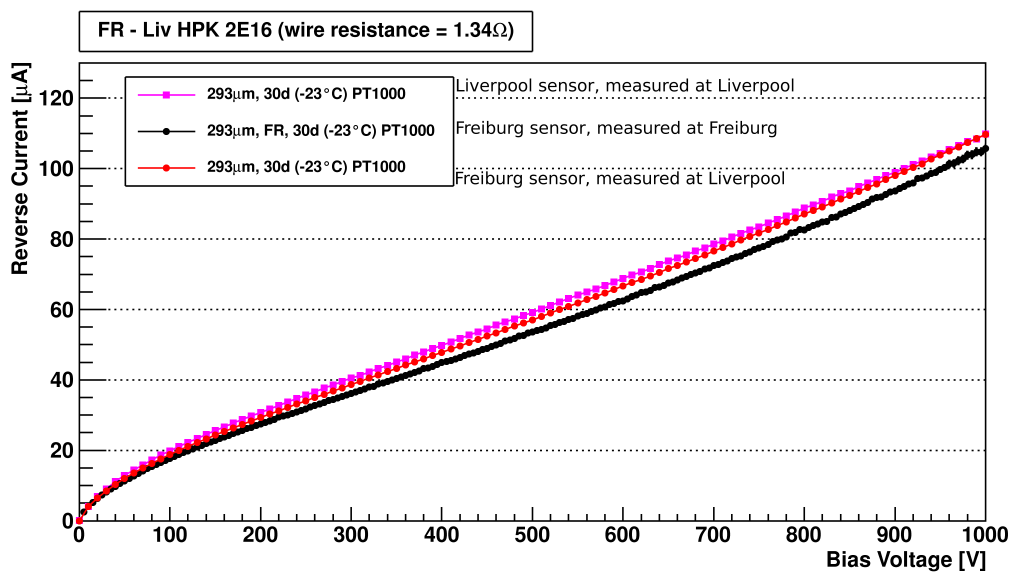


Figure 6.33.: Direct current comparison between Freiburg and Liverpool for the HPK sensors irradiated to $2 \times 10^{16} \text{ n}_{\text{eq}}/\text{cm}^2$. The measurements at Liverpool were done in the freezer at a temperature of -23°C while the Freiburg measurement was done with the Peltier cooling system at -23°C as well. For the Liverpool temperature values the wire resistance was taken into account.

fluctuations, using an effective energy of 1.214 eV. The device from Freiburg was measured twice, once at Freiburg and once at Liverpool. It can be seen that both Liverpool measurements show good agreement, although they are from different sensors. The Freiburg measurement on the other hand is lower. In the Freiburg system the PT1000 resistance is directly converted to a temperature value and only this value is written to the output file. At Liverpool the resistance is stored and it is therefore possible to test different conversion methods. Because only a two wire measurement was used at Liverpool, the wire resistance had to be subtracted from the measured PT1000 resistance. By changing the wire resistance the measured temperature changes and it is possible to investigate a general temperature offset in the measurements.

The best agreement has been found for a wire resistance of $0\ \Omega$, as can be seen in Figure 6.34. This indicates that, although they use a three wire setup, the measurements at Freiburg do not include the wire resistance. The observed effect in the current values is small, but could have a larger influence on the effective energy. Therefore the Liverpool analysis has been done again with no wire resistance. In Figure 6.35 it can be seen that the small wire resistance has no significant influence on the effective energy.

Several possible causes of differences between Freiburg and Liverpool have been investigated to find the cause for the difference in the effective energy at high fluences.

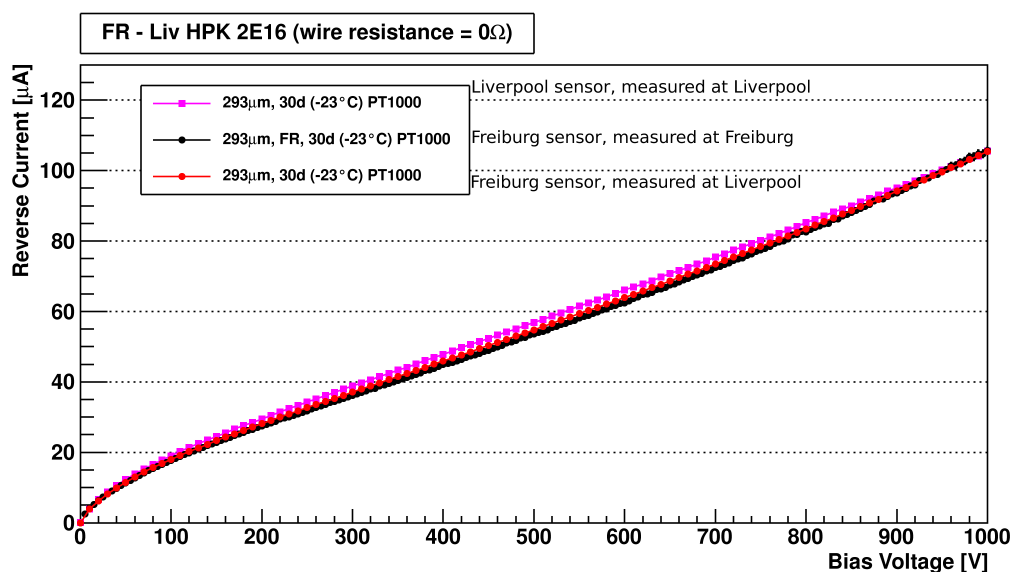


Figure 6.34.: Direct current comparison between Freiburg and Liverpool for the HPK sensors irradiated to $2 \times 10^{16} n_{\text{eq}}/\text{cm}^2$. The measurements at Liverpool were done in the freezer at a temperature of -23°C while the Freiburg measurement was done with the Peltier cooling system at -23°C as well. For the Liverpool temperature values the wire resistance was set to $0\ \Omega$.

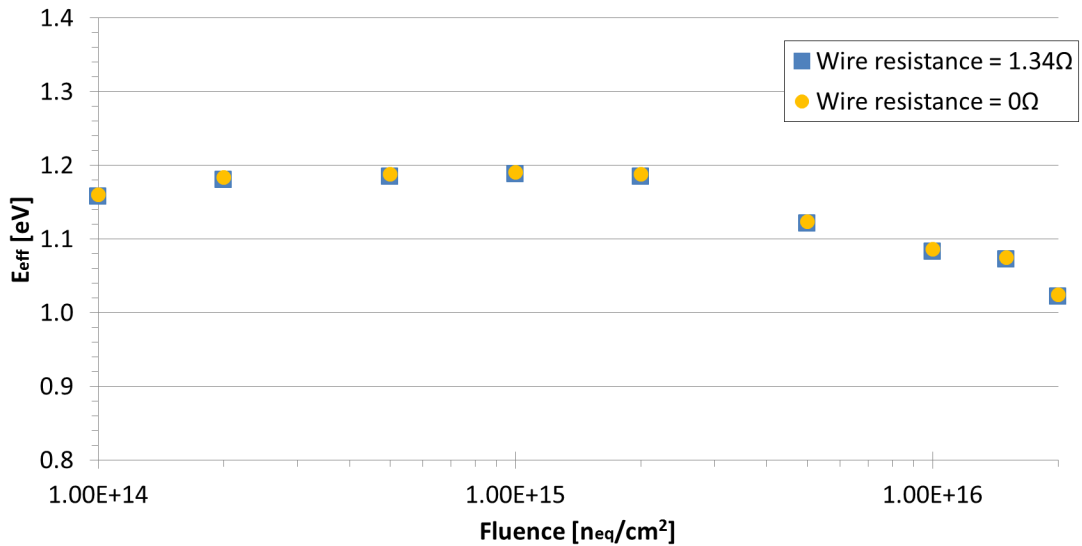


Figure 6.35.: Effective Energy comparison with and without wire resistance for the temperature measurements. The data for the HPK sensors at a total annealing time of 30 d were used.

None of them had any significant influence on the results. The currents could only be compared at one temperature due to the different measurement temperatures. Further steps could be to find the optimal parameter for the Liverpool Peltier system and use it to measure the current at various temperatures. Then it would be possible to use a fit with various values to obtain the effective energy, rather than using just two different temperature values. The measurements with the exchange samples have definitely proven that there is a systematic difference between Freiburg and Liverpool which needs further clarification.

6.9. Summary

Several sensors with thicknesses of 50 μm , 108 μm , 143 μm and 293 μm have been irradiated with fluences from $1 \times 10^{12} \text{ n}_{\text{eq}}/\text{cm}^2$ to $2 \times 10^{16} \text{ n}_{\text{eq}}/\text{cm}^2$. The reverse bias current has been measured at two different temperatures to determine the effective energy. Comparing the currents for different sensor types at the same fluence shows that at very high fluences the current per sensor area becomes independent of the sensor thickness and has the same value for all devices with a nearly linear voltage dependence.

The effective energy has been calculated for each measured voltage. A total value for each sensor was calculated in different ways resulting in slightly different values and uncertainties. When plotting the effective energy as a function of the fluence it has been shown that up to approximately $1 \times 10^{15} \text{ n}_{\text{eq}}/\text{cm}^2$ the results are fairly constant and comparable with the literature value. For higher fluences E_{eff} decreases with increasing fluence. The sensors were measured at three room temperature annealing steps: 0.3 days, 10 days and 30 days and at all steps the decrease of E_{eff} at high fluences has been observed.

For the determination of the current related damage rate the currents had to be scaled to 21°C. It has been shown that using different values for E_{eff} has an influence on the results. In this context the term geometric current related damage rate α^* was introduced, which uses the geometric volume instead of the unknown depleted volume. For all annealing comparisons the effective energy value was obtained by plotting the average value at each fluence in a graph and fitting it with a straight line. A horizontal line was used for low fluences with fit results comparable to the literature value. The decrease with increasing irradiation fluence for higher fluences was represented by a slope of the line. It has been shown that the low fluence α^* values ($\leq 2 \times 10^{15} \text{ n}_{\text{eq}}/\text{cm}^2$) reach the expected literature value for high voltages. For the Micron sensors they even exceed it for very high voltages. The high fluence results are lower and show a clear hierarchy with the thickest sensor having the lowest α^* value. With increasing annealing time the relative deviation from the literature value for the high fluence α^* values decreases. One possible explanation for exceeding the literature value could be charge multiplication, which would increase the current. However, the onset of a breakdown would also have the same effect. A continuation of this study should include edge-TCT measurements to investigate the electric field of the irradiated samples.

A second set of 108 μm thick sensors has been measured at CERN and compared with the measurements at Liverpool. The currents are in agreement for most fluences. While a decrease of the effective energy at high fluences has been observed as well, the deviation from the literature value is smaller. The resulting geometric current related damage rate shows that the low as well as the high fluence graphs reach the literature value at high fluences, which deviates from the results obtained at Liverpool.

A newly developed Peltier based cold IV system at Liverpool was used to measure all sensors after a total annealing time of 30 days, which allowed a direct comparison with the freezer based old system. The effective energies are in good agreement with the previous observations, but deviations can be seen in the geometric current related damage rate.

Moritz Wiehe from the Albert-Ludwigs-Universität Freiburg has measured a second set of sensors with a Peltier system. The obtained effective energy does not show the observed deviation from the literature value at high fluence. Fitting all values with a horizontal line result in E_{eff} values that are in agreement with the literature value. While the α^* values for the 293 μm thick sensors are comparable with the Liverpool results, the values for other sensor thicknesses differ significantly. Several comparison tests, which included the exchange of sensors, have not revealed the reason for the difference in the effective energy for high fluences. More tests are necessary to find the cause and confirm which results are genuine.

7. Generation of a Shallow Irradiation Damage Layer in Silicon Strip Sensors

Different approaches have been tested to produce sensors with built-in charge multiplication, for example by changing the strip geometry (see chapter 4). A novel idea, first investigated for this thesis, is to use damage from a controlled irradiation to create an approximately 10 to 20 μm thick multiplication layer close to the silicon strip sensor surface. Irradiation of silicon changes the effective doping concentration. With different concentrations in the main bulk and the damage layer a difference of the electric field is expected, which should lead to charge multiplication. The advantage of this method is that the effective doping concentration difference between the bulk and the damage layer should stay constant, even when the whole sensor is irradiated, because there were no differences in the unirradiated material.

A different approach to create a multiplication layer are Low Gain Avalanche Detector (LGADs), in which doping is used to create the layer below the cathode [Sad14]. Because of the different initial doping concentrations it might be possible that the multiplication factor does not stay constant after irradiation due to the different damage types in the bulk and the multiplication layer. This makes the approach investigated in this chapter a favourable method to create a sensor with charge multiplication.

Creating the damage layer requires a very precise tuning of the irradiation parameters. Geant4 simulations, presented in section 7.1, have been used to find the optimal values for beam energy and absorber thickness for the possible use of lead and perspex as absorber material. These have then been used to plan the irradiations at the Birmingham cyclotron. In section 7.2 the results of charge collection measurements are presented. First measurements were done directly after the proton irradiation (subsection 7.2.1). Most samples were then irradiated at Ljubljana [JSI16b] with neutrons to $1 \times 10^{15} \text{ n}_{\text{eq}}/\text{cm}^2$ and $5 \times 10^{15} \text{ n}_{\text{eq}}/\text{cm}^2$ to investigate the behaviour when the full sensors were irradiated (subsection 7.2.2).

This project has received funding from the European Union's Horizon 2020 Research and Innovation programme under Grant Agreement no. 654168. Results have been presented at [Won16a, Won16b]

7.1. Geant4 Simulations and Irradiations

The aim of this study is to generate a shallow zone (≈ 10 to $20\ \mu\text{m}$) of irradiation damage at the strip surface of the silicon sensors. It was chosen to use the Birmingham irradiation facility [Uni16b, Der13] due to the strong collaboration with the University of Liverpool. The MC40 cyclotron produces a proton beam with a user selectable energy. While the standard irradiations are done at 27 MeV, for the generation of the shallow damages this energy is too high as the protons would traverse the full silicon sensor. Therefore a lower beam energy has to be chosen. Additionally it is possible to add an absorber in front of the silicon sensor to reduce further the beam energy.

Figure 7.1 shows a picture of the irradiation facility. The proton beam leaves the beam pipe and enters the cold box. A Faraday cup is placed behind the cold box to monitor the beam current, while the cold box is moved into the park position outside of the beam path. To prevent annealing during the irradiation the box is cooled by liquid nitrogen evaporation: from a dewar, liquid nitrogen is dropped into the box. When evaporating it cools the inside of the box and at the same time serves as a nitrogen source to avoid ice building up on the sample. The inside of the box can be seen in the left picture of Figure 7.2. The fan is used to guarantee a good circulation to ensure uniform cooling. Temperature and humidity sensors are used to control the cooling. Additional tubes can be used to flush the box with room temperature nitrogen. In the middle picture the carbon fibre frame for mounting the sensors

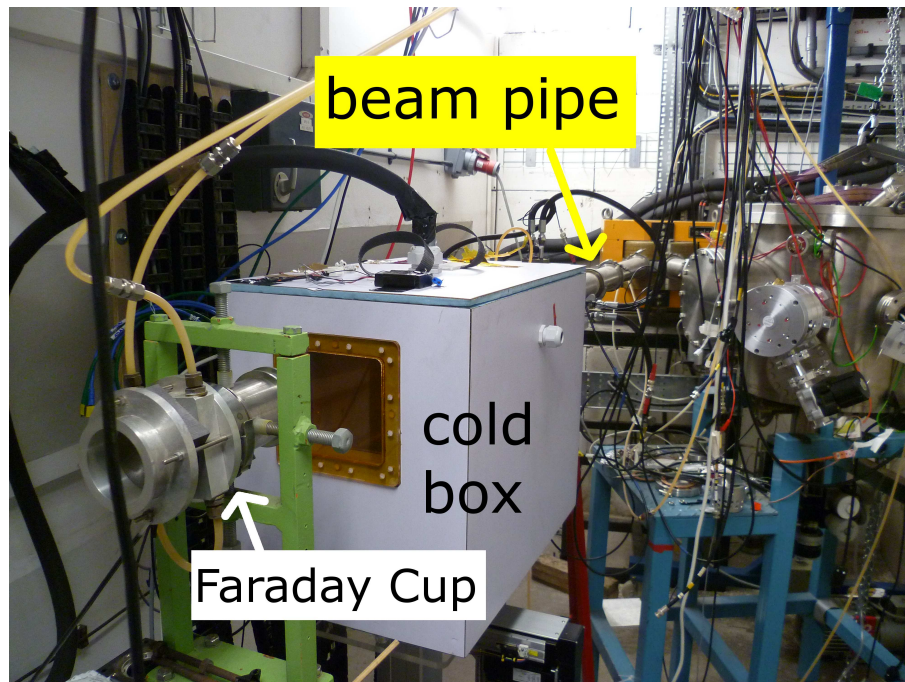


Figure 7.1.: Picture of the Birmingham irradiation facility.

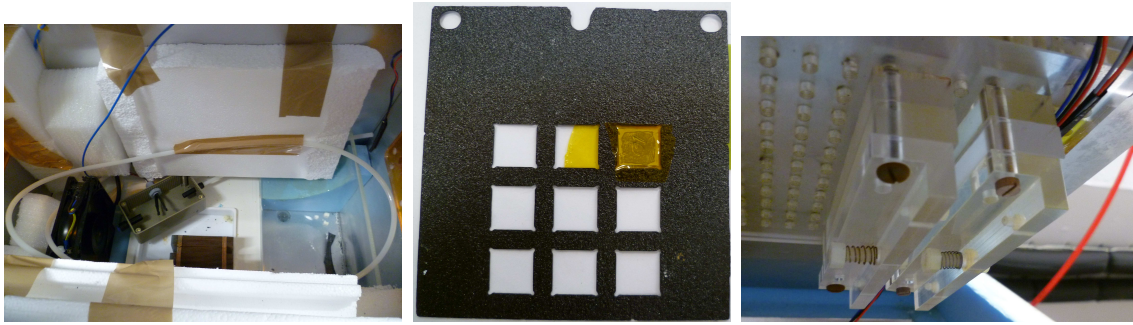


Figure 7.2.: Left: the inside of the cold box with a fan for uniform air flow and temperature/humidity sensors at the bottom to control the cooling. Additional tubes allow it to flush the box with nitrogen. Middle: carbon fibre frame with nine rectangular holes to position sensors. One of the holes in this picture is occupied by a nickel foil which is attached with Kapton and used for dosimetry. Right: mounting for the frames. The spring loading mechanism allows the fast mounting of frames without the use of tools.

is shown. The nine rectangular holes are approximately $(1 \times 1) \text{ cm}^2$ and allow the positioning of Hamamatsu mini sensors by fixing them with Kapton tape from the backside. For Micron sensors the holes are too small. They are placed across the opening and fixed as well with Kapton. Special caution must be exercised in order not to break the sensor. The frame is attached to a mount on the lid of the box (right picture). A spring loading mechanism allows to attach and detach the frames fast without the use of any tools. This is useful when the frames need to be removed after irradiation: while they are slightly radioactive it is important to minimize the exposure time and therefore handle them fast.

7.1.1. Simulation Details

Geant4 [Gea16] is a toolkit that allows the simulation of particles when passing through matter. It has been used to simulate the irradiation at Birmingham for low energy protons. This simulation is based on the example B2b of the Geant4 software package. A basic model of the facility has been created to incorporate all materials that are situated between the proton beam and the silicon sensor. The details of the simulation can be seen in Figure 7.3. Protons are generated at the upstream side and fly towards the downstream side. The ‘World’ box represents the simulated area and is filled with air while the ‘general particle source’ is used to create the protons in the centre of the upstream wall. Various proton energies with a Gaussian energy distribution and a sigma of 0.1 MeV have been used. The protons leave the beam pipe through a $25 \mu\text{m}$ thick window made of titanium. After 14.98 mm in air they reach the first $50 \mu\text{m}$ thick Mylar window of the cold box, followed by a second

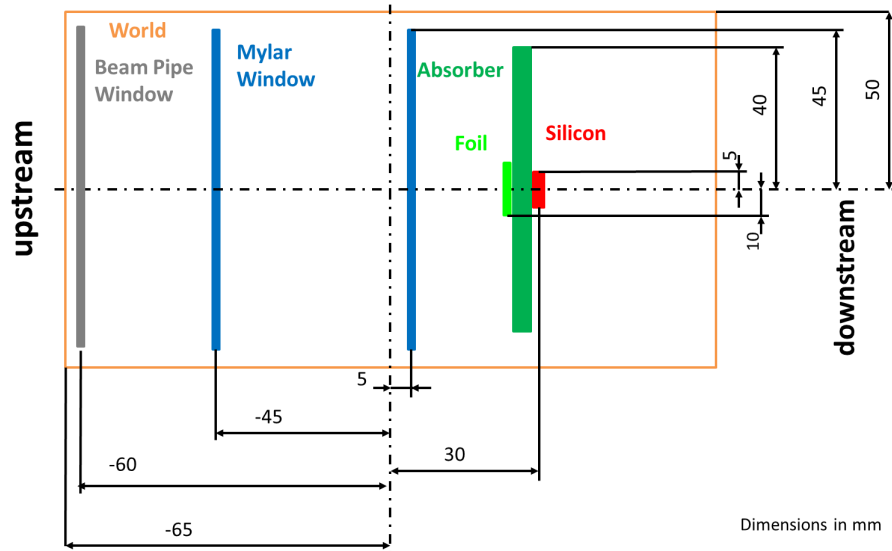


Figure 7.3.: Sketch of the Geant4 simulation details of the Birmingham irradiation facility. All x dimensions are from the centre of the component to resemble the Geant4 dimension convention. The protons from the cyclotron enter from the left side.

50 mm further downstream. The silicon sample has been placed 25 mm away from the second window with the absorber in front. Simulations were done with different absorber thicknesses and two materials: perspex and lead. For the dosimetry a 25 μm thick nickel foil is usually used, which could be placed before the absorber or between absorber and silicon. While the silicon position is fixed, the position of the nickel foil and the absorber depend on their thickness and the simulation mode. In all cases they are attached to each other.

The number of simulated protons was set to 1000 to perform the simulations in a reasonable time. For the physics model the standard Geant4 model FTFP_BERT has been used, as in the example B2b. At each simulated step the end-position and the energy-loss of the proton for that step were given. To minimize the disk space and required processing time a sensitive volume smaller than the ‘World’ volume has been defined, in which the standard step size has been reduced to 0.1 μm for a better resolution and only the data-points in this volume were stored for the further analysis processes. While in the standard simulations only the silicon was within the sensitive volume, some tests have been made where the absorber and the nickel foil were included as well to see how much energy is lost in which component.

Figure 7.4 shows the Geant4 simulation of 27 MeV protons. The particles pass through the three windows, a 25 μm thick nickel foil, a 300 μm thick lead absorber and the 300 μm thick silicon sensor. The total overview on the left side shows that after passing any material the beam widens due to multiple scattering, which is pronounced after the foil-absorber-silicon sandwich. A detailed view on the right

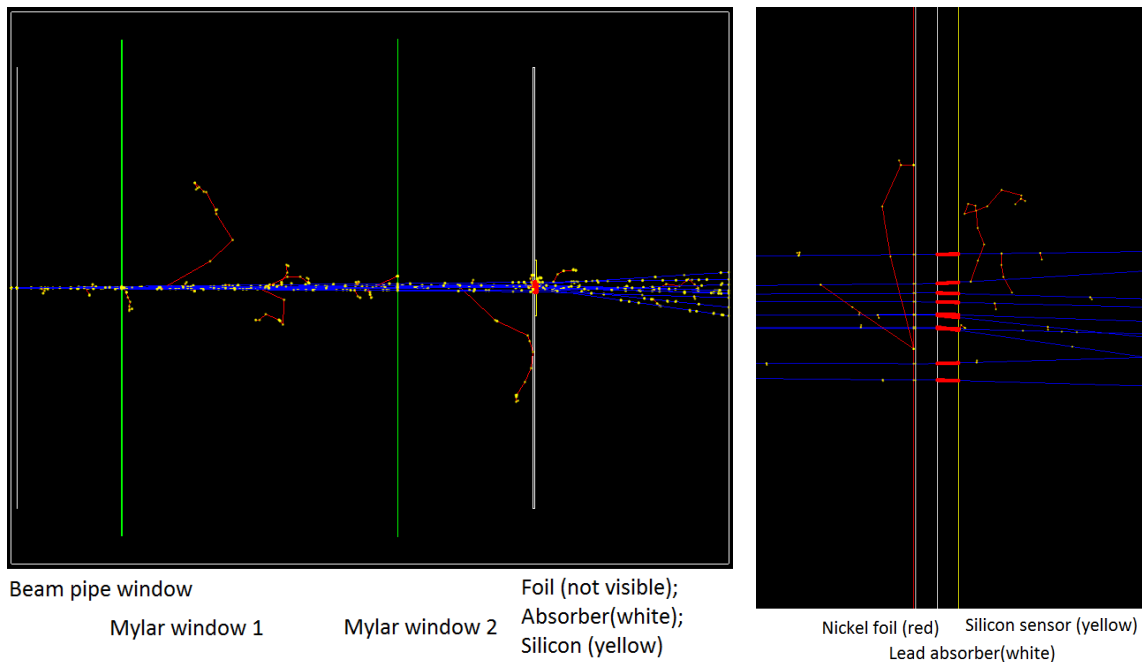


Figure 7.4.: Geant4 simulation of 27 MeV proton beam. The left picture shows the overview of the whole world, the picture on the right shows a detailed view of the interaction with the silicon sensor. Different colours have been used to distinguish the outline of the different components. The protons are generated in the centre on the left side and move to the right. Each yellow dot represents a interaction at which the trajectory of the particle changes and they are connected with blue lines for protons and red lines for electrons. In the sensitive volume of the silicon sensor the step size is reduced and each step is represented by a red dot. Because of the small distance between the steps they look like a thick red line. The protons are all created without a momentum in y -direction therefore the spread perpendicular to the flight path is only caused by multiple scattering and it increases clearly after passing through the dense lead-silicon sandwich.

side shows the difference in the number of steps: in the silicon sensor they are represented by red dots and it is not possible to distinguish them, while on the outside there are hardly any visible.

7.1.2. Simulations for the First Irradiation

The plan for the first irradiation was to tune the beam energy, as well as the absorber thickness, to find the optimal combination in which the protons only travel approximately $20\ \mu\text{m}$ into the silicon sensor. Additionally two absorber materials were tested: perspex and lead. It has to be noted that in this first simulations the beam pipe window was not included and the nickel foil for the dosimetry was placed

in front of the absorber. A sandwich structure, where foil, absorber and silicon are attached to each other, was chosen because it is easy to mount into the cold box.

Initial simulations in coarse steps for the beam energy as well as the absorber thickness helped to find the optimal window for both. The detailed simulations for the first irradiation were done from 10.8 MeV to 12.0 MeV in 0.1 MeV steps. The minimum value was given by the irradiation facility. Although it would be possible to reach lower energies by using different machine settings, it would be preferred not to do this. For lead the thickness was varied from 275 μm to 325 μm in 5 μm steps and for perspex from 950 to 1050 μm in 10 μm steps. With these simulations different plots can be generated to choose the optimal beam parameter.

Using lead as the material for the absorber, it was discovered that 300 μm was the optimal choice for the thickness of the absorber. An absorber of 275 μm is too thin and even at the lowest energy the protons reach too far into the silicon. For 325 μm only the highest energies can reach the sensor and high beam energies also lead to larger tails of the Bragg peak. Figure 7.5 shows the position in the silicon sensor that protons of various energies can reach. To only get protons within the first 20 μm the beam energy should not exceed 11.6 MeV, at which the tail of the energy loss distribution is reasonably small. Another factor has to be taken into consideration: although the lowest penetration depth is reached at 11.0 MeV, the number of good events (events in which a proton reaches the silicon sensor) depends strongly on the energy as well.

Figure 7.6 shows the number of good events as function of the initial proton energy. For energies higher than approximately 11.8 MeV, nearly all of the simulated 1000

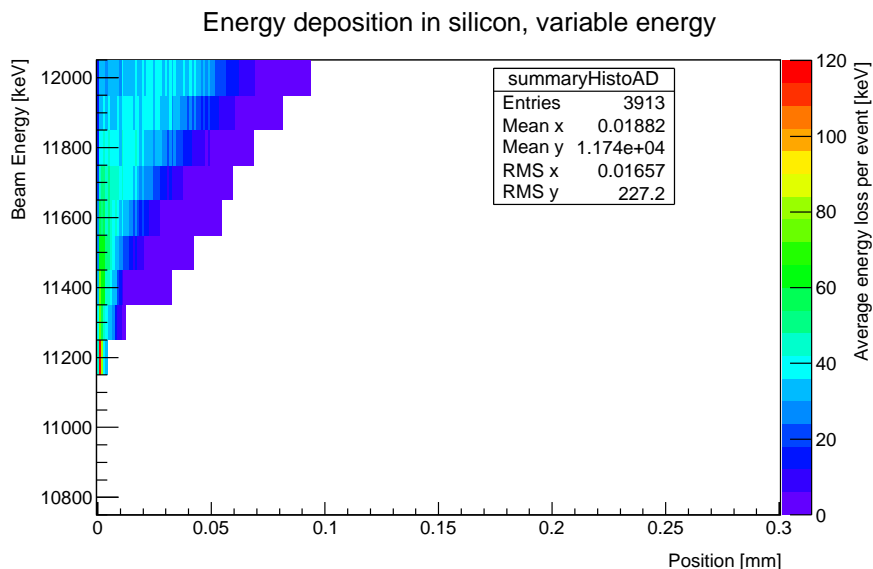


Figure 7.5.: Geant4 simulation, showing the positions in the silicon sensor that protons of various energies can reach with a 300 μm thick lead absorber.

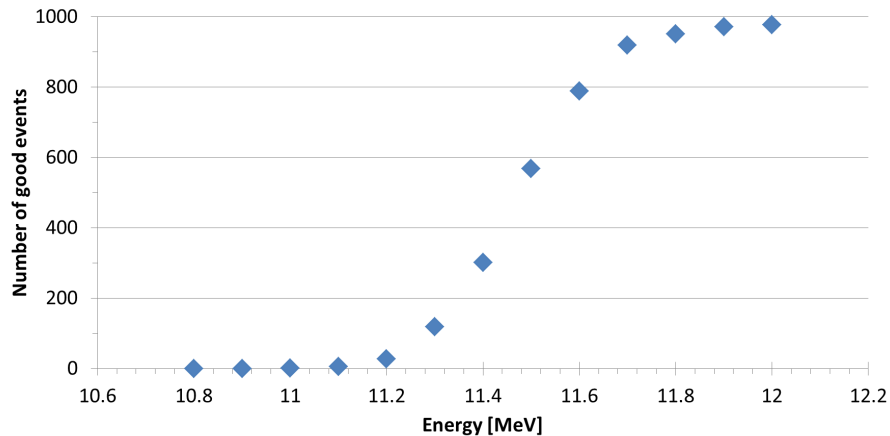


Figure 7.6.: Number of events in which a proton reaches the silicon for different beam energies, using the 300 μm thick lead absorber.

protons reach the silicon sensor, but at the same time they penetrate up to 50 μm into the silicon sensor. A good compromise between penetration depth and number of good events is 11.4 MeV. The lost energy (average of all events) as function of the silicon depth can be seen in Figure 7.7, which shows in green that the 302 protons which reached the silicon sensor lost almost all of their energy within the first 20 μm . The same considerations have been made to find the parameter for the perspex absorber with the result that a 1000 μm thick absorber and a beam energy of 11.2 MeV would result in a good energy loss distribution (see blue histogram), where the majority of the 187 protons are stopped within the first 25 μm .

The 300 μm lead absorber, as well as the 1000 μm thick perspex absorber were produced by the workshop of the Department of Physics at the University of Liverpool [Uni16c]. It was challenging to produce the $60 \times 60 \text{ mm}^2$ absorber to the required thickness within 10 μm where they had to be as flat as possible.

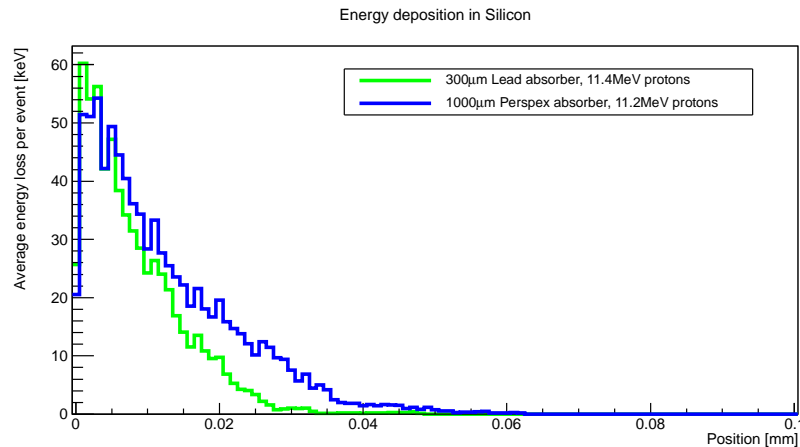


Figure 7.7.: Average energy deposition for 11.4 MeV protons after a 300 μm thick lead absorber in green and 11.2 MeV protons after a 1000 μm thick perspex absorber in blue.

7.1.3. First Irradiation in December 2015

One of the first tasks for the irradiation was the position finding. The cold box can be moved perpendicular to the beam line: horizontally as well as up and down. This allows to move samples in the beam and irradiate several by using a scan pattern (see Figure 7.8). Each scan starts at the 'Home' position and it is therefore important to measure the position of the sensors relative to 'Home'. Gafchromic film [Ash16] is used for this: this yellow film becomes black when it is irradiated and even a very short pulse is enough to produce a reaction. Figure 7.9 shows a picture where the film was used to measure the distances between 'Home' and the first sensor position. It can also be seen that the beam profile at the 'Home' position is rectangular, which is caused by a collimator at the exit of the beam pipe. With the known positions the scan path is programmed so that all samples are equally covered by the beam.

One little setback was given by the cyclotron operation: the tuning of the beam to a certain energy can take several hours, especially if the energy was never used before and no reference settings are available. While tuning parameter from previous irradiations were available for certain energies, this did not include 11.2 MeV and 11.4 MeV. It was decided to try 11.0 MeV for both absorbers. This would reduce the penetration depth, but also the number of good events. To see if the protons can travel the whole distance from the beam pipe to the Faraday cup, a large sheet of Gafchromic film was taped to the cup. In the left picture of Figure 7.10 it can be seen that the film became black after a short exposure with protons, but the areas that were covered with Kapton to fix it to the aluminium tube are still yellow. This is clearer in the right picture where the Kapton tape prevented the 11 MeV protons to reach the film, leaving the area under the tape unchanged.

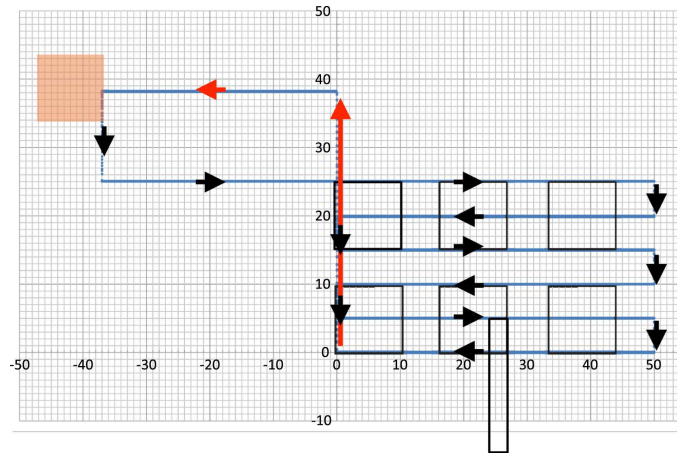


Figure 7.8.: Scan pattern at the Birmingham cyclotron from [Der15]. Each scan starts at the 'Home' position (red square) and then moves along the black arrows to irradiate all samples. At the end it returns to the 'Home' position along the red arrows. For the scans the entire cold box is moved whereas the beam is at a fixed position.

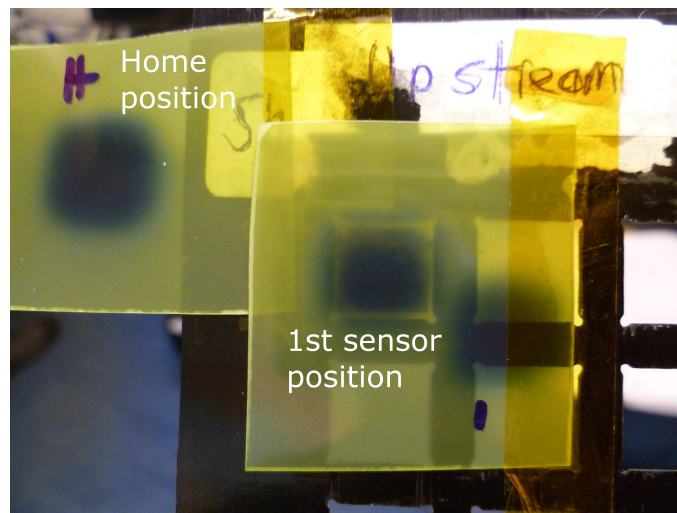


Figure 7.9.: Position finding at Birmingham irradiation facility. The 'Home' position is the start point for each scan.

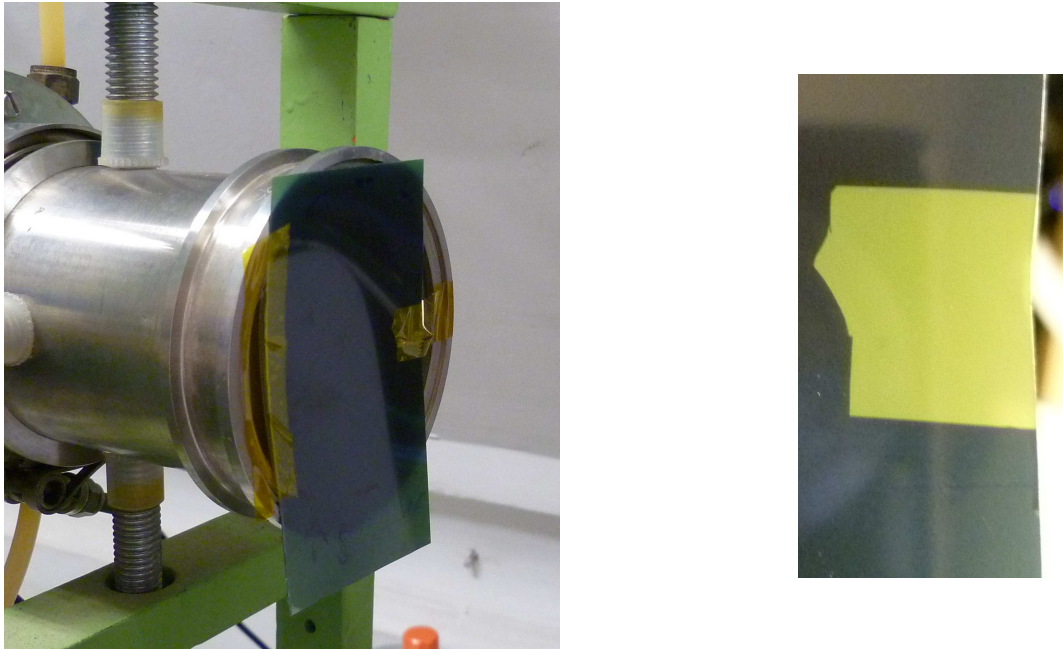


Figure 7.10.: Left: Gafchromic film before Faraday cup for 11 MeV beam. Right: close-up of film, where it was attached with Kapton.

For the final test before the planned irradiation the Gafchromic film was placed behind the perspex absorber while the nickel foil was in-front to get the same configuration as in the simulations. But in this test the film did not darken and also removing the foil did not show an effect. This led to the conclusion that particles were not reaching the film and that the beam energy of 11 MeV is too low. One reason could be that the beam pipe window, which was not included in the simulation, reduces the energy enough so that the protons can not reach the silicon sensor. The next higher available beam energy of 12 MeV was used for further tests.

A test with nickel, perspex and Gafchromic film has not shown any discolouration of the film, but after removing the nickel foil the film blackened slightly (see left picture in Figure 7.11). A similar effect has been observed with the lead absorber (right picture).

For the dosimetry with 27 MeV protons usually a nickel foil is used. Because the beam energy for this study is much lower, it had to be tested whether this is still possible. To do this a nickel foil was attached behind the perspex absorber and should stay in the proton beam for several minutes to get enough activity. The Faraday cup after the cold box did not register any protons when the beam started, which meant that they were all stopped within the absorber and the nickel foil. After approximately one minute, counts were registered in the Faraday cup and so the irradiation was stopped. The result can be seen in Figure 7.12: the Perspex had melted at the interaction point and foamed. After this incident Perspex has been excluded as absorber material because it could not withstand the irradiation



Figure 7.11.: Discolouration of the Gafchromic film after a very short exposition with 12 MeV protons, that penetrated a 1000 μm thick perspex absorber (left) or a 300 μm thick lead absorber (right).

process.

The lead absorber remained intact in a similar test, but the gamma-spectroscopy of a nickel foil after the absorber has not shown any activity peaks that could be used for dosimetry. Up to the submission date of this thesis no method was found to determine the irradiation fluence after the absorber as the energy of the protons after traversing the absorber is so low - too low to overcome the nuclear Coulomb barrier and so induce nuclear reactions and measurable radioactivity in the foil.

For the first full irradiation four silicon sensors and two nickel foils were used. The sensors were produced at Micron Semiconductor Ltd. and have the standard RD50 features. In Table 7.1 are all irradiated samples listed and their position in the frame can be seen in Figure 7.13. The aim for the irradiation was to reach a fluence of $1 \times 10^{15} \text{ n}_{\text{eq}}/\text{cm}^2$. With the used beam energy of 12 MeV, a beam current of $0.2 \mu\text{A}$ and a movement velocity of the cold box of 4 mm/s a total of 160 scans



Figure 7.12.: Perspex after a few minutes of irradiation with 11 MeV protons.

were required. During the irradiation the box was kept cold at a set temperature of -46°C .

Position	Identifier	Position
A	Nickel foil 44 l	downstream
B	2328-15-1	downstream
C	2328-15-4	upstream
D	2328-15-2	downstream
E	2328-15-3	downstream
F	Nickel foil 45 l	upstream

Table 7.1.: Mounting configuration for first irradiation with a fluence of $1 \times 10^{15} \text{ n}_{\text{eq}}/\text{cm}^2$ for all devices.

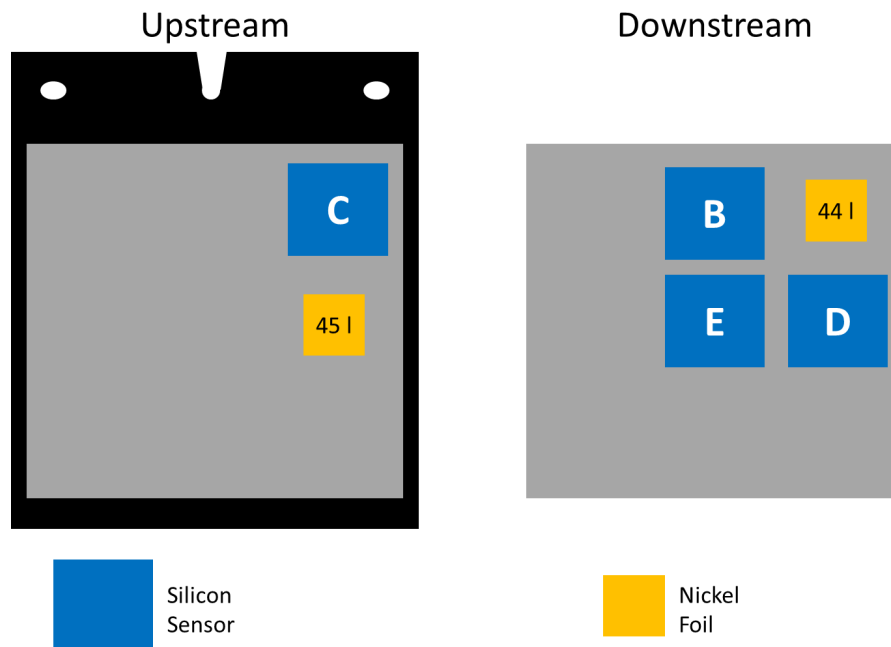


Figure 7.13.: Sketch of the mounting positions for the first Irradiation.

Dosimetry The dosimetry was done by John Wilson from the University of Birmingham [Wil16]. With the usual beam energy of 27 MeV Ni-57 is produced in the foil, which emits a characteristic gamma ray of 1377 keV. But with the lower beam energy this reaction does not occur. An alternative reaction produces Co-55 with a half-life time of 17.3 h and it emits several gamma rays, of which the most prominent has an energy of 931 keV. Measuring the nickel foil several times after the irradiation has shown that the reduction of the gamma peaks agreed well with the half-life of Co-55. But this has only worked for the foil before the absorber. The one downstream has

been measured as well and no gammas were observed; the activity was at the level of the background.

To achieve the target fluence a few conditions had to be taken into consideration: at an energy of a few MeV protons produce about five times more radiation damage¹ than at 27 MeV. However, from the simulation it could be seen that only about 10% of the protons reach the silicon sensor. Therefore twice as many initial protons are needed to get the target fluence after the absorber, which had to be taken into account when setting the number of scans. With an assumed proton energy of approximately 10.5 MeV at the nickel foil, the gamma spectroscopy 19 h after the irradiation resulted in a fluence of 0.84×10^{15} protons/cm².

7.1.4. Simulations after First Irradiation

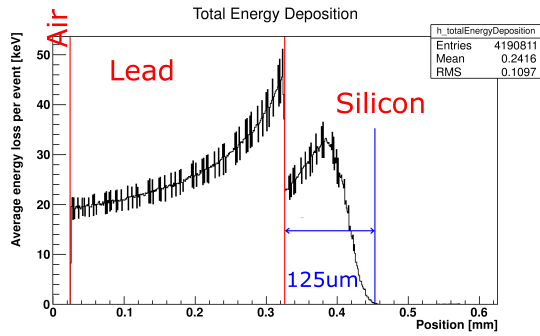
After the irradiation the beam pipe window was added into the simulation and the energy was set to 12 MeV. To see how much energy in each part of the target was lost, the sensitive volume was increased and included the nickel foil, the absorber and the silicon sensor. Four cases have been investigated, which were derived from the situation at the irradiation:

Case 1:	Lead	Silicon	Downstream	
Case 2:	Nickel	Lead		Silicon
Case 3:	Silicon	Lead		(Nickel)
Case 4:	Lead	Nickel		Silicon

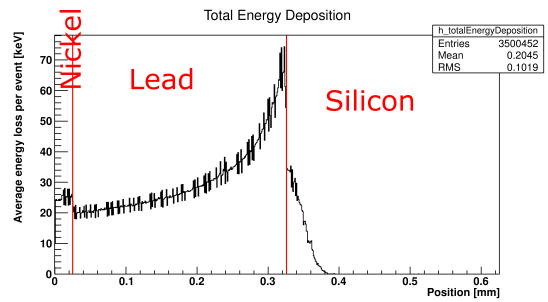
The first case resembles the irradiation where the silicon sensor was placed behind the absorber. Case two is similar to the nickel foil before the absorber, a silicon piece has been added to see how much energy is left after the protons pass the absorber. In the third case the sensor is placed upstream and it is expected that no protons reach the nickel foil downstream of the absorber. The last case was used to estimate how much energy the protons will have when they reach the nickel foil after the absorber. This could help to find a better material for the dosimetry by looking for something that can be activated with that energy.

Figure 7.14 shows the average energy loss in the different components for the four cases. In all pictures the Bragg peak is visible. It can also be seen that the energy loss in the different materials is different, resulting in larger steps in the distribution. From the graph of Case 1 (Figure 7.14a) it is clear that the protons can travel much further into the silicon sensor than planned. While a depth of approximately 20 μm was intended, the simulation shows the Bragg peak at approximately 50 μm and some protons penetrated more than 100 μm .

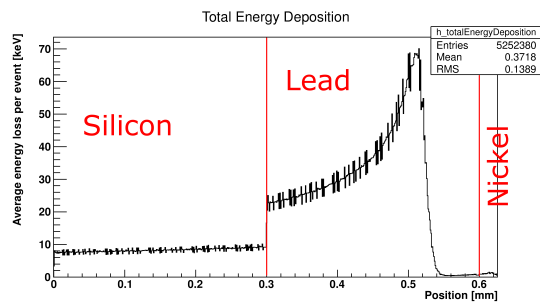
¹in terms of 1 MeV neutrons



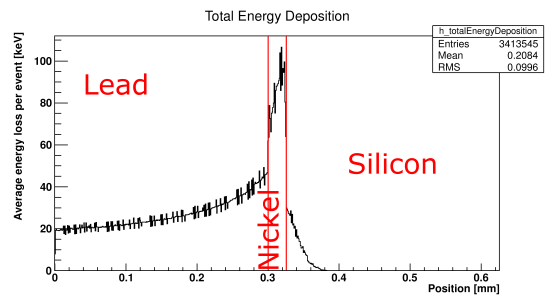
(a) Case 1



(b) Case 2



(c) Case 3



(d) Case 4

Figure 7.14.: Average Energy in the different components in the beam line for the four simulated cases.

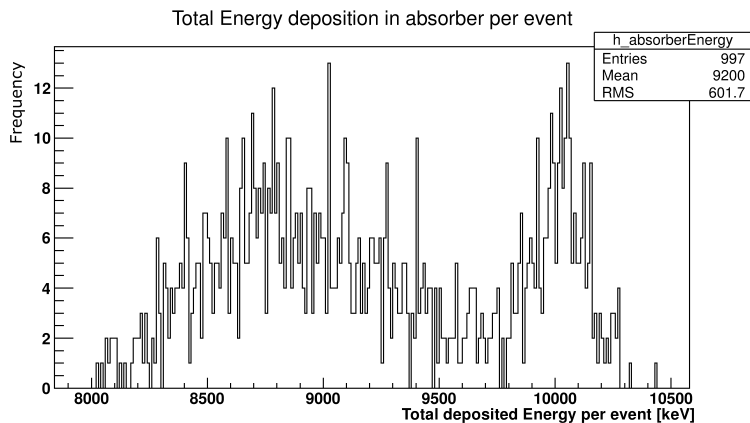


Figure 7.15.: Energy loss in lead for case two: Nickel - Lead - Silicon.

The total energy loss of each proton was filled in a histogram for each component and then fitted with the standard Gauss distribution of ROOT. Additionally the total energy loss of all protons has been fitted as well. The results can be seen in Table 7.2. For Case 2 there were two peaks in the lead histogram visible (see Figure 7.15). The reason could be that the protons have their Bragg peak in the absorber. For the analysis only the z-component of the particle tracks has been used. If a particle track is not perpendicular to the absorber plane the total path length is larger and therefore the particles may lose all their energy in the absorber which explains the peak at (10.00 ± 0.15) MeV. Those particles which reach the silicon sensor lose less energy in the absorber, resulting in the broader peak at (8.9 ± 0.5) MeV. It is noticeable that the total energy loss in all simulations is (10.75 ± 0.12) MeV, which means that from the (12.0 ± 0.1) MeV proton beam (1.25 ± 0.16) MeV are deposited in the beam pipe window, the Mylar windows and the air in-between. With this the proton energy in the nickel foil after the absorber (Case 4) can be calculated to (2.85 ± 0.35) MeV. Finding a material that can be activated by this energy would allow the dosimetry after the lead absorber.

Because the simulations have shown that after passing through the $300 \mu\text{m}$ absorber the protons reached more than $50 \mu\text{m}$ in the silicon sensor, new simulations were done to find a better absorber thickness. The beam energy was kept at 12 MeV and a nickel foil was added to the simulations, either before or after the absorber. In both cases the penetration depth is fairly similar. A small difference has been seen in the energy deposition spectrum (Figure 7.16). In the configuration where the nickel foil is placed after the absorber the distribution is slightly narrower. For the shown examples the absorber thickness was chosen to be $315 \mu\text{m}$ so that the majority of the protons is stopped within the first $20 \mu\text{m}$ in the silicon sensor and approximately 155 out of 1000 protons should reach the sensor.

Case	Energy loss [MeV]			
	1 st component	2 nd component	3 rd component	total
1		Lead 7.9 ± 0.3	Silicon 2.8 ± 0.4	10.75 ± 0.12
2	Nickel 0.61 ± 0.03	Lead 8.9 ± 0.5 10.00 ± 0.15	Silicon 1.3 ± 0.7	10.75 ± 0.12
3	Silicon 2.52 ± 0.08	Lead 8.23 ± 0.16	Nickel -	10.75 ± 0.12
4	Lead 7.9 ± 0.3	Nickel 2.2 ± 0.4	Silicon 1.0 ± 0.7	10.75 ± 0.12

Table 7.2.: Energy loss (from Gauss fit of the energy loss distribution) for simulated cases of 12 MeV protons and different absorber / silicon / nickel position configurations.

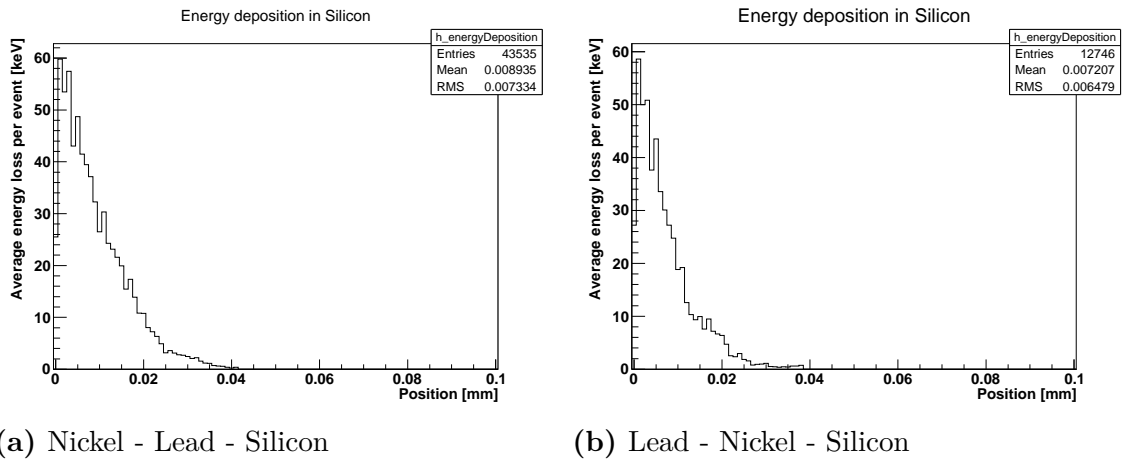


Figure 7.16.: Comparison of the energy loss of 12 MeV protons after a 315 μm thick lead absorber, depending on the 25 μm thick nickel foil position.

7.1.5. Second Irradiation in April 2016

For the second irradiation the beam parameters were kept the same as for the first: 12 MeV beam energy, 4 mm/s box movement speed and $0.2 \mu\text{A}$ beam current. A new lead absorber with a thickness of $315 \mu\text{m}$ was produced. The first task was to confirm that the absorber works and that protons can travel through it. For this purpose the absorber was placed in the beam line with a nickel foil behind it and at the end a Gafchromic film. According to the simulations, protons should be able to reach the film, but the tests with real protons have shown otherwise. It might be that the nickel absorbs too much of the energy so in a second test a different structure was chosen. The Gafchromic film was placed behind the absorber while half of the front was covered with a nickel foil. This would allow to use the foil for dosimetry of the incident protons. But in this test as well there was no change of colour of the Gafchromic film, meaning that no protons have passed the absorber.

The $300 \mu\text{m}$ thick absorber from the first irradiation was still available and a validation test with this was done. Like with the thicker absorber, the Gafchromic film was placed downstream of the absorber while half of the area was covered with a nickel foil placed upstream. A picture can be seen in Figure 7.17 (a). After the irradiation, discolourations of the Gafchromic film were visible (middle picture). The absorber position is highlighted with a white box. On the left side an unchanged band can be seen. Comparing the pictures it is clear that in this area the absorber was covered with Kapton tape to mount it. To the right of this a black band shows the area of the film that was only covered by the absorber. On the right side another unchanged area is visible, which is caused by the nickel foil. In this area two black lines can be recognized. Comparing the position with the absorber (Figure 7.17 (c)) it can be seen that there are large scratches in the lead. These were caused after the first irradiation when a scalpel was used to cut the Kapton and remove the nickel foil. The light discolouration in the left side of the absorber is most likely caused by a local thinning of the lead, which has the same effect as the scratches.

The conclusion from this validation test was that the $300 \mu\text{m}$ thick absorber works. Already the $25 \mu\text{m}$ thick nickel foil before the absorber provides enough material to stop all protons within the absorber. Additionally the same effect has been observed with a piece of Kapton foil. Small scratches provide sufficient absorber material loss to allow the protons to penetrate through lead and nickel and reach the object behind.

For the irradiation of the silicon sensors this has been kept in mind. Only parts of the absorber without scratches have been used. The original plan to use the nickel foil in a sandwich structure has been discarded. For the dosimetry the nickel foil was placed upstream with no silicon or absorber. For this irradiation different fluences were planned to investigate the effect on the collected charge. Because the same absorber as for the first irradiation was used the two additional fluences were $1 \times 10^{14} \text{ n}_{\text{eq}}/\text{cm}^2$ and $3 \times 10^{15} \text{ n}_{\text{eq}}/\text{cm}^2$. While the first was chosen to see low fluence

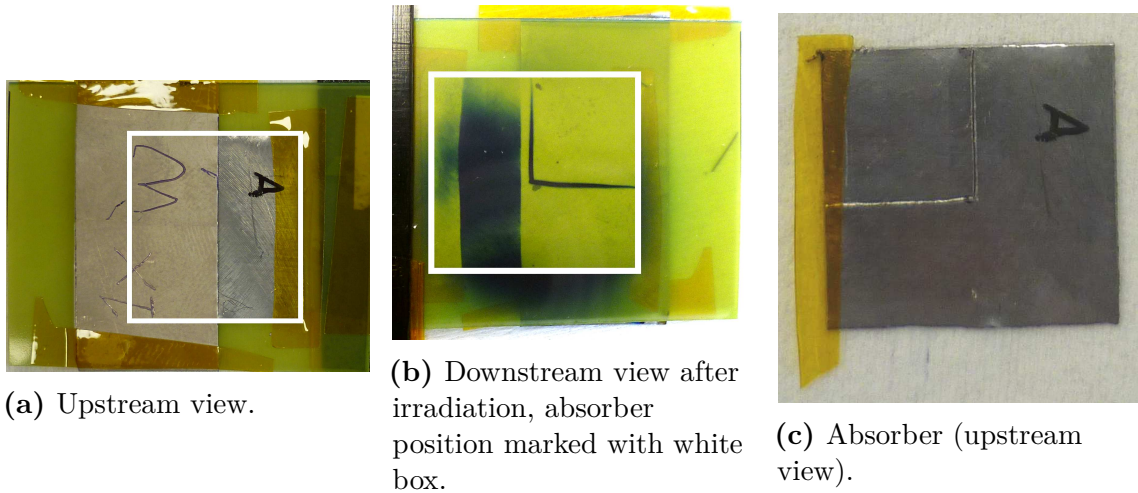


Figure 7.17.: Validation test of the 300 μm thick absorber for the second irradiation. The upstream view (left) shows the test construction like they would be seen by the protons. The downstream view shows the Gafchromic film after the irradiation, where the absorber position is highlighted with a white box. In the right picture the absorber is shown (upstream view).

effects, the higher one was limited by the irradiation time and the availability of the facility. A sketch of the mounting can be seen in Figure 7.18 while all used samples are summarized in Table 7.3.

Position	Identifier	Position	Fluence
1	Nickel foil 1k	upstream	
2	2328-16-1	downstream	$3 \times 10^{15} \text{ n}_{\text{eq}}/\text{cm}^2$
3	2328-16-2	downstream	
4	Nickel foil 2k	upstream	
5	2328-16-3	downstream	$1 \times 10^{14} \text{ n}_{\text{eq}}/\text{cm}^2$
6	2328-16-4	downstream	

Table 7.3.: Mounting configuration for second Irradiation

For the irradiation to $1 \times 10^{14} \text{ n}_{\text{eq}}/\text{cm}^2$ 16 scans were necessary while for $3 \times 10^{15} \text{ n}_{\text{eq}}/\text{cm}^2$ a total of 480 scans were done at two days. The box was cooled to -26°C and should have been kept at that temperature over night. A cooling failure resulted in warming up the sensors to room temperature for several hours, but this would have no major effect on the results.

After the irradiation the failure of the 315 μm thick absorber was further investigated. A possible explanation could be the type of Gafchromic film, that was used. The standard film is EBT3 [Ash16], which works fine for a 27 MeV proton

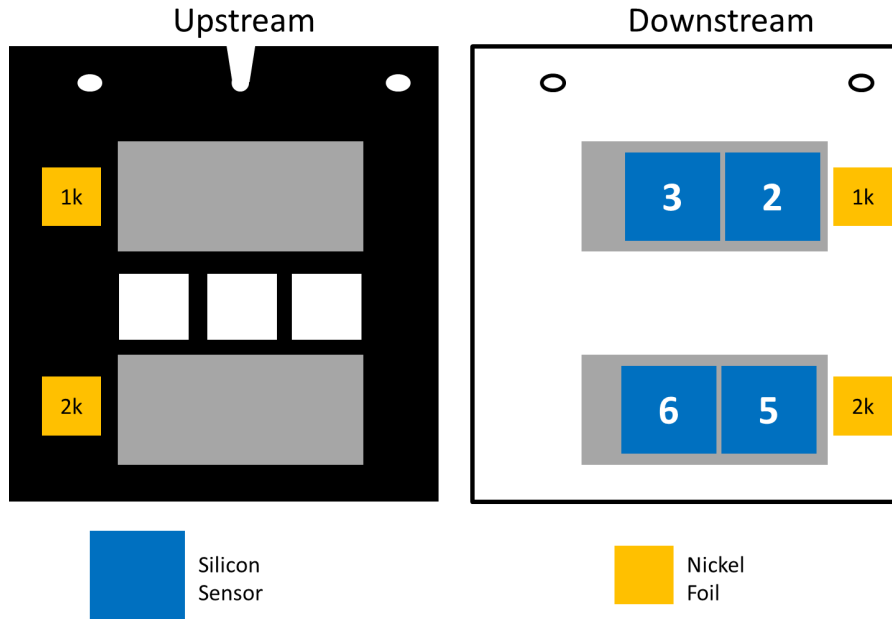


Figure 7.18.: Mounting for second irradiation.

beam. With the low energy and the attenuation in the absorber, the sensitivity and construction of the film becomes crucial. Figure 7.19a shows the cross section of this film. The sensitive material is covered with a $125\ \mu\text{m}$ thick polyester base on each side. The low energy protons after the lead absorber could be stopped within this layer and therefore not reach the active layer. According to the data sheet there is minimal response difference from $100\ \text{keV}$ into the MeV range. Therefore proton energies below $100\ \text{keV}$ do not lead to a reliable discolouration of the film. An alternative to EBT3 would be HD-V2, which has no polyester on one side (see Figure 7.19b) and therefore the full proton energy after the absorber is available in the active layer.

Geant4 simulations have been used to determine the proton energy in the active layer. For the polyester layer the material `G4_POLYETHYLENE` was used, which should resemble the same material properties. The simulations, shown in Figure 7.20, indicate that for the $300\ \mu\text{m}$ thick lead absorber the energy of the protons after passing the $125\ \mu\text{m}$ polyethylene layer is high enough to discolour the active material. For the $315\ \mu\text{m}$ thick absorber the remaining energy, indicated by the green area, is too low to result in a colour change of the film. These simulations lead to the conclusion that the $315\ \mu\text{m}$ thick lead absorber can be used, but the Gafchromic film was not suitable for this low beam energy application.

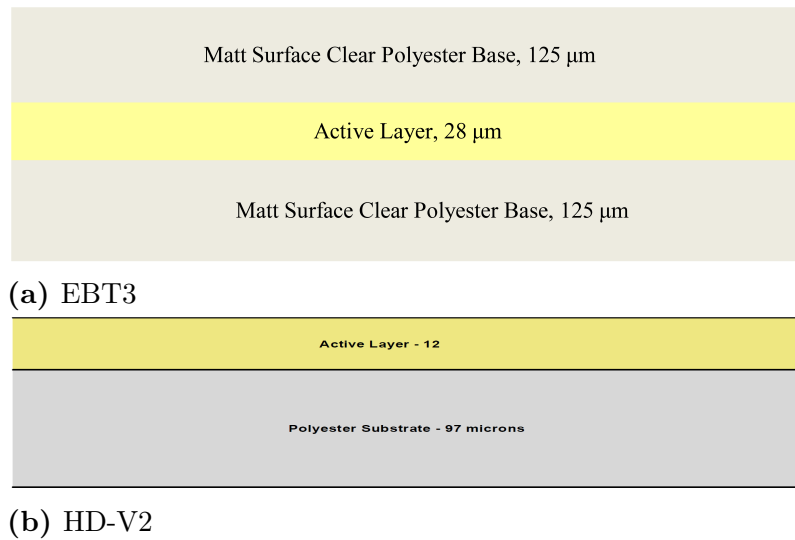


Figure 7.19.: Cross section of Gafchromic films. EBT3 has been used as the standard film, while HD-V2 would be a good alternative for the low energy irradiations where no polyester film is before of the sensitive material. (Figures form [Ash16])

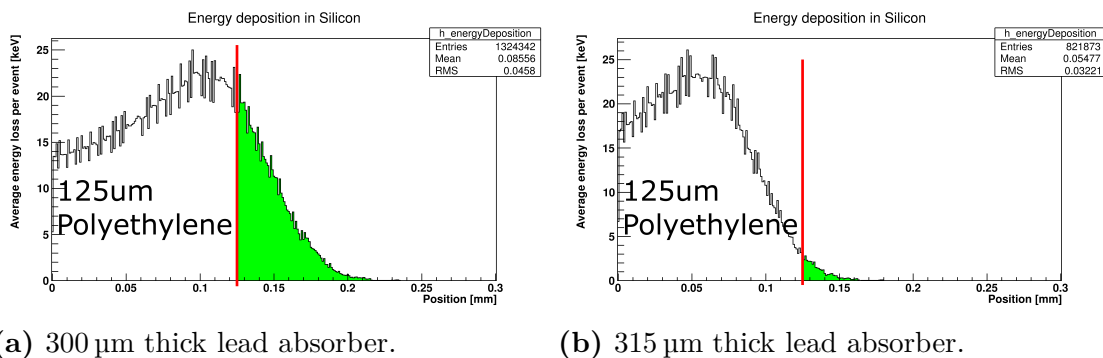


Figure 7.20.: Geant4 simulation of energy loss in Gafchromic film. The film has a 125 μm thick polyethylene layer before the active material. Protons need to pass this and have sufficient energy to cause discolouration. For 300 μm of lead enough energy is left (green area) while for the 315 μm thick absorber the energy loss is too high.

7.2. Measurement Results

The collected charge of all samples has been measured with the ALiBaVa system (section 3.2) after the irradiation at Birmingham. Additionally some sensors were irradiated at Ljubljana with neutrons to fluences of $1 \times 10^{15} \text{ n}_{\text{eq}}/\text{cm}^2$ and $5 \times 10^{15} \text{ n}_{\text{eq}}/\text{cm}^2$.

7.2.1. Measurements after Birmingham Irradiation

Figure 7.21 shows the collected charge after the creation of the damage layer at Birmingham. An unirradiated reference sample (red) has been added and it can be seen that the collected charge after irradiation decreases by more than a factor two. A peculiarity is the difference in the voltage dependence for the upstream sensor (black) compared to the other samples. While all downstream sensors have a nearly flat trend, the collected charge increases with increasing bias voltage for the upstream sample. The increase is comparable to measurements of other irradiated devices (see for example chapter 4 Figure 4.6).

Figure 7.22 shows only the downstream samples: A clear fluence dependence can be seen with the highest fluence having the lowest collected charge. This is in agreement with the classic expectation. All three samples irradiated to $1 \times 10^{15} \text{ n}_{\text{eq}}/\text{cm}^2$ show good agreement within 0.5 ke^- . The sensors from the second irradiation show a difference for those irradiated to the same fluence. For both fluences the blue curves show a higher collected charge than the green.

A systematic issue could be assumed. This becomes clear when looking at the position of the sensors in the cold box. The samples with the higher collected charge are those which were furthest away from the nickel foils and therefore the 'Home'

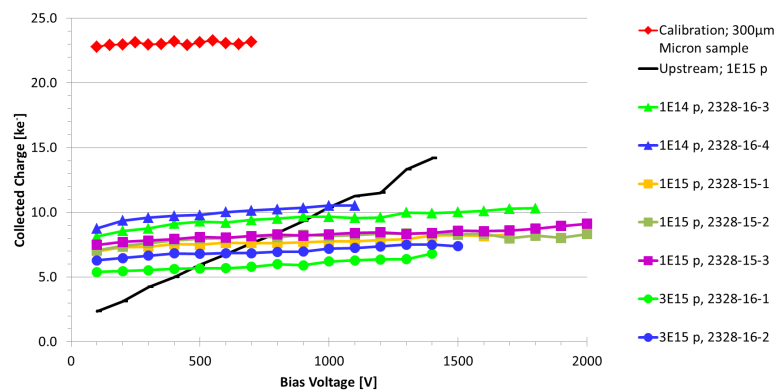


Figure 7.21.: Collected charge of all sensors after the Birmingham irradiation. Additionally a unirradiated calibration sample has been included with a collected charge of approximately 23 ke^- .

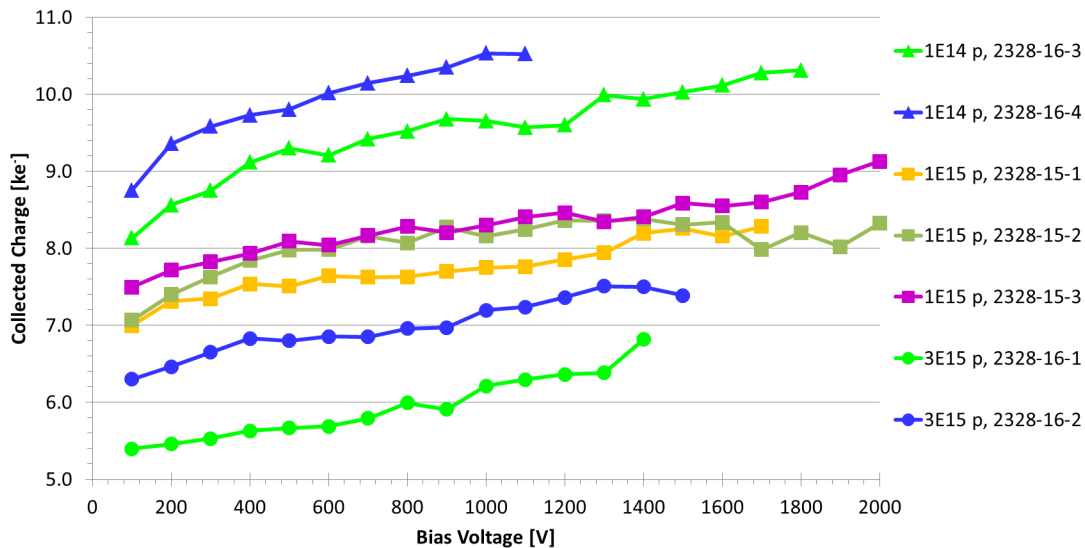


Figure 7.22.: Collected charge of all downstream sensors after the Birmingham irradiation.

position. In Figure 7.23 a simplified scan path for the $3 \times 10^{15} \text{ n}_{\text{eq}}/\text{cm}^2$ irradiation has been drawn on to a picture of the samples. The box is moved so that the proton beam, depicted as yellow square, follows the white lines from the ‘Home’ position to irradiate the whole area. After the last point the beam follows the purple line to go back to ‘Home’. In the picture the nickel foil can be seen on the left side of the mounting frame, while the silicon sensors are covered by the lead absorber, in the area without Kapton. At the left edge the proton beam starts completely outside of the nickel area and is then moved across the whole length to the right side. But here instead of moving to the point where the whole yellow square has passed the silicon area, it stops above the sensors to then move down and continue the scan. At the end the beam is moved across the outer right edge of the sensors to reach the ‘Home’ position. The usual way of the irradiation is to move the beam out of the sensor area before moving up or down to make sure the whole silicon area is irradiated uniformly. In this case it would be a justifiable assumption that the sensors on the right side have not reached the full fluence. This is supported by the collected charge measurements where they show more collected charge than the sensors in the centre of the scan path.

The sensor 2328-15-1, irradiated to $1 \times 10^{15} \text{ n}_{\text{eq}}/\text{cm}^2$ was annealed for 80 minutes at 60°C . While the other sensors from the same irradiation were stable up to 2000 V, this sample has shown high noise in several channels which affected the applied maximum voltage. After annealing the maximum voltage, that could be used, decreased even further. Figure 7.24 shows the collected charge of this sample before and after annealing and no significant difference can be seen. This is contrary to the expectation, where an increase in the charge for this beneficial annealing is expected for

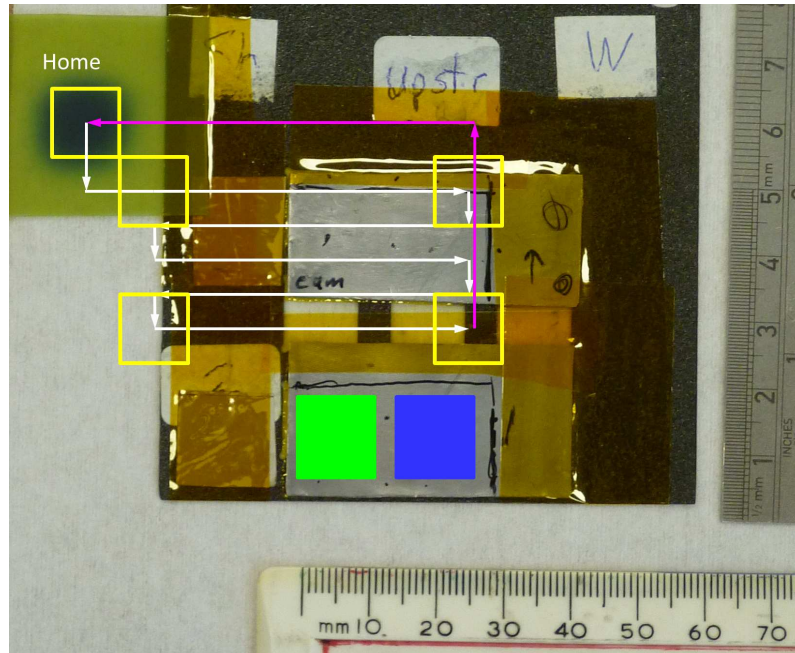


Figure 7.23.: Scan path for the irradiation to $3 \times 10^{15} n_{\text{eq}}/\text{cm}^2$. The proton beam, depicted as yellow square, is moved along the white lines to irradiate the sample. At the last point the box is moved in the down and then horizontal so that the beam follows the purple line. The sensor positions are indicated by the green and blue squares as an example in the lower part, but they are at the same position for the upper absorber (see Figure 7.18).

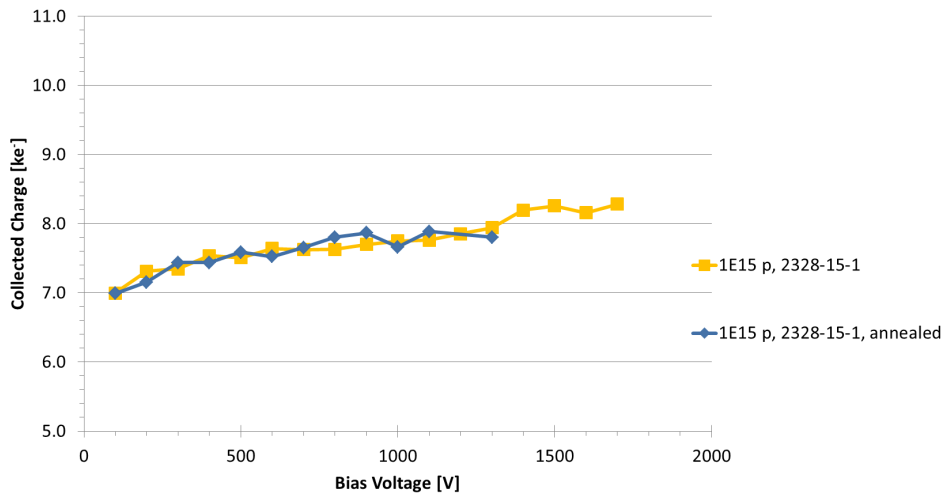


Figure 7.24.: Collected charge before and after annealing for sensor placed after the lead absorber and irradiated to $1 \times 10^{15} \text{ n}_{\text{eq}}/\text{cm}^2$ with protons.

voltages lower than the full depletion voltage. Additionally a decrease of the reverse bias current could be expected as well, which can not be seen in Figure 7.25.

7.2.2. Measurements after Ljubljana Irradiation

To see if the creation of the shallow radiation damages in the silicon sensor are beneficial for the charge collection, they were irradiated at Ljubljana to $1 \times 10^{15} \text{ n}_{\text{eq}}/\text{cm}^2$ and $5 \times 10^{15} \text{ n}_{\text{eq}}/\text{cm}^2$. For each fluence a control sample without damage layer was irradiated as well to compare the measurement results.

In Figure 7.26 the collected charge of the $1 \times 10^{15} \text{ n}_{\text{eq}}/\text{cm}^2$ upstream sensor is shown in comparison to the neutron irradiated reference samples. Both reference samples show the expected increase of the collected charge with increasing bias voltage. The charge of the upstream sensor is located between the two reference sensors, which indicates that the achieved fluence at Birmingham was higher than the target fluence. Because the upstream sensor received protons with a energy close to 12 MeV (no lead absorber) they pass through the silicon sensor like in a standard irradiation. This is supported by the reverse bias current, shown in the same figure on the right side. The current of the upstream sensor is higher than that of the $1 \times 10^{15} \text{ n}_{\text{eq}}/\text{cm}^2$, but lower than the $5 \times 10^{15} \text{ n}_{\text{eq}}/\text{cm}^2$ reference sample.

$1 \times 10^{15} \text{ n}_{\text{eq}}/\text{cm}^2$ neutron irradiation Figure 7.27 shows the collected charge of the sensors with the three different proton fluences after $1 \times 10^{15} \text{ n}_{\text{eq}}/\text{cm}^2$ neutron irradiation (green diamond). In each graph the neutron only irradiated reference sensor (black triangles) is shown as well as the collected charge after proton irradiation.

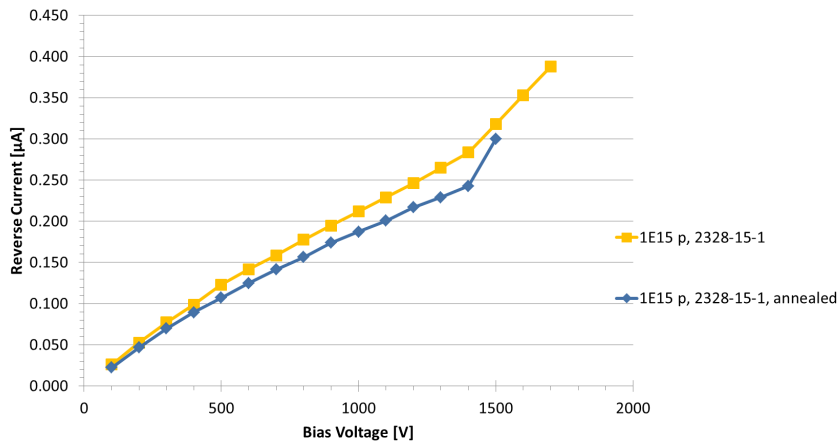


Figure 7.25.: Reverse bias current before and after annealing of 80 min at 60°C for the sensor placed after the lead absorber and irradiated to $1 \times 10^{15} \text{ n}_{\text{eq}}/\text{cm}^2$ with protons.

tion (blue squares). For all devices the collected charge after combined proton and neutron irradiation is smaller than the reference sample. While after the proton irradiation the charge is fairly stable with increasing bias voltage, the expected increase is observed for all neutron irradiated samples. All sensors reach the charge after proton irradiation at voltages higher than approximately 1000 V. It can be seen that the $1 \times 10^{14} \text{ n}_{\text{eq}}/\text{cm}^2$ and $1 \times 10^{15} \text{ n}_{\text{eq}}/\text{cm}^2$ sensors even exceed the initial collected charge at very high voltages. This could be caused by charge multiplication. It was not possible to bias the $3 \times 10^{15} \text{ n}_{\text{eq}}/\text{cm}^2$ sample above 1100 V to investigate whether this can be observed at high fluences as well.

The $1 \times 10^{15} \text{ n}_{\text{eq}}/\text{cm}^2$ sample was annealed after the neutron irradiation for 80 minutes at 60°C. The results are shown in the middle plot in red circles. Up to 1000 V the expected behaviour is observed: the collected charge is higher than before the annealing with a higher increase between 300 V and 800 V before reaching a plateau at high voltages at similar values then before the annealing. The excess, that was

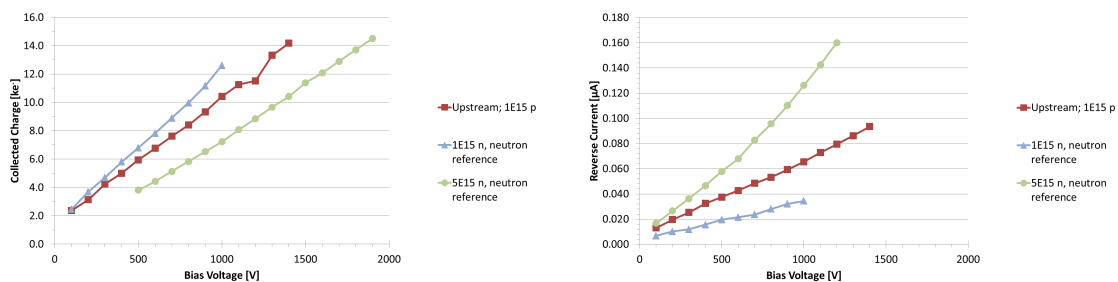


Figure 7.26.: Collected charge (left) and current (right) comparison of $1 \times 10^{15} \text{ n}_{\text{eq}}/\text{cm}^2$ upstream sensor with $1 \times 10^{15} \text{ n}_{\text{eq}}/\text{cm}^2$ and $5 \times 10^{15} \text{ n}_{\text{eq}}/\text{cm}^2$ neutron irradiated reference samples.

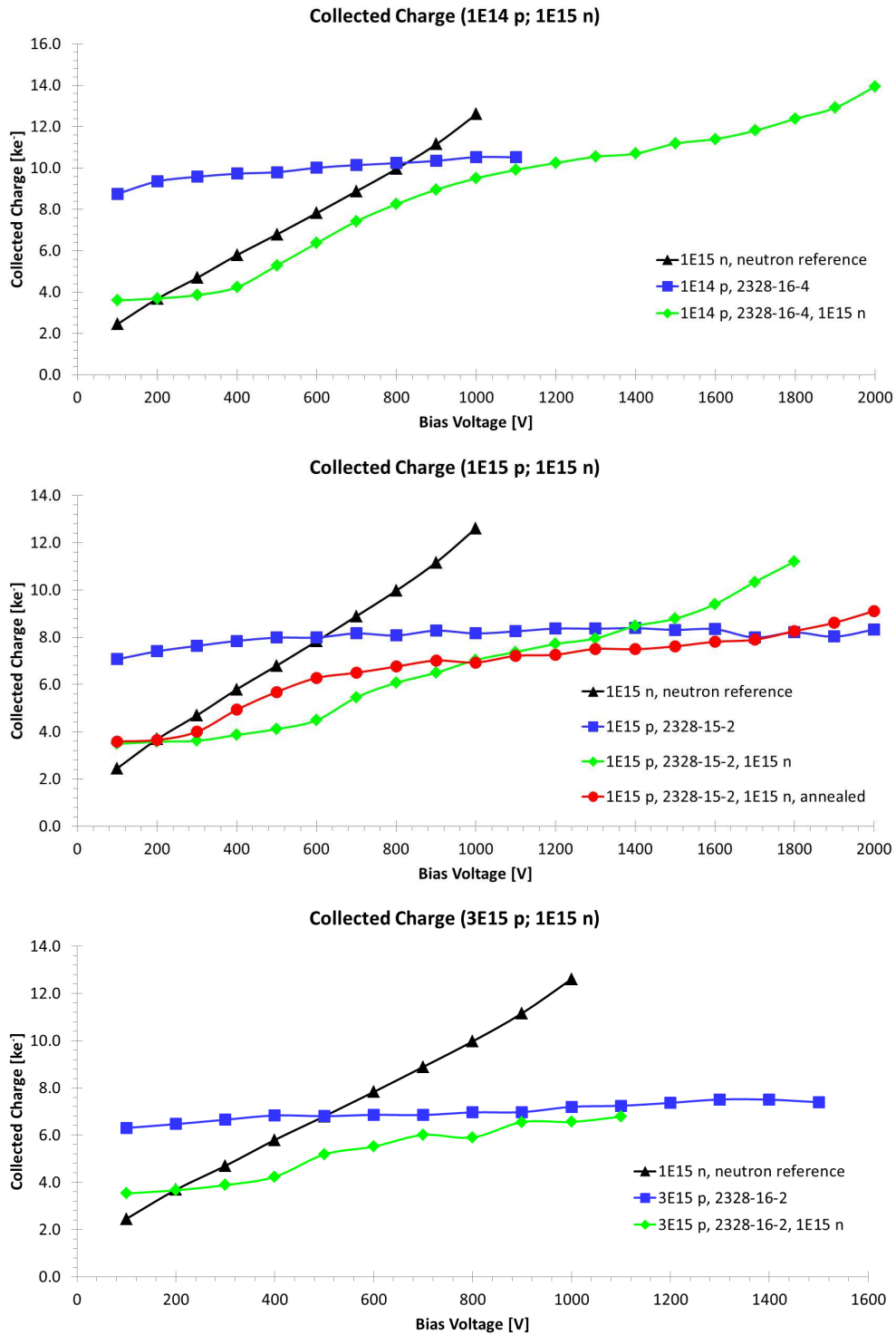


Figure 7.27.: Collected charge after $1 \times 10^{15} \text{ n}_{\text{eq}}/\text{cm}^2$ neutron irradiation. Top: $1 \times 10^{14} \text{ n}_{\text{eq}}/\text{cm}^2$ proton irradiation; Middle: $1 \times 10^{15} \text{ n}_{\text{eq}}/\text{cm}^2$ proton irradiation; Bottom: $3 \times 10^{15} \text{ n}_{\text{eq}}/\text{cm}^2$ proton irradiation. Black: neutron irradiated reference sample; Blue: after proton irradiation; Green: after proton and neutron irradiation.

observed at very high voltages disappeared and the values are in good agreement with the collected charge after proton irradiation.

The reverse bias current of the sample that was irradiated to $1 \times 10^{15} \text{ n}_{\text{eq}}/\text{cm}^2$ with protons and neutrons is shown in Figure 7.28. The neutron irradiated reference sensor shows the lowest reverse bias current. After proton irradiation the current is approximately five times higher. An unexpected evolution can be seen: the current is highest directly after proton irradiation while it decreases with additional neutron irradiation. This behaviour was observed for all samples regardless of the irradiation fluences. For the lower fluences the difference is more prominent, while it nearly disappears for the samples that were irradiation with protons to $1 \times 10^{15} \text{ n}_{\text{eq}}/\text{cm}^2$ and $3 \times 10^{15} \text{ n}_{\text{eq}}/\text{cm}^2$ and neutrons to $5 \times 10^{15} \text{ n}_{\text{eq}}/\text{cm}^2$. From previous studies it was shown that the reverse bias current increases with increasing irradiation fluence, which has also been shown in chapter 6. Therefore it would be expected that the current is highest after the combined irradiation. After annealing the current should decrease (section 2.4.3), but the reverse bias current for this sample has stayed at the same values for up to 1000 V and then even increases slightly for higher bias voltages.

$5 \times 10^{15} \text{ n}_{\text{eq}}/\text{cm}^2$ neutron irradiation The irradiation with neutrons to a fluence of $5 \times 10^{15} \text{ n}_{\text{eq}}/\text{cm}^2$ results in the collected charge plots shown in Figure 7.29. All sensors follow the observed behaviour: the collected charge after neutron irradiation is smaller than that of the reference sample, but the charge increases with increasing voltage. Due to the higher neutron fluence the charge level after proton irradiation is only reached by the sensor with the lowest proton fluence at 1800 V.

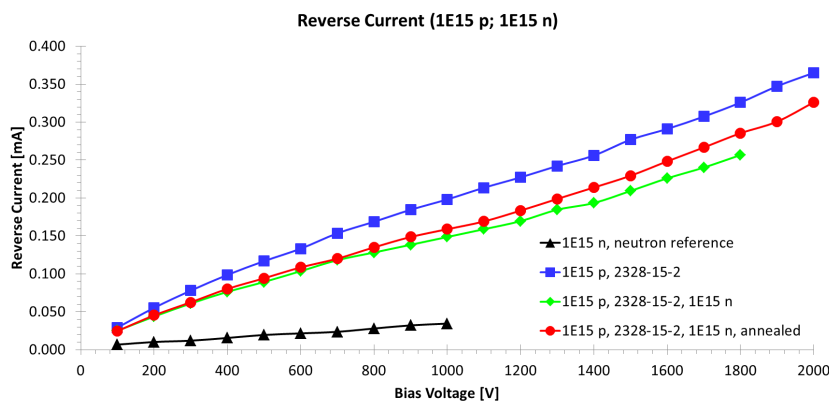


Figure 7.28.: Reverse bias current after irradiation with $1 \times 10^{15} \text{ n}_{\text{eq}}/\text{cm}^2$ protons (blue square) and $1 \times 10^{15} \text{ n}_{\text{eq}}/\text{cm}^2$ neutrons (green diamond). After neutron irradiation the sample was annealed as well (red circle). The black triangles show the neutron irradiated reference sample.

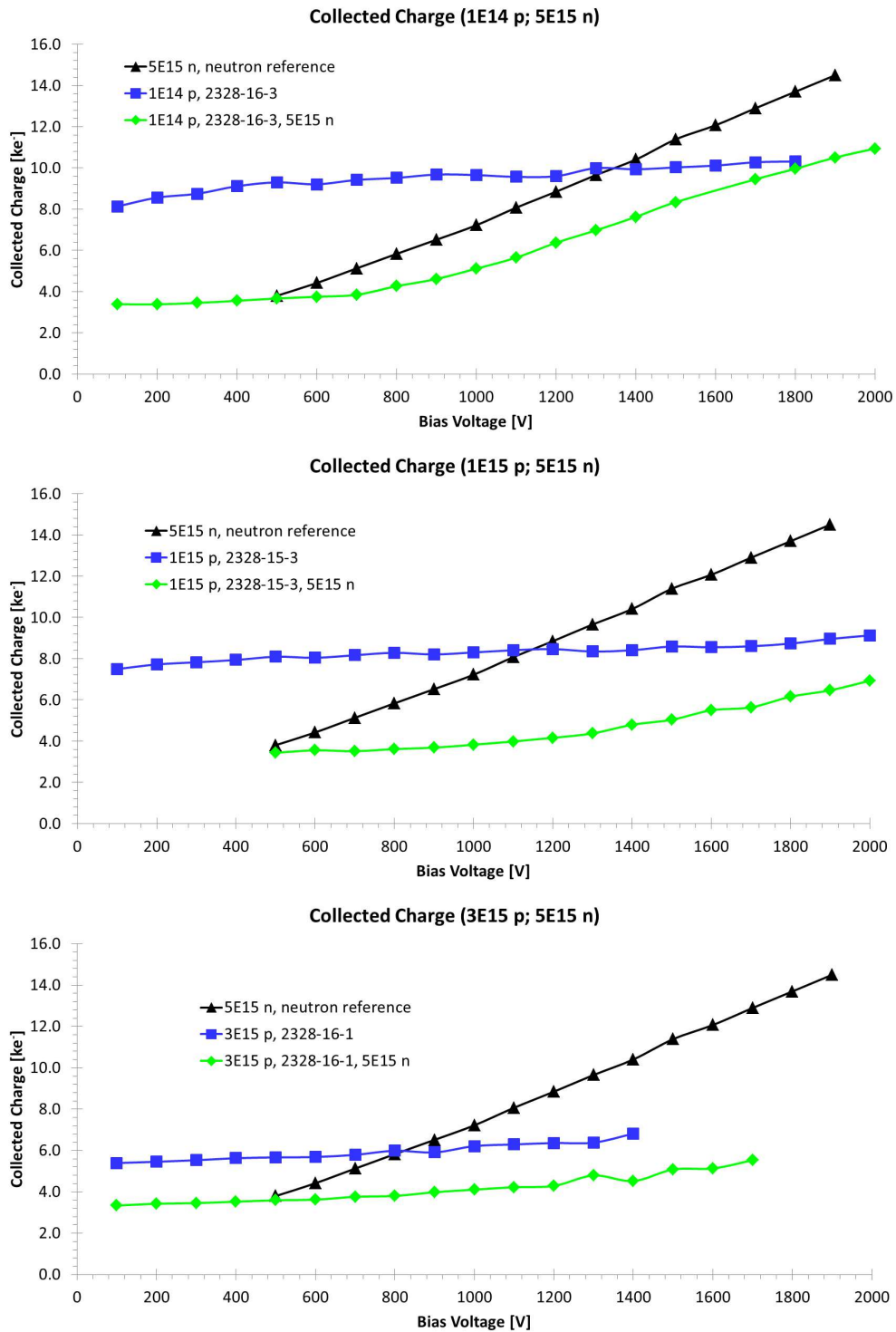


Figure 7.29.: Collected charge after $5 \times 10^{15} n_{eq}/cm^2$ neutron irradiation. Top: $1 \times 10^{14} n_{eq}/cm^2$ proton irradiation; Middle: $1 \times 10^{15} n_{eq}/cm^2$ proton irradiation; Bottom: $3 \times 10^{15} n_{eq}/cm^2$ proton irradiation. Black: neutron irradiated reference sample; Blue: after proton irradiation; Green: after proton and neutron irradiation.

7.3. Summary

The aim of the study presented in this chapter was the generation of a shallow radiation damage layer close to the strip surface of a silicon sensor. To do this they were irradiated at the proton cyclotron at Birmingham. Planning this irradiation required to simulate the beam line with Geant4 to find the optimal parameters for the beam energy and the absorber thickness. For the first irradiation a 300 μm thick lead absorber as well as a 1000 μm thick perspex absorber were produced. In both cases the simulated protons passed through the absorber and travelled approximately 20 μm into the silicon sensor before losing all their energy. While the simulation results required a individual beam energy between 11 MeV and 12 MeV, the conditions at the Birmingham cyclotron changed the plan.

For the irradiations a 12 MeV proton beam was used due to the availability of the machine settings and a failed initial test at 11 MeV. In a test over few minutes the perspex absorber melted, showing that this material is not suitable for this study. Four samples have been irradiated to a fluence of $1 \times 10^{15} \text{ n}_{\text{eq}}/\text{cm}^2$ with the lead absorber. While three have been placed after the absorber, the fourth was placed before as a control sample. Simulating all conditions showed a damage layer width of more than 100 μm .

Further simulations for a new irradiation, incorporating all beam line details and the energy of 12 MeV, showed that good results could be achieved with a 315 μm thick absorber. Testing this with protons showed no response in the Gafchromic film that was used for the beam verification. This might have been caused by the structure of the film, which has a 125 μm thick layer of polyethylene before the active material, which absorbed most of the proton energy. A different film type without polyethylene should be used for further tests. Because this was not known at the irradiation, the 300 μm thick lead absorber was used to irradiate four silicon sensors to $1 \times 10^{14} \text{ n}_{\text{eq}}/\text{cm}^2$ and $3 \times 10^{15} \text{ n}_{\text{eq}}/\text{cm}^2$, with two samples at each fluence.

Measurements with the ALiBaVa system have shown that the collected charge decreases with increasing irradiation fluence. Instead of having a strong voltage dependence, like the upstream sample, the collected charge is fairly stable up to 2000 V. The two samples per fluence of the second irradiation have shown a difference in the collected charge for the same fluence. It can be assumed that this was caused by the scanning mechanism where the box has not moved far enough to guarantee a uniform irradiation for one of the samples.

The sensors have been further irradiated with neutrons at Ljubljana to fluences of $1 \times 10^{15} \text{ n}_{\text{eq}}/\text{cm}^2$ and $5 \times 10^{15} \text{ n}_{\text{eq}}/\text{cm}^2$. Comparing the upstream sample with reference sensors has shown that the collected charge indicates the fluence was higher than the target of $1 \times 10^{15} \text{ n}_{\text{eq}}/\text{cm}^2$ but lower than $5 \times 10^{15} \text{ n}_{\text{eq}}/\text{cm}^2$. For all downstream sensors the collected charge was lower than the reference sample for all voltages. After $1 \times 10^{15} \text{ n}_{\text{eq}}/\text{cm}^2$ neutron irradiation some sensors have shown an

increased collected charge at very high voltages, compared to the values after proton irradiation. One sample was annealed for 80 minutes at 60°C and the excess disappeared in the following measurement.

The two irradiations have deepened the understanding of the Birmingham beam line for low energy irradiations. While the target depth of 10 to 20 μm for the damage layer has not been reached, the knowledge from the past tests is sufficient to achieve this in a future irradiation. The results from the collected charge measurements have not shown the desired charge multiplication at low bias voltages and the flat collected charge vs bias voltage behaviour is not understood.

8. Summary and Conclusion

Silicon strip sensors are widely used in current high energy physics experiments, including ATLAS, CMS, LHCb and ALICE at the Large Hadron Collider at CERN. For the high luminosity upgrade in 2022/2023 the sensors in ATLAS and CMS will be replaced. New technologies are under investigation so that the sensors can cope with the expected high radiation levels of up to $2 \times 10^{16} \text{ n}_{\text{eq}}/\text{cm}^2$. The topic of this thesis is the characterisation of irradiated planar silicon strip sensors for HL-LHC applications.

In chapter 4 different strip configurations have been investigated to utilize the charge multiplication effect. This can be beneficial for irradiated sensors by increasing the signal, that suffers from radiation damage. For this study the readout-strip pitch as well as the strip width have been changed. Some sensors have been produced with additional intermediate strips which were not read out, but were left floating or were connected to the bias ring. In the sensor production some of the steps have been modified: the implantation energy or the diffusion time was doubled. Most sensors were of the standard thickness of $305 \mu\text{m}$, but some have been only $150 \mu\text{m}$ thin. The collected charge of the sensors has been measured after proton irradiation to $1 \times 10^{15} \text{ n}_{\text{eq}}/\text{cm}^2$ and neutron irradiation to $1 \times 10^{15} \text{ n}_{\text{eq}}/\text{cm}^2$ and $5 \times 10^{15} \text{ n}_{\text{eq}}/\text{cm}^2$. A few have been annealed at room temperature up to 785 days.

Neither the unirradiated nor the proton irradiated sensors have shown signs of charge multiplication. After $1 \times 10^{15} \text{ n}_{\text{eq}}/\text{cm}^2$ neutron irradiation only one sensor (P80-W25, standard) has shown an increase in the collected charge. At this fluence only standard sensors were available. At $5 \times 10^{15} \text{ n}_{\text{eq}}/\text{cm}^2$ neutron irradiation different strip geometries as well as production types have been investigated. The lowest collected charge has been measured with the standard sensors. Thin sensors had higher collected charge at low bias voltages, but the values saturated at the expected value for unirradiated sensors. At voltages higher than 800 V , sensors with double diffusion energy showed the highest collected charge. Sensors with and without intermediate strips have been compared: sensors with biased intermediate strips have less collected charge than sensors without. For floating intermediate strips the results were not conclusive. The comparison of different width-over-pitch (W/P) ratios has indicated that a lower W/P ratio is better at high voltages, especially for double implant energy wafers. From these results it can be seen that sensors with a strip pitch of $80 \mu\text{m}$ and a strip width of $6 \mu\text{m}$ collect more charge than sensors with

a higher strip width. This can be improved by approximately 20% by doubling the implant energy.

Room temperature annealing of the neutron irradiated sensors has shown that at $1 \times 10^{15} \text{ n}_{\text{eq}}/\text{cm}^2$ the sensors behave as expected and show beneficial annealing, followed by reverse annealing. For the higher fluence the collected charge for bias voltages well above 1000 V increases at all annealing steps. At the same time the noise increases as well which is in good agreement with the expected behaviour for charge multiplication. Some of these devices were tested with a continuous application of high bias voltage ($>1000 \text{ V}$) for several days. This showed that the higher collected charge decrease with increasing measurement time. One possible explanation could be accumulated surface charge from the radioactive source. Measuring the device with an α -source pointing at the backside of the sensor could exclude this, but this requires changes of the ALiBaVa system that could not be implemented at Liverpool.

The material budget is one of the main parameters when designing a detector system. For silicon sensors it can be improved by using thinner sensors. While they require less bias voltage to fully deplete, the collected charge is smaller due to the reduced thickness. In chapter 5 measurements of $50 \mu\text{m}$ thick sensors are shown. They have been irradiated with neutrons up to $2 \times 10^{16} \text{ n}_{\text{eq}}/\text{cm}^2$. Up to $5 \times 10^{15} \text{ n}_{\text{eq}}/\text{cm}^2$ the collected charge reaches a plateau at a value comparable with an unirradiated sensor. For higher irradiation fluences the analysis of the ALiBaVa results becomes challenging due to random noise peaks being misidentified as signal peaks. Only at high bias voltages is a clear separation possible. The standard analysis method uses a convoluted Landau-Gauss distribution to fit the signal peak. To improve this new methods have been tested: in an iterative approach the noise peak was first fitted with a Gauss function and then subtracted from the total data set. The remaining signal data was fitted with the standard Landau-Gauss. In the second iteration the fitted signal was subtracted from the original total data and a new Gauss fit of the noise peak was performed. This has been subtracted from the total data and the remaining signal data has been fitted again with the convoluted Landau-Gauss to get the final signal value. In a third method the fit function was changed by adding a Gauss distribution to the Landau-Gauss for fitting the noise peak and the signal peak with a single function, taking into account that the signal might only appear as larger tail in the Gaussian noise peak.

Testing the methods with simulated data has shown that the new fit function (Gauss + Landau-Gauss) gives the best results, while with the iterative method the fitted signal value was higher than the value from the simulation parameters. Additionally all methods have been used to analyse real data. For low fluences all methods result in the same value, but they differ at higher fluences ($>5 \times 10^{15} \text{ n}_{\text{eq}}/\text{cm}^2$). The results from the iterative method are always the highest, while the standard method result in the lowest values, especially for the sensor irradiated to the highest

fluence of $2 \times 10^{16} \text{ n}_{\text{eq}}/\text{cm}^2$. While the obtained values follow a smooth curve for low fluences, the shape unsystematic for high fluences.

Annealing the sensor irradiated to $2 \times 10^{16} \text{ n}_{\text{eq}}/\text{cm}^2$ shows that the curve becomes smoother with increasing annealing time, but the observed differences of the analysis methods remain. The sensor was annealed at room temperature up to 30 days and it has been shown that the collected charge increases at each annealing step, which is caused by beneficial annealing. A second sensor, irradiated with protons to $1.98 \times 10^{16} \text{ n}_{\text{eq}}/\text{cm}^2$, shows a constant decrease of the collected charge due to reverse annealing.

The results in chapter 5 have shown that the measurement of the collected charge with the ALiBaVa system becomes challenging for high irradiation fluences and $50 \mu\text{m}$ thin sensors because the signal peak can not clearly be separated from the noise peak. Using a modified fit function can improve the analysis and results in a slightly higher charge values. The iterative method also result in higher signal values, but also for simulated data so that it can be concluded that this method is not reliable in finding the true collected charge value. It should be possible to improve the measurement by using a read-out chip with a lower electronic noise value, but this can not compensate for random noise peaks that create a fake signal.

While the strip geometry of a sensor is important for the signal of a passing charged particle, the design of a detector system requires the knowledge of the expected reverse bias current at a certain voltage and irradiation fluence to plan the powering scheme. It has been shown that the current of a silicon sensor can be scaled to different temperatures and this scaling depends on the effective energy E_{eff} . Additionally a relationship of the reverse bias current and the irradiation fluence has been found with the current related damage rate α as scaling parameter. The literature values for these variables have been determined for fluences up to $1 \times 10^{15} \text{ n}_{\text{eq}}/\text{cm}^2$. The study presented in chapter 6 had the aim to investigate these parameters for higher fluences up to $2 \times 10^{16} \text{ n}_{\text{eq}}/\text{cm}^2$. To do this planar silicon strip sensors with different thicknesses (50, 108, 143 and $293 \mu\text{m}$) have been irradiated from $1 \times 10^{12} \text{ n}_{\text{eq}}/\text{cm}^2$ to $2 \times 10^{16} \text{ n}_{\text{eq}}/\text{cm}^2$.

One first result from the direct comparison of the reverse bias currents at one fluence for sensors with different thicknesses was that at very high fluences the current per sensor area becomes independent of the sensor thickness and has a nearly linear voltage dependence.

The effective energy has been calculated for each device by measuring it at two different temperatures and reversing the current scaling equation. For some sensors it has been shown that the value is constant for the used bias voltage range from 0 V to 1000 V (500 V for $50 \mu\text{m}$ thick sensors). But for others it increases or decreases. Therefore different E_{eff} values have been used for the further analysis.

Plotting the effective energy as function of the fluence indicates that up to approximately $1 \times 10^{15} \text{ n}_{\text{eq}}/\text{cm}^2$ the values are comparable with the literature value. For higher fluences E_{eff} decreases with increasing fluence. The measurements have been repeated after room temperature annealing steps of 10 days and 30 days with no change in the observed behaviour. A second set of sensors from the same irradiation (and when possible from the same wafer) has been measured at the University of Freiburg, Germany. There the effective energy stays constant for all fluences at a value comparable with the literature value. Several comparison tests have been done, including the exchange of sensors, and it has been shown that all measurements at one site are self-consistent, but measuring the same device at the two sites result in different values for the highly irradiated devices. This indicates a systematic difference between the two measurement setups, which has to be investigated further. In the current scaling equation the effective energy is in the numerator. Therefore the literature value gives an upper limit and using this equation to calculate the expected current at higher temperatures will always result in an upper limit of the current value. Together with the observed linearity of the current at high fluences it is possible to plan the power requirements for high radiation applications.

For the calculation of the current related damage rate the currents had to be scaled to 21°C . Using different values for E_{eff} had an influence on the results. In this context the geometric current related damage rate α^* was introduced: the definition of α requires the knowledge of the depleted volume. Therefore only measurements of a fully depleted sensor should be used, but at very high fluences it is not possible to fully deplete the sensors. Thus the geometric volume was used instead to calculate α^* . When the sensor is fully depleted both values should be equal. It has been shown that the low fluence α^* values ($\leq 2 \times 10^{15} \text{ n}_{\text{eq}}/\text{cm}^2$) reaches the expected literature value for high voltages. Some sensors even exceed this value. This could be explained by charge multiplication, where the current is higher than the plateau value, or by the beginning of breakdown. For higher fluences the values are lower and show a clear hierarchy with the thickest sensor having the lowest α^* value. This is in good agreement with the intuitive assumption that in a thicker sensor a smaller percentage of the sensor is depleted. With increasing annealing time the deviation of α^* from the literature value decreases. The results of α^* from Liverpool are comparable with the results from Freiburg. Because the expected current of an irradiated silicon sensor depends directly on the current related damage rate, the measurement results show that the literature value can be used as an upper limit on the expected current for high fluences. For a continuation of this study it would be beneficial to include edge-TCT measurements, which allow the reconstruction of the electric field and thus allow the use of the actual depleted volume.

In the context of this study a new Peltier based IV system has been designed and built at Liverpool. With additional modifications of the measurement program, the speed and accuracy of current and sensor-temperature measurements has been increased. A comparison with the old freezer based system shows that the results are comparable. However the Peltier system allows a better temperature control as

well as the possibility to reach lower temperatures.

Charge multiplication in silicon strip sensors happens in high electric fields where the primary electron (or hole) gets enough energy to generate a secondary electron-hole pair. It is possible to change the strip geometry to create a small high field region. A different attempt has been investigated in chapter 7: a well defined irradiation should be used to create a shallow damage layer close to the strip surface. This damage layer will create a high electric field to initiate charge multiplication. A similar approach is used in Low Gain Avalanche Detectors (LGAD) where the multiplication layer is produced by doping.

The damage layer has to be at the strip surface and only a few microns thin so that the position resolution is not affected. For the presented study the proton beam at the Birmingham irradiation facility is used. Geant4 simulations of the irradiation facility were made to determine the optimal beam parameters. Because of the facility requirements the proton energy can not be as low as desired. Therefore an absorber in front of the silicon sensor is used. Two materials were simulated and tested: perspex and lead. The first test with perspex has shown that this is not suitable because the absorber melted in the beam line within few minutes. The lead absorber, milled at the workshop at Liverpool to the required thickness, worked as expected.

In the first proton irradiation sensors were irradiated to a fluence of $1 \times 10^{15} \text{ n}_{\text{eq}}/\text{cm}^2$ with a 300 μm thick lead absorber and in the second proton irradiation additional sensors were irradiated to $1 \times 10^{14} \text{ n}_{\text{eq}}/\text{cm}^2$ and $3 \times 10^{15} \text{ n}_{\text{eq}}/\text{cm}^2$ with the same absorber. The limit in irradiation fluence was given by the limited time window for the irradiation. With longer beam times higher fluences can be achieved. For setting up the devices and to verify that protons pass the absorber and reach the silicon sensor Gafchromic film was used. While the simulation showed that some protons should reach the absorber with a 315 μm thick absorber for the second irradiation no change in the film has been seen. After the irradiation it was discovered that the Gafchromic film has a 125 μm thick polyester base in front of the active layer. This would stop the low energy protons so that no reaction could be observed. For future tests a different film has to be used, which has no polyester layer.

After the first proton irradiation, the sensors have been measured with the ALiBaVa system. The collected charge plots showed a fairly horizontal voltage dependence, which only increased slightly up to 2000 V. The charge collection profile is different than for sensors after a standard irradiation, indicating that the irradiation with low energy protons has some effects on the device. It was clearly visible that the sensors with the lowest fluence had the highest collected charge. Additionally it was observed that for the second proton irradiation sensors with the same expected fluence had different collected charge values. Comparing the beam area with the sensor position showed that some sensors did not get the full fluences, which is in

good agreement with the higher collected charge for those devices.

All sensors have been irradiated afterwards with neutrons to fluences of $1 \times 10^{15} \text{ n}_{\text{eq}}/\text{cm}^2$ and $5 \times 10^{15} \text{ n}_{\text{eq}}/\text{cm}^2$. For all fluences the collected charge at lower voltages was smaller than before the neutron irradiation. Only at voltages above 1000 V the collected charge reached the same values that have been measured after the proton irradiation. For some devices the charge even increased further which could be an indicator of charge multiplication. For all irradiations the 300 μm thick lead absorber was used and the simulations showed that the damage layer was approximately 125 μm thick. This is much more than the initial plan of 10 to 20 μm . The performed irradiations and simulations have deepened the understanding of the Birmingham irradiation facility. With this experience it should be possible to create a 10 to 20 μm thick damage layer in silicon strip sensors with a new irradiation.

A. Appendix

A.1. ALiBaVa Daughterboard Calibration Factors

When populating the daughterboards with the label GLC, a wrong resistor for signal amplifiers was used. This has been corrected at some point which is shown in different calibration factors of GLC03 and GLC06. The calibration factors of GLC06 with the exchanged resistor are comparable to the calibration factors of the other boards.

Daughterboard	Sensor	Calibration factor [e^- /ADC]		Date
		full gain	half gain	
A8	ATLAS07	85.2 ± 0.3	169.7 ± 0.7	13/03/2013
	Micron	75.7 ± 0.5	152.5 ± 0.6	22/10/2013
	Micron	80.2 ± 0.4	158.5 ± 0.6	18/02/2014
GLC03	ATLAS07	119.1 ± 0.5	238.6 ± 1.0	21/02/2013
GLC06	Micron	61.9 ± 0.3	123.9 ± 0.6	17/01/2014
GLC19	Micron	62.1 ± 0.2	124.1 ± 0.5	18/01/2016
H7	ATLAS12	61.1 ± 0.3	122.6 ± 0.6	24/09/2013
	Micron	61.5 ± 0.2	124.4 ± 0.5	06/11/2013
	ATLAS07	61.5 ± 0.4	126.6 ± 0.5	06/11/2013
	ATLAS07	58.0 ± 0.4	118.2 ± 0.7	12/03/2015
	CERN Micron	56.8 ± 0.3	117.2 ± 0.6	16/01/2014
H6	ATLAS07	57.8 ± 0.3	117.9 ± 0.6	09/06/2014
CM calibration for old data		77.2		

Table A.1.: Calibration Values for all ALiBaVa daughterboards. The values of GLC03 differ from the other GLC board due to wrong resistors on the boards. They have been changed, when this error was discovered.

A.2. Beetle Chip Settings

For the measurements with the ALiBaVa system a specific type of settings is used: the kazu settings.

Variable	Current Value	Thesis Brown	Description
CompCtral	9	9	comparator control
Ibuf	9	10	front-end buffer bias current
Icurrbuf	119	119	output buffer bias current
Ipipe	13	13	pipe-amp bias current
Ipre	5	75	pre-amplifier bias current
Isf	29	29	multiplexer buffer bias current
Isha	10	10	shaper bias current
Itp	0	0	test pulse bias current
Ivltbuf	29	29	pipe-amp buffer bias current
Latency	126	128	trigger latency
ROCtrl	26	26	readout control
RclkDiv	0	0	ratio between Rclk and Sclk
Vd	140	140	pipe-amp reset potential
Vdcl	107	107	pipe-amp reference voltage
Vfp	31	31	pre-amplifier feedback voltage
Vfs	102	102	shaper feedback voltage
Vrc	0	0	comparator RC time constant

Table A.2.: Kazu Settings, description from [Löc06a]

Compared to the values used in the MSc thesis of Henry Brown the value for Ipre is different in the current kazu setting (should be 75), probably since middle of 2013. This only affects the gain and should not have an influence on the data because the calibration is done for each board.

The Latency value can vary for different setups and has to be chosen so that the peak of the signal profile is visible in the time window.

A.3. Charge Multiplication Sensors

Sensor label	Label in thesis	Measured at	Radiation particle	Fluence [$n_{\text{eq}}/\text{cm}^2$]
2935-2-23	P40-W6, std	Freiburg	-	-
2935-10-4	P40-W6, extra diff	Freiburg	-	-
2935-5-2	P40-W15, std	Freiburg	-	-
2935-5-4	P40-W15-I6, std	Freiburg	-	-
2935-10-3	P40-W15-I6, extra diff	Freiburg	-	-
2912-3-3	P40-W15-F6, 2E imp	Freiburg	-	-
2912-2-5	P40-W15-I15, 2E imp	Freiburg	-	-
2912-2-3	P40-W27, 2E imp	Freiburg	-	-
2935-2-19	P80-W6, std	Freiburg	-	-
2912-3-5	P80-W6, 2E imp	Freiburg	-	-
2935-2-11	P80-W25, std	Freiburg	-	-
2935-2-11	P80-W25, std	Freiburg	-	-
2935-5-3	P80-W25, std	Freiburg	-	-
2935-2-8	P80-W25-I10, std	Freiburg	-	-
2912-2-2	P80-W25-I10, 2E imp	Freiburg	-	-
2912-2-1	P80-W25-F10, 2E imp	Freiburg	-	-
2935-2-7	P80-W25-I30, std	Freiburg	-	-
2935-2-32	P80-W25-I35, std	Freiburg	-	-
2935-2-29	P80-W25-F35, std	Freiburg	-	-
2935-2-26	P100-W10, std	Freiburg	-	-
2912-2-8	P100-W10, 2E imp	Freiburg	-	-
2935-2-1	P100-W33, std	Freiburg	-	-
2935-10-1	P100-W33-I33, std	Freiburg	-	-
2912-2-6	P100-W33-I33, 2E imp	Freiburg	-	-
2935-2-27	P100-W70, std	Freiburg	-	-
2935-2-23P	P40-W6, std	Freiburg	p	1×10^{15}
2935-5-2P	P40-W15, std	Freiburg	p	1×10^{15}
2935-5-4P	P40-W15-I6, std	Freiburg	p	1×10^{15}
2935-2-19P	P80-W6, std	Freiburg	p	1×10^{15}
2912-3-5P	P80-W6, 2E imp	Freiburg	p	1×10^{15}
2935-5-3P	P80-W25, std	Freiburg	p	1×10^{15}
2935-2-8P	P80-W25-I10, std	Freiburg	p	1×10^{15}
2935-2-11P	P80-W25-F10, std	Freiburg	p	1×10^{15}
2935-2-7P	P80-W25-I30, std	Freiburg	p	1×10^{15}
2935-2-16P	P80-W25-F35, std	Freiburg	p	1×10^{15}
2935-2-26P	P100-W10, std	Freiburg	p	1×10^{15}
2912-2-8P	P100-W10, 2E imp	Freiburg	p	1×10^{15}

Continued on next page

Continued from previous page				
Sensor label	Label in thesis	Measured at	Radiation particle	Fluence [$n_{\text{eq}}/\text{cm}^2$]
2935-2-1P	P100-W33, std	Freiburg	p	1×10^{15}
2935-2-27P	P100-W70, std	Freiburg	p	1×10^{15}
2935-7-3-4-L	P40-W15-F6, std	Liverpool*	n	1×10^{15}
2935-8-3-1L	P40-W15-I15, std	Freiburg	n	1×10^{15}
2935-7-2-8-L	P40-W15-I15, std	Liverpool*	n	1×10^{15}
2935-7-3-1-L	P40-W15-I15, std	Liverpool*	n	1×10^{15}
2935-8-3-3L	P40-W15-F15, std	Freiburg	n	1×10^{15}
2935-7-3-3-L	P40-W15-F15, std	Liverpool*	n	1×10^{15}
2935-8-1-15L	P80-W6, std	Freiburg	n	1×10^{15}
2935-7-1-15-L	P80-W6, std	Liverpool*	n	1×10^{15}
2935-8-1-14L	P80-W25, std	Freiburg	n	1×10^{15}
2935-7-1-14-L	P80-W25, std	Liverpool*	n	1×10^{15}
2935-8-2-6L	P80-W25-I10, std	Freiburg	n	1×10^{15}
2935-7-2-6-L	P80-W25-I10, std	Liverpool*	n	1×10^{15}
2935-8-2-8L	P80-W25-F10, std	Freiburg	n	1×10^{15}
2935-8-2-5L	P80-W25-I35, std	Freiburg	n	1×10^{15}
2935-7-2-5-L	P80-W25-I35, std	Liverpool*	n	1×10^{15}
2935-7-2-7-L	P80-W25-F35, std	Liverpool*	n	1×10^{15}
2935-8-1-13L	P80-W60, std	Freiburg	n	1×10^{15}
2935-7-1-13-L	P80-W60, std	Liverpool*	n	1×10^{15}
2935-8-1-21H	P40-W6, std	Freiburg	n	5×10^{15}
2935-7-1-21-H	P40-W6, std	Liverpool*	n	5×10^{15}
2935-8-1-20H	P40-W15, std	Freiburg	n	5×10^{15}
2935-7-1-20-H	P40-W15, std	Liverpool	n	5×10^{15}
2935-7-3-2-H	P40-W15-I6, std	Liverpool	n	5×10^{15}
2935-7-3-4-H	P40-W15-F6, std	Liverpool	n	5×10^{15}
2935-7-2-8-H	P80-W25-F10, std	Liverpool	n	5×10^{15}
2935-8-3-1H	P40-W15-I15, std	Freiburg	n	5×10^{15}
2935-7-3-1-H	P40-W15-I15, std	Liverpool	n	5×10^{15}
2935-7-3-3-H	P40-W15-I15, std	Liverpool*	n	5×10^{15}
2935-7-1-19-H	P40-W27, std	Liverpool*	n	5×10^{15}
2935-8-1-15H	P80-W6, std	Freiburg	n	5×10^{15}
2935-7-1-15-H	P80-W6, std	Liverpool	n	5×10^{15}
2912-3-1-15H	P80-W6, 2E imp	Freiburg	n	5×10^{15}
2935-10-1-15H	P80-W6, extra diff	Freiburg	n	5×10^{15}
2885-5-1-15-H	P80-W6, thin	Liverpool	n	5×10^{15}
2499-7-1-15-H	P80-W6, thick	Liverpool	n	5×10^{15}
2935-8-1-14H	P80-W25, std	Freiburg	n	5×10^{15}

Continued on next page

Continued from previous page				
Sensor label	Label in thesis	Measured at	Radiation particle	Fluence [$n_{\text{eq}}/\text{cm}^2$]
2912-3-1-14H	P80-W25, 2E imp	Freiburg	n	5×10^{15}
2935-10-1-14H	P80-W25, extra diff	Freiburg	n	5×10^{15}
2885-5-1-14-H	P80-W25, thin	Liverpool	n	5×10^{15}
2488-7-1-14-H	P80-W25, thick	Liverpool*	n	5×10^{15}
2935-7-2-6-H	P80-W25-I10, std	Liverpool*	n	5×10^{15}
2935-8-2-8H	P80-W25-F10, std	Freiburg	n	5×10^{15}
2935-8-2-5H	P80-W25-I35, std	Freiburg	n	5×10^{15}
2935-7-2-7-H	P80-W25-I35, std	Liverpool*	n	5×10^{15}
2935-7-2-5-H	P80-W25-I35, std	Liverpool*	n	5×10^{15}
2935-7-1-13-H	P80-W50, std	Liverpool	n	5×10^{15}
2935-8-1-13H	P80-W60, std	Freiburg	n	5×10^{15}
2912-3-1-13H	P80-W60, 2E imp	Freiburg	n	5×10^{15}
2935-10-1-13H	P80-W60, extra diff	Freiburg	n	5×10^{15}
2885-5-1-13-H	P80-W60, thin	Liverpool	n	5×10^{15}
2488-7-1-13-H	P80-W60, thick	Liverpool*	n	5×10^{15}
2912-2-1-18-H	P100-W10, 2E imp	Liverpool	n	5×10^{15}
2885-5-1-18H	P100-W10, thin	Freiburg	n	5×10^{15}
2488-7-1-18H	P100-W10, thick	Freiburg	n	5×10^{15}
2488-7-1-17H	P100-W33, thick	Freiburg	n	5×10^{15}
2935-10-1-10-H	P100-W33-I15, extra diff	Liverpool*	n	5×10^{15}
2935-10-1-9-H	P100-W33-I33, extra diff	Liverpool	n	5×10^{15}
2935-10-1-11-H	P100-W33-F33, extra diff	Liverpool	n	5×10^{15}
2885-5-1-16H	P100-W70, thin	Freiburg	n	5×10^{15}

Table A.3.: List of all charge multiplication sensors with the actual sensor label, the label used in this thesis, the measurement site, the irradiation type (protons of neutrons) and the fluence. Sensors indicated with ‘*’ after the site were measured by the author of this thesis. The label in this thesis includes the strip pitch P, the strip width W and if an intermediate strip is used its width for biased (I) or floating (F) strips.

A.4. List of Sensors for IV study

Sensor label	Thickness [μm]	Fluence [$\text{n}_{\text{eq}}/\text{cm}^2$]	Irradiation type
W72-BZ2-P5	293	1×10^{12}	protons
W72-BZ2-P8	293	5×10^{12}	protons
W72-BZ2-P20	293	1×10^{13}	protons
W52-BZ2-P2	293	5×10^{13}	protons
W52-BZ6-P24	293	1×10^{14}	protons
W53-BZ6-P12	293	5×10^{14}	protons
W53-BZ6-P24	293	1×10^{15}	protons
W277-BZ5-P11	293	2×10^{14}	neutrons
W264-BZ5-P21	293	2×10^{15}	neutrons
W72-BZ3-P21	293	5×10^{15}	neutrons
W73-BZ2-P17	293	1×10^{16}	neutrons
W104-BZ2-P8	293	1.5×10^{16}	neutrons
W104-BZ2-P17	293	2×10^{16}	neutrons
2437-14-L	143	2×10^{14}	neutrons
2437-14-N	143	5×10^{14}	neutrons
2437-14-P	143	1×10^{15}	neutrons
2437-14-R	143	2×10^{15}	neutrons
2437-14-C	143	5×10^{15}	neutrons
2437-14-D	143	1×10^{16}	neutrons
2437-14-E	143	2×10^{16}	neutrons
2923-2-L	108	2×10^{14}	neutrons
2923-2-N	108	5×10^{14}	neutrons
2923-2-P	108	1×10^{15}	neutrons
2923-2-H	108	2×10^{15}	neutrons
2923-2-B	108	5×10^{15}	neutrons
2923-2-C	108	1×10^{16}	neutrons
2923-2-E	108	2×10^{16}	neutrons
3107-3-3	50	1×10^{15}	neutrons
3107-3-9	50	2×10^{15}	neutrons
3107-3-10	50	5×10^{15}	neutrons
3107-3-14	50	1×10^{16}	neutrons
3107-3-21	50	2×10^{16}	neutrons

Continued on next page

Continued from previous page			
Sensor label	Thickness [μm]	Fluence [$\text{n}_{\text{eq}}/\text{cm}^2$]	Irradiation type
Tested at CERN			
2923-2-M	108	2×10^{14}	neutrons
2923-2-O	108	5×10^{14}	neutrons
2923-2-Q	108	1×10^{15}	neutrons
2923-2-S	108	2×10^{15}	neutrons
2923-2-A	108	5×10^{15}	neutrons
2923-2-D	108	1×10^{16}	neutrons
2923-2-H	108	2×10^{16}	neutrons

Table A.4.: List of all measured sensors for the IV study. The proton irradiation was done at Birmingham and the neutron irradiation at Ljubljana.

A.5. Micron and Hamamatsu Detector Properties

Property	Micron RD50 design	ATLAS07 mini
Manufacturer	Micron Semiconductor Ltd. [Mic16]	Hamamatsu Photonics KK. [Ham16]
Type	n-in-p	n-in-p
Bias ring dimensions	$1.0593 \times 1.0594 \text{ cm}^2$	$0.8061 \times 0.8360 \text{ cm}^2$
Active area*	$1.0985 \times 1.0973 \text{ cm}^2$	$0.8348 \times 0.8600 \text{ cm}^2$
Number of strips	131	104
Strip pitch	$80 \mu\text{m}$	$74.5 \mu\text{m}$

Table A.5.: Properties of used silicon sensors.

*: active area of Micron sensors is estimated while it has been calculated for the ATLAS07 sensors.

A.6. Effective Energy

Annealing Time	Constant Part a [eV]	Decreasing Part		Intersection [$n_{\text{eq}}/\text{cm}^2$]
		a [eV]	b $\left[\frac{\text{eV}}{n_{\text{eq}}/\text{cm}^2}\right]$	
0.3 d	1.1554 ± 0.0005	3.67 ± 0.11	0.167 ± 0.007	1.16×10^{15}
1 d ^(a)	1.122 ± 0.012	3.51 ± 0.16	0.154 ± 0.010	3.12×10^{15}
10 d	1.1601 ± 0.0005	5.0 ± 0.2	0.243 ± 0.014	3.85×10^{15}
30 d	1.1731 ± 0.0007	4.6 ± 0.2	0.220 ± 0.013	3.58×10^{15}
1 d, CERN ^(b)	1.149 ± 0.005	1.58 ± 0.08	0.030 ± 0.005	4.2×10^{14}
30 d, Peltier ^(c)	1.1743 ± 0.0005	3.5 ± 0.2	0.149 ± 0.014	3.53×10^{15}

^(a): only 50 μm samples

^(b): only 108 μm samples, measured at CERN

^(c): without 50 μm samples, measured with Peltier system

Table A.6.: Results of the straight line fits for the effective energy vs fluence plots, where the values of the different sensor types were fitted together. The average E_{eff} values were used to obtain these fit results.

B. Acronyms and Abbreviations

Notation	Description
AC	Alternating current
ADC	Analogue-to-Digital Converter; also used as unit for the signal obtained from the ADC
ALiBaVa system	Analogue Liverpool Barcelona Valencia system; measurement kit using the analogue Beetle front-end chip for measurements of silicon sensors [Ali16a]
ALICE	A Large Ion Collider Experiment; dedicated to measure generated particles in lead-lead collisions [ALI16b]
ASIC	Application Specific Integrated Circuit; computer chip with specific circuit
ATLAS	A Toroidal LHC ApparatuS [ATL16]
CERN	Conseil Européen pour la Recherche Nucléaire; European Organization for Nuclear Research [CER16a]
CMS	Compact Muon Solenoid [CMS16]
CM	Charge Multiplication
CV	Measurement of capacitance (C) as function of voltage (V)
d	silicon sensor thickness
DC	Direct current
DPG	Deutsche Physikalische Gesellschaft (German physical society)
DUT	Device Under Test
E_A	Acceptor energy level
E_C	lowest energy level of the conduction band
E_D	Donor energy level
E_{eff}	Effective energy, used to scale currents of silicon sensors, literature value: (1.214 ± 0.014) eV [Chi13]
E_F	Fermi energy level
E_G	Band gap energy ($E_G = E_C - E_V$)
E_i	Fermi level in an intrinsic semiconductor
E_V	highest energy level of the valence band
eTCT	edge-Transient Current Technique

Notation	Description
eV	electron Volt: Energy of a electron when it is accelerated over a potential difference of 1 Volt; in SI-units 1 eV = $1.6021766208(98) \times 10^{-19}$ J [Par16b]
ϵ_0	Permittivity in vacuum: $8.854187817 \times 10^{-12}$ F/m [Par16b]
ϵ_{Si}	Permittivity of silicon: $\epsilon_{Si} = 11.9 \cdot \epsilon_0$ [Sze07]
FZ	Float Zone
GUI	Graphical User Interface
HEP	High Energy Physics
HL-LHC	High Luminosity LHC; upgrade of the current LHC in 2022/2023
HV	High Voltage
I_R	Reverse bias current
IV	Measurement of current (I) as function of voltage (V)
k_B	Boltzmann constant: $8.6173303(50) \times 10^{-5}$ eV/K [Par16b] at room temperature ($T = 20^\circ\text{C}$) $k_B T \approx 25.3$ meV
κ	Hardness factor
LHC	Large Hadron Collider
LHCb	Large Hadron Collider beauty experiment; dedicated to record the decay of particles which contain b and anti-b quarks [LHC16]
MIP	Minimum Ionizing Particle
MPV	Most Probable Value
μ	charge carrier mobility in silicon (at 300 K): $\mu_n = 1.450$ cm ² /(Vs), $\mu_p = 500$ cm ² /(Vs) [Sze07]
n	density of free electrons
N_A	acceptor concentration p-doped silicon
N_C	effective density of states in conduction band
N_D	donor concentration in n-doped silicon
$N_{e/h}$	number of electron-hole pairs
N_{eff}	Effective doping concentration
n_{eq}	1 MeV neutron equivalent unit for irradiation fluences (see NIEL scaling hypothesis in subsection 2.4.1).
n_i	intrinsic carrier concentration
n_T	number of ions produced through ionization

Notation	Description
N_V	effective density of states in valence band
NIEL	Non Ionizing Energy Loss
p	density of free holes
P	Strip pitch
P80-W25-I10	sensor with a strip pitch of 80 μm , a strip width of 25 μm and a biased intermediate strip of 10 μm width; ‘F’ is used for floating intermediate strips.
PCB	Printed Circuit Board
Φ	(Irradiation) fluence
Φ_{eq}	1 MeV neutron equivalent fluence (see NIEL scaling hypothesis in subsection 2.4.1).
RD50	CERN collaboration to investigate radiation hard semiconductor devices for very high luminosity colliders [Mol16]
RMS	root mean square; $x_{RMS} = \sqrt{\frac{1}{N} \sum_{i=1}^N x_i^2}$
ρ	Resistivity
SCR	Space Charge Region, also known a depleted region: region in doped silicon without mobile/free charge carriers.
SNR	Signal-to-Noise ration
SPS	Super Proton Synchrotron
σ_x	uncertainty of variable x (standard deviation)
T	temperature (in $^{\circ}\text{C}$ unless otherwise specified)
TCT	Transient Current Technique
TDC	Time-to-Digital Converter
V_b	Bias voltage
V_{bi}	Built-in voltage
V_{dep}	Full depletion voltage
w_{dep}	Depletion width
W/P	Width-over-Pitch ratio for silicon strip sensors

List of Figures

2.1. Energy loss for different materials.	17
2.2. Difference between insulator, semiconductor and conductor.	27
2.3. Bond pictures for doped silicon.	27
2.4. Schematic band diagram for doped silicon.	28
2.5. pn-junction without and with external applied voltage.	29
2.6. pn-junction in band model.	30
2.7. Example for V_{dep} determination from capacitance measurement.	31
2.8. Ideal current-voltage characteristics.	31
2.9. 3D schematic sketch of a strip sensor.	33
2.10. Schematic of Czochralski and Float Zone crystal growth.	35
2.11. Overview of sensor production steps.	36
2.12. Production of sensor bias resistor.	37
2.13. Schematic view of depletion vs bias voltage.	38
2.14. Schematic view of a traversing particle in a strip detector.	39
2.15. Signal strength in channels depending on particle trajectory.	40
2.16. Equivalence diagram of the different noise sources.	42
2.17. Exemplary selection of bulk damages after irradiation.	43
2.18. Effects of different defect levels.	44
2.19. Band-gap overview of some defect levels in silicon.	45
2.20. N_{eff} evolution with annealing time.	47
2.21. Diagram of strip isolations to counter surface radiation damages.	49
2.22. $\Delta I/V$ as function of the irradiation fluence.	51
3.1. Pictures of probe station.	56
3.2. User interface of probe station LabVIEW program.	57
3.3. Old cold IV setup.	58
3.4. Temperature measurement in cold IV freezer	58
3.5. New cold IV system.	59
3.6. Temperature comparison Freezer - PID	60
3.7. Picture of CERN IV setup.	61
3.8. Schematic drawing of a β -system.	62
3.9. Expected collected charge vs device thickness.	63
3.10. Picture of ALiBaVa daughterboard	64
3.11. Picture of ALiBaVa motherboard	64
3.12. Schematic block diagram of the Beetle readout chip [L6c06a].	65
3.13. Picture of ALiBaVa test-box	65

3.14. Schematic overview for full gain / half gain.	66
3.15. Raw data signals, showing Gaussian shape.	67
3.16. Pedestal values for each channel before and after analysis.	68
3.17. Noise for all channels before and after analysis.	70
3.18. Sketch of ALiBaVa timing.	70
3.19. Time profile of RS-run.	71
3.20. Time cut for maximal cluster charge.	71
3.21. Cluster charge fit.	73
3.22. Cluster position of source run allows to see the position of the source.	73
3.23. Cluster distribution with bad channels.	74
3.24. Unirradiated Collected Charge vs Voltage	75
3.25. Unirradiated Collected Charge vs Temperature	76
3.26. Unirradiated Calibration vs Temperature	77
4.1. Example of charge multiplication.	79
4.2. Strip geometry for charge multiplication sensors	81
4.3. Electric field simulations for different strip widths.	82
4.4. Collected charge of unirradiated CM sensors.	83
4.5. Noise and SNR of unirradiated CM sensors.	84
4.6. Collected charge of CM sensors irradiated to $1 \times 10^{15} \text{ n}_{\text{eq}}/\text{cm}^2$ (p).	84
4.7. Noise of CM sensors irradiated to $1 \times 10^{15} \text{ n}_{\text{eq}}/\text{cm}^2$ (proton).	85
4.8. Charge collection comparison of FR and Liv ($1 \times 10^{15} \text{ n}_{\text{eq}}/\text{cm}^2$, n).	86
4.9. Collected charge of CM sensor after irradiation to $1 \times 10^{15} \text{ n}_{\text{eq}}/\text{cm}^2$	86
4.10. Noise of CM sensor after neutron irradiation to $1 \times 10^{15} \text{ n}_{\text{eq}}/\text{cm}^2$	87
4.11. Reverse bias current of CM sensor; $1 \times 10^{15} \text{ n}_{\text{eq}}/\text{cm}^2$; scaled to -25°C	88
4.12. Comparison of Freiburg and Liverpool after $5 \times 10^{15} \text{ n}_{\text{eq}}/\text{cm}^2$	89
4.13. Comparison Freiburg - Liverpool with new calibration value.	89
4.14. Collected Charge after $5 \times 10^{15} \text{ n}_{\text{eq}}/\text{cm}^2$ neutron irradiation.	90
4.15. Repeated measurement of 'P80-W25, thick' sensor.	90
4.16. Examination of intermediate strips after $5 \times 10^{15} \text{ n}_{\text{eq}}/\text{cm}^2$	91
4.17. Collected charge versus W/P ratio for different wafer types.	92
4.18. Collected charge for 'P80-W25-I35, std' after annealing.	94
4.19. SNR vs annealing time for P80-W25-I35; $5 \times 10^{15} \text{ n}_{\text{eq}}/\text{cm}^2$	95
4.20. Collected charge for 'P80-W60' after room temperature annealing.	97
4.21. Collected charge for 'P80-W25' after room temperature annealing	98
4.22. 'P80-W25, thick'; $5 \times 10^{15} \text{ n}_{\text{eq}}/\text{cm}^2$: SNR vs annealing time.	99
4.23. Longterm bias; 'P80-W60, std'; $1 \times 10^{15} \text{ n}_{\text{eq}}/\text{cm}^2$; 1500 V	100
4.24. Longterm bias; 'P80-W60, std'; $1 \times 10^{15} \text{ n}_{\text{eq}}/\text{cm}^2$; 40 d ann.; 1600 V	100
4.25. Longterm bias; 'P80-W25-I10, std'; $5 \times 10^{15} \text{ n}_{\text{eq}}/\text{cm}^2$; 1500 V	102
4.26. Temperature during longterm test of 'P80-W25-I10, std'.	103
4.27. I_R during longterm test of 'P80-W25-I10, std'.	103
4.28. Longterm test; 'P80-W25-F35, std'; $5 \times 10^{15} \text{ n}_{\text{eq}}/\text{cm}^2$; 1700 V	104
4.29. Longterm test (T and I); 'P80-W25-F35, std'; $5 \times 10^{15} \text{ n}_{\text{eq}}/\text{cm}^2$	105

5.1.	Collected charge of all 50 μm thick samples directly after irradiation.	110
5.2.	Noise of all 50 μm thick samples after irradiation.	111
5.3.	Signal shift with increasing bias voltage.	113
5.4.	Comparison of noise only data with real data.	114
5.5.	Example for fit with Method 1.	115
5.6.	Different steps of data analysis Method 2.	116
5.7.	Example for fit with Method 3.	117
5.8.	Example graphs for one simulation.	118
5.9.	Test 1 combined histogram for noise and signal.	119
5.10.	Test 1 results: The true MPV is subtracted from the fitted MPV.	119
5.11.	Test 2 combined histogram for noise and signal.	120
5.12.	Test 2 results: The true MPV is subtracted from the fitted MPV.	120
5.13.	Results of the physical tests.	122
5.14.	Collected charge MPV for different seed cut values (standard is 3.5).	123
5.15.	Number of events for different seed cut values.	123
5.16.	Comparison of analysis methods with 50 μm sensors after irradiation.	124
5.17.	Collected charge difference compared to 'Method 1'.	125
5.18.	Collected charge vs annealing time (2922-1).	126
5.19.	Noise vs annealing time (2922-1).	126
5.20.	Collected charge of 3107-6-20 at various annealing steps.	127
5.21.	Collected charge vs annealing time (3107-6-20).	128
6.1.	Cold IV measurement PCB.	132
6.2.	PT1000 temperature approximation difference.	133
6.3.	Reverse bias current of unirradiated sensors.	135
6.4.	Capacitance graph with full depletion voltage.	136
6.5.	Reverse bias current for HPK sensors after irradiation.	137
6.6.	Current comparison for different thicknesses at $1 \times 10^{15} \text{ n}_{\text{eq}}/\text{cm}^2$	137
6.7.	Current comparison for different thicknesses at $2 \times 10^{16} \text{ n}_{\text{eq}}/\text{cm}^2$	138
6.8.	Reverse bias current for 293 μm sensor, irradiated to $1 \times 10^{15} \text{ n}_{\text{eq}}/\text{cm}^2$	139
6.9.	Example of effective energy calculation.	140
6.10.	Effective energy histogram from example analysis.	141
6.11.	'Ill-behaved' example for an effective energy plot.	142
6.12.	Effective energy values vs fluence (0.3 d).	143
6.13.	E_{eff} values after 0.3 d annealing for all sensor thicknesses.	145
6.14.	Average E_{eff} values after annealing.	146
6.15.	Contour graph to show E_{eff} variation for temperature variation.	147
6.16.	E_{eff} and temperature for 293 μm sensor at $1 \times 10^{16} \text{ n}_{\text{eq}}/\text{cm}^2$	148
6.17.	$\Delta I/V$ vs Φ of the HPK sensors (0.3 d annealing)	150
6.18.	α^* with different IV scaling methods.	153
6.19.	α^* after 0.3 d annealing (E_{eff} : all sensors fit, Average).	154
6.20.	α^* for 50 μm samples, scaled fitted average E_{eff}	155
6.21.	α^* (total fit average) after 10 days of annealing.	156
6.22.	α^* (total fit average) after 30 days of annealing.	157

6.23.	Current comparison Liverpool - CERN.	158
6.24.	Average E_{eff} for 108 μm devices measured at CERN.	158
6.25.	α^* for samples measured at CERN.	159
6.26.	IV comparison freezer-Peltier after 30 d annealing.	160
6.27.	Effective energy for all sensor types measures with the Peltier system.	161
6.28.	Current related damage rate for the Peltier system.	161
6.29.	Effective energy measured at Freiburg [Wie16a].	163
6.30.	α^* measured at Freiburg.	164
6.31.	Comparison of Liverpool and Freiburg analysis scripts.	165
6.32.	Sensor swap and measurement at Liverpool and Freiburg.	166
6.33.	Direct current comparison between Freiburg and Liverpool.	166
6.34.	Direct current comparison between Freiburg and Liverpool.	167
6.35.	Effective Energy for different wire resistances.	168
7.1.	Picture of the Birmingham irradiation facility.	172
7.2.	Pictures of inside of cold box and sensor mount.	173
7.3.	Sketch of the Geant4 simulation.	174
7.4.	Geant4 simulation of 27 MeV proton beam.	175
7.5.	Simulation for 300 μm lead absorber, various energies.	176
7.6.	Number of good events (300 μm lead).	177
7.7.	Average energy deposition for Lead and Perspex.	178
7.8.	Scan pattern at Birmingham from [Der15].	179
7.9.	Position finding at Birmingham irradiation facility.	179
7.10.	Gafchromic film before Faraday cup for 11 MeV beam.	180
7.11.	Gafchromic film discolouration for 12 MeV beam.	181
7.12.	Perspex after a few minutes of irradiation.	181
7.13.	Sketch of the mounting positions for the first Irradiation.	182
7.14.	Energy loss in different components for four simulated cases.	184
7.15.	Energy loss in lead for case 2.	185
7.16.	Simulation comparison of 12 MeV protons after 315 μm lead.	186
7.17.	Validation of the 300 μm thick absorber for the second irradiation.	188
7.18.	Mounting for second irradiation.	189
7.19.	Cross section of Gafchromic films.	190
7.20.	Geant4 simulation of energy loss Gafchromic film.	190
7.21.	Collected charge of all sensors after Birmingham irradiation.	191
7.22.	Collected charge of downstream sensors after Birmingham irradiation.	192
7.23.	Scan path for the irradiation to $3 \times 10^{15} \text{ n}_{eq}/\text{cm}^2$	193
7.24.	Collected charge before and after annealing after proton irradiation.	194
7.25.	Reverse bias current of annealed sensors.	195
7.26.	Collected charge and current comparison of upstream sensor.	195
7.27.	Collected charge after $1 \times 10^{15} \text{ n}_{eq}/\text{cm}^2$ neutron irradiation.	196
7.28.	Reverse bias current of one sensor after irradiation and annealing.	197
7.29.	Collected charge after $5 \times 10^{15} \text{ n}_{eq}/\text{cm}^2$ neutron irradiation.	198

List of Tables

2.1.	Hardness factor for different irradiation centres	46
2.2.	Time factors for accelerated annealing.	48
2.3.	Impact of the ΔT on the effective energy uncertainty.	51
2.4.	Parameters of leakage current annealing at 21°C.	52
2.5.	Parameter for longterm annealing of α [Mol99].	53
3.1.	Variables values for ALiBaVa analysis.	69
3.2.	Fit Parameter of temperature dependent ALiBaVa calibration.	76
4.1.	Charge multiplication wafer details.	80
4.2.	W/P ratio for sensor comparison.	91
4.3.	Sensors for annealing study.	93
5.1.	List of 50 μm thick sensors, irradiated at Ljubljana.	110
5.2.	Parameter for simulated noise and signal for Test 1 and Test 2.	118
5.3.	Parameter for physical simulation for noise and signal.	121
6.1.	Active Area for all sensor types.	148
6.2.	Expected literature values for α at several annealing steps.	150
6.3.	Effective energy values measured at Freiburg.	162
7.1.	Mounting configuration for first Irradiation.	182
7.2.	Energy loss for simulated cases of 12 MeV protons.	186
7.3.	Mounting configuration for second Irradiation	188
A.1.	Calibration Values for ALiBaVa daughterboards.	207
A.2.	Kazu Settings, description from [Löc06a]	208
A.3.	List of all charge multiplication sensors	211
A.4.	List of Sensors from IV study.	213
A.5.	Properties of used silicon sensors.	213
A.6.	Analysis results for E_{eff} ; total Average.	214

Bibliography

- [Aad12] Aad, G. et al. *Observation of a new particle in the search for the Standard Model Higgs boson with the ATLAS detector at the LHC*. In *Physics Letters B*, vol. 716(1):pp. 1 – 29 (2012). doi:<http://dx.doi.org/10.1016/j.physletb.2012.08.020>. URL <http://www.sciencedirect.com/science/article/pii/S037026931200857X>.
- [Act16] Active Cool. *Understanding Thermoelectric Cooling* (October 2016). URL <http://www.activecool.com/technotes/thermoelectric.html>.
- [Ali16a] Alibavasytems. *Webpage* (January 2016). URL <http://www.alibavasytems.com/>.
- [ALI16b] ALICE. *ALICE webpage* (October 2016). URL <http://aliceinfo.cern.ch/Public/Welcome.html>.
- [Ara16] Araki, M. *PID CONTROL* (October 2016). URL <http://www.eolss.net/ebooks/Sample%20Chapters/C18/E6-43-03-03.pdf>.
- [Ash16] Ashland. *Ashland Gafchromic radiotherapy films* (June 2016). URL <http://www.ashland.com/products/gafchromic-radiotherapy-films>.
- [ATL12] ATLAS, C. *Letter of Intent for the Phase-II Upgrade of the ATLAS Experiment*. Tech. Rep. CERN-LHCC-2012-022. LHCC-I-023, CERN, Geneva (Dec 2012). URL <https://cds.cern.ch/record/1502664>. Draft version for comments.
- [ATL16] ATLAS Experiment. *ATLAS experiment webpage* (October 2016). URL <https://atlas.cern/>.
- [Bet12a] Betancourt, C. et al. *A charge collection study with dedicated RD50 charge multiplication sensors*. In *Nuclear Science Symposium and Medical Imaging Conference (NSS/MIC), 2012 IEEE*, pp. 1657–1660 (Oct 2012). doi:10.1109/NSSMIC.2012.6551393.

- [Bet12b] Betancourt, C. et al. *A Charge Collection Study with Dedicated RD50 Charge Multiplication Sensors*. talk at 21st RD50 workshop (November 2012). URL https://indico.cern.ch/event/200290/session/3/contribution/19/attachments/298528/417231/Betancourt_RD50_Nov12.pdf.
- [Bet13a] Betancourt, C. et al. *A charge collection study with dedicated RD50 charge multiplication sensors*. In Nuclear Instruments and Methods in Physics Research Section A: Accelerators, Spectrometers, Detectors and Associated Equipment, vol. 730:pp. 62 – 65 (2013). doi:<http://dx.doi.org/10.1016/j.nima.2013.05.186>. URL <http://www.sciencedirect.com/science/article/pii/S0168900213008127>. Proceedings of the 9th International Conference on Radiation Effects on Semiconductor Materials Detectors and Devices, October 9-12 2012.
- [Bet13b] Betancourt, C. et al. *Charge Collection Measurements on Dedicated RD50 Charge Multiplication SSDs*. Talk at 23rd RD50 workshop (November 2013). URL https://indico.cern.ch/event/265941/session/3/contribution/18/attachments/474009/656118/23_rd50_CERN.pdf.
- [Bic88] Bichsel, H. *Stragglers in thin silicon detectors*. In Reviews of Modern Physics, Vol. 60, No. 3 (July 1988).
- [Buc16] Buckland, M. *Electrical field simulations for different strip widths*. Private communication. (March 2016).
- [CER16a] CERN. *CERN webpage* (October 2016). URL www.cern.ch.
- [CER16b] CERN. *Standard Model in particle physics*. (October 2016). URL <https://home.cern/about/physics/standard-model>.
- [Chi95] Chilingarov, A. et al. *Radiation studies and operational projections for silicon in the ATLAS inner detector*. In Nuclear Instruments and Methods in Physics Research Section A: Accelerators, Spectrometers, Detectors and Associated Equipment, vol. 360(1):pp. 432 – 437 (1995). doi:[http://dx.doi.org/10.1016/0168-9002\(95\)00110-7](http://dx.doi.org/10.1016/0168-9002(95)00110-7). URL <http://www.sciencedirect.com/science/article/pii/0168900295001107>.
- [Chi13] Chilingarov, A. *Temperature dependence of the current generated in Si bulk*. In Journal of Instrumentation, vol. 8(10):p. P10003 (2013). URL <http://stacks.iop.org/1748-0221/8/i=10/a=P10003>.
- [Chu16a] Chu, S. et al. *WWW Table of Radioactive Isotopes: Strontium-90* (January 2016). URL <http://nucleardata.nuclear.lu.se/toi/nuclide.asp?iZA=380090>.

- [Chu16b] Chu, S. et al. *WWW Table of Radioactive Isotopes: Yttrium-90* (January 2016). URL <http://nucleardata.nuclear.lu.se/toi/nuclide.asp?iZA=390090>.
- [CMS16] CMS experiment. *CMS experiment webpage* (October 2016). URL <http://cms.web.cern.ch/>.
- [Der13] Dervan, P. et al. *The Birmingham Irradiation Facility*. In Nuclear Instruments and Methods in Physics Research Section A: Accelerators, Spectrometers, Detectors and Associated Equipment, vol. 730:pp. 101 – 104 (2013). doi:<http://dx.doi.org/10.1016/j.nima.2013.05.156>. URL <http://www.sciencedirect.com/science/article/pii/S0168900213007675>.
- [Der15] Dervan, P. et al. *Upgrade to the Birmingham Irradiation Facility*. In Nuclear Instruments and Methods in Physics Research Section A: Accelerators, Spectrometers, Detectors and Associated Equipment, vol. 796:pp. 80 – 84 (2015). doi:<http://dx.doi.org/10.1016/j.nima.2015.02.005>. URL <http://www.sciencedirect.com/science/article/pii/S0168900215001734>. Proceedings of the 10th International Conference on Radiation Effects on Semiconductor Materials Detectors and Devices.
- [ESA16] ESA. *Planck's new cosmic recipe* (October 2016). URL <http://sci.esa.int/planck/51557-planck-new-cosmic-recipe/>.
- [Far16] Farnell element14. *PT1000 product webpage* (March 2016). URL <http://uk.farnell.com/ist-innovative-sensor-technology/p1k0-232-6w-a-010/sensor-pt1000-600-c-class-a/dp/1266941?Ntt=1266941>.
- [Gea16] Geant4 collaboration. *Geant4 webpage* (April 2016). URL <https://geant4.web.cern.ch/geant4/>.
- [Gla16] Glaser, M. et al. *CERN proton irradiation facility; Webpage* (March 2016). URL <https://irradiation.web.cern.ch/irradiation/>.
- [Gon16] Gonella, L. *The Birmingham irradiation facility*. Talk at 28th RD50 workshop (December 2016). URL <https://agenda.infn.it/getFile.py/access?contribId=6&sessionId=6&resId=0&materialId=slides&confId=11109>.
- [Gru93] Grupen, C. *Teilchendetektoren*. BI Wissenschaftsverlag Mannheim Leipzig Wien Zürich (1993).
- [Ham16] Hamamatsu. *Hamamatsu Photonics KK. webpage* (October 2016). URL <http://www.hamamatsu.com>.

- [Har09] Hartmann, F. *Evolution of Silicon Sensor Technology in Particle Physics*. Springer Tractas in Modern Physics (2009). doi:10.1007/978-3-540-44774-0.
- [Hen16] Henkel AG & Co. KGaA. *Tra-Duct 2902 webpage* (July July 2016). URL <http://www.henkel-adhesives.com/product-search-1554.htm?nodeid=8799572262913>.
- [Her12] Hernández, R. M. *Design, development and implementation of a readout system for microstrip silicon sensors. Upgrade for test beam measurements*. Ph.D. thesis, Universidad de Valencia; Departamento de Ingeniería Electrónica (2012).
- [ISE16] ISEG. *High voltage power supply webpage* (January 2016). URL <http://iseg-hv.com/en/products/detail/SHQ>.
- [JSI16a] JSI. *Jožef Stefan Institute webpage* (February 2016). URL <https://www.ijs.si/ijsw/V001/JSI>.
- [JSI16b] JSI. *Jožef Stefan Institute webpage* (February 2016). URL <http://www.rcp.ijs.si/en/index.html>.
- [Kei16a] Keithley. *Keithley 2410 high voltage power supply webpage* (January 2016). URL <http://www.keithley.co.uk/products/dcac/voltagesource/highvoltage/?mn=2410>.
- [Kei16b] Keithley. *Keithley 2000 multimeter webpage* (March 2016). URL <https://www.keithley.co.uk/products/dcac/dmm/?mn=2000E>.
- [KIT16a] KIT. *Karlsruhe Institute of Technology irradiation webpage* (February 2016). URL <https://www.ekp.kit.edu/english/264.php>.
- [KIT16b] KIT. *Karlsruhe Institute of Technology webpage* (February 2016). URL <https://www.kit.edu/english/>.
- [Kle05] Kleinknecht, K. *Detektoren für Teilchenstrahlung*. Teubner (2005).
- [Köh11] Köhler, M. *Double-Sided 3D silicon Detectors for the High-Luminosity LHC*. Ph.D. thesis, Albert-Ludwigs-Universität Freiburg im Breisgau (July 2011).
- [Kra14] Kramberger, G. et al. *Modeling of electric field in silicon micro-strip detectors irradiated with neutrons and pions*. In JINST, vol. 9(10):p. P10016 (2014). doi:10.1088/1748-0221/9/10/P10016.
- [Küh15] Kühn, S. et al. *RD50 Collaboration Overview: Development of New Radiation Hard Detectors*. Frontier Detectors for Frontier Physics: 13th Pias Meeting on Advanced Detectors (talk) (May 2015). URL <https://agenda.infn.it/getFile.py/access?contribId=203&sessionId=7&resId=0&materialId=slides&confId=8397>.

-
- [LHC16] LHCb experiment. *LHCb experiment webpage* (October 2016). URL <http://lhcb-public.web.cern.ch/lhcb-public/>.
- [Löc06a] Löchner, S. *Development, Optimisation and Characterisation of a Radiation Hard Mixed-Signal Readout Chip for LHCb*. Phd thesis, Ruperto-Carola University of Heidelberg (2006).
- [Löc06b] Löchner, S. et al. *The Beetle Reference Manual*. Tech. rep., Max-Planck-Institute for Nuclear Physics, Heidelberg, Germany (August 2006). URL http://www.kip.uni-heidelberg.de/lhcb/Publications/BeetleRefMan_v1_3.pdf.
- [Lut99] Lutz, G. *Semiconductor Radiation Detectors*. Springer (1999).
- [Mar14] Marshall, Z. et al. *Simulation of Pile-up in the ATLAS Experiment*. In *Journal of Physics: Conference Series*, vol. 513(2):p. 022024 (2014). URL <http://stacks.iop.org/1742-6596/513/i=2/a=022024>.
- [Max17] Max Planck Society, Munich. *MPG HLL History* (January 2017). URL http://www.hll.mpg.de/04_ueberuns/geschichte.html.
- [Mic16] Micron Semiconductor Ltd. *webpage* (February 2016). URL <http://www.micronsemiconductor.co.uk>.
- [Mol99] Moll, M. *Radiation Damage in Silicon Particle Detectors*. Ph.D. thesis, Universität Hamburg (1999).
- [Mol16] Moll, M. *RD50 webpage* (January 2016). URL <http://rd50.web.cern.ch/rd50/>.
- [Nat16] National Instruments Corporation. *Homepage of LabVIEW from National Instruments* (January 2016). URL <http://www.ni.com/labview/>.
- [Par16a] Particle Data Group. *Webdocument: Passage of particles through matter* (August 2016). URL <http://pdg.lbl.gov/2015/reviews/rpp2015-rev-passage-particles-matter.pdf>.
- [Par16b] Particle Data Group. *Particle Data Group Physical Constants webpage* (March 2016). URL <http://pdg.lbl.gov/2015/reviews/rpp2015-rev-phys-constants.pdf>.
- [Pel16] Peltier Element. *Product webpage with data sheets* (January 2016). URL <http://uk.rs-online.com/web/p/peltier-modules/4901474/>.
- [PID16] PID PR59 controller. *Product webpage with data sheets* (January 2016). URL <http://uk.rs-online.com/web/p/peltier-module-controllers/4901553/>.

- [POR16] PORTFAB Modular Building Systems. *Clean room classification* (January 2016). URL <http://www.portafab.com/cleanroom-classification.html>.
- [ROO16] ROOT team. *ROOT Homepage* (January 2016). URL root.cern.ch.
- [ROO17] ROOT team. *CERN ROOT RMS* (January 2017). URL <https://root.cern.ch/root/html534/TH1.html#TH1:GetRMS>.
- [RS 16] RS Components Ltd. *RS online webpage for Araldite Rapid 24 ml Syringe Epoxy Adhesive* (April 2016). URL <http://uk.rs-online.com/web/p/products/7560102/>.
- [Sad14] Sadrozinski, H. *Low-Gain Avalanche Detectors*. Poster at IEEE NUCLEAR SCIENCE SYMPOSIUM & MEDICAL IMAGING CONFERENCE 21ST SYMPOSIUM ON ROOM-TEMPERATURE SEMICONDUCTOR X-RAY AND GAMMA-RAY DETECTORS, Seattle, USA (November 2014). URL <https://rd50.web.cern.ch/rd50/doc/talks/2014-11-IEEE-2014-LGAD-poster-4%203-sm.pdf>.
- [Sch16] Schulz, J. *PT1000 temperature conversion webpage* (March 2016). URL http://www.code10.info/index.php?option=com_content&view=article&id=82:measuring-temperature-platinum-resistance-thermometers&catid=60:temperature&Itemid=83.
- [Spi09] Spieler, H. *Semiconductor Detector Systems*. Oxford University Press (2009).
- [Sze07] Sze, S. M. et al. *Physics of Semiconductor Devices*. John Wiley & Sons, Inc. (Third Edition, 2007).
- [Tsu14] Tsurin, I. *IV-PCB design, private communication*. (2014).
- [Uni16a] Universität Freiburg. *Abteilung Prof. K. Jakobs, Physikalisches Institut, Albert-Ludwigs-Universität Freiburg* (August 2016). URL <http://portal.uni-freiburg.de/jakobs/>.
- [Uni16b] University of Birmingham. *Birmingham Cyclotron webpage* (April 2016). URL <http://www.np.ph.bham.ac.uk/pic/cyclotron>.
- [Uni16c] University of Liverpool. *University of Liverpool, Department of Physics workshop webpage*. (May 2016). URL <https://www.liverpool.ac.uk/particle-physics/infrastructure/workshop/>.
- [Wal10] Walz, M. *Charakterisierung von planaren Siliziumstreifendetektoren zum Einsatz am LHC-Upgrade*. Diplomarbeit, Albert Ludwigs Universität Freiburg (2010).

- [Wie16a] Wiehe, M. *Private communication (figures in high resolution)* (April 2016).
- [Wie16b] Wiehe, M. et al. *Messungen des Leckstroms zur Bestimmung der effektiven Bandlücke und Schädigungskonstante stark bestrahlter Siliziumsensoren*. Talk at DPG-Frühjahrstagung, Hamburg 01.03.2016 (March 2016).
- [Wik16] Wikipedia. *PID controller theory* (January 2016). URL https://en.wikipedia.org/wiki/PID_controller.
- [Wil16] Wilson, J. A. *Private communication concerning dosimetry results of low energy irradiation in December 2015 at the Birmingham irradiation facility*. (06/01/2016).
- [Won13a] Wonsak, S. et al. *Combined Measurement Results of dedicated RD50 Charge Multiplication Sensors*. talk at 22nd RD50 workshop (June 2013). URL https://indico.cern.ch/event/209612/session/3/contribution/21/attachments/325730/454280/Wonsak_RD50.pdf.
- [Won13b] Wonsak, S. et al. *Status of Silicon Strip Sensor Measurements at Liverpool*. Talk at 23rd RD50 workshop (November 2013). URL <https://indico.cern.ch/event/265941/session/3/contribution/33/attachments/474015/656129/RD50-Talk-Wonsak.pdf>.
- [Won14a] Wonsak, S. et al. *Status of Silicon Strip Sensor Measurements at Liverpool*. Talk at 24th RD50 workshop (June 2014). URL <https://indico.cern.ch/event/307015/session/6/contribution/11/attachments/585108/805399/Wonsak-RD50-June2014.pdf>.
- [Won14b] Wonsak, S. et al. *Status of Silicon Strip Sensor Measurements at Liverpool*. Talk at 25th RD50 workshop (November 2014). URL <https://indico.cern.ch/event/334251/session/5/contribution/8/attachments/652598/897352/Wonsak-RD50-November2014.pdf>.
- [Won14c] Wonsak, S. et al. *Charge Collection Efficiency of micro-strip Silicon Sensors designed for studying Charge Multiplication after Hadron irradiation*. Talk at 10th International Conference on Position Sensitive Detectors (PSD10) (September 2014). URL <https://indico.cern.ch/event/174805/session/19/contribution/122/attachments/223571/312993/PSD10-Wonsak.pdf>.

- [Won15a] Wonsak, S. et al. *Measurements of the reverse current of highly irradiated silicon sensors*. In Nuclear Instruments and Methods in Physics Research Section A: Accelerators, Spectrometers, Detectors and Associated Equipment, vol. 796:pp. 126 – 130 (2015). doi:<http://dx.doi.org/10.1016/j.nima.2015.04.027>. URL <http://www.sciencedirect.com/science/article/pii/S0168900215005008>. Proceedings of the 10th International Conference on Radiation Effects on Semiconductor Materials Detectors and Devices.
- [Won15b] Wonsak, S. et al. *IV-characterization of silicon sensors irradiated up to $2E16n_{eq}/cm^2$* . Talk at 27th RD50 workshop (December 2015). URL https://indico.cern.ch/event/456679/session/0/contribution/15/attachments/1198693/1743327/RD50_Dez2015_Wonsak.pdf.
- [Won15c] Wonsak, S. et al. *Thin Silicon Detectors for Tracking in High Radiation Environments*. Talk at 27th RD50 workshop (December 2015). URL https://indico.cern.ch/event/456679/session/0/contribution/19/attachments/1198700/1743553/RD50_Dez2015_Thin.pdf.
- [Won15d] Wonsak, S. et al. *Tests of $50\mu m$ thick silicon micro-strip sensors after extreme fluences up to $3 \times 10^{16} n_{eq}/cm^2$* . Talk at 26th RD50 workshop (June 2015). URL <https://indico.cern.ch/event/381195/session/3/contribution/11/attachments/759547/1041893/Wonsak-RD50-June2015.pdf>.
- [Won16a] Wonsak, S. *Reverse bias current characterisation of silicon strip sensors and shallow radiation damage generation*. Talk at 11th 'Trento' Workshop on Advanced Silicon Radiation Detectors (February 2016). URL http://indico.cern.ch/event/452766/contributions/1117345/attachments/1232545/1808087/Trento-2016_Wonsak.pdf.
- [Won16b] Wonsak, S. *Generation shallow radiation damages at the strip surface with low energy protons*. Talk at 28th RD50 workshop (June 2016). URL <https://agenda.infn.it/getFile.py/access?contribId=18&sessionId=5&resId=0&materialId=slides&confId=11109>.
- [Wun92] Wunstorff, R. *Systematische Untersuchungen zur Strahlenresistenz von Silizium-Detektoren für die Verwendung in Hochenergiephysik-Experimenten*. Ph.D. thesis, Universität Hamburg (1992).

Acknowledgement

I want to express my deepest gratitude to my supervisors Gianluigi Casse and Michael Moll for giving me this unique opportunity to work in the field of silicon sensor development. Being part of the RD50 collaboration has been a pleasure and the discussions at the workshops have been very inspiring.

Coming to Liverpool as a foreigner was a huge change for me and I am grateful for the warm welcome of my fellow PhD students and the whole high energy physics group. I am much obliged for the help of Dean Forshaw, who explained me the measurement systems at Liverpool. Special thanks go to Ilya Tsurin who always had time for my questions about sensors and his valuable help with the ALiBaVa system. Being one of the few people in the clean room it was always good to see Mike Wormald. Without his wire-bonding none of the measurements would have been possible and his cheerful attitude caused many laughter. Paul Dervan has organized the irradiations at Birmingham and I am thankful for his help and for showing me the facility. I would like to thank Anthony Affolder, Ashley Greenall, Michael Lockwood, Marko Milovanovic and Jon Taylor for their support. I also want to express my gratitude to Helen Hayward for proof reading my thesis, even though she already had to read another thesis from her own PhD student. Thank you very much also to the workshop who made all the nice mechanical pieces for the cold IV setup. I am very thankful to Kevin McCormick for accepting the challenge on making the thin lead and perspex absorbers within the very tight constraints.

Some of the work in my thesis has been done in close collaboration with the physics group of Professor Jakobs at the university of Freiburg. I want to thank Christopher Betancourt, Susanne Kühn, Ulrich Parzefall and Moritz Wiehe for their contributions and the valuable discussions.

In my short time at CERN Christian Gallrapp, Hannes Neugebauer and Marcos Fernandez Garcia have helped me a lot. Thank you for showing me the measurement systems and being patient with all my requests.

I want to thank the irradiation teams at Ljubljana and Birmingham for sometimes performing the irradiations on very short notice. Special thanks goes to the Birmingham team for their help with the irradiation for the shallow damage layer creation.

Last but not least I want to thank my family very much for all their support.